



HAL
open science

In operando study of lithium batteries by coupling X-ray photoelectron spectroscopy and impedance spectroscopy

Jorge Eduardo Morales Ugarte

► To cite this version:

Jorge Eduardo Morales Ugarte. In operando study of lithium batteries by coupling X-ray photoelectron spectroscopy and impedance spectroscopy. Chemical Physics [physics.chem-ph]. Université Grenoble Alpes, 2019. English. NNT : 2019GREAI082 . tel-02506388

HAL Id: tel-02506388

<https://theses.hal.science/tel-02506388>

Submitted on 12 Mar 2020

HAL is a multi-disciplinary open access archive for the deposit and dissemination of scientific research documents, whether they are published or not. The documents may come from teaching and research institutions in France or abroad, or from public or private research centers.

L'archive ouverte pluridisciplinaire **HAL**, est destinée au dépôt et à la diffusion de documents scientifiques de niveau recherche, publiés ou non, émanant des établissements d'enseignement et de recherche français ou étrangers, des laboratoires publics ou privés.

THÈSE

Pour obtenir le grade de

DOCTEUR DE LA COMMUNAUTE UNIVERSITE GRENOBLE ALPES

Spécialité : Matériaux, Mécanique, Génie civil, Electrochimie (2MGE)

Arrêté ministériel : 25 mai 2016

Présentée par

Jorge Eduardo MORALES UGARTE

Thèse dirigée par **Renaud BOUCHET**, Professeur, Grenoble INP et co-dirigée par **Anass BENAYAD** Ingénieur de recherche, CEA Grenoble et co-encadrée par **Catherine SANTINI**, Directeur de recherche CNRS.

Préparée au sein de la **Plateforme de Nanocaractérisation (CEA-LITEN)** et du **Laboratoire d'Electrochimie et de Physico-Chimie des Matériaux et des Interfaces (LEPMI)** dans l'**École Doctorale Ingénierie - Matériaux, Mécanique, Environnement, Energétique, Procédés, Production (I-MEP2)**

Étude *operando* des accumulateurs au lithium par couplage de spectroscopie à photoémission des rayons X et spectroscopie d'impédance

***In operando* study of lithium batteries by coupling X-ray photoelectron spectroscopy and impedance spectroscopy**

Thèse soutenue publiquement le **10 décembre 2019**, devant le jury composé de :

Madame Fannie ALLOIN

Directeur de recherche, LEPMI INP-Grenoble, Présidente du jury

Monsieur Arnaud ETCHEBERRY

Directeur de recherche émérite, Institut Lavoisier de Versailles (ILV), Rapporteur

Monsieur François TRAN VAN

Professeur, Université de Tours, Rapporteur

Monsieur Michel ARMAND

Directeur de recherche émérite, CIC EnergiGUNE, Examineur

Monsieur Renaud BOUCHET

Professeur, LEPMI INP-Grenoble, Directeur de thèse

Monsieur Anass BENAYAD

Ingénieur de recherche, CEA Grenoble, co-directeur de thèse

Madame Catherine SANTINI

Directeur de recherche, LCOMS C2P2 Lyon, co-encadrante de thèse



Remerciements

Ce travail a été réalisé dans le cadre d'une collaboration entre le CEA-LITEN, particulièrement la Plateforme de Nanocaractérisation PFNC, le LEPMI et le laboratoire C2P2 de Lyon et financé par FONDECYT-CONCYTEC. Je tiens à remercier les responsables des différentes institutes qui m'ont permis la réalisation de ce projet de thèse, dans les meilleures conditions financières et techniques.

Mes remerciements s'adressent aux messieurs Arnaud Etcheverry (directeur de recherche CNRS - ILV Versailles) et Francois Tran Van (professeur - Université de Tours) pour l'honneur qu'ils m'ont fait en acceptant de juger ce travail en tant que rapporteurs.

Je remercie Mme. Fannie Alloin (directrice de recherche CNRS - LEPMI) pour sa participation à mon jury de thèse et son temps.

Je remercie également M. Michel Armand (directeur de recherche CNRS - CIC EnergiGUNE) d'avoir accepté de juger ce travail en consacrant une partie de son temps et pour sa participation à mon jury de thèse.

Je remercie les trois personnes qui m'ont guidé pendant toutes ces années : mon directeur de thèse, Pr. Renaud Bouchet, et mes encadrants, Dr. Anass Benayad et Dr. Catherine Santini. Je vous remercie pour votre patience, encouragement et suivi de ce travail. Merci pour les discussions pendant nos réunions et votre aide dans la rédaction du manuscrit. Pour m'avoir appris le XPS, l'impédance et les liquides ioniques.

Il a été un plaisir de pouvoir travailler à la PFNC où j'ai eu l'occasion de trouver des permanents, post-docs, thésards et stagiaires avec d'excellentes qualités personnelles. Ma gratitude spécialement à : Mathieu F., Djawhar F., Arnaud B., Viktoriia G., Eric L., Amal B., Maxime G., Valentin A., Manon B., Amanda G., Jayanth C., Munique M., Charlotte Z., Luis G., Vincent G., Zineb F., Rohmer L., Yagmur C, Youcef K, Julien S., Taylor B., Lucien P.

Ma gratitude aussi pour les ingénieurs, chercheurs et techniciens du DEHT-CEA bâtiment C2, ainsi comme ceux qui j'ai côtoyés au quotidien du groupe MIEL-LEPMI qui ont contribué à ma formation et m'ont aidé avec les manip pendant ma thèse.

Un reconocimiento especial a mis colegas de oficina: Maiglid M., Maria P., Pablo F. y Carla X.

Este trabajo no hubiera sido posible sin el apoyo de mis amigos peruanos y latinos que me han ayudado a soportar el día a día en esta aventura grenoblense.

Por ultimo agradezco a toda mi familia (María Elena, Dante, Diana, Sonia) por su continuo apoyo a pesar de todos estos años lejos de ellos.

Acknowledgement

This research was funded by “Fondo Nacional de Desarrollo Científico, Tecnológico y de Innovación Tecnológica” FONDECYT-CONCYTEC-PERU (grant contract number 232-2015-FONDECYT).

Table of contents

General introduction	1
CHAPTER 1: General aspects and state of the art	7
1.1. Introduction.....	8
1.2. Basic fundamentals of lithium metal battery system.....	10
1.3. Electrode materials.....	11
1.3.1. Positive electrodes.....	11
1.3.2. Negative electrodes.....	13
1.4. Electrolytes.....	14
1.5. Ionic liquids based electrolytes.....	15
1.6. The solid electrolyte interphase.....	19
1.6.1. Historical background.....	19
1.6.2. Characterization of the SEI.....	20
1.7. SEI in IL-based electrolytes accumulators.....	24
1.8. Challenges of the SEI face to lithium dendrite growth.....	25
1.9. Characterization of the dendrite nucleation and growth.....	27
1.9.1. Morphology of the dendrites and the Chazalviel's model.....	27
1.9.2. Dendrite observations with IL based electrolytes.....	29
1.10. Strategies to mitigate dendrite growth.....	30
1.10.1. Stabilizing the SEI with additives.....	30
1.10.2. Building an artificial SEI layer.....	31
1.10.3. Enhancing of the shear modulus of the electrolyte.....	31
1.10.4. Effect of surface roughness.....	32
1.11. The <i>operando</i> protocols of characterization.....	32
1.12. Conclusions and objectives of the thesis.....	33
CHAPTER 2: Methodologies and reference studies	47
2.1. Introduction.....	48
2.2. Methodology.....	49
2.3. Experimental part.....	50
2.3.1. Imidazolium ionic liquids based electrolyte synthesis.....	50
2.3.2. Electrolyte preparation.....	52
2.3.3. Assembly of the electrochemical systems.....	53
2.3.4. Ionic conductivity measurements.....	54
2.4. Characterization protocols.....	55
2.4.1. Electrochemical impedance spectroscopy.....	55
2.4.2. Cyclic voltammetry.....	56

2.4.3.	X-ray photoelectron spectroscopy.....	56
2.4.4.	Scanning electron microscopy and Auger spectroscopy.....	58
2.5.	Reference study of the ILs electrolytes.....	58
2.5.1.	Ionic conductivity of the ILs.....	58
2.5.2.	Characterization by XPS of the neat ILs, the associated electrolytes and organic doped ILs.....	63
2.5.3.	Characterization of the pristine lithium electrode by XPS.....	72
2.6.	Conclusions.....	74

CHAPTER 3: Stability of ionic liquids based electrolytes in contact with lithium metal in open-circuit condition..... 79

3.1.	Introduction.....	80
3.2.	Study of the stability of IL based electrolytes at OCV.....	82
3.2.1.	Evolution of the electrolyte and interphase resistances.....	82
3.2.2.	Chemical environment evolution of the bulk electrolyte and the interface upon aging at OCV conditions.....	94
3.2.3.	Intermediate conclusions about the degradation mechanisms.....	101
3.3.	Effect of cation methylation and ILs based electrolyte solvent doping.....	105
3.3.1.	The effect of the methylation.....	106
3.3.2.	The effect of the additives.....	108
3.4.	Conclusions.....	111

CHAPTER 4: Behavior of the ionic liquid based electrolytes in contact with lithium metal under polarization..... 116

4.1.	Introduction.....	117
4.2.	Electrochemical window of the IL-based electrolytes.....	118
4.2.1.	Literature review.....	118
4.2.2.	IL-based electrolytes behavior under oxidation.....	120
4.2.3.	Effect of the additives and the cations.....	122
4.2.4.	Behavior of the IL-based electrolytes under reduction.....	126
4.2.5.	Performances of the IL-based electrolytes below 0 V vs. Li ⁺ /Li.....	128
4.5.	Study by XPS of the reduction of the system lithium/copper.....	129
4.6.	The Li/Li system under the application of an electrical current.....	136
4.6.1.	Experimental part.....	136
4.6.2.	The Chazalviel's model.....	137
4.6.3.	Experimental verification of the inverse-square law $\tau \propto 1/J^2$	141
4.6.4.	Transport properties of the electrolytes.....	146
4.7.	<i>Post-mortem</i> XPS analysis of the cells after chronopotentiometry.....	151
4.8.	SEM/AES analyses of the electrodes after chronopotentiometry.....	155
4.8.1.	The regime of divergence of the potential.....	155

4.8.2.	The regime of short-circuits	157
4.9.	Conclusions	159
CHAPTER 5: Operando XPS a novel approach for the study of lithium/electrolyte interphase.....		164
5.1.	Introduction	165
5.2.	Operando characterization for battery technology	165
5.2.1.	Optical techniques	166
5.2.2.	Electron beam based techniques.....	168
5.2.3.	X-ray techniques	171
5.2.4.	Scanning Probe Microscopy.....	171
5.2.5.	Neutron based techniques.....	172
5.2.6.	X-ray photoelectrons spectroscopy	172
5.2.7.	Conclusion.....	174
5.3.	OXPS Experimental set-up	174
5.3.1.	XPS spectrometer and sample holder up-grade.....	174
5.3.2.	Cell design.....	176
5.3.3.	OXPS sampling and protocol	177
5.3.4.	OXPS sample optimization and connectivity to the potentiostat	178
5.3.5.	X-ray beam and acquisition parameter optimization.....	179
5.4.	OXPS study of the interface lithium/imidazolium based IL electrolyte, result and discussion	180
5.4.1.	OXPS study of lithium/IL based electrolyte/lithium under chronoamperometry 180	
5.4.2.	OXPS study of lithium/IL based electrolyte/lithium at the OCV.....	182
5.4.3.	OXPS study of the interface Lithium/IL electrolyte under polarization	183
5.5.	Conclusions	187
General conclusions		191
APPENDIX 1: Electrochemical impedance spectroscopy		195
APPENDIX 2: X-ray photoelectron spectroscopy		200
APPENDIX 3: Binding energies, relative atomic concentrations and FWHM of the XPS core levels of IL based electrolytes.....		204

General introduction

The energy constitutes a vital element for our daily life. The consumption of energies based on oil, coal, gas and hydraulic sources have contributed to increase the quality of life in the modern society. Nonetheless, this accelerated development requires the replacement of the energy based on fossil energy by alternative sources such as solar, wind, geothermal, hydrogen and biofuel. Moreover, these alternative energies need of performant storage systems that ensure the correct management of the energy demand.^{1,2}

Among the entire range of energy storage systems, the lithium-ion batteries (LIB) occupy a preponderant position because of its extended use in most of the electronic mobile devices and in the growing industry of the electric vehicles.^{3,4} In order to satisfy all of these demands, LIB must overcome several challenges: be safer and able to furnish an important energy density ($>350\text{Wh/kg}$), lower price ($<100\$/\text{kWh}$), allow several cycles of charge-discharge and extended life.⁵⁻⁷ Therefore, current research is intended to find an optimal combination of electrode materials with non-flammable and electrochemically stable electrolytes.

In this context, ionic liquids (ILs),⁸⁻¹⁰ molten salts at room temperature, have been regarded as new solvents for batteries because of their extraordinary properties included a retarded inflammability, high thermal (up to $300\text{ }^\circ\text{C}$)¹¹ and electrochemical stability (electrochemical window up to 5 V)¹² and low vapor pressure ($\sim 10^{-10}\text{ Pa}$ at room temperature).^{13,14}

Regarding the ILs, several studies have been carried out in the context of the collaboration between the CEA-LITEN-Grenoble and C2P2-LCOMS-Lyon. For instance, the performances of several imidazolium-based ILs have been tested with relative success in the systems: $\text{Li}_4\text{Ti}_5\text{O}_{12}$ (LTO) / LiFePO_4 (LFP), graphite (C_{gr}) / LFP and LTO/ $\text{LiNi}_{1/3}\text{Mn}_{1/3}\text{Co}_{1/3}\text{O}_2$ (NMC).^{15,16}

On the other hand, lithium metal is considered as the ultimate anode for batteries because of its large theoretical electrochemical capacity ($3.86\text{ Ah}\cdot\text{g}^{-1}$) and the fact that have the lowest electrochemical potential (-3.04 V vs. standard hydrogen electrode).¹⁷⁻¹⁹ However, the performances of lithium metal batteries (LMB) are seriously affected by

the phenomenon of dendrite growth^{20–24} and the side reactions between the electrolyte and the lithium surface. For this reason, a detailed study of the interfaces electrolyte/lithium metal is necessary for the viability of these systems.

The electrochemical processes happening at this interphase are intimately related to the formation of passive layers on the lithium surface, commonly known as the solid electrolyte interphase (SEI).^{25,26} Among all the characterization techniques of the SEI, the electrochemical impedance spectroscopy (EIS)^{27,28} considered to be non-destructive, can provide in real time during the information on the electrical properties of the electrode/electrolyte interphase during the battery operating (*operando* mode). Nonetheless, the EIS does not inform about the morphology and chemical composition of the SEI. These data require surface sensitive characterization techniques, such as X-ray photoelectron spectroscopy (XPS)

In this work, we have developed a methodology coupling EIS and XPS, supported by Auger and scanning electron microscopy (AES/SEM). Specially, XPS a non-destructive technique with a depth resolution of ~5 nm, is ideal to follow of the chemical evolution of the SEI in different electrochemical conditions.

During my Master internship, in the context of the CEA-LITEN-Grenoble and C2P2-LCOMS-Lyon collaboration, we have applied this methodology to the study the reaction of ILs with graphite electrodes at open circuit conditions,²⁹ and during the first discharge cycle.³⁰ In my PhD work, these studies were extended to the lithium metal electrodes, in collaboration with the LEPMI-INP-Grenoble laboratory.

To our knowledge, the literature about of the reactivity of IL based electrolytes with lithium metal is partial,^{31–34} and several questions about the thickness, morphology, chemical composition of the SEI and the degradation mechanisms and transport properties of the IL based electrolytes remain not well understood as far as the problem of the formation of the dendrites.

Therefore, in this PhD work, we propose to compare the reactivity of lithium metal *vis-à-vis* two different ILs: 1-hexyl-3-methylimidazolium bis(trifluoromethylsulfonyl)imide (C₁C₆ImTFSI) and 1-hexyl-3-methyl-imidazolium

bis(fluorosulfonyl)imide (C_1C_6ImFSI). In addition, two strategies to improve the stability and the performance of these ILs are tested : the methylation of the $C_1C_6Im^+$ cation,³⁵ and the use of organic additives such as vinylene carbonate (VC) and fluoroethylenecarbonate (FEC),^{36,37} both modifying the molecular structure of the electrolytes and their physicochemical properties such as the viscosity.

Additionally, all of these studies constitute a solid base for the development of a new protocol of characterization of interphases by the *operando* XPS technique. This new analytical development, allows to monitor the change in the chemical environment of the SEI at quasi-real time and pave the way for a better understanding of its formation and evolution and its impact on the dendrite growth.

This work of thesis is outlined as follows:

In chapter 1, a basic description about the lithium based batteries is given introducing the current challenges in these systems. The most important electrode materials and electrolytes are also described, with emphasis in the ILs as safer electrolytes. Then, the concept of SEI is introduced by describing its main properties as far as the techniques used for its characterization. Special interest is given to the SEI formed in the lithium metal electrode and its impact in the performances and the dendrite growth.

In chapter 2, we detail the methodology, coupling electrochemical techniques with physicochemical surface analysis techniques of characterization, used to study the reference IL based electrolytes and the pristine lithium electrode surface. Further to the reference study, we have established, based on EIS measurements, a simple model to correlate ionic conductivities of the different IL and IL based electrolytes to their electronic structure probed by XPS. This reference study was extended to the chemical structure of pristine lithium foil surface before its use in a battery system.

The chapter 3 is devoted to the study of the reactivity of the IL based electrolytes against lithium metal electrodes in open circuit conditions. The phenomena of decomposition of the IL based electrolyte and the mechanisms of formation of a SEI are studied in mode *operando* by EIS and through the *post-mortem* analysis of Li/IL electrolyte/Li coin cells by XPS. A comparison of the estimated thicknesses and the

chemical compositions of the SEI with different IL based electrolytes is showed. The role of the methylation of the alkyl methyl imidazolium ($C_1C_nIm^+$) and the addition of additives VC and FEC is analyzed.

The chapter 4, treat the behavior of the different lithium/IL electrolytes/lithium under polarization. The kinetic of dendrite growth in the different studied system was studied in the framework of J. N. Chazalviel model.^{38–40} A correlation between the electrochemical window stability of different studied electrolyte and the SEI formation and composition was established. The SEI chemical structure as far as the transport properties were discussed with regard the nature of the electrolyte, for instance the effect of the anion, cation and additives.

Finally, the chapter 5 is dedicated to the development of a new and challenging methodology to perform *operando* XPS to study the interface lithium/electrolyte. A state of the art of the developed *operando* techniques for battery characterization is presented. The detailed protocols including, cell design, set-up optimization and cell cycling and validation is discussed based on coupled post-mortem and *operando* approach.

REFERENCES

- (1) Whittingham, M. S. History, Evolution, and Future Status of Energy Storage. *Proc. IEEE* **2012**, 100 (Special Centennial Issue), 1518–1534.
- (2) Acar, C. A Comprehensive Evaluation of Energy Storage Options for Better Sustainability. *Int. J. Energy Res.* **2018**, 42(12), 3732–3746.
- (3) Tarascon, J. M.; Armand, M. Issues and Challenges Facing Rechargeable Lithium Batteries. *Nature* **2001**, 414 (November), 359–367.
- (4) Armand, M.; Tarascon, J.-M. Building Better Batteries. *Nature* **2008**, 451 (7179), 652–657.
- (5) Tarascon, J. M. Key Challenges in Future Li-Battery Research. *Philos. Trans. R. Soc. A Math. Phys. Eng. Sci.* **2010**, 368 (1923), 3227–3241.
- (6) Van Noorden, R. The Rechargeable Revolution: A Better Battery. *Nature* **2014**, 507 (7490), 26–28.
- (7) Liu, J.; Bao, Z.; Cui, Y.; Dufek, E. J.; Goodenough, J. B.; Khalifah, P.; Li, Q.; Liaw, B. Y.; Liu, P.; Manthiram, A.; et al. Pathways for Practical High-Energy Long-Cycling Lithium Metal Batteries. *Nat. Energy* **2019**, 4 (3), 180–186.
- (8) Holbrey, J. D.; Seddon, K. R. Ionic Liquids. *Clean Technol. Environ. Policy* **1999**, 1 (4), 223–236.
- (9) Armand, M.; Endres, F.; MacFarlane, D. R.; Ohno, H.; Scrosati, B. Ionic-Liquid Materials for the Electrochemical Challenges of the Future. *Nat. Mater.* **2009**, 8 (8), 621–629.
- (10) Appetecchi, G. B.; Montanino, M.; Passerini, S. Ionic Liquid-Based Electrolytes for High Energy, Safer Lithium Batteries. *ACS Symp. Ser.* **2012**, 1117 (January),

- 67–128.
- (11) Lewandowski, A.; Świdzka-Mocek, A. Ionic Liquids as Electrolytes for Li-Ion Batteries—An Overview of Electrochemical Studies. *J. Power Sources* **2009**, 194 (2), 601–609.
 - (12) Galiński, M.; Lewandowski, A.; Stepniak, I. Ionic Liquids as Electrolytes. *Electrochim. Acta* **2006**, 51 (26), 5567–5580.
 - (13) Bier, M.; Dietrich, S. Vapor Pressure of Ionic Liquids. *Molecular Physics*, Taylor & Francis, **2010**, 108 (02), 211–214.
 - (14) Paulechka, Y. U.; Zaitsau, D. H.; Kabo, G. J.; Strechan, A. A. Vapor Pressure and Thermal Stability of Ionic Liquid 1-Butyl-3-Methylimidazolium Bis (Trifluoromethylsulfonyl) Amide. **2005**, 439, 158–160.
 - (15) Srour, H.; Rouault, H.; Santini, C. C. Study on Cycling Performance and Electrochemical Stability of 1-Hexyl-3-Methylimidazolium Bis(Trifluoromethanesulfonyl)Imide Assembled with $\text{Li}_4\text{Ti}_5\text{O}_{12}$ and LiFePO_4 at 333 K. *J. Electrochem. Soc.* **2013**, 160 (6), A781–A785.
 - (16) Srour, H.; Chancelier, L.; Bolimowska, E.; Gutel, T.; Mailley, S.; Rouault, H.; Santini, C. C. Ionic Liquid-Based Electrolytes for Lithium-Ion Batteries: Review of Performances of Various Electrode Systems. *J. Appl. Electrochem.* **2016**, 46 (2), 149–155.
 - (17) Cheng, X.-B.; Zhang, R.; Zhao, C.-Z.; Zhang, Q. Toward Safe Lithium Metal Anode in Rechargeable Batteries: A Review. *Chem. Rev.* **2017**, 117, 15, 10403–10473.
 - (18) Lin, D.; Liu, Y.; Cui, Y. Reviving the Lithium Metal Anode for High-Energy Batteries. *Nat. Publ. Gr.* **2017**, 12 (3), 194–206.
 - (19) Xu, W.; Wang, J.; Ding, F.; Chen, X.; Nasybulin, E.; Zhang, Y.; Zhang, J.-G. Lithium Metal Anodes for Rechargeable Batteries. *Energy Environ. Sci.* **2014**, 7 (2), 513–537.
 - (20) Steiger, J.; Kramer, D.; Mönig, R. Mechanisms of Dendritic Growth Investigated by in Situ Light Microscopy during Electrodeposition and Dissolution of Lithium. *J. Power Sources* **2014**, 261, 112–119.
 - (21) Li, L.; Li, S.; Lu, Y. Suppression of Dendritic Lithium Growth in Lithium Metal-Based Batteries. *Chem. Commun.* **2018**, 54 (50), 6648–6661.
 - (22) Brissot, C.; Rosso, M.; Chazalviel, J. N.; Baudry, P.; Lascaud, S. In Situ Study of Dendritic Growth in Lithium/PEO-Salt/Lithium Cells. *Electrochim. Acta* **1998**, 43, 10–11, 1569–1574.
 - (23) Rosso, M.; Brissot, C.; Teyssot, A.; Dollé, M.; Sannier, L.; Tarascon, J. M.; Bouchet, R.; Lascaud, S. Dendrite Short-Circuit and Fuse Effect on Li/Polymer/Li Cells. *Electrochim. Acta* **2006**, 51 (25), 5334–5340.
 - (24) Nishikawa, K.; Mori, T.; Nishida, T.; Fukunaka, Y.; Rosso, M. Li Dendrite Growth and Li^+ Ionic Mass Transfer Phenomenon. *J. Electroanal. Chem.* **2011**, 661 (1), 84–89.
 - (25) Peled, E. The Electrochemical Behavior of Alkali and Alkaline Earth Metals in Nonaqueous Battery Systems—The Solid Electrolyte Interphase Model. *J. Electrochem. Soc.* **1979**, 126 (12), 2047.
 - (26) Peled, E. Film Forming Reaction at the Lithium/Electrolyte Interface. *J. Power Sources* **1983**, 9 (3), 253–266.
 - (27) Aurbach, D.; Zaban, A. Impedance Spectroscopy of Lithium Electrodes. *J. Electroanal. Chem.* **1993**, 348 (1–2), 155–179.
 - (28) Qu, D.; Wang, G.; Kafle, J.; Harris, J.; Crain, L.; Jin, Z.; Zheng, D. Electrochemical Impedance and Its Applications in Energy-Storage Systems. *Small Methods* **2018**,

- 2 (8), 1700342.
- (29) Bolimowska, E.; Morales-Ugarte, J. E.; Rouault, H.; Santos-Peña, J.; Santini, C.; Benayad, A. Influence of the Vinylene Carbonate on the Wetting and Interface Chemical Structure of Doped Ionic Liquid Electrolyte at Porous Graphite Surface. *J. Phys. Chem. C* **2017**, 121 (30), 16166–16173.
- (30) Morales-Ugarte, J. E.; Bolimowska, E.; Rouault, H.; Santos-Peña, J.; Santini, C. C.; Benayad, A. EIS and XPS Investigation on SEI Layer Formation during First Discharge on Graphite Electrode with a Vinylene Carbonate Doped Imidazolium Based Ionic Liquid Electrolyte. *J. Phys. Chem. C* **2018**, 122 (32), 18223–18230.
- (31) Howlett, P. C.; Brack, N.; Hollenkamp, a. F.; Forsyth, M.; MacFarlane, D. R. Characterization of the Lithium Surface in N-Methyl-N-Alkylpyrrolidinium Bis(Trifluoromethanesulfonyl)Amide Room-Temperature Ionic Liquid Electrolytes. *J. Electrochem. Soc.* **2006**, 153 (3), A595-A606.
- (32) Best, a. S.; Bhatt, a. I.; Hollenkamp, a. F. Ionic Liquids with the Bis(Fluorosulfonyl)Imide Anion: Electrochemical Properties and Applications in Battery Technology. *J. Electrochem. Soc.* **2010**, 157 (8), A903-A911.
- (33) Basile, A.; Bhatt, A. I.; O'Mullane, A. P. Stabilizing Lithium Metal Using Ionic Liquids for Long-Lived Batteries. *Nat. Commun.* **2016**, 7 (11794), 1–11.
- (34) Schmitz, P.; Jakelski, R.; Pyschik, M.; Jalkanen, K.; Nowak, S.; Winter, M.; Bieker, P. Decomposition of Imidazolium-Based Ionic Liquids in Contact with Lithium Metal. *ChemSusChem* **2017**, 10 (5), 876–883.
- (35) Noack, K.; Schulz, P. S.; Paape, N.; Kiefer, J.; Wasserscheid, P.; Leipertz, A. The Role of the C2 Position in Interionic Interactions of Imidazolium Based Ionic Liquids: A Vibrational and NMR Spectroscopic Study. *Phys. Chem. Chem. Phys.* **2010**, 12 (42), 14153–14161.
- (36) Michan, A. L.; Parimalam, B. S.; Leskes, M.; Kerber, R. N.; Yoon, T.; Grey, C. P.; Lucht, B. L. Fluoroethylene Carbonate and Vinylene Carbonate Reduction: Understanding Lithium-Ion Battery Electrolyte Additives and Solid Electrolyte Interphase Formation. *Chem. Mater.* **2016**, 28 (22), 8149–8159.
- (37) Zhang, X. Q.; Cheng, X. B.; Chen, X.; Yan, C.; Zhang, Q. Fluoroethylene Carbonate Additives to Render Uniform Li Deposits in Lithium Metal Batteries. *Adv. Funct. Mater.* **2017**, 27 (10), 1–8.
- (38) Chazalviel, J. N. Electrochemical Aspects of the Generation of Ramified Metallic Electrodeposits. *Phys. Rev. A* **1990**, 42 (12), 7355–7367.
- (39) Brissot, C.; Rosso, M.; Chazalviel, J. N.; Lascaud, S. Dendritic Growth Mechanisms in Lithium/Polymer Cells. *J. Power Sources* **1999**, 81-82, 925–929.
- (40) Rosso, M.; Gobron, T.; Brissot, C.; Chazalviel, J. N.; Lascaud, S. Onset of Dendritic Growth in Lithium/Polymer Cells. *J. Power Sources* **2001**, 97–98, 804–806.

CHAPTER 1: General aspects and state of the art

In this first chapter, the different technologies of batteries and the current challenges of the lithium metal based batteries are introduced. A general insight about the different electrode materials and electrolytes is presented given emphasis in the electrolytes based on ionic liquids as a possible solution to mitigate the safety problems of flammable electrolytes. The different studies about the interactions of electrolytes and electrodes that lead to the formation of a solid electrolyte interphase (SEI) are discussed. To introduce the work of this thesis a special interest is given to the formation of the SEI on lithium metal electrode surfaces and of its impact on the battery performance and on the dendritic growth that constitute one of the main impediments for the commercialization of lithium metal battery systems.

1.1.	Introduction	8
1.2.	Basic fundamentals of lithium metal battery system.....	10
1.3.	Electrode materials	11
1.3.1.	Positive electrodes.....	11
1.3.2.	Negative electrodes	13
1.4.	Electrolytes.....	14
1.5.	Ionic liquids based electrolytes	15
1.6.	The solid electrolyte interphase.....	19
1.6.1.	Historical background	19
1.6.2.	Characterization of the SEI	20
1.7.	SEI in IL-based electrolytes accumulators	24
1.8.	Challenges of the SEI face to lithium dendrite growth	25
1.9.	Characterization of the dendrite nucleation and growth.....	27
1.9.1.	Morphology of the dendrites and the Chazalviel's model.....	27
1.9.2.	Dendrite observations with IL based electrolytes	29
1.10.	Strategies to mitigate dendrite growth.....	30
1.10.1.	Stabilizing the SEI with additives	30
1.10.2.	Building an artificial SEI layer.....	31
1.10.3.	Enhancing of the shear modulus of the electrolyte	31
1.10.4.	Effect of surface roughness	32
1.11.	The <i>operando</i> protocols of characterization.....	32
1.12.	Objectives of the thesis	33

1.1.Introduction

Increasing world population and rise in standards of living have been the two reasons behind ever growing energy demand.¹ During the last two centuries, the production of energy has been sustained by the discovery and exploitation of fossil fuels such as coal, oil and natural gas. In order to mitigate the impact of this exploitation in the economy as far as in the pollution of the environment, alternative sources to fossil fuels like hydroelectric, nuclear, and renewable energies are taken into account for a more sustainable development of the society.

In contrast with the hydroelectric (limited and geo-localized) and nuclear energies (nonrenewable with safety and recycling concerns), renewable sources (RS) based on wind and sun offer potential game-changing clean energy. Unfortunately, they are intermittent sources that cannot be reinjected directly in the grid. All these RS would benefit from powerful energy storage units, like high-energy batteries, to properly balance source variability with the substantial variability in demand for power.²

A battery is an electrochemical device that converts chemical energy into electric energy through electrochemical reactions occurring at the electrodes, which are separated by an electrolyte. Different technologies of batteries have been developed since the 19th century such as lead-acid, nickel-cadmium, lithium-ion batteries (LIB) and lithium metal batteries (LMB). All these technologies are compared in Figure 1.1-a and contrasted with other chemical storage media, Figure 1.1-b.

By the year 2017, the best commercial Li-ion cells were able to furnish a specific energy density of 250 Wh.kg⁻¹ and a volumetric energy density of 700 Wh.L⁻¹.³ Nonetheless, further increasing of the specific energy density requires electrode materials with higher capacity and/or that give higher cell voltage.

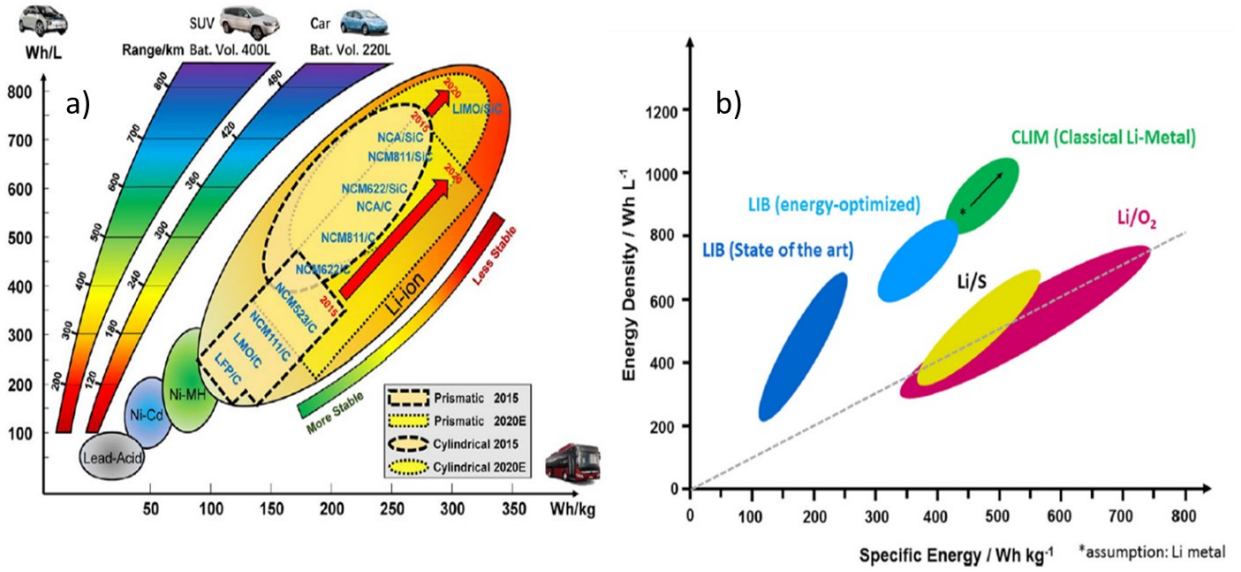


Figure 1.1 a) Comparison of the different battery technologies in terms of volumetric and gravimetric energy density and roadmap for the LIB,⁴ b) Comparison between the current LIB technology and the future developments including LMB, Li-S and Li-O₂.⁵

Figure 1.2 shows the energy consumption of the main applications powered by batteries. Clearly, current technologies need an increase of energy density in order to integrate a new generation of electric vehicles that would pave the way to a sustainable transportation system.

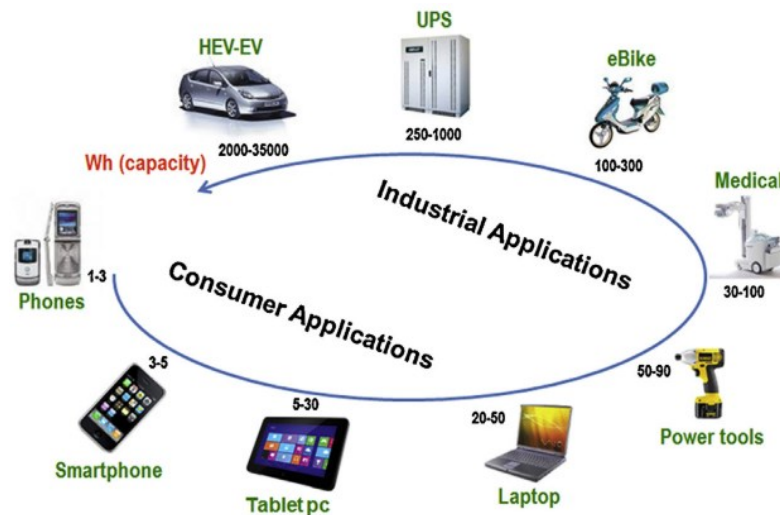


Figure 1.2 The scope of use of rechargeable batteries.⁶

1.2. Basic fundamentals of lithium metal battery system

In a general way, a Li-ion battery is constituted by two electrodes (positive and negative) separated by a porous separator soaked by a polar electrolyte. The current trend for the next generation of batteries goes with drastic safety requirements, especially when it concerns LMB technology. In this frame, the battery design intends to either modify lithium surface through passivation (*ex* and *in situ*) to reduce or control the lithium dendrite growth or by the replacement of volatile organic electrolyte by non-flammable electrolyte. Another approach is emerging and consists on building an all-solid-state battery by replacing the separator-electrolyte system by a solid electrolyte such as a polymer electrolyte (SPE), gel polymer electrolyte (GPE) or ceramic conducting electrolyte.⁷⁻¹⁰

The operating principle of this battery is depicted in Figure 1.3. The negative electrode is lithium metal. The positive electrode is composed by a host material ([H]) that allows the insertion and disinsertion of the Li^+ ions. In electrochemistry, we distinguished the anode as the electrode at which the oxidation reaction occurs, and the cathode as the electrode at which the reduction reaction occurs.

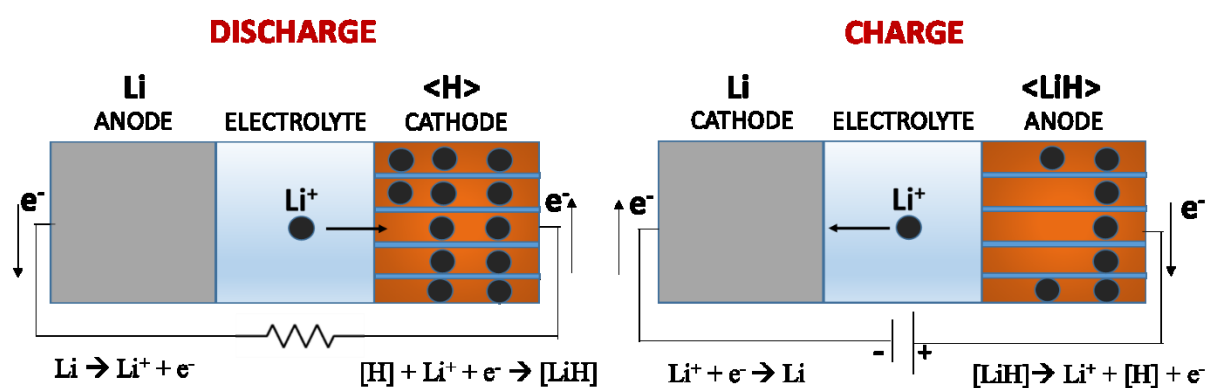


Figure 1.3 Scheme of the redox processes happening in a battery during charge and discharge.

During the discharge step, a lithium oxidation takes place at the negative electrode (anode). The Li^+ ions cross the electrolyte to be inserted into the host material, whereas the electrons travel through the external circuit and participate to the reduction at the positive electrode (cathode). During the charge process, the reverse reactions occur: the oxidation takes place at the positive electrode (anode) and the reduction at the negative electrode (cathode). These processes are resumed in Table 1.1.

Table 1.1 Redox reactions happening during the discharge and charge of a LMB.

	Positive electrode	Negative electrode
Discharge	$[H] + Li^+ + e^- \rightarrow [LiH]$	$Li \rightarrow Li^+ + e^-$
Charge	$[LiH] \rightarrow [H] + Li^+ + e^-$	$Li^+ + e^- \rightarrow Li$

From practical perspectives, the lithium batteries must provide high energy density, long cycle life, high safety, and being low cost. The cycle life of a battery is strongly affected by numerous factors: the solid electrolyte interphase (SEI) formation, dendrite growth, irreversible redox process, etc., that are driven by temperature, cycling rate.

1.3. Electrode materials

1.3.1. Positive electrodes

The choice of electrode active materials must meet several requirements such as high potential with regards to Li potential, good reversibility of the intercalation/deintercalation processes, high specific capacity together with high ionic/electronic conductivity.

Since the first TiS_2 electrode materials,^{11,12} research was focused on layered oxide transition material,¹³ such as lithium cobalt oxide ($LiCoO_2$, LCO), lithium nickel cobalt manganese oxide ($LiNi_{1-x-y}Mn_xCo_yO_2$, NMC), lithium nickel cobalt aluminum oxide ($LiNi_{1-x-y}Co_xAl_yO_2$, NCA) and tends to reach ultimate high potential metal oxide electrode $LiNiO_2$.¹⁴ The commercial LCO-based LIB can achieve a high voltage up to 3.7 V vs. Li^+/Li and delivers a quite stable capacity of $\sim 150 \text{ mAh.g}^{-1}$.¹⁵ The major limitations are high cost, low thermal stability, and capacity fade at high current rates or during deep cycling.¹⁶

In the same family of lamellar compounds, $LiNi_{0.33}Co_{0.33}Mn_{0.33}O_2$ (NMC 111) has already been commercialized for automobile applications due to its high capacity and outstanding safety characteristics. However, its capacity of 155 mAh.g^{-1} is quite low for use in next-generation EVs applications.¹⁷ Recently, a large part of the efforts have been focused on the variation of the stoichiometry between Ni, Co and Mn, knowing that i) Ni provides a high capacity but poor thermal stability, ii) Mn maintains the structural stability insuring the cycle life and safety, iii) Co offers increased electronic conductivity

resulting in an excellent rate capability. For instance, $\text{LiNi}_{0.8}\text{Co}_{0.1}\text{Mn}_{0.1}\text{O}_2$ (NMC 811) can achieve capacities up to 230 mAh.g^{-1} within a potential range of 3 to 4.5 V vs. Li^+/Li .¹⁸

NCA has high usable discharge capacity (200 mAh.g^{-1}) and long storage calendar life compared to conventional Co-based oxide cathode. NCA cathode has found relatively widespread commercial use, for example, in Panasonic batteries for Tesla EVs.¹⁹ However, it was reported that capacity fade may be severe at elevated temperature (40–70°C) due to solid electrolyte interphase (SEI) growth together with micro-cracks growth at grain boundaries.^{16,20,21}

In addition to the layered structures, two main other families have been investigated: the spinels,²² such as LiMn_2O_4 and the olivines,^{23,24} such as LiFePO_4 (LFP).

Spinel materials are a very attractive choice as cathode material for lithium-ion rechargeable batteries due to their economic and environmental advantages over LCO, however it suffers from a strong Mn dissolution which reduces the cycle life. Besides, a significant improvement in energy density (vs. Li) and cycle life was reported when adding a second transition element, *i.e.* $\text{LiM}_x\text{Mn}_{2-x}\text{O}_4$ with $M = \text{Ni}, \text{Co}, \text{and Cu}$.²⁵ Unfortunately, high potential (4.7 V vs. Li^+/Li) $\text{LiNi}_{0.5}\text{Mn}_{1.5}\text{O}_4$ always suffers from severe capacity deterioration and poor thermal stability because of the instability of carbonates based electrolytes,²⁶ and decomposition of LiPF_6 .²⁷

LFP is the representative material for the olivine structure with a capacity of 170 mAh.g^{-1} , a low cost compared to LCO and a high intrinsic safety. However, it owns a very low electrical conductivity. To improve this, carbon-coated LFP is an attracting cathode material for application in batteries designed for high power applications. Nonetheless, LFP has a low potential 3.43 V vs. Li^+/Li which reduces its energy density (vs. Li). Attention is also focused on alternate olivine material, such as LiMnPO_4 and LiCoPO_4 .²⁸

The vanadium pentoxide (V_2O_5) is a cathode material with a layered crystalline structure. This typical intercalation compound has large theoretical capacities of 294 mAh.g^{-1} for two Li^+ or 437 mAh.g^{-1} for three Li^+ intercalation/deintercalation,²⁹ which are much larger than those of traditional cathode materials, such as LCO and LFP.

However, V_2O_5 has disadvantages of low electrical conductivity and slow lithium ion diffusion, resulting in poor cycling stability and rate capability.³⁰

The vanadium oxides, LiV_3O_8 present interesting performance thanks to their high specific capacity with 3 Li intercalations/deintercalations about 280 mAh.g^{-1} . Nonetheless, this cathode suffers also from an inherently low electronic conductivity ($10^{-6} \text{ S.cm}^{-1}$) and reduced Li^+ diffusion coefficients ($10^{-13} \text{ cm}^2.s^{-1}$).³¹

1.3.2. Negative electrodes

Because of its properties, lithium seems to be the best choice as a material for negative electrode. It owns the lowest reduction potential of all known elements (-3.04 V vs. the standard hydrogen electrode (SHE)) and a theoretical specific capacity of 3860 mAh.g^{-1} allowing the realization of cells with an extremely high specific energy depending on the cathode material (Li-lithium transition oxide 440 Wh.kg^{-1} , Li-S 650 Wh.kg^{-1} and Li-air 950 Wh.kg^{-1}).³ Nonetheless, lithium metal based batteries suffer from two main problems: the growth of dendrites and the continuous consumption of lithium due to the continuous healing of SEI along cycling formation (i. e. low Coulombic efficiency).³²

To circumvent this issue, graphite has been proposed giving rise in the 90th to the well-known Li-ion technology. It shows a rather flat potential profile at potentials below 0.5 V vs. Li^+/Li , offering a specific capacity of 370 mAh.g^{-1} . Although graphite is the most used material in commercial LIB, it is still weak in terms of safety, as solvents can forcibly co-intercalate and exfoliate the graphite with large release of heat.^{33,34}

Several metalloid lithium alloys like Si, Sb, Sn, have been proposed as anode materials with capacities of 660, 994 and 3579 mAh.g^{-1} , respectively.³⁵ However, such materials suffer from volume expansion (until 400 % for the Si).³⁶ To overcome this issues several strategies including size control through nano-structuration or using their oxide form such as SnO, $SnSiO_x$.³⁷

Very promising alternative for graphite especially in power application is the spinel-structured $Li_4Ti_5O_{12}$ (LTO). However, LTO operates at a potential of about 1.55 V vs. Li^+/Li with a capacity of 170 mAh.g^{-1} . In spite of this inconvenient, LTO potential is far

from the lithium voltage plating and no dendritic formation can occur, which ensures good safety.³⁸

1.4. Electrolytes

The role of the electrolyte is to allow the ionic transfer between both, positive and negative, electrodes within broad electrochemical stability window, between 0 and 5 V vs. Li^+/Li , in order to avoid their degradation upon lithium intercalation/de-intercalation.

Electrolytes must have high ionic conductivity, above $1 \text{ mS}\cdot\text{cm}^{-1}$ at room temperature and low electronic conductivity. We can distinguish two families of electrolyte, solid ionic conductor based on ceramic or polymer, and liquid electrolytes.

Liquid electrolytes are mainly lithium salts (*e.g.*, lithium hexafluorophosphate (LiPF_6), lithium bis(trifluoromethanesulfonyl)imide (LiTFSI)), dissolved in aprotic organic solvents (ethylene carbonate (EC), diethyl carbonate (DEC), dimethyl carbonate (DMC) or ethyl methyl carbonate (EMC)) in order to assure the conduction of Li^+ ions in between the two electrodes. For instance, the combination $\text{LiPF}_6/\text{EC}/\text{DMC}$ is the prototype of electrolyte for LIB.

Among the alternative lithium salts, LiTFSI has the inconvenient to de-passivate the aluminum current collector of the positive electrode inducing its corrosion. This obstacle can be overcome by adding proper additives such as fluoroethylene carbonate (FEC) or vinylene carbonate (VC).³⁹

Recently, lithium bis(fluorosulfonyl)imide (LiFSI) has been of great interest because of their ability to form a relatively homogeneous (SEI) rich in LiF on the negative electrode without corroding of the aluminum current collector.⁴⁰ However, this salt has a poor thermal stability (decomposition temperature: 343 K) in comparison with the very stable LiTFSI (657 K).⁴¹

Regarding the electrolyte solvents, alkyl carbonates used in LIB are not the best choice for LMB because of their poor cathodic stability against lithium metal.³⁴ In contrast, the ether solvents favor the formation of compact and flat Li deposits with relatively higher

cycling efficiency whereas carbonate solvents lead to porous and dendritic Li deposits with lower cycling efficiency.⁴⁰ However, carbonate solvents have better oxidative stability, which is essential for the high-voltage Li batteries.

Ether solvents include 1,2-dimethoxyethane (DME, glyme), tetraethylene glycol dimethyl ether (TEGDME, tetraglyme), 1,3-dioxolane (DOL), 1, 4-dioxane (DX) and tetrahydrofuran (THF).⁴²⁻⁴⁴ In Table 1.2, a comparison of electrolyte ionic conductivities is given. Note that the conductivities are in the range of 1-10 mS.cm⁻².

However, the high vapor pressure and flammability of all these solvents lead to strong safety issues which impeded the mass development for large li-ion battery. One possible alternative is the use of ionic liquid.

Table 1.2 Ionic conductivities of LiPF₆ and LiTFSI salts dissolved in common organic solvents. All ionic conductivities are obtained for 1 mol.L⁻¹ of Li-salt dissolved in 1:1 solvent mixtures measured (a) by weight and (b) by volume at room temperature.⁴⁵

Salt	Solvent	Conductivity (mS.cm ⁻¹)
LiPF ₆	EC-DMC ^a	10.8
LiTFSI	EC-DMC ^a	9
LiTFSI	DME-DOL ^b	11
LiTFSI	TEGDME-DOL ^b	7

1.5. Ionic liquids based electrolytes

ILs are defined as molten salts having melting point at temperatures below 373 K. As ILs are constituted only by ions. The cation is commonly organic whereas the anion could be organic or inorganic. These ions are typically large and asymmetric in order to reduce the interaction between them. This explain their low melting points. They own some remarkable properties including retarded flammability, low vapor pressure ($\sim 10^{-10}$ Pa at room temperature), high temperature of decomposition (up to 573 K), and the ability to dissolve inorganic, organic and some polymer materials. They have been signaled as potential candidates for electrolytes solvents, electrodeposition, double layer supercapacitors, fuel cells, dye-sensitized solar cells, carbon dioxide reduction, water splitting and bioscience.^{33,41,46-49}

ILs are of great interest because of their safety properties. During the process of a battery charge, the heat developed, when it is not effectively dissipated, produces a fast increase of temperature that could trigger exothermic reactions with frequently destructive results of the main components of the battery and the risk of explosion and fire. This mechanism of battery failure is known as thermal runaway.^{4,50–52} However, the main inconvenient with ILs based electrolytes is their high viscosity which limits their transport properties. The low mobility of Li^+ results in low limiting current density in the Li-ion cells.⁵³

Positive electrode materials for the next generation of batteries need electrolytes with a high stability at high potentials ($> 4.5 \text{ V vs. Li}^+/\text{Li}$). Most of the electrolytes are not stable against lithium metal. contrary to the combination of conducting polymer and ILs, named as gel polymer electrolytes, which are at the spot light of lithium metal based battery.⁵⁴

In battery applications, the most popular choices of anion are by far the bis(trifluoromethanesulfonyl)imide (TFSI⁻ or NTf₂⁻) and the bis(fluorosulfonyl)imide (FSI⁻).⁴¹ The main cations and anions for batteries are given in Figure 1.4.

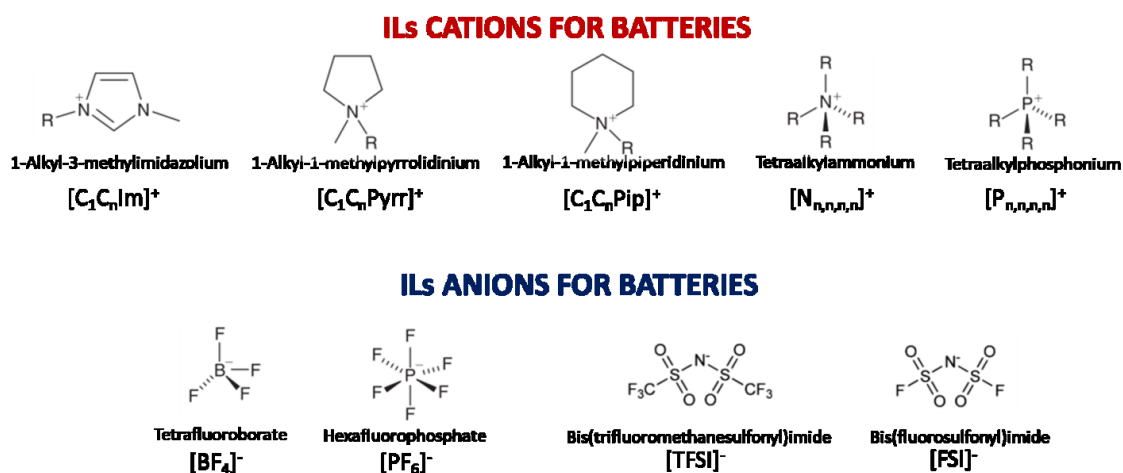


Figure 1.4 The list of most used cations and anions of ILs based electrolytes for lithium battery technology.⁵⁵

Regarding the cations, the 1-alkyl-3-methylimidazolium cation ($\text{C}_n\text{C}_1\text{Im}^+$) is constituted by an alkyl chain that can be tuned ($n = 1, 2, 3, \text{etc.}$) in order to get different electrochemical properties. Tokuda *et al.*⁵⁶ have studied the effect of the variation of the

alkyl chain length on melting points, density, viscosity, conductivity, and self-diffusion coefficients. For instance, $C_1C_2\text{ImTFSI}$ exhibits a higher density and conductivity than $C_1C_4\text{ImTFSI}$ and $C_1C_6\text{ImTFSI}$.

However, several reports indicate that imidazolium-based ILs are not stable at low potentials because of the acidity of the proton at the position C2 of the imidazolium ring.^{41,57,58} Thus, deprotonation of the imidazolium ring can occur with the formation of N-heterocyclic carbenes (NHCs) and other decomposition products.⁵⁹ Watanabe *et al.*⁴¹ indicated that cathodic decomposition at 303 K of $C_1C_2\text{Im}^+$ and pyridinium cations with TFSI anion occurs at 0.6 V vs. Li^+/Li and 1.6 V vs. Li^+/Li , respectively. These potentials are more positive than those for aliphatic quaternary ammonium (AQA, including pyrrolidinium and piperidinium) and aliphatic quaternary phosphonium (AQP) cations.^{60,61}

Improvement of the stability of the alkyl imidazolium cation by grafting a methyl group (*i.e.*, $C_1C_1C_n\text{Im}^+$) has been reported by Schmitz *et al.*⁶² Despite of this, the performance of $C_1C_1C_4\text{ImTFSI}/\text{LiTFSI}$ (0.3 mol.L^{-1}) in a Li/LFP system decrease significantly after 90 cycles at 313 K. However, same authors have previously reported that imidazolium-based ILs could be used in LMB with the addition of additives such as the fluoroethylene carbonate (FEC).⁵⁷

Regarding, the use of imidazolium-based ILs with additives, Srour *et al.*⁶³ have studied the combination $C_1C_6\text{ImTFSI}/\text{LiTFSI}$ (1 mol.L^{-1}), with 5 % of vinylene carbonate (VC), in graphite/LFP cells, obtaining a capacity of 120 mAh.g^{-1} at 0.1 C beyond 30 cycles at 333 K.

Finally, the replacement of TFSI by FSI anion could be a solution to work with low potential anodes. In this context, Matsui *et al.*⁶⁴ have reported the performance of $C_1C_2\text{ImFSI}/\text{LiTFSI}$ (0.45 mol.L^{-1}) in a Li/NMC system giving a capacity of 163 mAh.g^{-1} during 50 cycles at a regime of 1 C. It has also been reported that when FSI is selected as anion of the neat IL, *e.g.*, $C_1C_2\text{ImFSI}/\text{LiTFSI}$ can provide a stable, reversible capacity for a graphitized negative electrode without any additives or solvents at ambient temperature.⁶⁵

A study of reference of the properties of imidazolium-based ILs that takes into account different anions (TFSI, FSI), the role of the methylation of the cation and the role of the additives (FEC, VC) from a fundamental approach is necessary to remove any controversy. For this reason, we made such a study (described in chapter 2) that will serve as point of departure for analyzing the reactivity of these ILs based electrolytes against lithium metal.

In contrast with the imidazolium, the pyrrolidinium family of ILs has been described by several authors as more stable at low potentials and, as a consequence, more suitable for working with lithium metal electrode.^{57,66-68} The most popular cations of this family are N-methyl-N-propylpyrrolidinium (Pyr_{13}^+) and N-butyl-N-methylpyrrolidinium (Pyr_{14}^+).

Schmitz *et al.*⁵⁷ have demonstrated an enhanced cycling performance in a Li/LFP system in the presence of $\text{Pyr}_{14}\text{TFSI} + 0.3 \text{ mol.L}^{-1} \text{ LiTFSI}$, giving a capacity of 130 mAh.g^{-1} at 0.2 C at 313 K over 150 cycles, in comparison with $\text{C}_1\text{C}_2\text{ImTFSI}$ and $\text{C}_1\text{C}_4\text{ImTFSI}$. Nevertheless, the addition of 5 % (FEC) to these imidazolium ILs results in a similar performance than in the case of $\text{Pyr}_{14}\text{TFSI}$.

New types of ILs based electrolytes are continuously being testing in different LIB systems. They include for example, N-methoxy-ethyl-N-methylpyrrolidinium TFSI ($\text{Pyr}_{12\text{O}1}\text{TFSI}$), N-N-diethyl-N-methyl-(2-methoxyethyl)ammonium TFSI (DEMETFSI)⁶⁹ or the phosphonium family ($\text{P}_{11\text{li}4}\text{FSI} + 3.8 \text{ mol.kg}^{-1} \text{ LiFSI}$).⁷⁰

Recently, Chen *et al.*⁷¹ reported a novel imidazolium-based ionic liquid 1-trimethylsilylmethyl -3-butylimidazole bis-(trifluoromethylsulfonyl)imide or [SiM-BIM]TFSI, which achieves a capacity of 151 mAh.g^{-1} and a Coulombic efficiency of 99.7% at a 0.1C rate when is cycled in a Li/LFP system.

In Table 1.3 the main electrochemical properties for selected ILs have been collected. Note that in general ILs based on FSI anion exhibit a higher ionic conductivity than their analogous with TFSI anion. The electrochemical windows of ILs based on pyrrolidinium and piperidinium are reported wider than the imidazolium based ILs.

Table 1.3 Electro and physicochemical properties of ILs at 298.15 K.

Ionic liquid	Conductivity (mS.cm⁻¹)	Viscosity (mPa.s)	Electrochemical window (V)	References
C ₁ C ₂ ImTFSI	9.0 (8.3)	32 (33)	4.6	56,72
C ₁ C ₄ ImTFSI	3.88	50	4.6	56
C ₁ C ₆ ImTFSI	2.20 (2.18)	68 (71)	-	56,73
C ₁ C ₂ ImFSI	15.4	18	4.5	72
C ₁ C ₄ ImFSI	8.16	33	-	73
Pyr ₁₄ TFSI	3.22 (3.93)	76 (78)	-	74,75
Pyr ₁₃ FSI	8.2	40	5.3	72
Pip ₁₃ TFSI	1.4	151	5.9	72
Pip ₁₃ FSI	3.7	95	5.6	72

Many efforts have been made in order to increase the conductivities of solid polymer electrolytes (SPE) combining them with ILs known as polymer ionic liquids (PILs) or poly(ionic liquid)s. Another strategy consists in the preparation of gel type polymer electrolytes (GPE) in which ILs have been added as plasticizers.^{47,54,76,77}

In addition, the investigation of the decomposition products from the electrolytes formed at the interface of the lithium metal anode as well as of the cathode under different conditions is crucial to avoid thermal runaway and to improve the overall performance of the battery. For this, the characterization of the redox processes happening at the interphases electrode/electrolyte is necessary.

1.6. The solid electrolyte interphase

1.6.1. Historical background

By the end of the 1970s, Peled⁷⁸ presented a detailed model for the passivation layer which covers alkali and alkaline-earth metals in non-aqueous battery systems. This was called the Solid Electrolyte Interphase (SEI) model. This film results from the precipitation of corrosion products of the electrolyte/anode.

By extension, the SEI is not exclusive of metallic electrodes and can occur on any other electrodes such as graphite. The nature (composition, thickness, morphology) and the stability of the SEI control the battery performance, the irreversible charge “loss”, the

rate capability and the cyclability. In the case of graphite electrode its exfoliation and its safety are highly correlate to the quality of the SEI.⁷⁹

The formation of the SEI is not exclusive of the negative electrode, but relatively few studies have been performed of the SEI in cathode materials, called cathode electrolyte interphase CEI.^{80,81} This is mostly related to the fact that the negative electrodes such as lithium or graphite operate at low potentials where important degradation processes of the electrolytes occur.

Peled⁸² proposed also a mechanism of SEI growth depending on the time and the diffusion coefficient ($l \propto \sqrt{D t}$) and described some properties of the SEI formed on lithium in contact with the electrolyte THF-LiClO₄ (1 mol.L⁻¹). These properties are depicted in Table 1.4. Note that the thickness of the SEI is in the order of some nanometers for this case.

Table 1.4 Properties of the SEI formed in lithium with THF-LiClO₄ electrolyte.⁸²

SEI property	OCV	Stripping	Plating
Reaction resistance ($\Omega \cdot \text{cm}^2$)	110	23.5	12.6
SEI thickness (\AA)	180	360	36
SEI resistivity ($10^{-7} \Omega \cdot \text{cm}$)	6.1	0.65	3.5

1.6.2. Characterization of the SEI

1.6.2.1. General structure and chemical composition of the SEI

When the SEI was proposed by the first time it was conceived as a single layer that allowed the Li⁺ conduction alone.⁷⁸ Latter, when more properties were discussed and analyzed, it was proposed a double layer structure composed by a thin but compact layer near the electrode and a thick but porous layer near the electrolyte.⁸²

Currently, the mosaic model composed by multiple organic and inorganic layers is widely accepted.⁸³ The thin compact layers close to the electrode are composed by

inorganic lithium compounds such as Li_2O , Li_2CO_3 and LiF . These inorganic species are thermodynamically stable in contact with lithium metal.⁸⁴ The layers farther from the electrode comprise mainly organic compounds.

Aurbach *et al.*⁸⁵ validated the mosaic model by a combination of FTIR, XPS and EIS analysis (Figure 1.5). They proved the formation of compact layers of around 10 nm composed mainly of inorganic salts (Li_2O , Li_3N and LiF), and porous outer layers of organic byproducts (ROCO_2Li , ROLi , LiOH , RCOO_2Li , *etc.*).

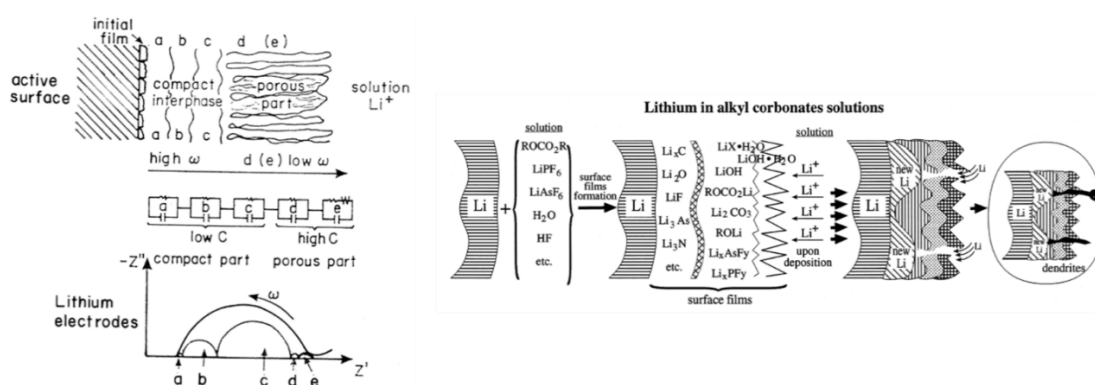


Figure 1.5. General multilayer model and equivalent electrical circuit of the impedance spectrum related to the SEI of the lithium electrode in contact with alkyl carbonate based electrolytes.⁸⁵

Obviously, the situation differs for each electrolyte needing a combination of analytical techniques (*in situ* and *post-mortem*) to determine all properties of the SEI.

1.6.2.2. Electric characterization

Few techniques are able to characterize the SEI during the operation of the battery system. The electrochemical impedance spectroscopy (EIS) is the most important technique allowing to impedance of all components of a cell (electrode, electrolyte and their interfaces) in real time.

Although the basic theory of EIS is known,⁸⁶ the main problem of this technique is the implementation of an univocal equivalent circuit model that correctly fits the EIS spectra and at the same time furnishes physical information of the studied system.

Different kinds of models have been proposed by Aurbach and Zaban⁸⁷, Thevenin⁸⁸ on lithium electrodes. Furthermore, Bouchet *et al.*⁸⁹ use EIS to calculate the diffusion coefficient and conductivity of the SEI in lithium polymer cells, and Wohde *et al.*⁹⁰ calculate the Li^+ transference number in Li/Li cells containing LP30 and IL based electrolytes, nonetheless the results of these properties need to be contrasted with other techniques.

1.6.2.3. Surface morphology characterization

By using scanning electron microscopy (SEM), images of the lithium dendrites on nickel substrates in different solvents {ethylene carbonate (EC) + tetrahydropyran (THP), dimethoxyethane, dimethylcarbonate (DMC), propylenecarbonate (PC) and γ -butyrolactone (GBL)} doped with $\text{LiN}(\text{SO}_2\text{C}_2\text{F}_5)_2$ (LiBETI) or LiTFSI salts have been reported.⁹¹ With LiBETI based electrolytes, the deposit is uniform and composed by fine particles, whereas using LiTFSI a dendritic morphology and a decrease of the cycling efficiency are obtained.

The atomic force microscopy (AFM) has furnished important information about the changes of morphology of the SEI at different voltage steps through *in-situ* analysis of graphite electrodes.⁹²⁻⁹⁴

Regarding the lithium metal, AFM proved the morphologies of lithium electrodes in a variety of alkyl carbonates solutions (PC, EC, DMC, DEC) and lithium salts (LiPF_6 , LiClO_4 , LiAsF_6 , LiTFSI).⁹⁵ These observations confirm that the surface films have a mosaic-type and non-uniform multilayered structure in nanometer and even in micrometer scale.

In contrast with the previous results, Mogi *et al.*⁹⁶ have investigated the formation of surface films after electrodeposition of lithium on nickel substrates at $0.5 \text{ mA}\cdot\text{cm}^{-2}$ in electrolytes composed by LiClO_4 salt dissolved in PC, doped with different additives such as VC, FEC and ethylene sulfite (ES). They conclude that only FEC is able to improve the cycled efficiency of lithium metal and the AFM study reveals a uniform, closely packed layer of particle-like deposits of 100-150 nm in diameter. In addition, the EIS

demonstrates that the surface produced by PC+FEC is less resistive than with the other additives.

Finally, recently, transmission electron cryo-microscopy (cryo-TEM) has been used to analyze the thickness as well as the composition of the SEI. Cryo-protection not only helps to minimize damage from air and the beam, but also preserves the intrinsic structure of the samples, which enables us to image the structure of the light compounds at the nano/atomic scale, such as Li metal and its solid-state electrolyte interphase (SEI).^{97,98}

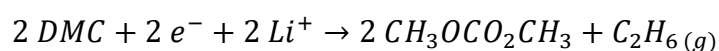
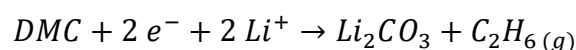
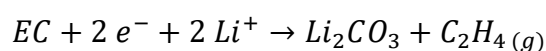
1.6.2.4. Chemical characterization

Chemical characterization of the SEI is mainly performed by Fourier-transform infrared spectroscopy (FTIR)⁹⁹ and X-ray photoelectron spectroscopy (XPS),¹⁰⁰ as well as Raman^{101,102} and Auger spectroscopies (AES)^{103,104} and nuclear magnetic resonance (NMR)^{105,106} but in a low extent.

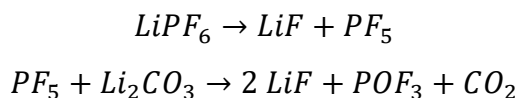
Herein, the interest in using these techniques is to investigate the different degradation mechanisms of the electrolytes that forms the surface layers, but also to get knowledge about the mechanisms of insertion/disinsertion of the Li⁺ ions in the host electrodes.

Leroy *et al.*, Dedryvère *et al.*^{107,108} have studied the formation of the SEI on graphite by means of a combination of AFM and XPS techniques during the cycling of LCO/graphite cells with LiPF₆/EC/DEC/DMC as electrolyte. During the charging up to 3.8 V, the main phenomenon is the formation of Li₂CO₃ to the formation of small amounts of LiF and CH₃OCO₂Li. Finally, at the end of the charge (4.2 V) the main compound of the outer part of the SEI is LiF associated with a small amount of CH₃OCO₂Li and probably Li₂CO₃ resulting mainly to the decomposition of the salt.

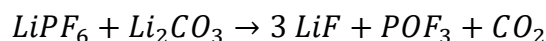
The mechanisms of formation of Li₂CO₃ and ROCO₂Li byproducts of the decomposition of alkyl carbonate solvents are extensively reported in the literature:¹⁰⁹



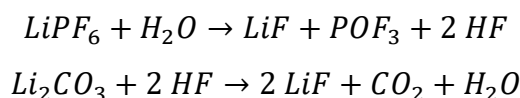
The following mechanisms for the formation of LiF are proposed:



which leads to:



Nonetheless, the reactivity of certain contaminants such as moisture, and their role in the SEI formation are also discussed:



Several byproducts are also considered, *e.g.* the polymer resulting from the breakdown of cyclic carbonates,¹¹⁰ or the formation of lithium oxalates,¹¹¹ ($\text{Li}_2\text{C}_2\text{O}_4$) and succinates ($\text{LiO}_2\text{CCH}_2\text{CH}_2\text{CO}_2\text{Li}$).¹¹² Nonetheless, the formation of certain compounds has only been predicted by chemical reactions and their experimental evidence is under discussion since the current *ex-situ* protocols of characterization have some limitations such as the risk of contamination of the electrode surface during their transport in adapted environments (glove box, transfer vessel) and the process of removing traces of electrolyte by washing processes using organic solvents.

1.7. SEI in IL-based electrolytes accumulators

Our group have performed detailed studies combining EIS and XPS of the reaction of imidazolium based ILs on graphite electrodes. For instance, the signature of the core peaks of $\text{C}_1\text{C}_6\text{ImTFSI}$ doped with LiTFSI salt and VC additive in contact with glass fiber separators and graphite have been registered by XPS technique.¹¹³ This study of reference has been used as support for study the evolution of the SEI at different potentials during the first discharge of a graphite electrode.¹¹⁴

In contrast, the studies of the SEI formed by ILs based electrolytes on lithium metal electrodes are not abundant. Howlett *et al.*¹¹⁵ have studied the SEI formed in a lithium

electrode in contact with N-methyl-N-alkylpyrrolidinium bis(trifluoromethanesulfonyl)imide (Pyr_{r1x}TFSI) doped with 0.5 mol.kg⁻¹ LiTFSI after galvanostatic cycling of a Li/Cu system at 0.25 mA.cm⁻².

The SEI was largely composed of lithium salts byproducts resulting from the reduction of the TFSI anion (Li₂S₂O₄, Li₂NSO₂CF₃, Li_xC₂F_y and LiF) covered by persistent traces of ionic liquid, as well as Li₂O, LiOH and Li₂CO₃ coming from the initial lithium native layers. The measurements by FTIR confirm these results. Nonetheless, FTIR shows the presence of products resulting from the cation reduction. The exact mechanism of the formation of these byproducts is not well established. However, they could result via the formation of an amide, or of a CF₃ radical.

Carbonate and carbonyl species were also present on the Li surface which can be components of the native film. Based on XPS etching profile and EIS measurements, the thickness of the SEI was estimated to 200 - 300 nm, and the inner layers mainly composed by LiF and Li₂O.

Girard *et al.*,⁷⁰ using IL trimethyl(isobutyl)phosphonium bis(fluorosulfonylimide) (P_{111i4}FSI) doped with 3.8 mol.kg⁻¹ of LiFSI salt in Li/Li symmetrical cells polarized with a current density of 1.5 mA.cm⁻² at 50 °C confirmed by XPS that SEI is mainly composed by degradation byproducts of the anion FSI (LiF, Li₂O, Li₂S, LiSO₂ and Li₂NSO₂F). However, there is no evidence of a reduction of the cation.

These works highlight the role of the decomposition of the anion in the formation of the SEI (LiF, LiS_xO_y, Li₂S). However, the role of the cations is not well understood and the experimental evidences of cation degradation byproducts are not clear. Although the main components of the SEI have been identified, their relative abundance and their impact on the morphology of the lithium electrodeposition and the cycling performance have not been yet discussed.

1.8.Challenges of the SEI face to lithium dendrite growth

Aurbach *et al.*¹¹⁶ based on Peled's work and AFM observations proposed the breakdown and the reparation of the SEI films on Li electrodes during Li plating/stripping cycles as it is shown in Figure 1.6.

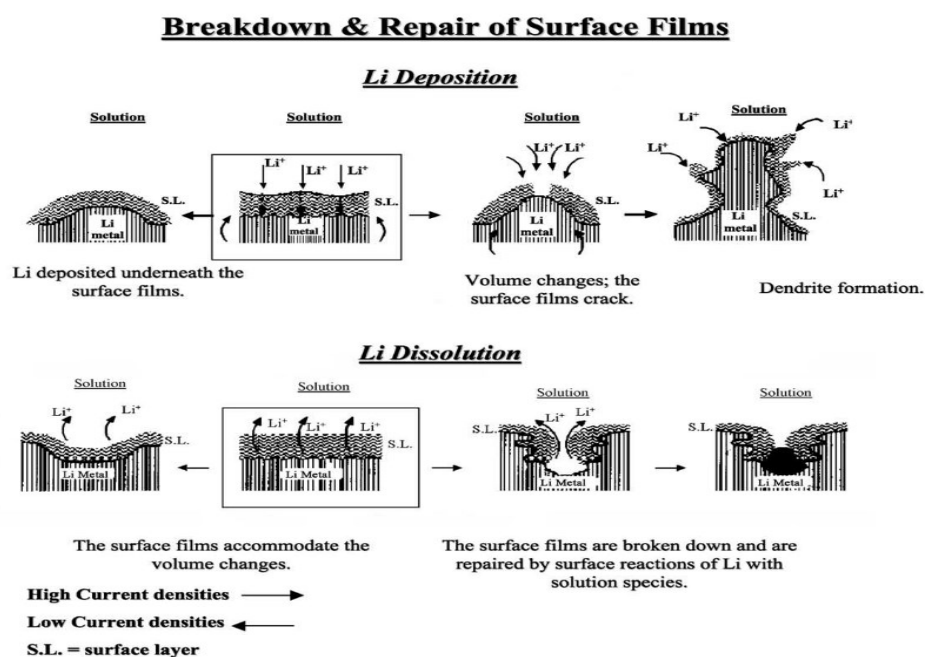


Figure 1.6. A description of the morphology and breakdown mechanisms of the SEI in lithium electrodes during Li plating and Li stripping.¹¹⁶

Upon Li plating/stripping, the SEI cannot accommodate the morphological change of the Li surface, and thus can be broken down, leading to highly non-uniform Li deposition engendering dendrites. The breakdown of the SEI leads also to the exposure of fresh Li to the electrolyte and the formation of a new SEI film. This causes further consumption of the bare Li, which decreases the cycling efficiency of the Li electrode.^{117,118}

In conclusion, the formation of a uniform, chemically stable and flexible SEI layer would mitigate the formation of dendrites and loss of capacity. Nonetheless, the knowledge of the SEI properties such as structure and chemical composition, electronic and ionic conductivities are still under investigation since a mathematical or experimental model that correlates SEI properties and lithium metal behavior is not still finalized.

To sum-up based on the original Peled's description, an ideal SEI must have the following properties^{119,120}:

- a. Proper thickness, thick enough to be completely insulating to electrons, but not too thick to limit the Li ion migration resistance.
- b. High ionic conductivity to reduce migration resistance of Li ions through the SEI.
- c. Uniform chemical composition and morphological texture to ensure homogeneous current distribution

- d. Good mechanical strength and flexibility to endure the volume changes of the electrode

As the control of the SEI properties are intimately related to the control of dendrite growth, the different strategies to obtain a better SEI will be presented after a short description of the dendrite nucleation and growth models.

1.9.Characterization of the dendrite nucleation and growth

1.9.1. Morphology of the dendrites and the Chazalviel's model

Lithium dendrite morphologies have been observed *in-situ* by optical microscope,^{121–123} whereas *ex-situ* studies of lithium electrodes after plating have been performed by Scanning Electron Microscope (STM),^{91,124,125} Atomic Force Microscope (ATM),^{95,126} and Transmission Electron Microscope (TEM).¹²⁷ Note that the dendrite structures are atypical. In general, the plated Li morphology does not consist of regular branched, tree-like structures, instead, Li tends to plate from solution as particles/nodules or whiskers/needles/filaments, which can aggregate into more complex constructs.¹²⁸ These dendrite morphologies have been described by Arakawa,¹²⁹ Yamaki¹³⁰ and Steiner,¹³¹ who propose different explanations about the mechanism of growth based on optical observations. In spite of these efforts, these observations are not correlated with an appropriated mathematical model that takes into account the different electrochemical properties of the system.

Regarding the last point, and based on the electrochemical model proposed by Chazalviel,¹³² important works to validate this model were carried out by Brissot, Rosso *et al.*^{121,133–135} This model predicts two different regimes of dendrite growth, which depends on a threshold current density called the Sand current density J^* (*i.e.* the diffusion limited current density). If the current density is higher than this threshold ($J > J^*$), the voltage of the cell is expected to diverge after a time τ_d , which corresponds to the time where the ionic concentration in the electrolyte reaches zero at the cathode interface leading to the formation of a space charge layer. The formed space charge layer is the driving force for the dendrite nucleation, thus, τ_d coincides with the onset time of dendrite nucleation. Assuming, a fast dendrite growth compared to the nucleation time, Chazalviel showed that a short-circuit should occur at a time $\tau_{sc} < \tau_d$. Instead of this, if $J < J^*$ the

potential is expected to reach a stationary regime (with an interfacial ionic concentration strictly positive) where the dendrites do not grow because they do not nucleate.

The current density J^* only depends on the transport properties of the electrolyte (diffusion coefficient and lithium ion transport number), and the distance between the electrodes. Important predictions of the Chazalviel's model is that the time of divergence (and thus short-circuit) follows a law in the inverse-square of the current density, *i.e.* τ_d & $\tau_{sc} \propto 1/J^2$, in accordance with the Sand's law.¹³⁶

As an example, Figure 1.7 shows different lithium morphologies depending on the applied current density in lithium polymer systems. Note that at low current density, the dendrite morphology is needle-like, whereas it becomes mossy-like when the current density is increased.

However, the works of Brissot and Rosso have demonstrated that even at a current density below J^* the potential falls down at a time τ_{sc} , as a consequence of the growth of fine dendrites that leads to the occurrence of short-circuit in the system.¹³⁴ They proposed a modified version of the Chazalviel's model taking into account a distribution of the current density over the lithium surface.

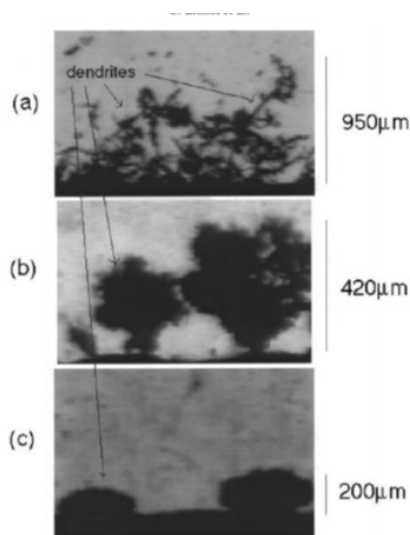


Figure 1.7. Optical observations of lithium dendrites, obtained with different current densities: a) $J=0.2 \text{ mA.cm}^{-2}$ (needle-like), b) $J=0.7 \text{ mA.cm}^{-2}$ (tree-like), c) $J=1.3 \text{ mA.cm}^{-2}$ (bush-like).¹³³

1.9.2. Dendrite observations with IL based electrolytes

Sano *et al.*¹³⁷ have performed *in-situ* optical microscope using an adapted cell with nickel as working electrode and C₁C₂ImFSI and Pyr₁₃TFSI laden with LiTFSI lithium salt and vinylene carbonate (VC) additive, as electrolytes. Using the same amount of plated lithium (3 C.cm⁻²), they observed by *post-mortem* different morphologies depending on the nature of the electrolyte and on the applied current density (see Table 1.5).

Table 1.5 Different dendrites morphologies depending on the type of electrolyte and the applied current density, based on a charge of 3 C.cm⁻² of electrodeposition.¹³⁷

Electrolyte	Current density ($\mu\text{A.cm}^{-2}$)	Morphology
C ₁ C ₂ ImFSI + LiTFSI	150	Coarse dendrite
C ₁ C ₂ ImFSI + LiTFSI	50	Coarse dendrite
C ₁ C ₂ ImFSI + LiTFSI + VC	150	Coarse dendrite
Pyr ₁₃ TFSI + LiTFSI	50	Fine dendrite
Pyr ₁₃ TFSI + LiTFSI + VC	50	Fine granular particle

The deposited particles are very different in size for the case of the combinations using C₁C₂ImFSI (from 20 μm to 200 μm in diameter), whereas for the combinations using Pyr₁₃TFSI particles are very small with sizes around 5 nm, confirmed by SEM analysis.

The particle shape is dendritic for the samples C₁C₂ImFSI, C₁C₂ImFSI + VC, and Pyr₁₃TFSI, but granular for the sample of Pyr₁₃TFSI + VC. Dendritic growth is suppressed and planar growth is promoted using Pyr₁₃TFSI and VC as additives.

Although other authors have reported the inhibition of dendrites using IL based electrolytes,^{138,139} to the best of our knowledge the work of Sano *et al.* is probably the only one that compares different ILs based electrolytes (including or not the use of VC).

Although it is reported that: i) pyrrolidinium based ILs are more stable at low potentials than imidazoliums,⁴¹ and ii) the addition of additives (such as VC) may create a better passivation on the lithium surface, no further studies correlating the transport properties of these electrolytes and their degradation mechanisms against lithium with the chemical state of the interphases and the performances of these systems have been carried out. In this context, our work is intended to complete these lacks in the understanding of the reactivity of IL based electrolytes against lithium metal.

1.10. Strategies to mitigate dendrite growth

Zhang *et al.*¹⁴⁰ highlighted the following trends to prevent dendrite growth:

1. Decrease of the current density
2. Formation of a stable and flexible SEI film
3. Increasing of the Li^+ transference number
4. Enhancing of the shear modulus of the electrolyte

These requirements can be obtained by introducing changes in the conventional electrolytes and modifications of the surface of the lithium anode. Most of studies include the addition of organic solvents to electrolyte to create a more stable and uniform SEI.

1.10.1. Stabilizing the SEI with additives

The addition of additives such as vinylene carbonate (VC),^{113,141,142} fluoroethylene carbonate (FEC)^{57,143,144} and LiNO_3 ,¹⁴⁵ affords *in situ* formation of SEI with high uniformity and stability which are the most effective and convenient routes to mitigate Li dendrite growth. Especially, the fluorinated solvents such as FEC react on the Li surface leading to a LiF-rich SEI.

LiF does not have excellent ion conductivity compared to other solid electrolyte materials (ion conductivity of $\text{LiF} < 10^{-9} \text{ S.cm}^{-1}$),¹⁴⁶ but it has high chemical stability against lithium metal and organic electrolyte materials. Particularly, during charging cycles with limited Li ion transport from the electrolyte to anode surface, undesirable Li dendrites are more likely to nucleate and to grow within the SEI at the $\text{Li}_2\text{CO}_3/\text{Li}$ interface than at the LiF/Li interface.¹⁴⁷

However, most of the additives are either chemically reactive to the cathode materials or electrochemically instable at high potentials. As a consequence, their amount in the electrolytes must be strictly limited (typically 5% vol.).⁴⁰

Dendrite-free Li deposition was recently achieved in carbonate electrolyte by using salts of Cs^+ and of Rb^+ as additives, which functioned by a ‘self-healing electrostatic shield’ mechanism.¹⁴⁸ Compared with the dendritic Li morphology in a control electrolyte, a considerable improvement in deposition quality was observed.

LiNO_3 is an important additive in ether electrolytes, especially for Li–S batteries,¹⁴⁹ but can also stabilize the Li anode when combined with Li polysulfide.¹⁵⁰ In the presence of both additives, Li can be plated into a pancake-shaped morphology without dendrites in ether electrolyte, which cannot be achieved with LiNO_3 alone.

1.10.2. Building an artificial SEI layer

One commonly adopted approach to stabilize the SEI involves covering the Li surface with a protective layer before cycling. Artificial SEI can be formed by controlled exposure of Li with chosen chemicals. For example, the reaction between substituted-silane and the natural OH-terminated layer on clean Li surface results in a protective coating stable under static conditions with low initial impedance and slow impedance growth when exposed to organic electrolytes.¹⁵¹ Tetraethoxysilane-generated silicate coating has been even more effective in improving cycle life.¹⁵² Other approaches include the use: of N_2 gas to form Li_3N ,¹⁵³ of Al_2O_3 ,¹⁵⁴ of Li_3PO_4 ,¹⁵⁵ of carbon thin films,¹⁵⁶ and of hollow carbon nanospheres.¹⁵⁷

1.10.3. Enhancing of the shear modulus of the electrolyte

In contrast with the commercial separators for LIB that tend to be thin, it has been proposed that dendrite formation can be inhibited by incorporating a solid separator/electrolyte, especially one with an acceptable ionic conductivity and a high shear modulus of approximately twice that of Li (*i.e.*, 9 GPa).^{158,159} Therefore, solid polymer electrolytes (SPEs) were proposed.¹⁶⁰

To further increase the shear modulus of SPEs to prevent dendrite propagation, block copolymers have been studied in which a polystyrene component creates a rigid structure, while a poly(ethylene oxide) (PEO) component dissolves a Li salt to create an ionic transport percolated pathway.^{161–163} This type of electrolyte remains an actively studied topic. Continuous efforts have been made to further improve their ionic conductivity and mechanical strength.

Solid electrolytes with an even higher modulus, such as inorganic (crystalline or glassy) electrolytes, have also been developed.^{164,165} Nonetheless, such high modulus materials often adhere poorly to the electrode surface, which significantly increases the interfacial resistance during cycling. Furthermore, most inorganic solid electrolytes have a very narrow electrochemical stability window and are thermodynamically unstable with a Li metal anode.^{166,167}

1.10.4. Effect of surface roughness

The rough surface of the current collector can lead to uneven charge distribution and allow Li to deposit faster on the tips of the substrate due to the concentrated ion flux. These newly-formed Li electrodeposits amplify the surface roughness of the electrode and cause the formation of more dendritic structures. The sharp dendritic structures of Li pierce the separator to cause short circuits and even explosions.¹⁶⁸

The main underlying principle is increasing the specific surface area thus decreasing the effective current density and the resulting overpotential. As known from science of metallurgy, the shape of the overpotential profiles is mainly influenced by the change in the electrode surface.¹⁶⁹ For instance, Becking *et al.*¹⁷⁰ propose a roll-press technique to flatten and to thin the native surface film of the lithium metal anode, which improves the performances of lithium electrodes.

1.11. The *operando* protocols of characterization

The characterization of the chemical environment of the SEI frequently requires the use of *post-mortem* experiments to extract and to prepare the electrodes to analyze their morphology, structure, surface...etc. Although the *post-mortem* results are largely accepted by the scientific community through several years of research, there exist some controversies about the possibility of alteration of the chemical state of the electrodes during the disassembling of the cells, the washing of the electrodes and their transport until the characterization equipment.

In addition, the knowledge of the redox processes obtained by these techniques is limited because of the impossibility of observing redox processes in real time. These remarks

lead to the necessity of development of *operando* characterization techniques. However, the implementation of such protocol for the study of the SEI constitutes a true challenge.

For the case of the development of *operando* XPS, a first objective consists in the conception of an electrochemical setup that can reproduce the behavior of a true battery and that can be implemented into the XPS chamber. In addition, the material constituting the *operando* cell must be inert face to the electrolyte and adapted to an ultra-high vacuum environment. Some examples of this kind of cells can be found in the works of Weingarth *et al.*¹⁷¹ and Wibowo *et al.*¹⁷²

Between the most recent works of the *operando* XPS technique we can cite the efforts of Nandasiri *et al.*¹⁷³ in the study of Li-S batteries and the works of Wu *et al.*¹⁷⁴ and Wood *et al.*¹⁷⁵ in the field of solid-state batteries. However, their conclusions are still under debate. In fact, in most of the cases, the authors do not compare the *operando* results with the reference results obtained with real battery. Furthermore, a complete electrochemical characterization of the *operando* cell (*e.g.*, using EIS technique) before and under cycling is omitted. Finally, the origin of the systematic chemical shift of the peaks position is not well elucidated since it can be attributed either to true redox processes or to the influence of parasite currents or charge effects in the cell. Therefore, more complete studies are necessary.

In our work, we have established new setups and protocols to perform *operando* XPS to study the reactivity of lithium metal toward ionic liquid based electrolytes. Our approach is based on a parallel XPS/EIS studies in order to follow the SEI and the lithium dendrite growth in lithium battery.

1.12. Objectives of the thesis

Through this chapter, we have revised the main challenges of the current battery systems that can be summarized in the increase of the energy density and the improvement of the safety. For this, new types of electrode and electrolyte materials are needed. In this context, the study of LMB systems using IL based electrolytes has a great significance in the current research of batteries.

Far from just testing the performance of the different IL based electrolytes, in this PhD, we propose a deep analysis of their electrochemical properties and electronic structure to better understand their reactivity against lithium metal.

Therefore, we will start this work in chapter 2 with a reference study of the ionic conductivities of these ILs doped with LiTFSI and solvent additives VC and FEC. These measurements will be described with a thermodynamic model (Vogel-Fulcher-Tammann VFT). The variations of thermodynamic properties such as the activation volume and the glass transition temperature can be related with the changes on the molecular structure upon the nature of the cation or the anion, and the addition of LiTFSI or additives. To complete this reference study, a study by XPS of the initial chemical state of these ILs based electrolytes which, in certain cases, can be correlated with the evolution of the physical parameters extracted from their conductivity measurements., The XPS analysis of the surface of pristine lithium electrodes is also presented.

In the third chapter, the stability of the different combinations of IL based electrolytes against lithium in open circuit voltage (OCV) conditions is investigated. From the bibliographic chapter 1, it can be noted that few fundamental studies pay attention to the SEI formed in OCV, but focus directly on what occurs after cycling processes. In addition, the stability of the IL is only correlated to their reduction potential limit, without taking in account the possible heterogeneities of these ionic media. Herein, we expect to correlate the different evolution of the impedance of both bulk electrolytes and interphases, with the evolution of the chemical state by means of the *post-mortem* XPS analysis of the separator and lithium electrodes surfaces. This will help us to understand the degradation processes of the ILs based electrolyte on the lithium surface that leads to different morphologies and chemical composition of the SEI.

The next objective (chapter 4) is to extend the previous study in OCV to dynamic conditions with the application of an electrical current in order to characterize the dendrite growth. For this, different electrochemical methods have been applied (impedance spectroscopy, chronopotentiometry, cyclic voltammetry). Herein, we expect to correlate the transport properties of the IL based electrolytes with the behavior under polarization of the cell. We will complement all this study with XPS and SEM/AES measurements of

the chemical state and morphology of the SEI, in order to propose alternatives to mitigate the dendrite growth.

Finally, our last objective is to develop the *operando* XPS protocol as a new way to study the redox processes occurring in real time at the interfaces (chapter 5). In order to achieve this objective, all the previous studies constitute the pedestal that allows us to validate the *operando* results in term of electrochemical behavior.

Thus, this thesis intends to present a study of the reactivity of ILs based electrolytes against lithium metal based on the correlations of electrochemical techniques and surface characterization techniques (XPS, AES). As a first step, the electrochemical properties of the IL will be revised following with the study of their stability and the mechanisms of formation of the SEI at OCV and under polarization conditions. All these studies will serve as a basis for the development of a new protocol of characterization (*operando* XPS) that is expected to pave the way to a better understanding of the redox processes happening at the electrode/electrolyte interphases.

REFERENCES

- (1) Acar, C. A Comprehensive Evaluation of Energy Storage Options for Better Sustainability. *Int. J. Energy Res.* **2018**, 42 (12), 3732–3746.
- (2) Thackeray, M. M.; Wolverton, C.; Isaacs, E. D. Electrical Energy Storage for Transportation—Approaching the Limits of, and Going beyond, Lithium-Ion Batteries. *Energy Environ. Sci.* **2012**, 5 (7), 7854.
- (3) Lin, D.; Liu, Y.; Cui, Y. Reviving the Lithium Metal Anode for High-Energy Batteries. *Nat. Publ. Gr.* **2017**, 12 (3), 194–206.
- (4) Feng, X.; Ouyang, M.; Liu, X.; Lu, L.; Xia, Y.; He, X. Thermal Runaway Mechanism of Lithium Ion Battery for Electric Vehicles: A Review. *Energy Storage Mater.* **2018**, 10 (December 2016), 246–267.
- (5) Placke, T.; Kloepsch, R.; Dühnen, S.; Winter, M. Lithium Ion, Lithium Metal, and Alternative Rechargeable Battery Technologies: The Odyssey for High Energy Density. *J. Solid State Electrochem.* **2017**, 21 (7), 1939–1964.
- (6) Yoo, H. D.; Markevich, E.; Salitra, G.; Sharon, D.; Aurbach, D. On the Challenge of Developing Advanced Technologies for Electrochemical Energy Storage and Conversion. *Mater. Today* **2014**, 17 (3), 110–121.
- (7) Xu, K. Electrolytes and Interphases in Li-Ion Batteries and Beyond. *Chem. Rev.* **2014**, 114 (23), 11503–11618.
- (8) Li, Q.; Chen, J.; Fan, L.; Kong, X.; Lu, Y. Progress in Electrolytes for Rechargeable Li-Based Batteries and Beyond. *Green Energy Environ.* **2016**, 1, 1–25.

- (9) Zhu, M.; Wu, J.; Wang, Y.; Song, M.; Long, L.; Siyal, S. H.; Yang, X.; Sui, G. *Recent Advances in Gel Polymer Electrolyte for High-Performance Lithium Batteries*, *J. Energy Chem.* **2019**, 37, 126-142.
- (10) Adachi, G.-Y.; Imanaka, N.; Aono, H., Fast Li⁺ Conducting Ceramic Electrolytes, *Adv. Mater.* **1996**, 8(2) 127–135.
- (11) Lévy, F. *Intercalated Layered Materials*; Springer Netherlands: Dordrecht, 1979.
- (12) Jones, S. D.; Akridge, J. R. A Thin-Film Solid-State Microbattery. *J. Power Sources* **1993**, 44 (1–3), 505–513.
- (13) Mizushima, K.; Jones, P. C.; P.J., W.; J.B, G. Li_xCoO₂ (0<x<1): A New Cathode Material For Batteries Of High Energy Density. *Mat. Res. Bull.* **1980**, 15, 783–789.
- (14) Dahn, J. R.; von Sacken, U. V.; Juzkow, M. W.; Al-Janaby, H. Rechargeable LiNiO₂/Carbon Cells. *J. Electrochem. Soc.* **1991**, 138 (8), 2207–2211.
- (15) Dai, X.; Zhou, A.; Xu, J.; Lu, Y.; Wang, L.; Fan, C.; Li, J. Extending the High-Voltage Capacity of LiCoO₂ Cathode by Direct Coating of the Composite Electrode with Li₂CO₃ via Magnetron Sputtering. *J. Phys. Chem. C* **2016**, 120, 422-430.
- (16) Nitta, N.; Wu, F.; Lee, J. T.; Yushin, G. Li-Ion Battery Materials: Present and Future. *Mater. Today* **2015**, 18 (5), 252–264.
- (17) Noh, H. J.; Youn, S.; Yoon, C. S.; Sun, Y. K. Comparison of the Structural and Electrochemical Properties of Layered Li[Ni_xCo_yMn_z]O₂ (x = 1/3, 0.5, 0.6, 0.7, 0.8 and 0.85) Cathode Material for Lithium-Ion Batteries. *J. Power Sources* **2013**, 233, 121-130.
- (18) Pham, H. Q.; Hwang, E. H.; Kwon, Y. G.; Song, S. W. Approaching the Maximum Capacity of Nickel-Rich LiNi_{0.8}Co_{0.1}Mn_{0.1}O₂ Cathodes by Charging to High-Voltage in a Non-Flammable Electrolyte of Propylene Carbonate and Fluorinated Linear Carbonates. *Chem. Commun.* **2019**, 55 (9), 1256–1258.
- (19) Uitz, M.; Sternad, M.; Breuer, S.; Täubert, C.; Traußnig, T.; Hennige, V.; Hanzu, I.; Wilkening, M. Aging of Tesla’s 18650 Lithium-Ion Cells: Correlating Solid-Electrolyte-Interphase Evolution with Fading in Capacity and Power. *J. Electrochem. Soc.* **2017**, 164 (14), A3503-A3510.
- (20) Bloom, I.; Jones, S. A.; Battaglia, V. S.; Henriksen, G. L.; Christophersen, J. P.; Wright, R. B.; Ho, C. D.; Belt, J. R.; Motloch, C. G. Effect of Cathode Composition on Capacity Fade, Impedance Rise and Power Fade in High-Power, Lithium-Ion Cells. *J. Power Sources* **2003**, 124 (2), 538-550.
- (21) Itou, Y.; Ukyo, Y. Performance of LiNiCoO₂ Materials for Advanced Lithium-Ion Batteries. In *Journal of Power Sources*; **2005**, 146 (1-2), 39-44.
- (22) Thackeray, M. M.; David, W. I. F.; Bruce, P. G.; Goodenough, J. B. Lithium Insertion into Manganese Spinels. *Mater. Res. Bull.* **1983**, 18 (4), 461–472.
- (23) Padhi, A. K.; Nanjundaswamy, K. S.; Goodenough, J. B. Phospho-Olivines as Positive-Electrode Materials for Rechargeable Lithium Batteries. *J. Electrochem. Soc.* **1997**, 144 (4), 1188-1194.
- (24) Chung, S. Y.; Bloking, J. T.; Chiang, Y. M. Electronically Conductive Phospho-Olivines as Lithium Storage Electrodes. *Nat. Mater.* **2002**, 1, 123-128.
- (25) Mukerjee, S.; Yang, X. Q.; Sun, X.; Lee, S. J.; McBreen, J.; Ein-Eli, Y. In Situ Synchrotron X-Ray Studies on Copper-Nickel 5 V Mn Oxide Spinel Cathodes for Li-Ion Batteries. *Electrochim. Acta* **2004**, 49 (20), 3373–3382.

- (26) Dumaz, P. Comportement Electrochimique de Matériaux à Haut Potentiel : LiCoPO_4 et $\text{LiNi}_{1/3}\text{Mn}_{3/2}\text{O}_4$, en Électrodes Couches Minces ou Composites., Thèse Doctorale, LEPMI Grenoble INP, 2017.
- (27) Yi, T. F.; Mei, J.; Zhu, Y. R. Key Strategies for Enhancing the Cycling Stability and Rate Capacity of $\text{LiNi}_0.5\text{Mn}_1.5\text{O}_4$ as High-Voltage Cathode Materials for High Power Lithium-Ion Batteries. *J. Power Sources* **2016**, 316, 85–105.
- (28) Scrosati, B.; Garche, J. Lithium Batteries: Status, Prospects and Future. *J. Power Sources* **2010**, 195 (9), 2419–2430.
- (29) Pan, A.; Zhang, J. G.; Nie, Z.; Cao, G.; Arey, B. W.; Li, G.; Liang, S. Q.; Liu, J. Facile Synthesized Nanorod Structured Vanadium Pentoxide for High-Rate Lithium Batteries. *J. Mater. Chem.* **2010**, 20, 9193-9199.
- (30) Shin, J.; Jung, H.; Kim, Y.; Kim, J. Carbon-Coated V_2O_5 Nanoparticles with Enhanced Electrochemical Performance as a Cathode Material for Lithium Ion Batteries. *J. Alloys Compd.* **2014**, 589, 322-329.
- (31) Song, H.; Liu, Y.; Zhang, C.; Liu, C.; Cao, G. Mo-Doped LiV_3O_8 nanorod-Assembled Nanosheets as a High Performance Cathode Material for Lithium Ion Batteries. *J. Mater. Chem. A* **2015**, 3, 3547-3558.
- (32) Xu, W.; Wang, J.; Ding, F.; Chen, X.; Nasybulin, E.; Zhang, Y.; Zhang, J.-G. Lithium Metal Anodes for Rechargeable Batteries. *Energy Environ. Sci.* **2014**, 7 (2), 513–537.
- (33) Armand, M.; Endres, F.; MacFarlane, D. R.; Ohno, H.; Scrosati, B. Ionic-Liquid Materials for the Electrochemical Challenges of the Future. *Nat. Mater.* **2009**, 8 (8), 621–629.
- (34) Etacheri, V.; Marom, R.; Elazari, R.; Salitra, G.; Aurbach, D. Challenges in the Development of Advanced Li-Ion Batteries: A Review. *Energy Environ. Sci.* **2011**, 4 (9), 3243–3262.
- (35) Antitomaso, P.; Fraisse, B.; Stievano, L.; Biscaglia, S.; Aymé-Perrot, D.; Girard, P.; Sougrati, M. T.; Monconduit, L. SnSb Electrodes for Li-Ion Batteries: The Electrochemical Mechanism and Capacity Fading Origins Elucidated by Using Operando Techniques. *J. Mater. Chem. A* **2017**, 5, 6546-6555.
- (36) Mukhopadhyay, A.; Sheldon, B. W. Deformation and Stress in Electrode Materials for Li-Ion Batteries. *Prog. Mater. Sci.* **2014**, 63 (January), 58–116.
- (37) Liu, X.; Zhu, X.; Pan, D. Solutions for the Problems of Silicon–Carbon Anode Materials for Lithium-Ion Batteries. *R. Soc. Open Sci.* **2018**, 5 (6).
- (38) Loeffler, N.; Bresser, D.; Passerini, S. Secondary Lithium-Ion Battery Anodes: From First Commercial Batteries to Recent Research Activities. *Johnson Matthey Technol. Rev.* **2015**, 59 (1), 34–44.
- (39) Kalhoff, J.; Eshetu, G. G.; Bresser, D.; Passerini, S. Safer Electrolytes for Lithium-Ion Batteries: State of the Art and Perspectives. *ChemSusChem* **2015**, 8 (13), 2154–2175.
- (40) Zhang, S. S. Problem, Status, and Possible Solutions for Lithium Metal Anode of Rechargeable Batteries. *ACS Appl. Energy Mater.* **2018**, 1 (3), 910–920.
- (41) Watanabe, M.; Thomas, M. L.; Zhang, S.; Ueno, K.; Yasuda, T.; Dokko, K. Application of Ionic Liquids to Energy Storage and Conversion Materials and Devices. *Chem. Rev.* **2017**, 117, 10, 7190-7239.
- (42) Park, M. S.; Ma, S. B.; Lee, D. J.; Im, D.; Doo, S.-G.; Yamamoto, O. A Highly Reversible Lithium Metal Anode. *Sci. Rep.* **2014**, 4, 3815.

- (43) Qian, J.; Henderson, W. a; Xu, W.; Bhattacharya, P.; Engelhard, M.; Borodin, O.; Zhang, J.-G. High Rate and Stable Cycling of Lithium Metal Anode. *Nat. Commun.* **2015**, 6, 6362.
- (44) Miao, R.; Yang, J.; Xu, Z.; Wang, J.; Nuli, Y.; Sun, L. A New Ether-Based Electrolyte for Dendrite-Free Lithium-Metal Based Rechargeable Batteries. *Sci. Rep.* **2016**, 6 (February), 21771.
- (45) Younesi, R.; Veith, G. M.; Johansson, P.; Edstrom, K.; Vegge, T. Lithium Salts for Advanced Lithium Batteries: Li-Metal, Li-O₂, and Li-S. *Energy Environ. Sci.* **2015**, 8 (7), 1905–1922.
- (46) Galiński, M.; Lewandowski, A.; Stepniak, I. Ionic Liquids as Electrolytes. *Electrochim. Acta* **2006**, 51 (26), 5567–5580.
- (47) Appetecchi, G. B. Safer Electrolyte Components for Rechargeable Batteries. *Phys. Sci. Rev.* **2018**, 4 (3).
- (48) MacFarlane, D. R.; Tachikawa, N.; Forsyth, M.; Pringle, J. M.; Howlett, P. C.; Elliott, G. D.; Davis, J. H.; Watanabe, M.; Simon, P.; Angell, C. a. Energy Applications of Ionic Liquids. *Energy Environ. Sci.* **2014**, 7 (1), 232–250.
- (49) Eftekhari, A.; Liu, Y.; Chen, P. Different Roles of Ionic Liquids in Lithium Batteries. *J. Power Sources* **2016**, 334, 221–239.
- (50) Liu, C.; Ma, X.; Xu, F.; Zheng, L.; Zhang, H.; Feng, W. F.; Huang, X. J.; Armand, M.; Nie, J.; Chen, H.; et al. Dendrite-Free and Performance-Enhanced Lithium Metal Batteries through Optimizing Solvent Compositions and Adding Combinational Additives. *J. Power Sources* **2012**, 8 (9), 252–264.
- (51) Wen, J.; Yu, Y.; Chen, C. A Review on Lithium-Ion Batteries Safety Issues: Existing Problems and Possible Solutions. *Mater. Express* **2012**, 2 (3), 197–212.
- (52) Wang, Q.; Ping, P.; Zhao, X.; Chu, G.; Sun, J.; Chen, C. Thermal Runaway Caused Fire and Explosion of Lithium Ion Battery. *J. Power Sources* **2012**, 208, 210–224.
- (53) Yoshida, K.; Tsuchiya, M.; Tachikawa, N.; Dokko, K.; Watanabe, M. Correlation between Battery Performance and Lithium Ion Diffusion in Glyme-Lithium Bis(Trifluoromethanesulfonyl)Amide Equimolar Complexes. *J. Electrochem. Soc.* **2012**, 159 (7).
- (54) Forsyth, M.; Porcarelli, L.; Wang, X.; Goujon, N.; Mecerreyes, D. Innovative Electrolytes Based on Ionic Liquids and Polymers for Next-Generation Solid-State Batteries. *Acc. Chem. Res.* **2019**, 52 (3), 686–694.
- (55) Kar, M.; Plechkova, N. V.; Seddon, K. R.; Pringle, J. M.; MacFarlane, D. R. Ionic Liquids—Further Progress on the Fundamental Issues. *Aust. J. Chem.* **2019**, 72 (2), 3–10.
- (56) Tokuda, H.; Hayamizu, K.; Ishii, K.; Bin, A.; Susan, H.; Watanabe, M. Physicochemical Properties and Structures of Room Temperature Ionic Liquids . 2 . Variation of Alkyl Chain Length in Imidazolium Cation Physicochemical Properties and Structures of Room Temperature Ionic Liquids . 2 . Variation of Alkyl Chain Length in Im. **2005**, 6103–6110.
- (57) Schmitz, P.; Jakelski, R.; Pyschik, M.; Jalkanen, K.; Nowak, S.; Winter, M.; Bieker, P. Decomposition of Imidazolium-Based Ionic Liquids in Contact with Lithium Metal. *ChemSusChem* **2017**, 10 (5), 876–883.
- (58) Macfarlane, D. R.; Forsyth, M.; Howlett, P. C.; Pringle, J. M.; Sun, J.; Annat, G.; Neil, W.; Izgorodina, E. I. Ionic Liquids in Electrochemical Devices and Processes: Managing Interfacial Electrochemistry. *Acc. Chem. Res.* **2007**, 40 (11), 1165–1173.
- (59) Sowmiah, S.; Srinivasadesikan, V.; Tseng, M. C.; Chu, Y. H. *On the Chemical Stabilities*

of *Ionic Liquids*; 2009; Vol. 14.

- (60) Matsumoto, H.; Sakaebe, H.; Tatsumi, K. Preparation of Room Temperature Ionic Liquids Based on Aliphatic Onium Cations and Asymmetric Amide Anions and Their Electrochemical Properties as a Lithium Battery Electrolyte. *Journal of Power Sources*; **2005**, 146 (1-2), 45-50.
- (61) Tsunashima, K.; Sugiya, M. Physical and Electrochemical Properties of Low-Viscosity Phosphonium Ionic Liquids as Potential Electrolytes. *Electrochem. commun.* **2007**, 9 (9), 2353-2358.
- (62) Schmitz, P.; Kolek, M.; Pyschik, M.; Jalkanen, K.; Nowak, S.; Winter, M.; Bieker, P. Modified Imidazolium-Based Ionic Liquids With Improved Chemical Stability Against Lithium Metal. *ChemistrySelect* **2017**, 2 (21), 6052–6056.
- (63) Srour, H.; Rouault, H.; Santini, C. Imidazolium Based Ionic Liquid Electrolytes for Li-Ion Secondary Batteries Based on Graphite and LiFePO₄. *J. Electrochem. Soc.* **2012**, 160 (1), A66–A69.
- (64) Matsui, Y.; Kawaguchi, S.; Sugimoto, T.; Kikuta, M.; Higashizaki, T.; Kono, M.; Yamagata, M.; Ishikawa, M. Charge-Discharge Characteristics of a LiNi_{1/3}Mn_{1/3}Co_{1/3}O₂ Cathode in FSI-Based Ionic Liquids. *Electrochemistry* **2012**, 80 (10), 808–811.
- (65) Ishikawa, M.; Sugimoto, T.; Kikuta, M.; Ishiko, E.; Kono, M. Pure Ionic Liquid Electrolytes Compatible with a Graphitized Carbon Negative Electrode in Rechargeable Lithium-Ion Batteries. *J. Power Sources* **2006**, 162 (1), 658–662.
- (66) Appetecchi, G. B.; Montanino, M.; Passerini, S. Ionic Liquid-Based Electrolytes for High Energy, Safer Lithium Batteries. *ACS Symp. Ser.* **2012**, 1117 (January), 67–128.
- (67) Bhatt, A. I.; Best, A. S.; Huang, J.; Hollenkamp, A. F. Application of the N-Propyl-N-Methyl-Pyrrolidinium Bis(Fluorosulfonyl)Imide RTIL Containing Lithium Bis(Fluorosulfonyl)Imide in Ionic Liquid Based Lithium Batteries. *J. Electrochem. Soc.* **2010**, 157 (1), A66.
- (68) Quartarone, E.; Mustarelli, P. Electrolytes for Solid-State Lithium Rechargeable Batteries: Recent Advances and Perspectives. *Chem. Soc. Rev.* **2011**, 40 (5), 2525–2540.
- (69) Elia, G. A.; Ulissi, U.; Jeong, S.; Passerini, S.; Hassoun, J. Exceptional Long-Life Performance of Lithium-Ion Batteries Using Ionic Liquid-Based Electrolytes. *Energy Environ. Sci.* **2016**, 9 (10), 3210–3220.
- (70) Girard, G. M. A.; Hilder, M.; Dupre, N.; Guyomard, D.; Nucciarone, D.; Whitbread, K.; Zavorine, S.; Moser, M.; Forsyth, M.; MacFarlane, D. R.; et al. Spectroscopic Characterization of the SEI Layer Formed on Lithium Metal Electrodes in Phosphonium Bis(Fluorosulfonyl)Imide Ionic Liquid Electrolytes. *ACS Appl. Mater. Interfaces* **2018**, 10 (7), 6719–6729.
- (71) Chen, N.; Guan, Y.; Shen, J.; Guo, C.; Qu, W.; Li, Y.; Wu, F.; Chen, R. Heteroatom Si Substituent Imidazolium-Based Ionic Liquid Electrolyte Boosts the Performance of Dendrite-Free Lithium Batteries. *ACS Appl. Mater. Interfaces* **2019**, 11 (12), 12154–12160.
- (72) Matsumoto, H.; Sakaebe, H.; Tatsumi, K.; Kikuta, M.; Ishiko, E.; Kono, M. Fast Cycling of Li/LiCoO₂ Cell with Low-Viscosity Ionic Liquids Based on Bis(Fluorosulfonyl)Imide [FSI]-. *J. Power Sources* **2006**, 160, 1308–1313.
- (73) Nazet, A.; Sokolov, S.; Sonnleitner, T.; Makino, T.; Kanakubo, M.; Buchner, R. Densities, Viscosities, and Conductivities of the Imidazolium Ionic Liquids [Emim][Ac],

- [Emim][FAP], [Bmim][BETI], [Bmim][FSI], [Hmim][TFSI], and [Omim][TFSI]. *J. Chem. Eng. Data* **2015**, 60 (8), 2400–2411.
- (74) Tokuda, H.; Ishii, K.; Susan, M. a B. H.; Tsuzuki, S.; Hayamizu, K.; Watanabe, M. Physicochemical Properties and Structures of Room-Temperature Ionic Liquids. 3. Variation of Cationic Structures. *J. Phys. Chem. B* **2006**, 110 (6), 2833–2839.
- (75) Sánchez-Ramírez, N.; Assresahegn, B. D.; Bélanger, D.; Torresi, R. M. A Comparison among Viscosity, Density, Conductivity, and Electrochemical Windows of N-n-Butyl-N-Methylpyrrolidinium and Triethyl-n-Pentylphosphonium Bis(Fluorosulfonyl Imide) Ionic Liquids and Their Analogues Containing Bis(Trifluoromethylsulfonyl) Imide . *J. Chem. Eng. Data* **2017**, 62 (10), 3437–3444.
- (76) Ueki, T.; Watanabe, M. Macromolecules in Ionic Liquids: Progress, Challenges, and Opportunities. *Macromolecules*. **2008**, 41, 11, 3739-3749.
- (77) Shaplov, A. S.; Marcilla, R.; Mecerreyes, D. Recent Advances in Innovative Polymer Electrolytes Based on Poly(Ionic Liquid)S. *Electrochim. Acta* **2015**, 175, 18-34.
- (78) Peled, E. The Electrochemical-Behavior of Alkali and Alkaline-Earth Metals in Non-Aqueous Battery Systems - the Solid Electrolyte Interphase Model. *J. Electrochem. Soc.* **1979**, 126 (12), 2047–2051.
- (79) Verma, P.; Maire, P.; Novák, P. A Review of the Features and Analyses of the Solid Electrolyte Interphase in Li-Ion Batteries. *Electrochim. Acta* **2010**, 55 (22), 6332–6341.
- (80) Edström, K.; Gustafsson, T.; Thomas, J. O. The Cathode-Electrolyte Interface in the Li-Ion Battery. In *Electrochimica Acta* **2004**, 50 (2-3), 397-403.
- (81) Nie, K.; Hong, Y.; Qiu, J.; Li, Q.; Yu, X.; Li, H.; Chen, L. Interfaces between Cathode and Electrolyte in Solid State Lithium Batteries: Challenges and Perspectives. *Frontiers in Chemistry*. **2018**, 6, 616.
- (82) Peled, E. Film Forming Reaction at the Lithium/Electrolyte Interface. *J. Power Sources* **1983**, 9 (3), 253–266.
- (83) Peled, E. Advanced Model for Solid Electrolyte Interphase Electrodes in Liquid and Polymer Electrolytes. *J. Electrochem. Soc.* **1997**, 144 (8), L208.
- (84) Yu, X.; Manthiram, A. Electrode-Electrolyte Interfaces in Lithium-Based Batteries. *Energy and Environmental Science*. **2018**, 11, 527-543.
- (85) Aurbach, D. Review of Selected Electrode-Solution Interactions Which Determine the Performance of Li and Li Ion Batteries. *J. Power Sources* **2000**, 89 (2), 206–218.
- (86) Qu, D.; Wang, G.; Kafle, J.; Harris, J.; Crain, L.; Jin, Z.; Zheng, D. Electrochemical Impedance and Its Applications in Energy-Storage Systems. *Small Methods* **2018**, 2 (8), 1700342.
- (87) Aurbach, D.; Zaban, A. Impedance Spectroscopy of Lithium Electrodes. *J. Electroanal. Chem.* **1994**, 367 (1–2), 15–25.
- (88) Thevenin, J. Passivating Films on Lithium Electrodes. An Approach by Means of Electrode Impedance Spectroscopy. *J. Power Sources* **1985**, 14 (1–3), 45–52.
- (89) Bouchet, R.; Lascaud, S.; Rosso, M. An EIS Study of the Anode Li/PEO-LiTFSI of a Li Polymer Battery. *J. Electrochem. Soc.* **2003**, 150 (10), A1385–A1389.
- (90) Wohde, F.; Balabajew, M.; Roling, B. Li⁺ Transference Numbers in Liquid Electrolytes Obtained by Very-Low-Frequency Impedance Spectroscopy at Variable Electrode Distances. *J. Electrochem. Soc.* **2016**, 163 (5), A714–A721.

- (91) Ota, H.; Sakata, Y.; Wang, X.; Sasahara, J.; Yasukawa, E. Characterization of Lithium Electrode in Lithium Imides/Ethylene Carbonate and Cyclic Ether Electrolytes. *J. Electrochem. Soc.* **2004**, *151* (3), A427-A436.
- (92) Campana, F. P.; Kötz, R.; Vetter, J.; Novák, P.; Siegenthaler, H. In Situ Atomic Force Microscopy Study of Dimensional Changes during Li + Ion Intercalation/de-Intercalation in Highly Oriented Pyrolytic Graphite. *Electrochem. commun.* **2005**, *7* (1), 107–112.
- (93) Inaba, M.; Jeong, S.-K.; Ogumi, Z. In Situ Scanning Probe Microscopy of Interfacial Phenomena in Batteries. *Interface* **2011**, *20* (3), 55–59.
- (94) Liu, T.; Lin, L.; Bi, X.; Tian, L.; Yang, K.; Liu, J.; Li, M.; Chen, Z.; Lu, J.; Amine, K.; et al. In Situ Quantification of Interphasial Chemistry in Li-Ion Battery. *Nat. Nanotechnol.* **2019**, *14* (1), 50–56.
- (95) Cohen, Y. S.; Cohen, Y.; Aurbach, D. Micromorphological Studies of Lithium Electrodes in Alkyl Carbonate Solutions Using in Situ Atomic Force Microscopy. *J. Phys. Chem. B* **2000**, *104* (51), 12282–12291.
- (96) Mogi, R.; Inaba, M.; Jeong, S. K.; Iriyama, Y.; Abe, T.; Ogumi, Z. Effects of Some Organic Additives on Lithium Deposition in Propylene Carbonate. *J. Electrochem. Soc.* **2002**, *149* (12), 1578–1583.
- (97) Li, Y.; Li, Y.; Pei, A.; Yan, K.; Sun, Y.; Wu, C. L.; Joubert, L. M.; Chin, R.; Koh, A. L.; Yu, Y.; et al. Atomic Structure of Sensitive Battery Materials and Interfaces Revealed by Cryo–Electron Microscopy. *Science* **2017**, *358* (6362), 506-510.
- (98) Wang, X.; Li, Y.; Meng, Y. S. Cryogenic Electron Microscopy for Characterizing and Diagnosing Batteries. *Joule*. **2018**, *2* (11), 2225-2234.
- (99) Aurbach, D. The Study of Electrolyte Solutions Based on Ethylene and Diethyl Carbonates for Rechargeable Li Batteries. *J. Electrochem. Soc.* **1995**, *142* (9), 2882.
- (100) Philippe, B.; Hahlin, M.; Edstrom, K.; Gustafsson, T.; Siegbahn, H.; Rensmo, H. Photoelectron Spectroscopy for Lithium Battery Interface Studies. *J. Electrochem. Soc.* **2016**, *163* (2), A178–A191.
- (101) Kong, F.; Kostecki, R.; Nadeau, G.; Song, X.; Zaghbi, K.; Kinoshita, K.; McLarnon, F. In Situ Studies of SEI Formation. *J. Power Sources* **2001**, *97-98*, 58–66.
- (102) Schmitz, R.; Ansgar Müller, R.; Wilhelm Schmitz, R.; Schreiner, C.; Kunze, M.; Lex-Balducci, A.; Passerini, S.; Winter, M. SEI Investigations on Copper Electrodes after Lithium Plating with Raman Spectroscopy and Mass Spectrometry. *J. Power Sources* **2013**, *233*, 110-114.
- (103) Aurbach, D.; Daroux, M.; Yeager, E. B. B.; McDougall, G. Spectroscopic Studies of Lithium in an Ultrahigh Vacuum System. *J. Electroanal. Chem.* **1993**, *358* (1–2), 63–76.
- (104) Morigaki, K. I.; Ohta, A. Analysis of the Surface of Lithium in Organic Electrolyte by Atomic Force Microscopy, Fourier Transform Infrared Spectroscopy and Scanning Auger Electron Microscopy. *J. Power Sources* **1998**, *76* (2), 159-166.
- (105) Bhattacharyya, R.; Key, B.; Chen, H.; Best, A. S.; Hollenkamp, A. F.; Grey, C. P. In Situ NMR Observation of the Formation of Metallic Lithium Microstructures in Lithium Batteries. *Nat. Mater.* **2010**, *9* (6), 504–510.
- (106) Chandrashekar, S.; Trease, N. M.; Chang, H. J.; Du, L. S.; Grey, C. P.; Jerschow, A. 7 Li MRI of Li Batteries Reveals Location of Microstructural Lithium. *Nat. Mater.* **2012**, *11*, 311–315.
- (107) Leroy, S.; Blanchard, F.; Dedryvère, R.; Martinez, H.; Carré, B.; Lemordant, D.; Gonbeau,

- D. Surface Film Formation on a Graphite Electrode in Li-Ion Batteries: AFM and XPS Study. *Surf. Interface Anal.* **2005**, 37 (10), 773–781.
- (108) Dedryvère, R.; Martinez, H.; Leroy, S.; Lemordant, D.; Bonhomme, F.; Biensan, P.; Gonbeau, D. Surface Film Formation on Electrodes in a LiCoO₂/Graphite Cell: A Step by Step XPS Study. *J. Power Sources* **2007**, 174 (2), 462–468.
- (109) Aurbach, D.; Zaban, A.; Ein-Eli, Y.; Weissman, I.; Chusid, O.; Markovsky, B.; Levi, M.; Levi, E.; Schechter, A.; Granot, E. Recent Studies on the Correlation between Surface Chemistry, Morphology, Three-Dimensional Structures and Performance of Li and Li-C Intercalation Anodes in Several Important Electrolyte Systems. *J. Power Sources* **1997**, 68 (1), 91–98.
- (110) Shkrob, I. A.; Zhu, Y.; Marin, T. W.; Abraham, D. Reduction of Carbonate Electrolytes and the Formation of Solid-Electrolyte Interface (SEI) in Lithium-Ion Batteries. 1. Spectroscopic Observations of Radical Intermediates Generated in One-Electron Reduction of Carbonates. *J. Phys. Chem. C* **2013**, 117 (38), 19255–19269.
- (111) Nie, M.; Lucht, B. L. Role of Lithium Salt on Solid Electrolyte Interface (SEI) Formation and Structure in Lithium Ion Batteries. *J. Electrochem. Soc.* **2014**, 161 (6), A1001–A1006.
- (112) Augustsson, A.; Herstedt, M.; Guo, J. H.; Edström, K.; Zhuang, G. V.; Ross, P. N.; Rubensson, J. E.; Nordgren, J. Solid Electrolyte Interphase on Graphite Li-Ion Battery Anodes Studied by Soft X-Ray Spectroscopy. *Phys. Chem. Chem. Phys.* **2004**, 6 (16), 4185–4189.
- (113) Bolimowska, E.; Morales-Ugarte, J. E.; Rouault, H.; Santos-Peña, J.; Santini, C.; Benayad, A. Influence of the Vinylene Carbonate on the Wetting and Interface Chemical Structure of Doped Ionic Liquid Electrolyte at Porous Graphite Surface. *J. Phys. Chem. C* **2017**, 121 (30), 16166–16173.
- (114) Morales-Ugarte, J. E.; Bolimowska, E.; Rouault, H.; Santos-Peña, J.; Santini, C. C.; Benayad, A. EIS and XPS Investigation on SEI Layer Formation during First Discharge on Graphite Electrode with a Vinylene Carbonate Doped Imidazolium Based Ionic Liquid Electrolyte. *J. Phys. Chem. C* **2018**, 122 (32), 18223–18230.
- (115) Howlett, P. C.; Brack, N.; Hollenkamp, a. F.; Forsyth, M.; MacFarlane, D. R. Characterization of the Lithium Surface in N-Methyl-N-Alkylpyrrolidinium Bis(Trifluoromethanesulfonyl)Amide Room-Temperature Ionic Liquid Electrolytes. *J. Electrochem. Soc.* **2006**, 153 (3), A595.
- (116) Aurbach, D.; Zinigrad, E.; Cohen, Y.; Teller, H. A Short Review of Failure Mechanisms of Lithium Metal and Lithiated Graphite Anodes in Liquid Electrolyte Solutions. *Solid State Ionics* **2002**, 148 (3–4), 405–416.
- (117) Kim, H.; Jeong, G.; Kim, Y. U.; Kim, J. H.; Park, C. M.; Sohn, H. J. Metallic Anodes for next Generation Secondary Batteries. *Chem. Soc. Rev.* **2013**, 42 (23), 9011–9034.
- (118) Lin, Y. X.; Liu, Z.; Leung, K.; Chen, L. Q.; Lu, P.; Qi, Y. Connecting the Irreversible Capacity Loss in Li-Ion Batteries with the Electronic Insulating Properties of Solid Electrolyte Interphase (SEI) Components. *J. Power Sources* **2016**, 309, 221–230.
- (119) Cheng, X.-B.; Zhang, R.; Zhao, C.-Z.; Zhang, Q. Toward Safe Lithium Metal Anode in Rechargeable Batteries: A Review. *Chem. Rev.* **2017**, 117 (15), 10403–10473.
- (120) Wang, A.; Kadam, S.; Li, H.; Shi, S.; Qi, Y. Review on Modeling of the Anode Solid Electrolyte Interphase (SEI) for Lithium-Ion Batteries. *npj Comput. Mater.* **2018**, 4 (1).
- (121) Brissot, C.; Rosso, M.; Chazalviel, J. N.; Lascaud, S. Dendritic Growth Mechanisms in Lithium/Polymer Cells. *J. Power Sources* **1999**, 81–82, 925–929.

- (122) Howlett, P. C.; MacFarlane, D. R.; Hollenkamp, A. F. A Sealed Optical Cell for the Study of Lithium-Electrode|electrolyte Interfaces. *J. Power Sources* **2003**, 114 (2), 277–284.
- (123) Nishida, T.; Nishikawa, K.; Rosso, M.; Fukunaka, Y. Optical Observation of Li Dendrite Growth in Ionic Liquid. *Electrochim. Acta* **2013**, 100, 333–341.
- (124) Steiger, J.; Kramer, D.; Mönig, R. Microscopic Observations of the Formation, Growth and Shrinkage of Lithium Moss during Electrodeposition and Dissolution. *Electrochim. Acta* **2014**, 136, 529–536.
- (125) Dollé, M.; Sannier, L.; Beaudoin, B.; Trentin, M.; Tarascon, J.-M. Live Scanning Electron Microscope Observations of Dendritic Growth in Lithium/Polymer Cells. *Electrochem. Solid-State Lett.* **2002**, 5 (12), A286.
- (126) Shen, C.; Hu, G.; Cheong, L.-Z.; Huang, S.; Zhang, J.-G.; Wang, D. Direct Observation of the Growth of Lithium Dendrites on Graphite Anodes by Operando EC-AFM. *Small Methods* **2018**, 2 (2), 1700298.
- (127) Zeng, Z.; Liang, W. I.; Liao, H. G.; Xin, H. L.; Chu, Y. H.; Zheng, H. Visualization of Electrode-Electrolyte Interfaces in LiPF₆/EC/DEC Electrolyte for Lithium Ion Batteries via in Situ TEM. *Nano Lett.* **2014**, 14 (4), 1745–1750.
- (128) Zhang, J.-G.; Xu, W.; Henderson, W. A. *Springer Series in Materials Science 249 Lithium Metal Anodes and Rechargeable Lithium Metal Batteries*; 2017.
- (129) Arakawa, M.; Tobishima, S. ichi; Nemoto, Y.; Ichimura, M.; Yamaki, J. ichi. Lithium Electrode Cycleability and Morphology Dependence on Current Density. *J. Power Sources* **1993**, 43 (1–3), 27–35.
- (130) Yamaki, J.; Tobishima, S.; Hayashi, K.; Keiichi Saito; Nemoto, Y.; Arakawa, M. A Consideration of the Morphology of Electrochemically Deposited Lithium in an Organic Electrolyte. *J. Power Sources* **1998**, 74 (2), 219–227.
- (131) Steiger, J.; Kramer, D.; Mönig, R. Mechanisms of Dendritic Growth Investigated by in Situ Light Microscopy during Electrodeposition and Dissolution of Lithium. *J. Power Sources* **2014**, 261, 112–119.
- (132) Chazalviel, J. N. Electrochemical Aspects of the Generation of Ramified Metallic Electrodeposits. *Phys. Rev. A* **1990**, 42 (12), 7355–7367.
- (133) Brissot, C.; Rosso, M.; Chazalviel, J. N.; Baudry, P.; Lascaud, S. In Situ Study of Dendritic Growth in Lithium/PEO-Salt/Lithium Cells. *Electrochim. Acta* **1998**, 43 (10-11), 1569–1574.
- (134) Rosso, M.; Brissot, C.; Teysot, A.; Dollé, M.; Sannier, L.; Tarascon, J. M.; Bouchet, R.; Lascaud, S. Dendrite Short-Circuit and Fuse Effect on Li/Polymer/Li Cells. *Electrochim. Acta* **2006**, 51 (25), 5334–5340.
- (135) Rosso, M.; Gobron, T.; Brissot, C.; Chazalviel, J. N.; Lascaud, S. Onset of Dendritic Growth in Lithium/Polymer Cells. *J. Power Sources* **2001**, 97–98, 804–806.
- (136) Sand, H. J. S. On the Concentration at the Electrodes in a Solution, with Special Reference to the Liberation of Hydrogen by Electrolysis of a Mixture of Copper Sulphate and Sulphuric Acid. *Philos. Mag.* **1901**, 1.
- (137) Sano, H.; Sakaebe, H.; Matsumoto, H. Observation of Electrodeposited Lithium by Optical Microscope in Room Temperature Ionic Liquid-Based Electrolyte. *J. Power Sources* **2011**, 196 (16), 6663–6669.
- (138) Basile, A.; Bhatt, A. I.; O’Mullane, A. P. Stabilizing Lithium Metal Using Ionic Liquids for Long-Lived Batteries. *Nat. Commun.* **2016**, 7 (11794), 1–11.

- (139) Schweikert, N.; Hofmann, A.; Schulz, M.; Scheuermann, M.; Boles, S. T.; Hanemann, T.; Hahn, H.; Indris, S. Suppressed Lithium Dendrite Growth in Lithium Batteries Using Ionic Liquid Electrolytes: Investigation by Electrochemical Impedance Spectroscopy, Scanning Electron Microscopy, and in Situ ^7Li Nuclear Magnetic Resonance Spectroscopy. *J. Power Sources* **2013**, 228, 237–243.
- (140) Zhang, K.; Lee, G. H.; Park, M.; Li, W.; Kang, Y. M. Recent Developments of the Lithium Metal Anode for Rechargeable Non-Aqueous Batteries. *Adv. Energy Mater.* **2016**, 1–14.
- (141) Aurbach, D.; Gamolsky, K.; Markovsky, B.; Gofer, Y.; Schmidt, M.; Heider, U. On the Use of Vinylene Carbonate (VC) as an Additive to Electrolyte Solutions for Li-Ion Batteries. *Electrochim. Acta* **2002**, 47 (9), 1423–1439.
- (142) Ota, H.; Sakata, Y.; Inoue, A.; Yamaguchi, S. Analysis of Vinylene Carbonate Derived SEI Layers on Graphite Anode. *J. Electrochem. Soc.* **2004**, 151 (10), A1659.
- (143) Michan, A. L.; Parimalam, B. S.; Leskes, M.; Kerber, R. N.; Yoon, T.; Grey, C. P.; Lucht, B. L. Fluoroethylene Carbonate and Vinylene Carbonate Reduction: Understanding Lithium-Ion Battery Electrolyte Additives and Solid Electrolyte Interphase Formation. *Chem. Mater.* **2016**, 28 (22), 8149–8159.
- (144) Zhang, X. Q.; Cheng, X. B.; Chen, X.; Yan, C.; Zhang, Q. Fluoroethylene Carbonate Additives to Render Uniform Li Deposits in Lithium Metal Batteries. *Adv. Funct. Mater.* **2017**, 27 (10), 1–8.
- (145) Barghamadi, M.; Best, A. S.; Bhatt, A. I.; Hollenkamp, A. F.; Mahon, P. J.; Musameh, M.; R  ther, T. Effect of LiNO_3 Additive and Pyrrolidinium Ionic Liquid on the Solid Electrolyte Interphase in the Lithium–Sulfur Battery. *J. Power Sources* **2015**, 295, 212–220.
- (146) Pan, J.; Cheng, Y. T.; Qi, Y. General Method to Predict Voltage-Dependent Ionic Conduction in a Solid Electrolyte Coating on Electrodes. *Phys. Rev. B - Condens. Matter Mater. Phys.* **2015**, 91, 134116.
- (147) Liu, Z.; Qi, Y.; Lin, Y. X.; Chen, L.; Lu, P.; Chen, L. Q. Interfacial Study on Solid Electrolyte Interphase at Li Metal Anode: Implication for Li Dendrite Growth. *J. Electrochem. Soc.* **2016**, 163 (3), A592–A598.
- (148) Ding, F.; Xu, W.; Graff, G. L.; Zhang, J.; Sushko, M. L.; Chen, X.; Shao, Y.; Engelhard, M. H.; Nie, Z.; Xiao, J.; et al. Dendrite-Free Lithium Deposition via Self-Healing Electrostatic Shield Mechanism. *J. Am. Chem. Soc.* **2013**, 135 (11), 4450–4456.
- (149) Aurbach, D.; Pollak, E.; Elazari, R.; Salitra, G.; Kelley, C. S.; Affinito, J. On the Surface Chemical Aspects of Very High Energy Density, Rechargeable Li–Sulfur Batteries. *J. Electrochem. Soc.* **2009**, 156 (8), A694–A702.
- (150) Li, W.; Yao, H.; Yan, K.; Zheng, G.; Liang, Z.; Chiang, Y. M.; Cui, Y. The Synergetic Effect of Lithium Polysulfide and Lithium Nitrate to Prevent Lithium Dendrite Growth. *Nat. Commun.* **2015**, 6, 7436.
- (151) Marchioni, F.; Star, K.; Menke, E.; Buffeteau, T.; Servant, L.; Dunn, B.; Wudl, F. Protection of Lithium Metal Surfaces Using Chlorosilanes. *Langmuir* **2007**, 23, 11597–11602.
- (152) Umeda, G. A.; Menke, E.; Richard, M.; Stamm, K. L.; Wudl, F.; Dunn, B. Protection of Lithium Metal Surfaces Using Tetraethoxysilane. *J. Mater. Chem.* **2011**, 21 (5), 1593–1599.
- (153) Wu, M.; Wen, Z.; Liu, Y.; Wang, X.; Huang, L. Electrochemical Behaviors of a Li_3N Modified Li Metal Electrode in Secondary Lithium Batteries. *J. Power Sources* **2011**, 196

- (19), 8091-8097.
- (154) Wang, L.; Zhang, L.; Wang, Q.; Li, W.; Wu, B.; Jia, W.; Wang, Y.; Li, J.; Li, H. Long Lifespan Lithium Metal Anodes Enabled by Al₂O₃ Sputter Coating. *Energy Storage Mater.* **2018**, 10, 16-23.
- (155) Li, N. W.; Yin, Y. X.; Yang, C. P.; Guo, Y. G. An Artificial Solid Electrolyte Interphase Layer for Stable Lithium Metal Anodes. *Adv. Mater.* **2016**, 28 (9), 1853-1858.
- (156) Zhang, Y. J.; Liu, X. Y.; Bai, W. Q.; Tang, H.; Shi, S. J.; Wang, X. L.; Gu, C. D.; Tu, J. P. Magnetron Sputtering Amorphous Carbon Coatings on Metallic Lithium: Towards Promising Anodes for Lithium Secondary Batteries. *J. Power Sources* **2014**, 266, 43-50.
- (157) Zheng, G.; Lee, S. W.; Liang, Z.; Lee, H.-W.; Yan, K.; Yao, H.; Wang, H.; Li, W.; Chu, S.; Cui, Y. Interconnected Hollow Carbon Nanospheres for Stable Lithium Metal Anodes. *Nat. Nanotechnol.* **2014**, 8, 618-623.
- (158) Monroe, C.; Newman, J. The Impact of Elastic Deformation on Deposition Kinetics at Lithium/Polymer Interfaces. *J. Electrochem. Soc.* **2005**, 152 (2), A396-A404.
- (159) Ferrese, A.; Newman, J. Mechanical Deformation of a Lithium-Metal Anode Due to a Very Stiff Separator. *J. Electrochem. Soc.* **2014**, 161 (9), A1350-A1359.
- (160) Armand, M. Polymer Solid Electrolytes - an Overview. *Solid State Ionics* **1983**, 9-10, 745-754.
- (161) Niitani, T.; Shimada, M.; Kawamura, K.; Dokko, K.; Rho Y.; Kanamura, K. Synthesis of Li⁺ ion Conductive PEO-PSt Block Copolymer Electrolyte with Microphase Separation Structure. *Electrochemical and Solid-State Letters* **2005**, 8 (8), A385-A388.
- (162) Hallinan, D. T.; Mullin, S. A.; Stone, G. M.; Balsara, N. P. Lithium Metal Stability in Batteries with Block Copolymer Electrolytes. *J. Electrochem. Soc.* **2013**, 160 (3), A464-A470.
- (163) Devaux, D.; Glé, D.; Phan, T. N. T.; Gignes, D.; Giroud, E.; Deschamps, M.; Denoyel, R.; Bouchet, R. Optimization of Block Copolymer Electrolytes for Lithium Metal Batteries. *Chem. Mater.* **2015**, 27 (13) 4682-4692.
- (164) Jung, Y. S.; Oh, D. Y.; Nam, Y. J.; Park, K. H. Issues and Challenges for Bulk-Type All-Solid-State Rechargeable Lithium Batteries Using Sulfide Solid Electrolytes. *Isr. J. Chem.* **2015**, 55 (5), 472-485.
- (165) Fu, J.; Yu, P.; Zhang, N.; Ren, G.; Zheng, S.; Huang, W.; Long, X.; Li, H.; Liu, X. In Situ Formation of a Bifunctional Interlayer Enabled by a Conversion Reaction to Initiatively Prevent Lithium Dendrites in a Garnet Solid Electrolyte. *Energy Environ. Sci.* **2019**, 12, 1404-1412.
- (166) Stone, G. M.; Mullin, S. A.; Teran, A. A.; Hallinan, D. T.; Minor, A. M.; Hexemer, A.; Balsara, N. P. Resolution of the Modulus versus Adhesion Dilemma in Solid Polymer Electrolytes for Rechargeable Lithium Metal Batteries. *J. Electrochem. Soc.* **2012**, 159 (3), A222-A227.
- (167) Zhu, Y.; He, X.; Mo, Y. Origin of Outstanding Stability in the Lithium Solid Electrolyte Materials: Insights from Thermodynamic Analyses Based on First-Principles Calculations. *ACS Appl. Mater. Interfaces* **2015**, 7 (42), 23685-23693.
- (168) Li, L.; Li, S.; Lu, Y. Suppression of Dendritic Lithium Growth in Lithium Metal-Based Batteries. *Chem. Commun.* **2018**, 54 (50), 6648-6661.
- (169) Gireaud, L.; Grugeon, S.; Laruelle, S.; Yrieix, B.; Tarascon, J. M. Lithium Metal Stripping/Plating Mechanisms Studies: A Metallurgical Approach. *Electrochem. commun.*

- 2006, 8 (10), 1639–1649.
- (170) Becking, J.; Gröbmeyer, A.; Kolek, M.; Rodehorst, U.; Schulze, S.; Winter, M.; Bieker, P.; Stan, M. C. Lithium-Metal Foil Surface Modification: An Effective Method to Improve the Cycling Performance of Lithium-Metal Batteries. *Adv. Mater. Interfaces* **2017**, 4 (16), 1700166.
- (171) Weingarth, D.; Foelske-Schmitz, a.; Wokaun, a.; Kötz, R. In Situ Electrochemical XPS Study of the Pt/[EMIM][BF₄] System. *Electrochem. commun.* **2011**, 13 (6), 619–622.
- (172) Wibowo, R.; Aldous, L.; Jacobs, R. M. J.; Manan, N. S. a; Compton, R. G. In Situ Electrochemical-X-Ray Photoelectron Spectroscopy: Rubidium Metal Deposition from an Ionic Liquid in Competition with Solvent Breakdown. *Chem. Phys. Lett.* **2011**, 517 (1–3), 103–107.
- (173) Nandasiri, M. I.; Camacho-Forero, L. E.; Schwarz, A. M.; Shutthanandan, V.; Thevuthasan, S.; Balbuena, P. B.; Mueller, K. T.; Murugesan, V. In Situ Chemical Imaging of Solid-Electrolyte Interphase Layer Evolution in Li-S Batteries. *Chem. Mater.* **2017**, 29 (11), 4728–4737.
- (174) Wu, X.; Villeveille, C.; Novák, P.; El Kazzi, M. Monitoring the Chemical and Electronic Properties of Electrolyte-Electrode Interfaces in All-Solid-State Batteries Using Operando X-Ray Photoelectron Spectroscopy. *Phys. Chem. Chem. Phys.* **2018**, 20 (16), 11123–11129.
- (175) Wood, K. N.; Steirer, K. X.; Hafner, S. E.; Ban, C.; Santhanagopalan, S.; Lee, S. H.; Teeter, G. Operando X-Ray Photoelectron Spectroscopy of Solid Electrolyte Interphase Formation and Evolution in Li₂S-P₂S₅ Solid-State Electrolytes. *Nat. Commun.* **2018**, 9, 2490.

CHAPTER 2: Methodologies and reference studies

The current development of the lithium metal batteries is intimately related to the comprehension of the chemical structure and the reactivity of the electrolytes at the surface of the lithium electrode. Thus, it is essential to understand the interfacial processes that induce the degradation of the electrolyte and lead to the decrease of the Coulombic efficiency and promote the growth of lithium dendrites. To tackle this objective, we proposed a study coupling electrochemical and surface techniques.

In this chapter, we describe the methodology developed to study the lithium reactivity towards ionic liquids (ILs) based electrolytes. The reference chemical structure analyzed by XPS of the ILs doped with a salt and/or a solvent, and of the neat lithium surface electrode will be especially emphasized.

2.1.	Introduction	48
2.2.	Methodology	49
2.3.	Experimental part	50
2.3.1.	Imidazolium ionic liquids based electrolyte synthesis	50
2.3.2.	Electrolyte preparation	52
2.3.3.	Assembly of the electrochemical systems	53
2.3.4.	Ionic conductivity measurements	54
2.4.	Characterization protocols	55
2.4.1.	Electrochemical impedance spectroscopy	55
2.4.2.	Cyclic voltammetry	56
2.4.3.	X-ray photoelectron spectroscopy	56
2.4.4.	Scanning electron microscopy and Auger spectroscopy	58
2.5.	Reference study of the ILs electrolytes	58
2.5.1.	Ionic conductivity of the ILs	58
2.5.2.	Characterization by XPS of the neat ILs, the associated electrolytes and organic doped ILs	63
2.5.3.	Characterization of the pristine lithium electrode by XPS	72
2.6.	Conclusions	74

2.1. Introduction

Ionic liquids (ILs) defined as room temperature molten salts, are liquid over a wide temperature range ($>300\text{ }^{\circ}\text{C}$) and result from the association of a bulky unsymmetrical organic cation with a weakly coordinating organic or inorganic anions.¹ Their versatile properties (low vapor pressure at room temperature, chemical stability, electrochemical properties, catalysis properties, etc.), over an extensive range of combinations, have attracted attention in several technological applications.²⁻⁷

Imidazolium is largely used as cation due to its low cost and facile chemical modification of the length, the number and the functionality of the alkyl chains. This cation is often associated to the (bis(trifluoromethylsulfonyl)imide), TFSI,⁸ and/or (bis(fluorosulfonyl)imide), FSI,⁹ anions due to their high thermal stability, low viscosity, and hydrophobicity that simplifies their purification.¹⁰ The combinations, when mixed with an appropriated lithium salt, such as (bis(trifluoromethanesulfonyl)imide)lithium, LiTFSI, have found some attractive applications as electrolyte in lithium battery technology.

The cycling performance of lithium based accumulators using such electrolytes has been widely studied, in term of wettability, life cycle, lithium/electrolyte stability and their reactivity in contact to lithium metal.^{8,11-14} Despite these interesting properties, the correlation between the chemical structure of imidazolium based IL and electrolytes and their performance are still under debate¹⁵⁻²⁰ more specifically, the role of the alkyl chain, the proton in the C2 position of the imidazolium ring, the effect of the anion FSI vs. TFSI, and the role of LiTFSI salt or solvent additives such as vinylene carbonate (VC) or fluoroethylene carbonate (FEC).

The macroscopic effects of the listed combinations, such as viscosity and ionic conductivity change and electrochemical windows stability, have been largely studied and listed by several authors.^{8,21,22} However, the specific influence of the anion, cation chemical structure and local charge screening through salt or solvent doping on the electronic structure change is still under debate.^{23,24}

The X-ray photoelectron spectroscopy, known as direct reliable method of characterization of the electronic structure of materials, has been used to probe the chemical structure of imidazolium-based IL system.^{25,26} In addition, the cation-anion interactions of neat ILs probed by XPS have been successfully correlated to NMR spectroscopy,²⁷ Raman spectroscopy²⁸ and theoretical calculations.²⁹

The electrolytes based on imidazolium ILs (1-hexyl-3-methylimidazolium bis(trifluoromethanesulfonyl)imide), C₁C₆ImTFSI, with or without vinylene carbonate, VC, and in association with LiTFSI (1 mol.L⁻¹) have been investigated in graphite based secondary batteries.^{12,13} The ILs based on the imidazolium cation and the TFSI anion present an important interest in the field of batteries because of their weak viscosity and high Li-salt solubility at room temperature.^{11,30} On the other hand, there is a growing interest in the ILs based on FSI (bis(fluorosulfonyl)imide) anion because of their higher conductivities and performance compared to TFSI anion.⁹

In this section, we present a reference study based on the cation and anion XPS related core levels peaks, of imidazolium ILs (C₁C₆ImTFSI), 1-hexyl-3-methylimidazolium bis(fluorosulfonyl)imide (C₁C₆ImFSI) and 1-hexyl-2,3-dimethylimidazolium bis(trifluoromethylsulfonyl)imide (C₁C₁C₆ImTFSI) neat IL and doped with LiTFSI, VC and fluoroethylene carbonate (FEC). This analysis will serve to discuss the evolution of the electronic structure of the cation with regards to the nature of the anion.

2.2. Methodology

The surface reactivity of lithium metal toward electrolytic media remains a crucial issue to optimize lithium metal based battery technology. In this framework, the future challenges for current lithium based storage reside in the improvement of their safety, their cyclability, and the increase of the energy density.

IL based electrolytes constitute an alternative as potential electrolyte for batteries thanks to their retarded flammability. However, their reactivity on the lithium electrode at the OCV and under electrochemical solicitations remains not well understood. The lithium surface is very reactive towards water and the electrolytic media, therefore careful methodologies must be undertaken in order to study the evolution of the solid electrolyte

interphase (SEI) in the presence of ILs based electrolyte. Herein, *in-situ* evolutions of the electrolyte and interface resistances measured by EIS was correlated with the final chemical environment of bulk electrolytes and lithium surfaces probed *post-mortem* by XPS on the electrodes and separators (Chapter 3 in open circuit condition and chapter 4 under polarization).

These studies, based on the coupling of two nondestructive and well-adapted techniques to characterize interfaces and surfaces, pave the path to a further understanding of the reactivity between lithium and imidazolium IL-based electrolytes and its impact on the formation of passive layers. This approach will be extended to a new development based on *operando* XPS conditions (Chapter 5).

Figure 2.1 summarizes the methodology used in this thesis to probe the evolution of the electric properties and chemical nature of the bulk and of the interfaces between the ILs and associated electrolyte, and the lithium metal thanks to *in-situ* and *ex-situ* EIS and XPS coupled experiments.

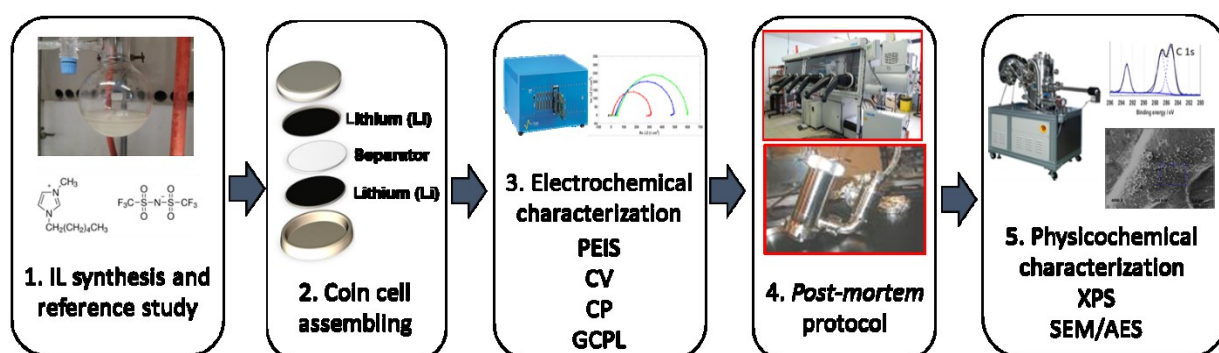


Figure 2.1 Methodology used in chapter 3 and 4 to study the reactivity of IL based electrolytes toward lithium metal electrodes.

2.3. Experimental part

2.3.1. Imidazolium ionic liquids based electrolyte synthesis

The chemical synthesis of imidazolium ILs is accomplished in two steps:

- The first step consists in the quaternization reaction, where imidazole is combined with an alkylating agent containing a halogen (chloride or bromide) as a leaving group, (*e.g.*, C_1C_6ImCl) (Figure 2.2).

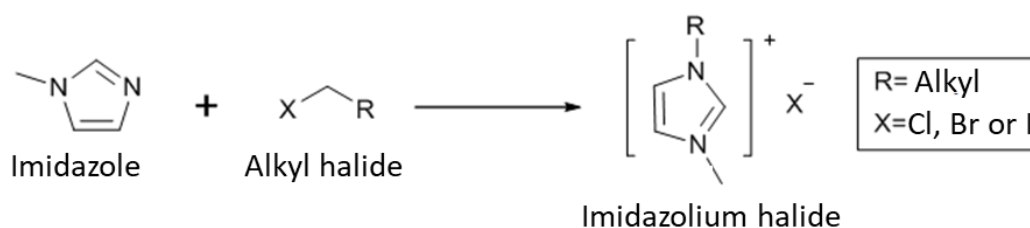


Figure 2.2 Quaternization reaction mechanism.

- In the second step, called metathesis (Figure 2.3), the anion in the imidazolium halide of the first step is replaced by the desired anion (*e.g.*, TFSI). The imidazolium halide in aqueous solution reacts with a salt of the selected anion (*e.g.*, LiTFSI). Both reactants are soluble in water, while the expected product *e.g.*, C₁C₆ImTFSI is not soluble in water and could be easily separated from the reactants as well from the resultant halide (*e.g.*, LiCl) through several washings with water.

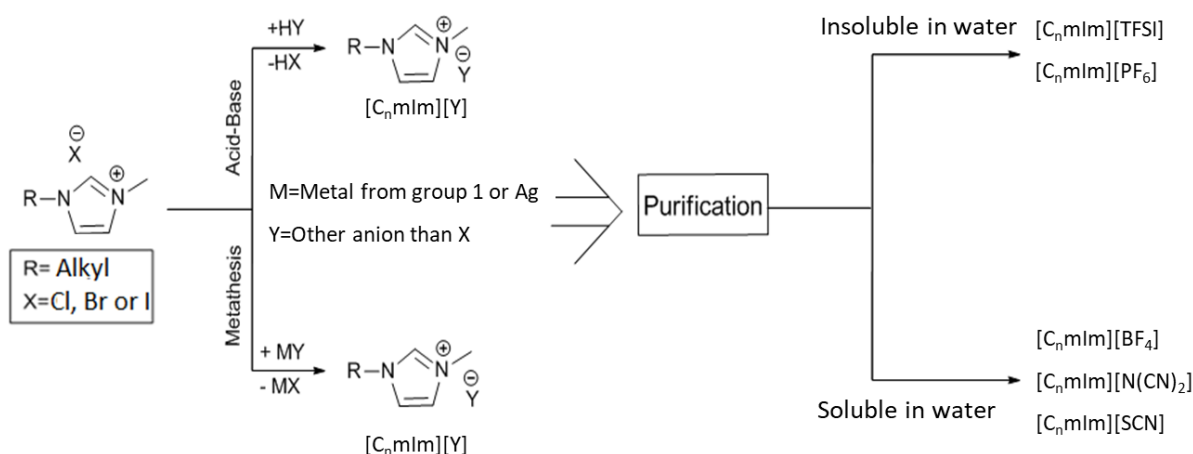


Figure 2.3 Schema of the metathesis reaction and purification.

In this work, we have synthesized three different types of IL based on the imidazolium cation family (Table 2.1):

Table 2.1 ILs studied in this work.

IL formula	IL name
C ₁ C ₆ ImTFSI	1-hexyl-3-methylimidazolium bis(trifluoromethylsulfonyl)imide
C ₁ C ₆ ImFSI	1-hexyl-3-methylimidazolium bis(fluorosulfonyl)imide
C ₁ C ₁ C ₆ ImTFSI	1-hexyl-2,3-dimethylimidazolium bis(trifluoromethylsulfonyl)imide

2.3.2. Electrolyte preparation

Prior the use of ILs in a battery system, they were stirred and dried under vacuum during one night at room temperature by using a Schlenk line (Figure 2.4). This method assures a content of water less than 10 ppm as it was measured by Karl-Fischer titration technique. The dry ILs were mixed with 1 mol.L⁻¹ of LiTFSI salt (lithium bis(trifluoromethanesulfonyl)imide, Solvionic), previously dried under vacuum in a Buchi oven at 60 °C during one night. Finally, the mixtures were stirred and dried again under vacuum one night at room temperature.



Figure 2.4 Schlenk line used for the synthesis and the drying of the ILs.

Two organic additives were selected to study their effect on the performance of ILs based electrolytes, vinylene carbonate (VC) and fluoroethylene carbonate (FEC) (5 % of volume).

The concentrations of LiTFSI and of the additives VC or FEC were optimized according to Srour et al.³¹ and Schmitz et al.³² studies. All the combinations analyzed in this work are listed in Table 2.2.

Table 2.2 ILs and electrolytes synthesized in this work.

ILs	Electrolytes
C ₁ C ₆ ImTFSI	C ₁ C ₆ ImTFSI + 1 mol.L ⁻¹ LiTFSI
	C ₁ C ₆ ImTFSI + 1 mol.L ⁻¹ LiTFSI + 5% VC
	C ₁ C ₆ ImTFSI + 1 mol.L ⁻¹ LiTFSI + 5% FEC
C ₁ C ₆ ImFSI	C ₁ C ₆ ImFSI + 1 mol.L ⁻¹ LiTFSI
C ₁ C ₁ C ₆ ImTFSI	C ₁ C ₁ C ₆ ImTFSI + 1 mol.L ⁻¹ LiTFSI

2.3.3. Assembly of the electrochemical systems

The electrochemical cells were assembled in CR-2032 coin cells in an argon filled glovebox (MBraun, content of H₂O, O₂ < 5 ppm) as illustrated in Figure 2.5.

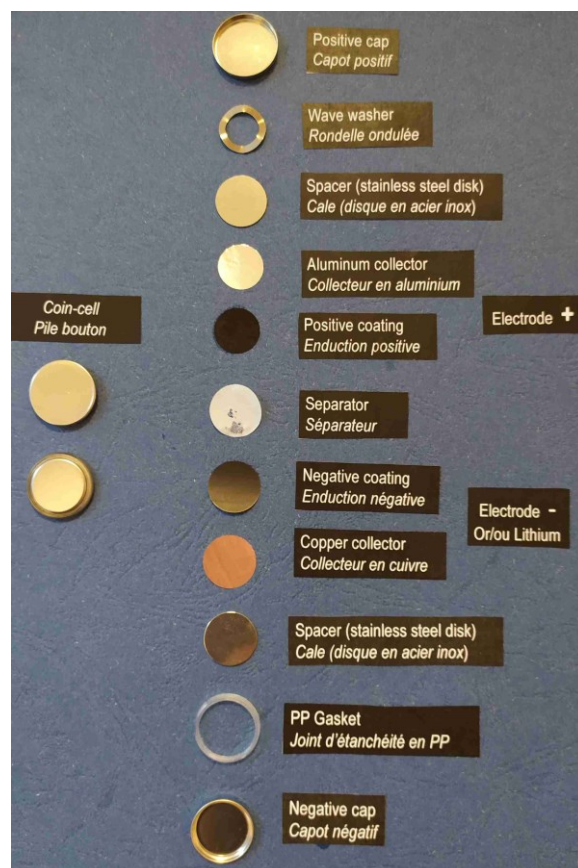


Figure 2.5 Schematic representation of the CR-2032 coin cell.³³

The electrodes were chosen depending on the type of study as it is described in Table 2.3. A separator (Freudenberg, Viledon FS 2207-25, thickness: 0.25 mm, diameter: 16.5 mm) soaked with 150 μ L of the electrolyte solution (large excess), was inserted between the two electrodes. Stainless steel discs (thickness: 0.5 mm, diameter: 16 mm) were used as spacers placed on the top and bottom of the cells.

Table 2.3 Different electrode configurations used in this work.

Type of study	Negative electrode	Positive electrode
Interaction of ILs electrolytes and lithium	Lithium	Lithium
Electrochemical window measurements	Lithium	Copper or stainless steel

Negative electrodes

Lithium electrodes were provided by Rockwood with a thickness of 135 μm . They were cut in discs of a diameter of 16 mm. No treatment has been used after reception. The lithium is stored under vacuum in an aluminum can, which is in argon filled glove box (MBraun, content of H_2O , $\text{O}_2 < 5$ ppm).

Positive electrodes

Copper and stainless steel (316L) were supplied by the CEA in discs of a diameter 16 mm.

2.3.4. Ionic conductivity measurements

Measurements of the ionic conductivity of ILs electrolytes were carried out by filling a conductivity cell (Radiometer, Pt electrodes) with 1.5 mL of electrolyte in a glove box. Then, the cell is hermetically sealed and heated in an oven (Memmert IPP30) between temperatures from 273.15 ± 0.1 K to 343.15 ± 0.1 K with steps of 10 K.

For each step of temperature, after a stabilizing time of 45 minutes, electrochemical impedance spectroscopy was performed with an input signal of 20 mV of amplitude. Measurements were recorded in the frequency range from 7 MHz to 100 Hz.

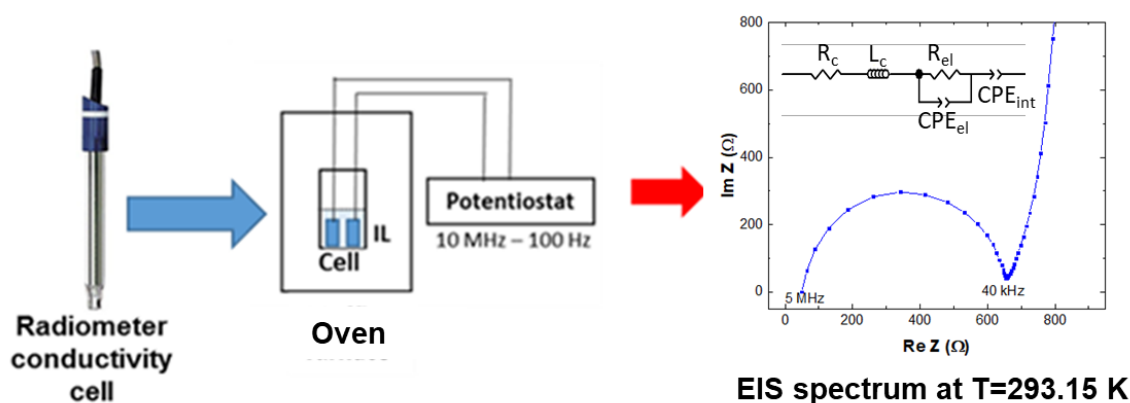


Figure 2.6 Schema of conductivity measurements and an example of the recorded impedance spectrum in Nyquist plot with the corresponding equivalent circuit used to extract the electrolyte resistance R_{el} .

A characteristic impedance spectrum, herein obtained at 293.15 K, is represented in Nyquist plot in Figure 2.6. At high frequency, the plot is characterized by a semicircular

loop that typically goes from 5 MHz to 40 kHz, corresponding to the electrolyte resistance, R_{el} . At lower frequencies, the plot shows the capacitive effect of the blocking electrode/IL interface, which in the ideal case is a vertical line parallel to the y-axis.

In order to determine the electrolyte resistance with improved accuracy, the spectra were fitted, using the ZView software (Scribner Associates Inc.) thanks to an equivalent electrical circuit (Figure 2.6) composed by an inductance L_c with a resistance R_c in series for the cables contribution, a resistance R_{el} in parallel with a constant phase element, CPE_{el} , and finally a CPE_{int} for the blocking electrodes. The values of the resistance R_{el} were converted into ionic conductivities knowing the value of the conductivity cell constant obtained after calibration using a reference solution (KCl 0.1 mol.L⁻¹ at 298.15 K).

2.4.Characterization protocols

2.4.1. Electrochemical impedance spectroscopy

In addition to the measurements of ionic conductivity, EIS technique (see Appendix 1) was also used to study to analyze the electrical properties of ILs electrolytes and their interfaces with the lithium electrodes in coin cells aged at OCV and under the application of a current (chronopotentiometry technique). All measurements were recorded thanks to a VMP-3 multichannel potentiostat (Bio- Logic Science Instruments).

2.4.1.1.Electrochemical tests under OCV

After assembly, the Li/Li coin cells were aged at the OCV during 7 days at 298.15 ± 0.1 K. EIS in the potentiostatic mode (PEIS, amplitude: 20 mV, 7 dots by decade, 1MHz-0.1Hz) was recorded during aging period following the step a, b and c:

- a) Just after assembly, a PEIS was made every 10 minutes during the first 100 minutes.
- b) Then, a PEIS every one hour, during the next 10 hours.
- c) And finally, a PEIS every 24 hours, the next 7 days.

2.4.1.2. Electrochemical tests under galvanostatic mode

All measurements were performed at 295.15 or 333.15 K. Before cycling, the Li/Li coin cell were kept 12 h at the OCV for stabilization. During this rest period, PEIS were performed according to the previous methodology (a) and (b). The lithium displacement from the anode to the cathode was performed by applying a constant current density (chronopotentiometry) from 30 to 150 $\mu\text{A}\cdot\text{cm}^{-2}$. An impedance measurement in galvanostatic mode (GEIS, amplitude 20 μA) was performed each 20 minutes until short-circuit of the cells or divergence of the potential.

All spectra were fitted using the ZView software (Scribner Associates Inc.). The fitting method depends on the electrical equivalent circuit used for each type of study and will be described in detail in further sections.

2.4.2. Cyclic voltammetry

Cyclic voltammetry (CV) was performed to determine the electrochemical window of the ILs based electrolytes. Coin cells were assembled as indicated in section 2.3.3 changing the electrodes depending on the studied phenomena.

For the study of the reduction processes, copper was chosen as working electrode (WE) and lithium as counter electrode (CE) and reference electrode (RE). After assembly, cells were rested at the OCV during 12 h for stabilization. Then, the CV was performed starting by three cycles between 2 to 0.05 V vs. Li^+/Li , then three cycles in between 2 to -0.1 V vs. Li^+/Li with a sweep rate of 0.1 $\text{mV}\cdot\text{s}^{-1}$.

For the study of the oxidation processes, stainless steel was chosen as working electrode (WE) and lithium as counter electrode (CE) and reference electrode (RE). After assembly, cells were left at the OCV during 12 h for stabilization. Then, the CV was performed during three cycles in between 3 to 4 V vs. Li^+/Li , followed by three cycles in between 3 to 5.2 V vs. Li^+/Li with a sweep rate of 0.1 $\text{mV}\cdot\text{s}^{-1}$.

2.4.3. X-ray photoelectron spectroscopy

Chemical characterization by XPS (see Appendix 2) was carried out using a Versaprobe II ULVAC-PHI spectrometer. A monochromatic beam (X-ray source $\text{Al-K}\alpha$

1486.6 eV) of 100 μm of diameter and 97 W of power was focused at the surface of the samples. High-resolution spectral analyses were performed using pass energy of 23 eV which corresponds to a resolution of 0.5 eV. All XPS measurements were carried out in an ultra-high vacuum chamber (7.10^{-8} Pa). The binding energy calibration was performed using $\text{Au}4f_{7/2}$ (83.9 eV), $\text{Ag}3d_{5/2}$ (368.2 eV) and $\text{Cu}2p_{3/2}$ (932.6 eV). The core level binding energies were recorded within an error of ± 0.1 eV.

All XPS spectra binding energies were corrected using the C1s line of alkyl groups in $\text{C}_1\text{C}_6\text{Im}^+$ cation at 285.0 eV.³⁴ Curve fitting and background subtraction were accomplished using Casa XPS software. Regarding the C1s core peaks, spectra were treated without background subtraction since line base of cation and anion related carbon peak are not matching. This point will be discussed in details with regards to the electronic structure of the cation-anion mixture. The spectra curve fitting was performed using a Voigt function, convolution product of Gaussian (80%) and Lorentzian (20%) distributions.

XPS measurements were performed on neat ILs and doped ILs droplets deposited on silicon substrates in glove box filled with argon (Mbraun, H_2O , $\text{O}_2 < 5$ ppm) and transferred to the XPS spectrometer through an air protected transfer vessel provided by ULVAC-PHI (Figure 2.7).



Figure 2.7 Transfer vessel and sample holder provided by ULVAC-PHI.

For the *post-mortem* analysis, the Viledon separator and the electrodes were taken after cells disassembling in the glove box to be transferred to the XPS spectrometer. Prior the transfer, the electrodes were washed with dimethyl carbonate solvent (DMC, Sigma Aldrich $\geq 99.9\%$, $H_2O < 10$ ppm) for 30 seconds and dried before XPS analyses. To check the impact of the washing by DMC, the initial lithium metal electrode has been analyzed both as received and after washing. As it will be shown in the last section of this chapter, in this condition, the washing does not lead to further carbonate peaks on the lithium surface.

2.4.4. Scanning electron microscopy and Auger spectroscopy

Parallel to the XPS study, the surface of the lithium samples was examined thanks to a PHI710 Scanning Auger Nanoprobe. This instrument integrates a scanning electron microscope and an Auger probe in order to examine both the morphology of the samples and investigate their chemical composition with a lateral resolution of few tens of nanometers.

2.5. Reference study of the ILs electrolytes

2.5.1. Ionic conductivity of the ILs

The ionic conductivities of neat ILs and ILs based electrolytes, as a function of temperature in the range from 273.15 to 343.15 K are gathered in Table 2.4 and their variations in Arrhenius coordinates are plotted in Figure 2.8.

Table 2.4 Ionic conductivities ($mS.cm^{-1}$) of ILs and electrolytes measured in the temperature range between 273.15 K and 343.15 K.

T (K)	C ₁ C ₆ Im TFSI	C ₁ C ₆ Im TFSI LiTFSI	C ₁ C ₆ Im TFSI LiTFSI VC	C ₁ C ₆ Im TFSI LiTFSI FEC	C ₁ C ₆ Im FSI	C ₁ C ₆ Im FSI LiTFSI	C ₁ C ₁ C ₆ Im TFSI	C ₁ C ₁ C ₆ Im TFSI LiTFSI
273.15	0.57	0.15	0.27	0.15	1.31	0.55	0.27	0.06
283.15	1.05	0.34	0.54	0.33	2.23	1.02	0.56	0.14
293.15	1.75	0.63	0.99	0.65	3.48	1.72	1.01	0.31
303.15	2.71	1.08	1.64	1.16	5.09	2.68	1.68	0.59
313.15	3.93	1.73	2.54	1.88	7.06	3.91	2.62	1.01
323.15	5.43	2.59	3.71	2.87	9.38	5.47	3.81	1.61
333.15	7.18	3.67	5.12	4.11	12.09	7.30	5.25	2.06
343.15	9.18	4.95	6.90	5.62	15.06	9.37	6.96	2.20

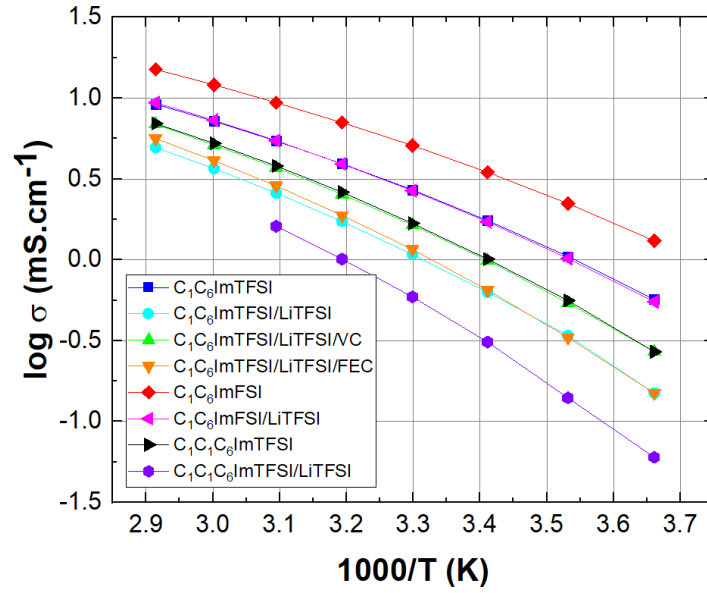


Figure 2.8 Ionic conductivities as function of temperature for the ILs and associated electrolytes.

The observed changes in conductivity versus temperature use to be explained by thermodynamic models such as the classical Arrhenius equation:

$$\sigma_{(T)} = \frac{\sigma_0}{T} \exp\left(\frac{-E_a}{kT}\right) \quad (\text{Eq. 2.1})$$

Where σ_0 is related to the number of charge carriers, E_a is the activation energy for ionic motions and k is the Boltzmann constant ($k = 1.38 \times 10^{-23} \text{ J} \cdot \text{K}^{-1}$). However, for ILs electrolytes, the Vogel-Tammann -Fulcher (VTF) equation, which is generally used for visco-elastic compound like polymer electrolytes,³⁵ is more appropriated regarding the curvature of the conductivity curves in the Arrhenius coordinates :

$$\sigma_{(T)} = \frac{\sigma_0}{\sqrt{T}} \exp\left(\frac{-B}{T - T_0}\right) \quad (\text{Eq. 2.2})$$

In this model, σ_0 is always related to the number of charge carriers, B is proportional to a critical volume necessary for the ions or the charged clusters to move,^{36,37} and T_0 is the ideal glass transition temperature which normally falls 50 K below the experimental (kinetics) glass transition, T_g .

The parameters obtained for the best fits ($\chi^2 < 99.9\%$) of the experimental conductivities using the VTF model are given in Table 2.5.

Table 2.5 Ionic conductivities at 298.15 K and the best VTF parameters for the ILs and associated electrolytes. The families depending on the IL have been associated by color.

	Combination	σ_0 (S.cm ⁻¹)	B (10 ² K)	T ₀ (K)	σ_{298} (mS.cm ⁻¹)
Neat ILs	C ₁ C ₆ ImTFSI	11.6	7.26	171.2	2.21
	C ₁ C ₁ C ₆ ImTFSI	13.0	7.62	178.2	1.31
	C ₁ C ₆ ImFSI	15.7	7.26	162.7	4.27
IL based electrolytes	C ₁ C ₆ ImTFSI + LiTFSI	13.0	8.20	177.4	0.85
	C ₁ C ₁ C ₆ ImTFSI + LiTFSI	15.4	8.81	182.8	0.43
	C ₁ C ₆ ImFSI + LiTFSI	13.8	7.56	170.0	2.19
Effect of additives	C ₁ C ₆ ImTFSI + LiTFSI + VC	20.9	8.98	166.9	1.29
	C ₁ C ₆ ImTFSI + LiTFSI + FEC	15.9	8.17	180.5	0.89

Tokuda *et al.*³⁸ have measured the ionic conductivities of several ILs in a range from 100 to -10 °C and they have calculated the VFT parameters. For the case of C₁C₆ImTFSI, they reported the values B = 7.31 ± 0.13 (10²K), T₀ = 168 ± 1 K and $\sigma_0/\sqrt{T} = 6.1 \pm 0.3$ Scm⁻¹, which are in perfect agree with our results. Furthermore, they have measured the viscosity and diffusion coefficients by PFG-NMR of the cation and anion.

For the case of C₁C₆ImTFSI/LiTFSI (1 mol.L⁻¹), Bolimowska *et al.*¹⁹ have measured both viscosity and diffusion coefficients of the cation, the anion and the lithium ion. By combining all these data, we can go a step further to describe the IL and associated electrolyte structuration. Indeed, the ionic conductivity for an ionic species i, σ_i , is related to the viscosity of the IL (resp. electrolyte), η , by the Stokes-Einstein relationship:

$$\sigma_i = \frac{z_i^2 F^2 C_i}{6N_a \pi \eta a_i} \quad (\text{Eq. 2.3})$$

Where z_i , C_i and a_i are the charge, the concentration, and the hydrodynamic radius of the ion i, respectively. F stands for the Faraday constant, and N_a the Avogadro number.

Assuming that the same microscopic mechanism occurs for ion motions in case of ionic migration or ionic diffusion, the Nernst-Einstein equation links σ_i and D_i according to:

$$\sigma_i = \frac{(z_i F)^2 C_i D_i}{RT} \quad (\text{Eq. 2.4})$$

Where R stands for the perfect gas constant and T (in K) for the temperature.

We can deduct from Eq. 2.3 and 2.4 the relationship between diffusion and viscosity:

$$D_i = \frac{RT}{6N_a\pi\eta a_i} \quad (\text{Eq. 2.5})$$

This last equation is interesting because it does not depend on the charge nor the concentration of the species, which allows estimating directly the hydrodynamic radius of a species i .

In Figure 2.9, we gathered the ionic conductivity, the ionic diffusion coefficients,³⁸ and the inverse of the viscosity³⁸ as a function of temperature for the neat $C_1C_6ImTFSI$ IL.

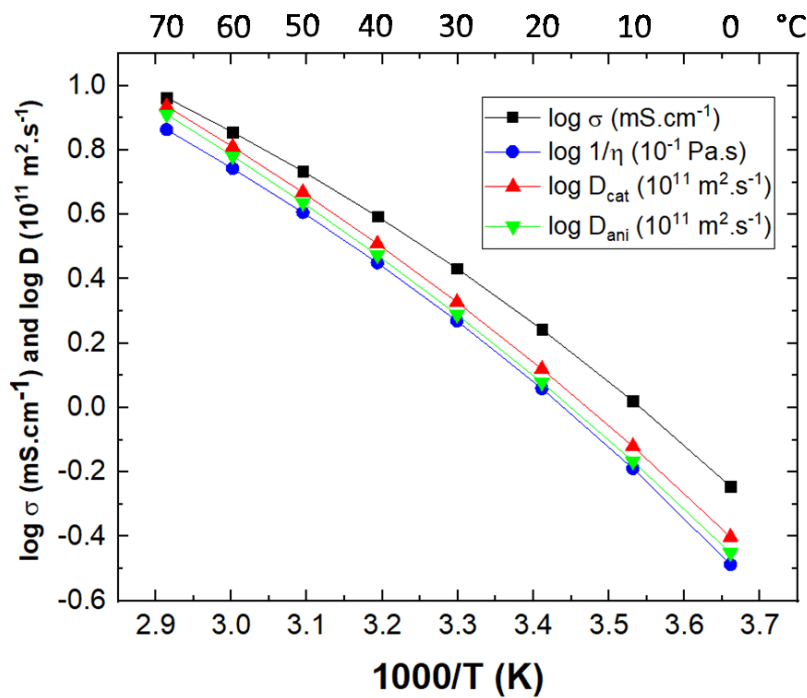


Figure 2.9 Evolution of the ionic conductivity, the ionic diffusion coefficients,³⁸ and the inverse of the viscosity³⁸ as a function of temperature for the neat $C_1C_6ImTFSI$.

We can see a very good correlation between the different sets of data, which demonstrates the validity of the theoretical background using the Eq. 2.3, 2.4 and 2.5 in this IL. Therefore, one can estimate the hydrodynamic radii using Eq. 2.5 at 298.15 K, and we obtain 0.17 nm for the cation $C_1C_6Im^+$ and 0.28 nm for the anion $TFSI^-$.

These values can be favorably compared to the rough estimate of the average molar radius of the anion + cation, ($r = ((3V_M)/(4\pi N_a))^{1/3}$), with V_M , the IL molar volume, $1/V_M = 3.05 \cdot 10^{-3} \text{ mol.cm}^{-3}$, *i.e.* $r = 0.5 \text{ nm}$. Thus, it shows that in the IL the ionic species move alone as $C_1C_6Im^+$ or $TFSI^-$.

We can evaluate the ionicity of the IL by making the ratio, called the Haven ratio³⁶, between the experimental conductivity and the Nernst-Einstein calculated conductivity from the diffusion coefficients (eq. 2.4). A value of 0.5 is obtained at 298.15 K in good concordance with Tokuda *et al.*,³⁸ which suggests that it exists a fast equilibrium between two populations; half of the ions forms pairs ($C_1C_6Im^+ \cdots TFSI^-$) whereas the other half can be considered as “free”.

In addition, at 298.15 K the ionic conductivity of the C_1C_6ImFSI is almost two times larger than for $C_1C_6ImTFSI$ and three times larger than for $C_1C_1C_6ImTFSI$. These results highlight the role of the FSI anion with regards of the ionic conductivity increase of the ILs.

Faster transport found in the FSI based ILs compared to TFSI based ILs is associated with the smaller size of FSI anion and the decrease of the viscosity.^{39,40} Therefore, for the neat ILs, T_0 increases from C_1C_6ImFSI , $C_1C_6ImTFSI$ to $C_1C_1C_6ImTFSI$ in good agreement with the increase of the viscosity (for reference, the viscosities of $C_1C_2ImTFSI$ and C_1C_2ImFSI are 35.6 cP and 24.5 cP, respectively, datasheet Solvionic) when FSI is replaced by TFSI, and when the proton at the C2 position is methylated.¹⁸

The addition of LiTFSI reduces the conductivity by 3, 2.5 and 2 times for $C_1C_1C_6ImTFSI$, $C_1C_6ImTFSI$ and C_1C_6ImFSI , respectively. Besides, the addition of VC (5 % vol.) increases the conductivity of the TFSI electrolyte by 1.5 times.

It is well known that the addition of a Li salt in a neat IL induces the formation of complexes $[Li-(X)_n]^{(n-1)-}$ (X: anion).^{19,41,42} For example, Li^+ and $[TFSI]^-$ may form complexes of $[Li(TFSI)_2]^-$ in $C_1C_2ImTFSI$ and $C_1C_4ImTFSI$.⁴² The hydrodynamic radius of Li^+ is increased due to the complex formation, and the viscosity of the mixture is increased with increasing Li salt concentration, resulting in a decrease in ionic conductivity.

To go further on the case of $C_1C_6ImTFSI/LiTFSI$ (1 mol.L⁻¹), using the Eq. 2.5 we can estimate the hydrodynamic radius of cation, anion and lithium ion taking the diffusion coefficients obtained by PFG-NMR. Interestingly, we obtain 0.15 nm for the $C_1C_6Im^+$ cation, which is very similar to the value found in the neat IL. For the anion TFSI⁻, we

obtain 0.47 nm, which is 1.7 times larger than in the neat IL, whereas the value found for the Li^+ lithium ion is 0.28 nm, confirming the formation of ionic complexes with larger hydrodynamic radius, *e.g.* $[\text{Li}(\text{TFSI})_2]^-$.^{19,41,42}

The variations observed in the VFT parameters σ_0 , B and T_0 allow to confirm the IL based electrolytes structuration. For example, the addition of LiTFSI salt leads systematically to an increase of T_0 for each specific IL which is in good agreement with the increase of the viscosity. Furthermore, an increase of the B parameter (the activation volume) is also observed, which confirms the formation of new ionic complexes with larger size, *e.g.* $[\text{Li}(\text{TFSI})_2]^-$. Finally, when adding the carbonate additives, a decrease of T_0 is obtained, whereas B and σ_0 strongly increase. These effects confirm the decrease of the viscosity, the increase of the number of free ions due to the solvation effect of the carbonates, which leads to an increase of the activation volume (solvated ions *vs.* ionic clusters).

2.5.2. Characterization by XPS of the neat ILs, the associated electrolytes and organic doped ILs

The chemical structure and the molar mass of the ILs based on the cations $\text{C}_1\text{C}_6\text{Im}$ and $\text{C}_1\text{C}_1\text{C}_6\text{Im}$ associated to the anions TFSI and FSI, as well as the structures corresponding to the organic additives VC and FEC and the salt LiTFSI is shown in Figure 2.10.

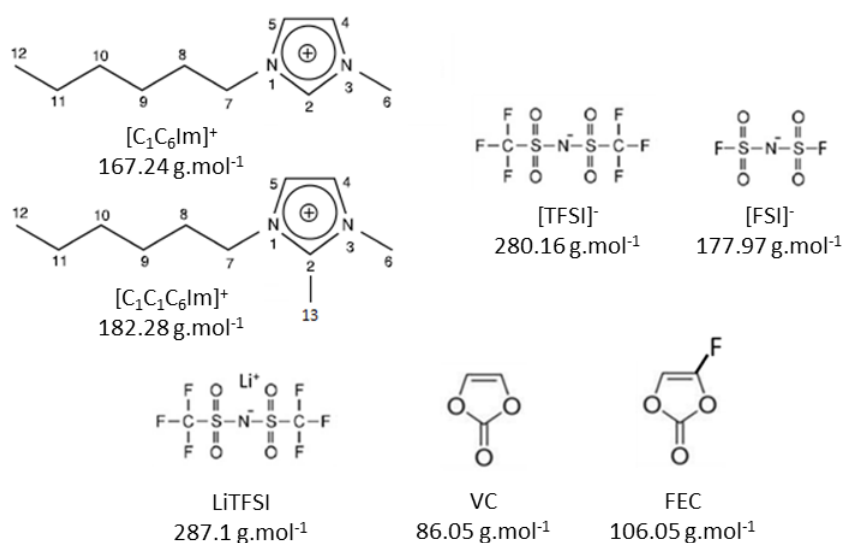


Figure 2.10 The chemical structures of $[\text{C}_1\text{C}_6\text{Im}]^+$, $[\text{C}_1\text{C}_1\text{C}_6\text{Im}]^+$, $[\text{TFSI}]^-$, $[\text{FSI}]^-$, $[\text{LiTFSI}]$, $[\text{VC}]$ and $[\text{FEC}]$.

The $[\text{C}_1\text{C}_6\text{Im}]^+$ cation is composed by an alkyl chain of C-C bonds, these carbons in the positions C8 to C12 are indexed as C_{alkyl} ²⁷. The imidazolium cycle is composed by C=C and C-N bonds, these carbons in the positions C2, C4, C5, C6 and C7 are labeled C_{hetero} . Besides, the cation $[\text{C}_1\text{C}_1\text{C}_6\text{Im}]^+$ results from the grafting of a methyl group (C13) to the C2 position in $\text{C}_1\text{C}_6\text{Im}^+$ ring. Concerning the anions, the difference between FSI and TFSI is the replacement of the group $^*\text{SO}_2\text{-F}$ by $^*\text{SO}_2\text{-CF}_3$. Furthermore, the structure of LiTFSI is similar to the anion TFSI with the addition of the ion Li^+ . Finally, the FEC solvent presents an additional fluorine atom in comparison with VC.

All these compounds have been analyzed by XPS. The survey spectra of the neat ILs are reported in Figure 2.11. All spectra show characteristic carbon, oxygen, nitrogen, sulfur and lithium bands related to the photoemission peaks. Furthermore, the spectra contain the Auger O_{KLL} , F_{KLL} transitions resulting from the second ionization process observed in XPS. The survey spectra of the electrolytes will not be shown because they are all similar. In order to get more detailed information about the chemical environment of the ILs, XPS high resolution spectra have been recorded.

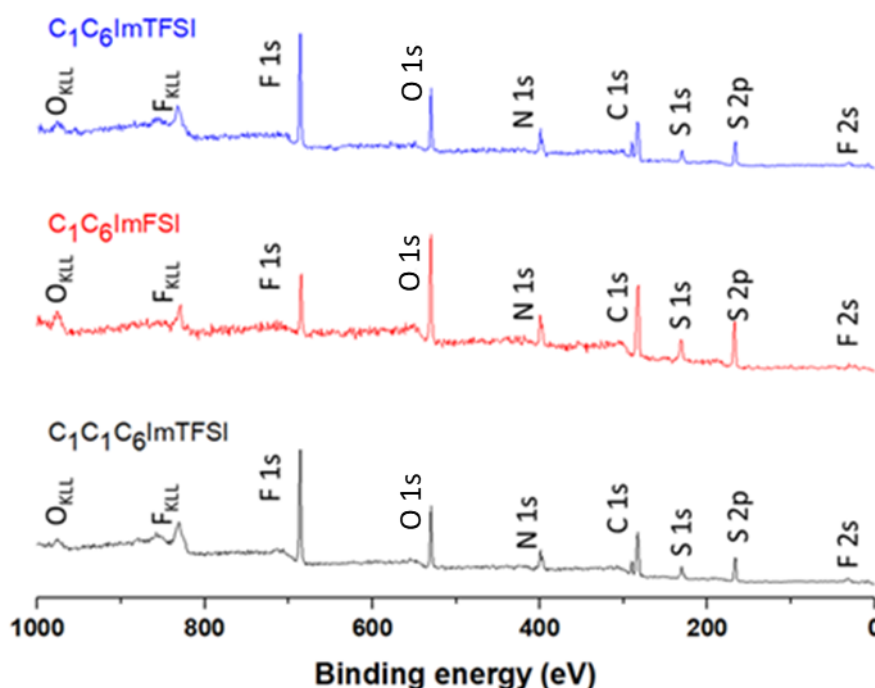


Figure 2.11 XPS survey spectra of the neat ILs.

All XPS core level charge corrections were achieved using the aliphatic carbon atoms of the cation alkyl chain, where the $\text{C}_{\text{alkyl}}1\text{s}$ peak is commonly corrected to 285.0 eV. Therefore, the C-C bonds of the (C_1C_6) alkyl chain correspond to the peak centered at 285.0 eV.

The C1s core level exhibit another peak around 286.8 eV assigned to C_{hetero} . Several authors have proposed different way to fit the C_{hetero} spectral band. For example, Lovelock *et al.*⁴³ have proposed a fit with a single component, whereas Smith *et al.*⁴⁴ proposed a fit with three components (a first peak for the position C2, a second one for C4 and C5 and a third one for C6 and C7, these three peaks are fitted by imposing a peak area ratio of 0.8:1.6:2.0 for the first, second and third component, respectively) to evidence the full heterostructure related carbons. In our case only one peak will be used to describe the chemical bonds related to C_{hetero} .

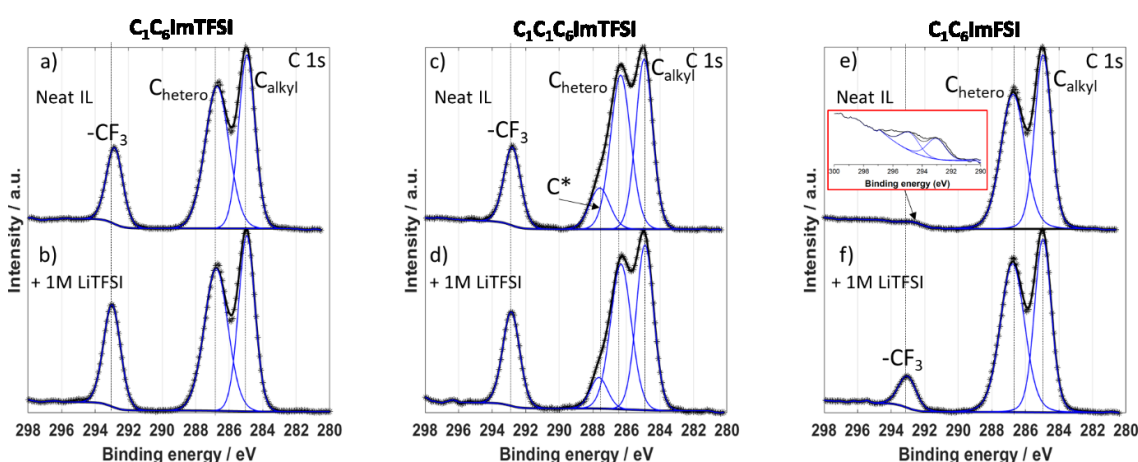


Figure 2.12 XPS high resolution C1s core level signature of IL and LiTFSI doped IL of (a-b) $C_1C_6\text{ImTFSI}$, (c-d) $C_1C_1C_6\text{ImTFSI}$, (e-f) $C_1C_6\text{ImFSI}$.

The peak at 293.0 eV is related to the $-\text{CF}_3$ group of the TFSI⁻ anion. In the case of ILs doped LiTFSI, as expected, we notice an increase of the intensity of this peak which is associated to the addition of LiTFSI salt (Figure 2.12-b-d-f).

We notice that the intensity ratio of the $C_{\text{alkyl}}/C_{\text{hetero}}$ peaks is almost similar in the case of $C_1C_6\text{ImTFSI}$ and $C_1C_6\text{ImFSI}$ (~ 0.8), but higher (~ 0.93) in the case of $C_1C_1C_6\text{ImTFSI}$. For $C_1C_1C_6\text{ImTFSI}$ (Figure 2.12-c), the presence of a new peak at 287.6 eV, labeled as C^* , is associated with the methyl radical attached to the C2 position. This peak could find an origin in the change in the electronic structure of the cation upon the change in the electronic density of the imidazolium ring upon methylation of position C2. NMR and vibrational spectroscopies proved that the methylation at the C2 atom induces: i) removal of the strong positive partial charge of the hydrogen atom leading to a decrease of the electron density at the C2 atom; ii) an increased electron densities at C1-N and C3-N position of the imidazolium ring due to positive inductive effect of the methyl group

pushing electrons into the ring and thus increasing the electron densities all over the ring, and iii), the neighboring nitrogen atoms withdraw electrons increasing the partial charges of the nitrogen atoms.⁴⁵

Consequently, as reported in literature,^{46,47} the observed XPS signal of the C2 carbon is shifted slightly towards higher binding energies (287.6 eV), and the C1s signals of C4 and C5 carbon atoms (286.3 eV for C₁C₁C₆ImTFSI vs. 286.7 eV for C₁C₆ImTFSI and C₁C₆ImFSI) are shifted towards lower binding energies.

On the other hand, we notice that the C1s in neat ILs and electrolytes exhibit two different levels of background below and above 291 eV. This can be assigned to the presence of a shake-up feature associated to the excitation of a valence electron from π orbital into an unoccupied π^* following the photoemission process. This feature is frequently observed in aromatic compounds.²⁵ Although connecting with alkyl chain, the ring of aromatic group constituted of four electrons on two N atoms and two electrons on three C atoms, gives rise to fully delocalized p_π electrons. The inset in Figure 2.12-e shows the shake-up feature indicating the presence of a complex structure with at least two bands π - π^* . The right interpretation of these bands needs quantum calculations support which is out of the scope of this thesis. To the best of our knowledge, this structure has not been discussed in the literature. That could find its origin in the electronic density of the π orbitals preferentially around the nitrogen atoms and the C4-C5 bonds.

The N1s core level, shown in Figure 2.13, corresponds to the signature of imidazolium cation nitrogen N_{cation} (~402.1 eV) and TFSI/FSI anion nitrogen N_{anion} (~399.5 eV) with a ratio $N_{\text{cation}}/N_{\text{anion}}$ equal to ~2 for neat ILs, which decreases upon addition of LiTFSI (Table 2.6).

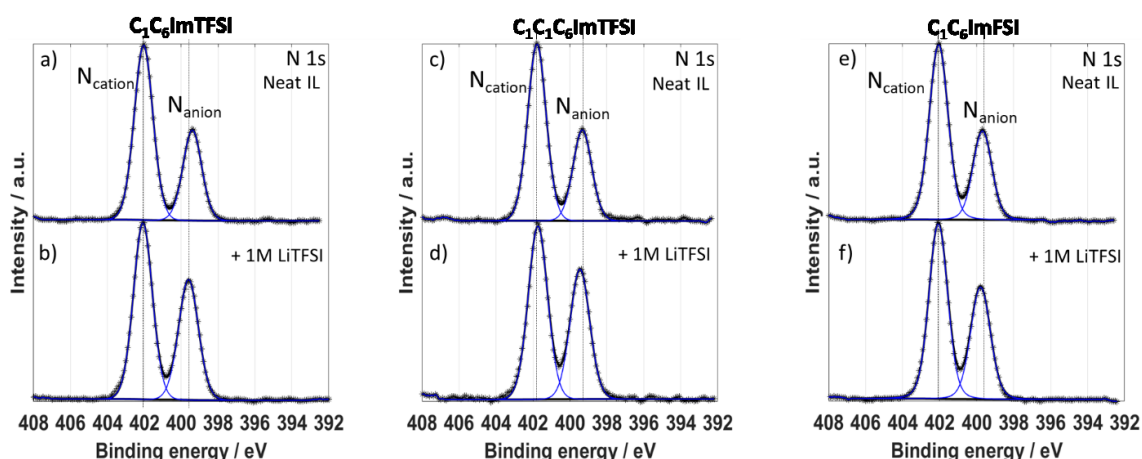


Figure 2.13 XPS high resolution N1s core level signature of IL and LiTFSI doped IL of (a-b) $C_1C_6ImTFSI$, (c-d) $C_1C_1C_6ImTFSI$, (e-f) C_1C_6ImFSI .

The evolution of the energy difference between N_{cation} and N_{anion} peaks binding energy position (ΔEN) in the spectra of the neat ILs and of ILs doped with LiTFSI evidence the changes in the interaction between anions and cations. This effect evolves in the following order:

$$\Delta EN_{C_1C_6ImTFSI} > \Delta EN_{C_1C_1C_6ImTFSI} > \Delta EN_{C_1C_6ImFSI}$$

Systematically, adding salt to the all IL media induced a decrease in the ΔEN value, while addition of organic additive on the electrolyte has no effect on ΔEN value (Table 2.6).

Table 2.6 Atomic concentration ratio N_{cation}/N_{anion} , binding energy difference $\Delta EN = E(N_{cation}) - E(N_{anion})$ and atomic concentration ratio C_{alkyl}/C_{hetero} .

IL electrolyte	N_{cation}/N_{anion} XPS	N_{cation}/N_{anion} theory	$\Delta EN(eV)$ $E(N_{cation}) - E(N_{anion})$	C_{alkyl}/C_{hetero} XPS
$C_1C_6ImTFSI$	1.9	2	2.6	0.8
$C_1C_1C_6ImTFSI$	1.9	2	2.5	0.9
C_1C_6ImFSI	2	2	2.4	0.9
$C_1C_6ImTFSI + LiTFSI$	1.4	1.5	2.5	0.9
$C_1C_6ImFSI + LiTFSI$	1.5	1.6	2.3	0.8
$C_1C_1C_6ImTFSI + LiTFSI$	1.3	-	2.3	1
$C_1C_6ImTFSI + LiTFSI + VC$	1.2	1.5	2.4	1
$C_1C_6ImTFSI + LiTFSI + FEC$	1.4	1.5	2.4	1.3

The O1s core level of the different neat ILs and electrolytes are reported in Figure 2.14. The binding energy of oxygen in $-\text{SO}_2\text{-CF}_3$ environment appears between 532.5 and 532.6 eV for both neat ILs $\text{C}_1\text{C}_6\text{ImTFSI}$ and $\text{C}_1\text{C}_1\text{C}_6\text{ImTFSI}$. For $\text{C}_1\text{C}_6\text{ImFSI}$, the signature of the $-\text{SO}_2\text{-F}$ bonds of the FSI anion appears at 532.9 eV in accordance with the higher electronegativity of F vs. $-\text{CF}_3$ group.

The addition of LiTFSI induces an energy shift toward higher binding energies of O1s peak by 0.3 ± 0.1 eV. In the framework where TFSI anions coordinates each Li-ion without neither forming $[\text{Li}(\text{TFSI})_2]^-$ ionic cluster nor more complex structure with Li-ions bridging TFSI, these results can be interpreted with regard of the change of the ionicity of oxygen atoms upon LiTFSI doping. In the other hand, the formation of $[\text{Li}(\text{TFSI})_2]^-$ like cluster may induce a charge transfer from TFSI $^-$ to highly electro-withdrawing Li^+ ions giving rise to O1s high energy binding shift.

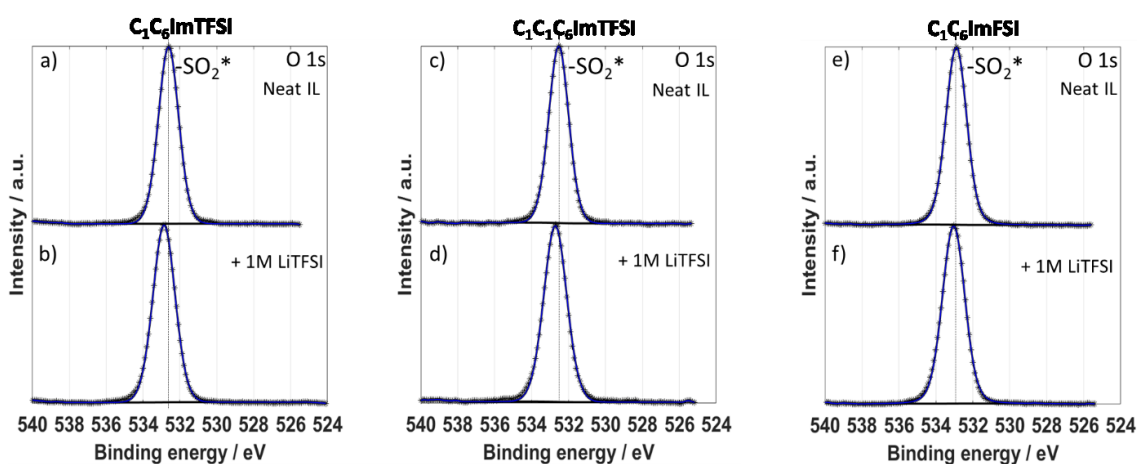


Figure 2.14 XPS high resolution O1s core level signature of IL and LiTFSI doped IL of (a-b) $\text{C}_1\text{C}_6\text{ImTFSI}$, (c-d) $\text{C}_1\text{C}_1\text{C}_6\text{ImTFSI}$, (e-f) $\text{C}_1\text{C}_6\text{ImFSI}$.

In order to confirm this result, we have analyzed the F1s and S2p core level evolution before and after LiTFSI doping (Figure 2.15 and Figure 2.16).

The F1s peak (Figure 2.15) is the signature of the fluorine in the bonds $-\text{SO}_2\text{-CF}_3$ (TFSI) at 688.8 eV and $-\text{SO}_2\text{-F}$ (FSI) 687.7 eV. After adding salt, we did not observe a significant change.

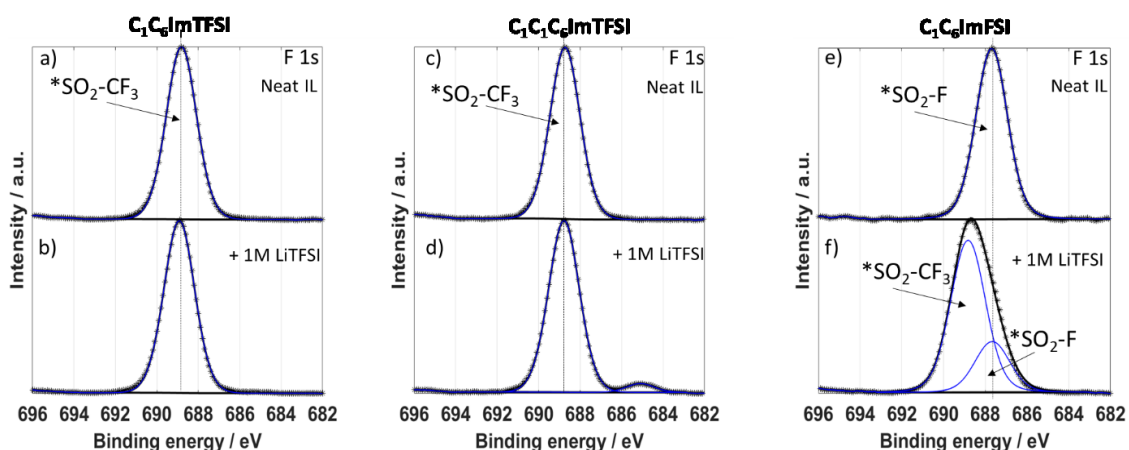


Figure 2.15 XPS high resolution F1s core level signature of IL and LiTFSI doped IL of (a-b) $C_1C_6ImTFSI$, (c-d) $C_1C_1C_6ImTFSI$, (e-f) C_1C_6ImFSI .

We noticed that in the case of LiTFSI doped C_1C_6ImFSI , the high intensity of F1s peak associated with salt can be related to a preferential positioning of salt at the interface IL/vacuum.

The S2p doublet $-SO_2-CF_3$ (TFSI) and $-SO_2-F$ (FSI) are observed at 168.9-170.1 eV and at 169.8-171.0 eV, respectively. Knowing that an increase of the electronic density induced by a charge transfer due to a reduction or a bonding with one neighboring electron-donor atom, leads to a decrease of the measured binding energy, and in contrast, a decrease of the electronic density, induced by an oxidation or a bonding with a neighboring electron-receiving atom, causes an increase of the binding energy. Hence, the S2p spectrum of the $-SO_2-F$ group exhibits an increase of the binding energy of 0.9 eV compared to $-SO_2-CF_3$, in accordance with the oxidizing effect of the higher electronegativity of fluorine in FSI atoms compared to $-CF_3$ group in TFSI.

The addition of LiTFSI induced an increase of the S2p binding energy of 0.2-0.3 eV, similarly to the change of ionicity of the oxygen group upon salt doping. These effects can be attributed to the formation of Li-TFSI ionic clusters, *i.e.* the strong electron acceptor Li^+ bonding the SO_2 groups.

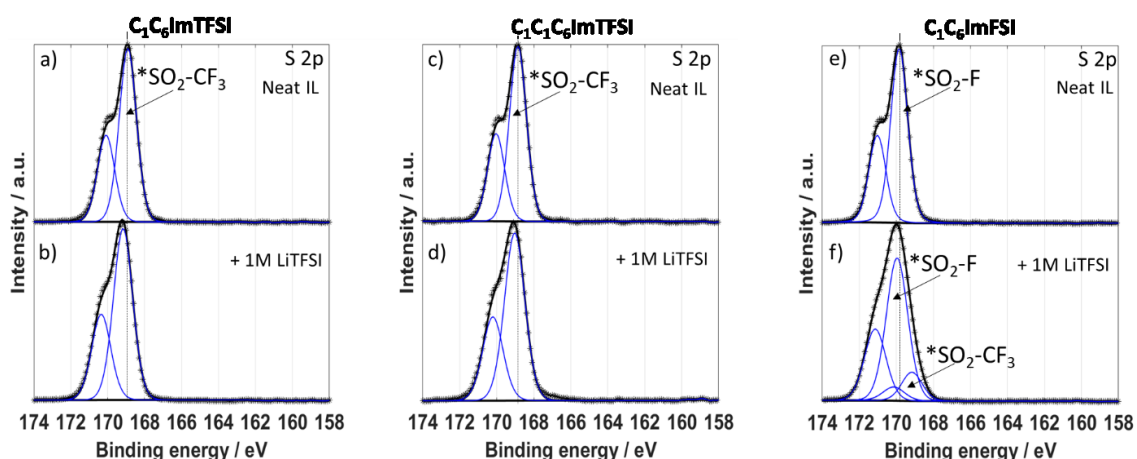


Figure 2.16 XPS high resolution S2p core level signature of IL and LiTFSI doped IL of (a-b) $C_1C_6ImTFSI$, (c-d) $C_1C_1C_6ImTFSI$, (e-f) C_1C_6ImFSI .

We have tested the effect of additives on the change of electronic structure of $C_1C_6ImTFSI$ doped with salt. The motivation of this study find its origin in a previous work,^{8,48} where it was evidenced that a lithium ion accumulator using $C_1C_6ImTFSI$ based electrolyte needs VC to exhibit better electrochemical behavior, especially at the negative graphite electrode.

For the VC, the C1s related spectrum in Figure 2.17 shows a low intensity shoulder, at 289 eV, labeled by “*”, which is assigned to the O-CO₂ group in VC or FEC. The low intensity contribution of this chemical state to the C1s peak is related to the low amount of solvent in the IL and/or an eventual evaporation under UHV conditions.

In addition, we notice an increase of the intensity of the C_{alkyl}1s peak after VC or FEC addition. That could find origin in the change of the alkyl configuration when the VC or FEC is added. This could have a direct effect on the macroscopic properties of the IL, such as viscosity and wettability, which could explain the increase of the ionic conductivity of $C_1C_6ImTFSI$ based electrolyte when VC is added moderately to the solution.

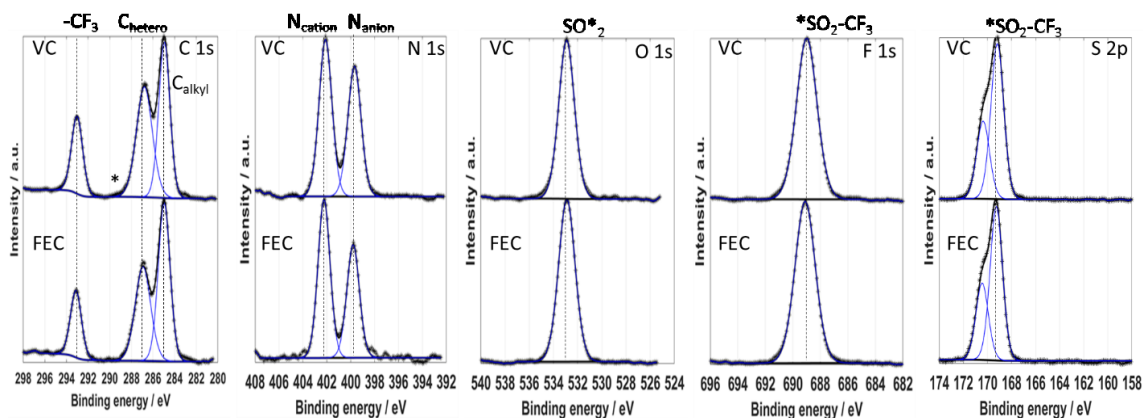


Figure 2.17 High resolution XPS of C1s, N1s, O1s, F1s and S2p core level signatures of LiTFSI doped IL C₁C₆ImTFSI mixed with 5% of VC and FEC.

Table 2.7 XPS relative shift of O1s, F1s and S2p core level in C₁C₆ImTFSI and LiTFSI, VC and FEC doped C₁C₆ImTFSI.

IL electrolyte	Shift in O1s peak	Shift in F1s peak	Shift in S2p peak
C ₁ C ₆ ImTFSI	0	0	0
C ₁ C ₆ ImTFSI/LiTFSI	+0.25	+0.1	+0.25
C ₁ C ₆ ImTFSI/LiTFSI/VC	+0.3	+0.2	+0.3
C ₁ C ₆ ImTFSI/LiTFSI/FEC	+0.3	+0.3	+0.35

2.5.3. Characterization of the pristine lithium electrode by XPS

The lithium foil used in this work was analyzed by XPS before and after ionic etching, the results are reported in Figure 2.18.

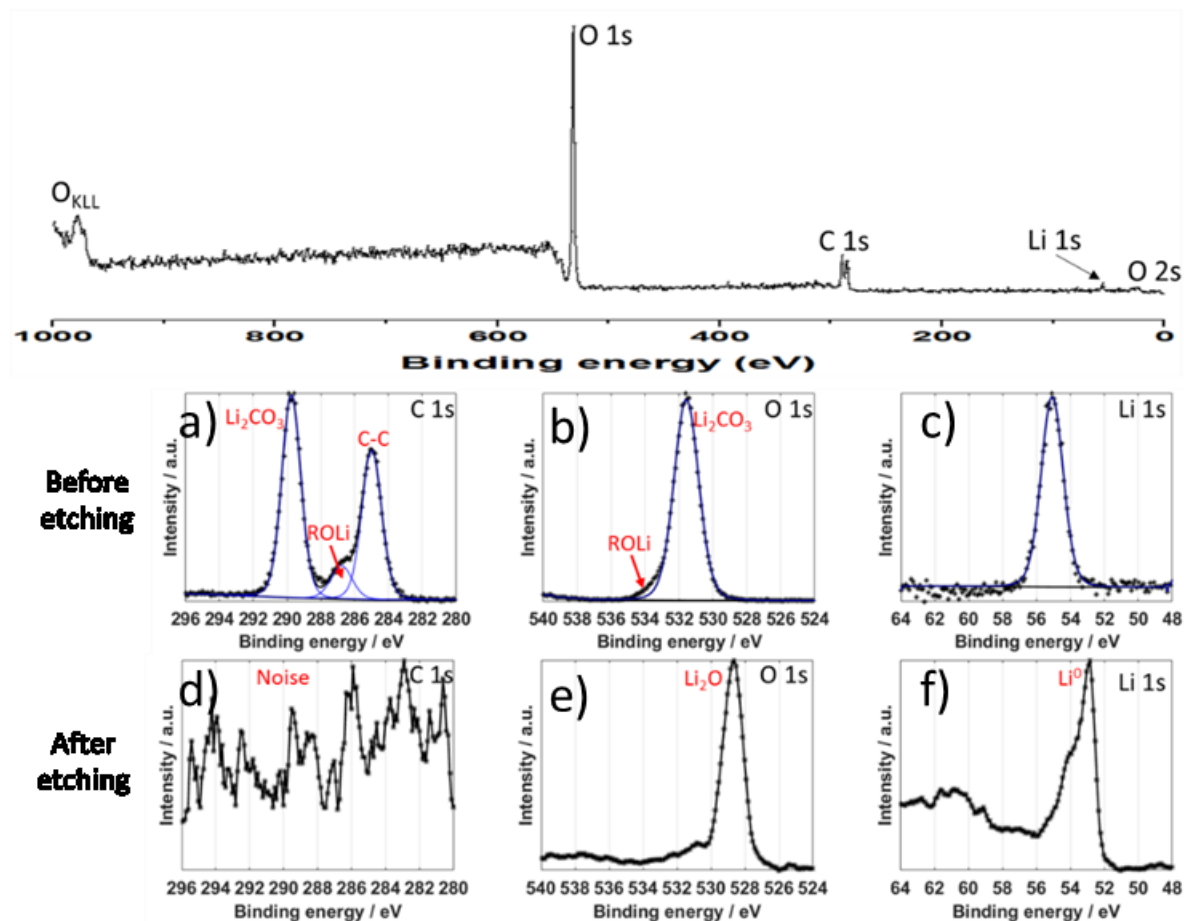


Figure 2.18 Survey and high resolution XPS spectra before sputtering and after sputtering of a lithium pristine foil.

Before etching, the lithium foil is covered by a Li₂CO₃ layer (C1s and O1s peak at 298.8 eV and 531.6 eV, respectively). The quantitative analysis determined that these elements are presented in the following concentration: C1s (30%), O1s (44%) and Li 1s (26%).

In order to remove the lithium carbonate layer, we performed ionic etching on the lithium foil using a monoatomic Ar⁺ ion beam with an energy of 2 keV focused in an area of 1 mm². After 30 min of sputtering, the carbonates have been completely removed (Figure 2.18 a-d) from the surface and the spectra shows the apparition of Li₂O (Figure 2.18 b-e) at 528.7 eV and metallic lithium (Li⁰) (Figure 2.18 c-f) at 52.9 eV with its

satellite peak around 60 eV. The Li_2O can be originated from Li_2CO_3 degradation under Ar^+ ion beam.

In addition, we have observed that washing the pristine electrode (by dipping several times into the solvent) with DMC for a time less than 30 s does not have a great impact in the chemical composition of the native layers. Nonetheless, the XPS results after washing a pristine lithium foil by rubbing the surface with a tissue paper soaked with DMC have demonstrate that some Li_2CO_3 can be removed by this mechanical action.

In Figure 2.19 it is demonstrate that the prolonged interaction of the Ar^+ ion beam on a lithium pristine foil (Figure 2.19, a-b) induces the apparition of new structures (Figure 2.19, c-d) that completely modifies the morphology and the chemical environment of the lithium surface.

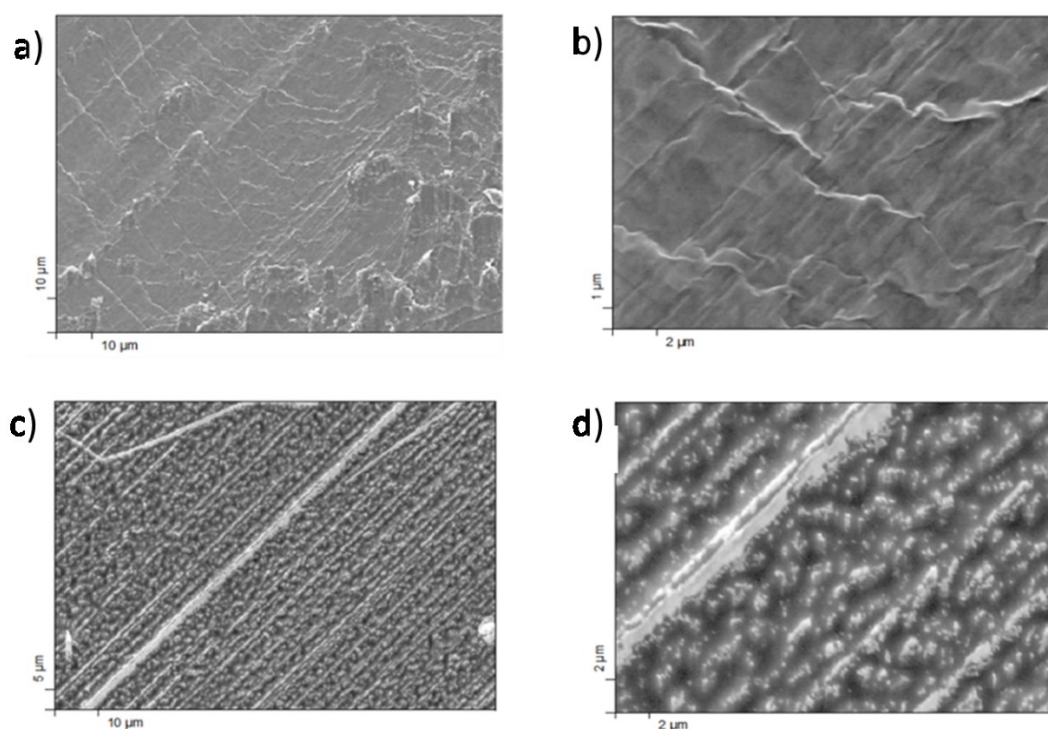


Figure 2.19 (a) and (b) Morphology of a pristine lithium foil, (c) and (d) new structures formed under the effect of the 2 keV Ar^+ ion beam.

Regarding the etching rate using a 2 keV Ar^+ ion beam of about 5 ± 2 nm/min, the Li_2CO_3 layer can be estimated to be 30 nm. This value change depending on the lithium storage condition, hence the effect of the thickness of Li_2CO_3 on the electrochemical

performance of the lithium electrode is under study by our group and will not be taken into consideration in this study.

Similarly, Gaz Cluster Ion Beam (GCIB) induces different surface roughnesses. A SEM image of the sputtered area using GCIB with cluster size of 2500 atoms and acceleration energy of 15 kV (Figure 2.20) shows the presence of needles-like structures where the summits are constituted of Li_2O . As the GCIB is known to non-destructive chemically, the presence of Li_2O after ionic and cluster etching suggest that the lithium surface is passivated by a Li_2O layer terminated with Li_2CO_3 film. Hence, neither GCIB nor Ar^+ ion beam will be used to study the bulk of lithium. Only the extreme surface will be probed by XPS.

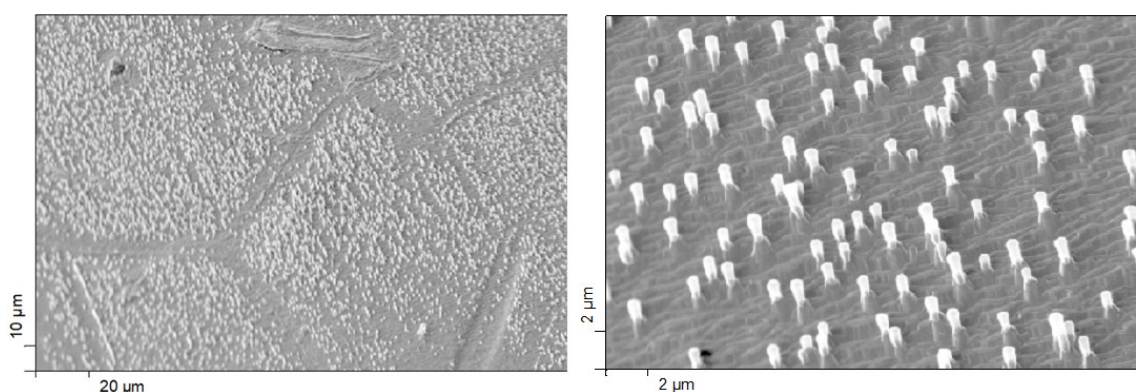


Figure 2.20 Structures formed on lithium surface under the effect of GCIB

2.6. Conclusions

In this chapter, the conductivity and electronic structure, based on EIS and XPS of the neat ILs $\text{C}_1\text{C}_6\text{Im TFSI}$, $\text{C}_1\text{C}_6\text{Im FSI}$ and $\text{C}_1\text{C}_1\text{C}_6\text{ImTFSI}$, as well as their electrolytes (ILs+LiTFSI) with and without solvent additives (VC and FEC), were presented.

The ionic conductivities of the different combinations were measured and fitted by a thermodynamic model (Vogel-Fulcher-Tamman, VFT). The variations of the thermodynamic parameters (B, activation volume and T_0 , glass transition temperature) were associated with the changes in the transport properties (conductivity and viscosity) upon the addition of LiTFSI salt and carbonate additives.

Thus, it was demonstrated that the increase of the viscosity when adding LiTFSI to neat ILs is related to an increase of the glass transition temperature T_0 . Besides, the

increase of the viscosity is also explained by an augmentation of the activation volume suggesting the formation of new ionic complexes such as $[\text{Li}(\text{TFSI})_2]^-$. In contrast, when adding carbonate additives, a decrease of T_0 is observed, whereas B and σ_0 strongly increase, which is in agree with the diminution of the viscosity.

We have estimated the hydrodynamic radius of cation, anion and lithium ion taking the diffusion coefficients obtained by PFG-NMR, giving rise to good correlation with literature data.

In addition, the XPS technique has allowed to correlate the variations of these macroscopic properties with the changes in the electronic structure depending on the type of cation or anion. We evidenced that the formation of $[\text{Li}(\text{TFSI})_2]^-$ like cluster may induced a charge transfer from TFSI^- to highly electro-withdrawing Li^+ ions giving rise to XPS core level shift. In the meantime, we have established a correlation between core level binding energy shift and the change of the anion size and the role of the methylation.

Thus, the replacement of the TFSI by the FSI anion drives to positively charge delocalization at the C2 position of the imidazolium cycle. On the other hand, the methylation of the imidazolium cation contributes to the reduction of the interaction of the cation and anion by means of non-delocalized and smeared coulomb interactions, leading to the change of the macroscopic properties of the ILs.

The second part of this chapter, was dedicated to probe the chemical composition of lithium metal used in this study. We evidence the presence of a passivation layer, covering the lithium surface, constituted of Li_2O buried beneath a Li_2CO_3 layer.

This reference study paves the way to the further analyses of the behavior of the library of tested ILs in contact with the lithium metal surface under open circuit voltage conditions (Chapter 3) and under the application of an electrical current (Chapter 4).

REFERENCES

- (1) Wasserscheid, P.; Welton, T. *Ionic Liquids in Synthesis*; Wiley-VCH: Weinheim, 2003.
- (2) Appetecchi, G. B.; Montanino, M.; Passerini, S. Ionic Liquid-Based Electrolytes for High Energy, Safer Lithium Batteries. *ACS Symp. Ser.* **2012**, 1117 (January), 67–128.

- (3) Watanabe, M.; Thomas, M. L.; Zhang, S.; Ueno, K.; Yasuda, T.; Dokko, K. Application of Ionic Liquids to Energy Storage and Conversion Materials and Devices. *Chem. Rev.* **2017**, 117 (10), 7190-7239.
- (4) Galiński, M.; Lewandowski, A.; Stepniak, I. Ionic Liquids as Electrolytes. *Electrochim. Acta* **2006**, 51 (26), 5567–5580.
- (5) Plechkova, N. V.; Seddon, K. R. Applications of Ionic Liquids in the Chemical Industry. *Chem Soc Rev* **2008**, 37 (1), 123–150.
- (6) Armand, M.; Endres, F.; MacFarlane, D. R.; Ohno, H.; Scrosati, B. Ionic-Liquid Materials for the Electrochemical Challenges of the Future. *Nat. Mater.* **2009**, 8 (8), 621–629.
- (7) MacFarlane, D. R.; Tachikawa, N.; Forsyth, M.; Pringle, J. M.; Howlett, P. C.; Elliott, G. D.; Davis, J. H.; Watanabe, M.; Simon, P.; Angell, C. a. Energy Applications of Ionic Liquids. *Energy Environ. Sci.* **2014**, 7 (1), 232–250.
- (8) Srour, H.; Rouault, H.; Santini, C. Imidazolium Based Ionic Liquid Electrolytes for Li-Ion Secondary Batteries Based on Graphite and LiFePO₄. *J. Electrochem. Soc.* **2012**, 160 (1), A66–A69.
- (9) Best, a. S.; Bhatt, a. I.; Hollenkamp, a. F. Ionic Liquids with the Bis(Fluorosulfonyl)Imide Anion: Electrochemical Properties and Applications in Battery Technology. *J. Electrochem. Soc.* **2010**, 157 (8), A903.
- (10) Huddleston, J. G.; Visser, A. E.; Reichert, W. M.; Willauer, H. D.; Broker, G. A.; Rogers, R. D. Characterization and Comparison of Hydrophilic and Hydrophobic Room Temperature Ionic Liquids Incorporating the Imidazolium Cation. *Green Chem.* **2001**, 3 (4), 156–164.
- (11) Srour, H.; Chancelier, L.; Bolimowska, E.; Gutel, T.; Mailley, S.; Rouault, H.; Santini, C. C. Ionic Liquid-Based Electrolytes for Lithium-Ion Batteries: Review of Performances of Various Electrode Systems. *J. Appl. Electrochem.* **2016**, 46 (2), 149–155.
- (12) Bolimowska, E.; Morales-Ugarte, J. E.; Rouault, H.; Santos-Peña, J.; Santini, C.; Benayad, A. Influence of the Vinylene Carbonate on the Wetting and Interface Chemical Structure of Doped Ionic Liquid Electrolyte at Porous Graphite Surface. *J. Phys. Chem. C* **2017**, 121 (30), 16166–16173.
- (13) Morales-Ugarte, J. E.; Bolimowska, E.; Rouault, H.; Santos-Peña, J.; Santini, C. C.; Benayad, A. EIS and XPS Investigation on SEI Layer Formation during First Discharge on Graphite Electrode with a Vinylene Carbonate Doped Imidazolium Based Ionic Liquid Electrolyte. *J. Phys. Chem. C* **2018**, 122 (32), 18223-18230.
- (14) Morales-Ugarte, J. E.; Benayad, A.; Santini, C. C.; Bouchet, R. EIS and XPS Study of Lithium Metal Surface Aging in Imidazolium-Based Ionic Liquids Electrolytes Performed at OCV. *ACS Appl. Mater. Interfaces* **2019**, 11 (24), 21955-21964.
- (15) Weingärtner, H. Understanding Ionic Liquids at the Molecular Level: Facts, Problems, and Controversies. *Angew. Chemie - Int. Ed.* **2008**, 47 (4), 654–670.
- (16) Kanai, K.; Nishi, T.; Iwahashi, T.; Ouchi, Y.; Seki, K.; Harada, Y.; Shin, S. Electronic Structures of Imidazolium-Based Ionic Liquids. *J. Electron Spectros. Relat. Phenomena* **2009**, 174 (1–3), 110–115.
- (17) Hapiot, P.; Lagrost, C. Electrochemical Reactivity in Room-Temperature Ionic Liquids. *Chem. Rev.* **2008**, 108 (7), 2238–2264.
- (18) Noack, K.; Schulz, P. S.; Paape, N.; Kiefer, J.; Wasserscheid, P.; Leipertz, A. The Role of the C2 Position in Interionic Interactions of Imidazolium Based Ionic Liquids: A Vibrational and NMR Spectroscopic Study. *Phys. Chem. Chem. Phys.* **2010**, 12 (42), 14153–14161.
- (19) Bolimowska, E.; Castiglione, F.; Devemy, J.; Rouault, H.; Mele, A.; Pádua, A. A. H.; Santini, C. C. Investigation of Li⁺ Cation Coordination and Transportation, by Molecular Modeling and NMR Studies, in a LiNTf₂-Doped Ionic Liquid-Vinylene Carbonate Mixture. *J. Phys. Chem. B* **2018**, 122 (36), 8560-8569.
- (20) Hammer, T.; Reichelt, M.; Morgner, H. Influence of the Aliphatic Chain Length of Imidazolium Based Ionic Liquids on the Surface Structure. *Phys. Chem. Chem. Phys.* **2010**, 12 (36), 11070–11080.

- (21) Nazet, A.; Sokolov, S.; Sonnleitner, T.; Makino, T.; Kanakubo, M.; Buchner, R. Densities, Viscosities, and Conductivities of the Imidazolium Ionic Liquids [Emim][Ac], [Emim][FAP], [Bmim][BETI], [Bmim][FSI], [Hmim][TFSI], and [Omim][TFSI]. *J. Chem. Eng. Data* **2015**, 60 (8), 2400–2411.
- (22) Miran Beigi, A. A.; Abdouss, M.; Yousefi, M.; Pourmortazavi, S. M.; Vahid, A. Investigation on Physical and Electrochemical Properties of Three Imidazolium Based Ionic Liquids (1-Hexyl-3-Methylimidazolium Tetrafluoroborate, 1-Ethyl-3-Methylimidazolium Bis(Trifluoromethylsulfonyl) Imide and 1-Butyl-3-Methylimidazolium Methylsulfate). *J. Mol. Liq.* **2013**, 177, 361–368.
- (23) Fumino, K.; Wulf, A.; Ludwig, R. The Cation-Anion Interaction in Ionic Liquids Probed by Far-Infrared Spectroscopy. *Angew. Chemie - Int. Ed.* **2008**, 47 (20), 3830–3834.
- (24) Kempter, V.; Kirchner, B. The Role of Hydrogen Atoms in Interactions Involving Imidazolium-Based Ionic Liquids. *J. Mol. Struct.* **2010**, 972 (1–3), 22–34.
- (25) Lovelock, K. R. J.; Villar-Garcia, I. J.; Maier, F.; Steinrück, H. P.; Licence, P. Photoelectron Spectroscopy of Ionic Liquid-Based Interfaces. *Chem. Rev.* **2010**, 110 (9), 5158–5190.
- (26) Ikari, T.; Keppler, A.; Reinmöller, M.; Beenken, W. J. D.; Krischok, S.; Marschewski, M.; Maus-Friedrichs, W.; Höfft, O.; Endres, F. Surface Electronic Structure of Imidazolium-Based Ionic Liquids Studied by Electron Spectroscopy. *e-Journal Surf. Sci. Nanotechnol.* **2010**, 8 (May), 241–245.
- (27) Cremer, T.; Kolbeck, C.; Lovelock, K. R. J.; Paape, N.; Wölfel, R.; Schulz, P. S.; Wasserscheid, P.; Weber, H.; Thar, J.; Kirchner, B.; et al. Towards a Molecular Understanding of Cation-Anion Interactions-Probing the Electronic Structure of Imidazolium Ionic Liquids by NMR Spectroscopy, X-Ray Photoelectron Spectroscopy and Theoretical Calculations. *Chem. - A Eur. J.* **2010**, 16 (30), 9018–9033.
- (28) Berg, R. W. Raman Spectroscopy and Ab-Initio Model Calculations on Ionic Liquids. *Monatshefte für Chemie* **2007**, 138, 1045–1075.
- (29) Hardacre, C.; Holbrey, J. D.; Nieuwenhuizen, M.; Youngs, T. G. A. ChemInform Abstract: Structure and Solvation in Ionic Liquids. *ChemInform* **2008**, 39 (6), 1146–1155.
- (30) Goodenough, J. B.; Kim, Y. Challenges for Rechargeable Li Batteries. *Chem. Mater.* **2010**, 22 (3), 587–603.
- (31) Srour, H.; Rouault, H.; Santini, C. C. Study on Cycling Performance and Electrochemical Stability of 1-Hexyl-3-Methylimidazolium Bis(Trifluoromethanesulfonyl)Imide Assembled with $\text{Li}_4\text{Ti}_5\text{O}_{12}$ and LiFePO_4 at 333 K. *J. Electrochem. Soc.* **2013**, 160 (6), A781–A785.
- (32) Schmitz, P.; Jakelski, R.; Pyschik, M.; Jalkanen, K.; Nowak, S.; Winter, M.; Bieker, P. Decomposition of Imidazolium-Based Ionic Liquids in Contact with Lithium Metal. *ChemSusChem* **2017**, 10 (5), 876–883.
- (33) Génies, S. Photomontage Developed by Dr. Sylvie Génies, CEA-LITEN.
- (34) Men, S.; Lovelock, K. R. J.; Licence, P. X-Ray Photoelectron Spectroscopy of Pyrrolidinium-Based Ionic Liquids: Cation-Anion Interactions and a Comparison to Imidazolium-Based Analogues. *Phys. Chem. Chem. Phys.* **2011**, 13 (33), 15244–15255.
- (35) Quartarone, E.; Mustarelli, P. Electrolytes for Solid-State Lithium Rechargeable Batteries: Recent Advances and Perspectives. *Chem. Soc. Rev.* **2011**, 40 (5), 2525–2540.
- (36) Déportes, C.; Duclot, M.; Fabry, P.; Fouletier, J.; Hammou, A.; Kleitz, M.; Siebert, E.; Souquet, J.-L. *Electrochimie Des Solides*; EDP Sciences: Grenoble, 1994.
- (37) Devaux, D.; Bouchet, R.; Glé, D.; Denoyel, R. Mechanism of Ion Transport in PEO/LiTFSI Complexes: Effect of Temperature, Molecular Weight and End Groups. *Solid State Ionics* **2012**, 227, 119–127.
- (38) Tokuda, H.; Hayamizu, K.; Ishii, K.; Bin, A.; Susan, H.; Watanabe, M. Physicochemical Properties and Structures of Room Temperature Ionic Liquids . 2 . Variation of Alkyl Chain Length in Imidazolium Cation. *J. Phys. Chem. B* **2005**, 109 (113), 6103–6110.

- (39) Borodin, O.; Gorecki, W.; Smith, G. D.; Armand, M. Molecular Dynamics Simulation and Pulsed-Field Gradient NMR Studies of Bis(Fluorosulfonyl)Imide (FSI) and Bis[(Trifluoromethyl)Sulfonyl]Imide (TFSI)-Based Ionic Liquids. *J. Phys. Chem. B* **2010**, *114* (20), 6786–6798.
- (40) Matsumoto, H.; Sakaebe, H.; Tatsumi, K.; Kikuta, M.; Ishiko, E.; Kono, M. Fast Cycling of Li/LiCoO₂ Cell with Low-Viscosity Ionic Liquids Based on Bis(Fluorosulfonyl)Imide [FSI]⁻. *J. Power Sources* **2006**, *160* (2 SPEC. ISS.), 1308–1313.
- (41) Borodin, O.; Smith, G. D.; Henderson, W. Li⁺ Cation Environment, Transport, and Mechanical Properties of the LiTFSI Doped. *J. Phys. Chem. B* **2006**, *110* (34), 16879–16886.
- (42) Lassègues, J. C.; Grondin, J.; Aupetit, C.; Johansson, P. Spectroscopic Identification of the Lithium Ion Transporting Species in LiTFSI-Doped Ionic Liquids. *J. Phys. Chem. A* **2009**, *113* (1), 305–314.
- (43) K. R. J. Lovelock, C. Kolbeck, T. Cremer, N. Paape, P. S. Schulz, P. Wasserscheid, F. Maier, H.-P. S. Influence of Different Substituents on the Surface Composition of Ionic Liquids Studied Using ARXPS. *J. Phys. Chem. B* **2009**, *113* (9), 2854–2864.
- (44) Smith, E. F.; Rutten, F. J. M.; Villar-Garcia, I. J.; Briggs, D.; Licence, P. Ionic Liquids in Vacuo: Analysis of Liquid Surfaces Using Ultra-High-Vacuum Techniques. *Langmuir* **2006**, *22* (22), 9386–9392.
- (45) Noack, K.; Schulz, P. S.; Paape, N.; Kiefer, J.; Wasserscheid, P.; Leipertz, A. The Role of the C2 Position in Interionic Interactions of Imidazolium Based Ionic Liquids: A Vibrational and NMR Spectroscopic Study. *Phys. Chem. Chem. Phys.* **2010**, *12* (42), 14153–14161.
- (46) Kolbeck, C.; Niedermaier, I.; Deyko, A.; Lovelock, K. R. J.; Taccardi, N.; Wei, W.; Wasserscheid, P.; Maier, F.; Steinrück, H. P. Influence of Substituents and Functional Groups on the Surface Composition of Ionic Liquids. *Chem. - A Eur. J.* **2014**, *20* (14), 3954–3965.
- (47) Liu, Y.; Chen, X.; Men, S.; Licence, P.; Xi, F.; Ren, Z.; Zhu, W. The Impact of Cation Acidity and Alkyl Substituents on the Cation-Anion Interactions of 1-Alkyl-2,3-Dimethylimidazolium Ionic Liquids. *Phys. Chem. Chem. Phys.* **2019**, *21* (21), 11058–11065.
- (48) Bolimowska, E. Étude Des Interfaces Électrodes / Électrolyte à Base de Liquides Ioniques Pour Batterie. *Univ. Claude Bernard Lyon 1* **2016**, *PhD thesis*.

CHAPTER 3: Stability of ionic liquids based electrolytes in contact with lithium metal in open-circuit condition

Lithium reactivity toward an electrolytic media that leads to passivation layer and electrolyte degradation, and dendrite growth phenomena constitute the main drawback for its use as an anode material for commercial lithium metal battery technology. Ionic liquids (ILs) were pointed out as promising electrolyte solvent candidates to prevent thermal runaway in lithium batteries. However, the reactivity of lithium toward such a kind of electrolyte is still under debate. In this chapter, the interaction between lithium metal and imidazolium-based ILs, 1-hexyl-3-methylimidazolium bis(trifluoromethylsulfonyl)imide ($C_1C_6ImTFSI$) and 1-hexyl-3-methylimidazolium bis-(fluorosulfonyl)imide (C_1C_6ImFSI), has been investigated based on the nondestructive methodology coupling electrochemical impedance spectroscopy (EIS) and X-ray photoelectron spectroscopy (XPS). The role of lithium salt ($LiTFSI$) and additives, vinylene carbonates (VC) and fluoroethylene carbonates (FEC), addition were also pointed, giving rise to the stability improvement of the electrolytic media toward the lithium anode. A direct correlation between the resistance of the bulk electrolyte and of the interface electrolyte/lithium, and chemical composition changes were established based on a detailed EIS and XPS combined study. Besides electrochemical and chemical surface change, the surface morphology modification upon aging will be discussed.

3.1.	Introduction	80
3.2.	Study of the stability of IL based electrolytes at OCV.....	82
3.2.1.	Evolution of the electrolyte and interphase resistances.....	82
3.2.2.	Chemical environment evolution of the bulk electrolyte and the interface upon aging at OCV conditions.....	94
3.2.3.	Intermediate conclusions about the degradation mechanisms.....	101
3.3.	Effect of cation methylation and ILs based electrolyte solvent doping	105
3.3.1.	The effect of the methylation	106
3.3.2.	The effect of the additives	108
3.4.	Conclusions	111

3.1. Introduction

Lithium metal has been regarded for longtime as ultimate alternatives for negative electrodes because of its low reduction potential (-3.04 V vs. standard hydrogen electrode) and large specific capacity (3.86 Ah.g⁻¹). Nevertheless, battery systems using lithium metal as anode suffer from a poor cycling performance as a result of a low Coulombic efficiency, and the growth of dendrites when lithium is cycled with most of the organic electrolytes.^{1,2}

Furthermore, because of its high reactivity with electrolytes, passive layers are formed onto the surface of lithium at the interface. These layers are termed as the Solid Electrolyte Interphase (SEI).³ It is widely accepted that the different properties of the SEI such as morphology, chemical composition and mechanical strength have a great impact on the cycling life of lithium based batteries, as well as on the dendrite growth phenomena.^{4,5}

SEI on lithium metal has been studied by several techniques such as scanning electron microscopy (SEM)⁶, transmission electron microscopy (TEM)^{7,8} and atomic force microscopy (AFM)⁹ for morphology, Fourier Transform Infrared spectroscopy (FTIR),¹⁰ X-ray Photoelectron Spectroscopy (XPS)^{11,12} for surface chemical composition, and Electrochemical Impedance Spectroscopy (EIS)¹³ for electrochemical properties.

Howlett *et al.*¹⁴ have characterized the SEI formed with lithium electrodes in contact with the N-methyl-N-alkylpyrrolidinium bis(trifluoromethylsulfonyl)imide (Pyr_{1,x}TFSI). By coupling EIS and XPS techniques, they proposed a bilayer model: an inner layer of about 180 nm composed mainly of LiF and Li₂O from the initial native layer on lithium, and an outer layer of about 40 nm composed of degradation products from TFSI (LiF, Li₂S₂O₄, LiSO₂CF₃, lithium sulfides and lithium nitrides) and Li₂CO₃ coming from the initial native layer.

Similarly, with N-methyl-N-propyl-pyrrolidinium bis(fluorosulfonyl)imide (Pyr₁₃FSI), Budi *et al.*,¹⁵ through *ab initio* molecular dynamic simulations and XPS studies, reported that the nature of SEI is resulting from the FSI anion decomposition. Their XPS results have been corroborated by the study performed by Basile *et al.*¹⁶ In

addition to the role of the FSI anion in the formation of the SEI, Basile *et al.* reported also the breakdown of the pyrrolidinium cation via a Hofmann elimination mechanism.

Olchewski *et al.*¹⁷ performed a XPS comparative study between three different ILs including 1-butyl-1-methylpyrrolidinium bis(fluorosulfonyl)imide (Pyrr₁₄FSI), 1-butyl-1-methylpyrrolidinium bis(trifluoromethylsulfonyl)imide (Pyrr₁₄TFSI), and 1-octyl-3-methylimidazolium bis(trifluoromethylsulfonyl)imide (C₁C₈ImTFSI) deposited by physical vapor deposition on a lithium layer. They demonstrated that TFSI anion is more stable than FSI anion when the cation is Pyrr₁₄⁺. Besides, they proved the decomposition of both cations Pyrr₁₄⁺ and C₁C₈Im⁺. Especially, C₁C₈Im⁺ is subject to complete decomposition and desorption and exhibits the formation of Li–N and Li–C bonds as remaining species.

In complement to these reports, it is known that imidazolium based cations show a poor cathodic stability. This instability is mainly attributed to the activity of the acidic hydrogen atom at the imidazolium ring in the C2 position.¹⁸ For example, it has been reported that neat ILs 1-ethyl-3-methylimidazolium bis(trifluoromethylsulfonyl)imide (C₁C₂ImTFSI) and 1-butyl-3-methylimidazolium bis(trifluoromethylsulfonyl)imide (C₁C₄ImTFSI) are not chemically stable *versus* metallic lithium in comparison with neat Pyrr₁₄TFSI.¹⁹

In addition, whatever the IL, it has been demonstrated that the cathodic limit is enlarged by the addition of a lithium salt such as LiTFSI.²⁰

In any case, to the best of our knowledge, the relation between the stability of these ILs and the electrical and chemical evolution of the formed interfaces at room temperature and in OCV conditions is still not clear and would benefit from a deep understanding of the specific chemical reactivity according to the chemical structure or composition of the ILs as well as the role of the additives.

Herein, in a tentative to analyse the reactivity of different imidazolium based ILs doped with LiTFSI and solvents (VC and FEC) onto the lithium surface, several symmetric Li/Li coin cell systems have been assembled, and their aging have been

characterized in open circuit condition by electrochemical impedance spectroscopy. The specific degradation processes of the cation, the anion and the solvent molecules will be discussed based on careful characterization protocols combining EIS and post-mortem XPS, the ante-mortem XPS analysis having been presented and discussed in chapter 2.

3.2. Study of the stability of IL based electrolytes at OCV

3.2.1. Evolution of the electrolyte and interphase resistances

Figure 3.1 shows the evolution, at the OCV, of the impedances measurements on symmetrical Li/Li coin cells configuration filled with neat IL and electrolytes as a function of time, at a temperature of 295.0 ± 0.3 K.

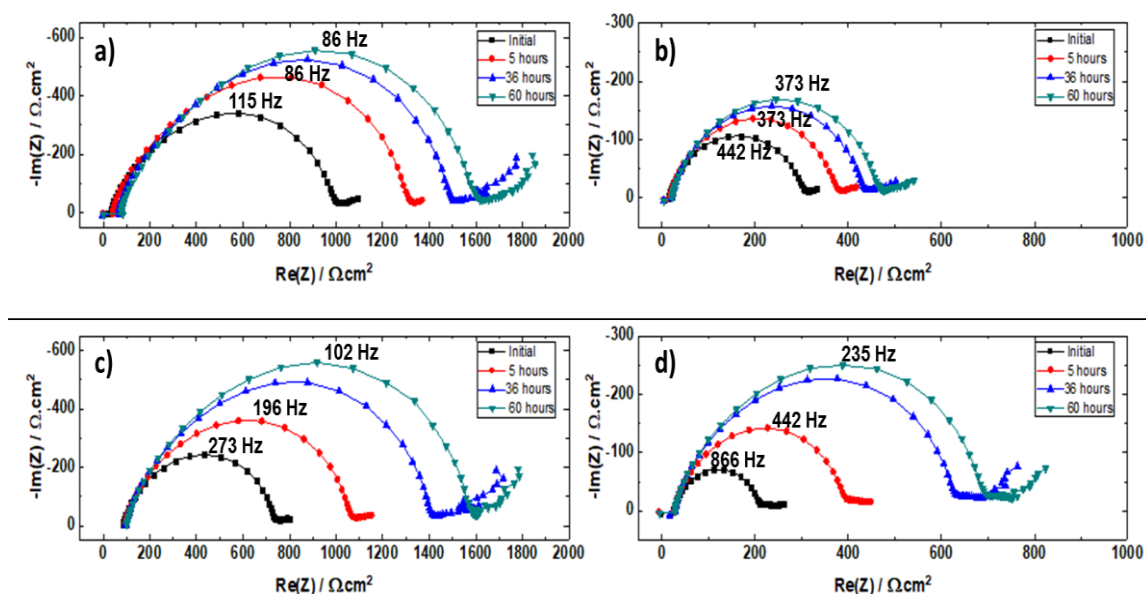


Figure 3.1 Evolution of the impedance response as a function of time of Li/Li coin cells containing (a) $C_1C_6ImTFSI$, (b) C_1C_6ImFSI , (c) $C_1C_6ImTFSI/LiTFSI$, and (d) $C_1C_6ImFSI/LiTFSI$ measured at OCV at 295 K.

The plots correspond to a Nyquist representation of the spectra which can be separated in three frequency domains:

At frequencies higher than 0.1 MHz, the impedance is dominated by the resistance of the bulk of the electrolyte R_{el} and contributions associated to the electric connections represented by a resistance R_c (typically 0.1Ω for our setting) in series with an inductance element L_c (typically 10^{-6} H for our setting).

The electrolyte effective conductivity, σ_{eff} , can be calculated thanks to R_{el} according to the equation 3.1:

$$\sigma_{eff} = \frac{d}{R_{el} * S} \quad (\text{Eq. 3.1})$$

Where d is the distance between the electrodes, *i.e.* the thickness of the separator, and S is the surface area of the electrode.

At middle frequencies (MF, 0.1 MHz – 1 Hz), Nyquist plot exhibits a dissymmetrical loop generally associated to the formation of surface layers due to the electrolyte degradation by-products onto the lithium surface, and to the electrochemical charge transfer. Finally, the tail at frequencies below 0.1 Hz is associated to diffusional processes.

The MF contribution increases as a function of aging time for all the ILs used. Due to its large dissymmetry, at least two circuits in series composed of a resistance in parallel with constant phase element (R_{int}/CPE) might be used to fit it. However, this equivalent electrical circuit (EEC) is non-univocal and always subject to debate.²¹⁻²³

In addition, using an EEC corresponds to a *a priori* parameterization of the experimental data with two main drawbacks: i) the physical meaning of each electrical element is not always obvious and ii) the non-unicity of the decomposition, especially when different phenomena occur in the same range of characteristic frequencies.

Therefore, as a first approach to probe the main changes of spectra during aging, we calculated a time difference impedance spectra, $\Delta Z_t(\omega)$, by subtracting for each pulsation the impedance obtained at a given aging time t , $Z_t(\omega)$, to the initial impedance, $Z_0(\omega)$, according to the following equation 3.2:

$$\Delta Z_t(\omega) = Z_t(\omega) - Z_0(\omega) \quad (\text{Eq. 3.2})$$

The Figure 3.2 shows the time difference impedance spectra resulting from the Eq. 3.2. The spectra exhibit only one semi-circle that roughly increases by a factor of two to three in 60 h for all the systems. For both neat ILs, we also observe a positive shift on the real

part of the impedance at high frequencies that shows an evolution of the bulk properties of the ILs.

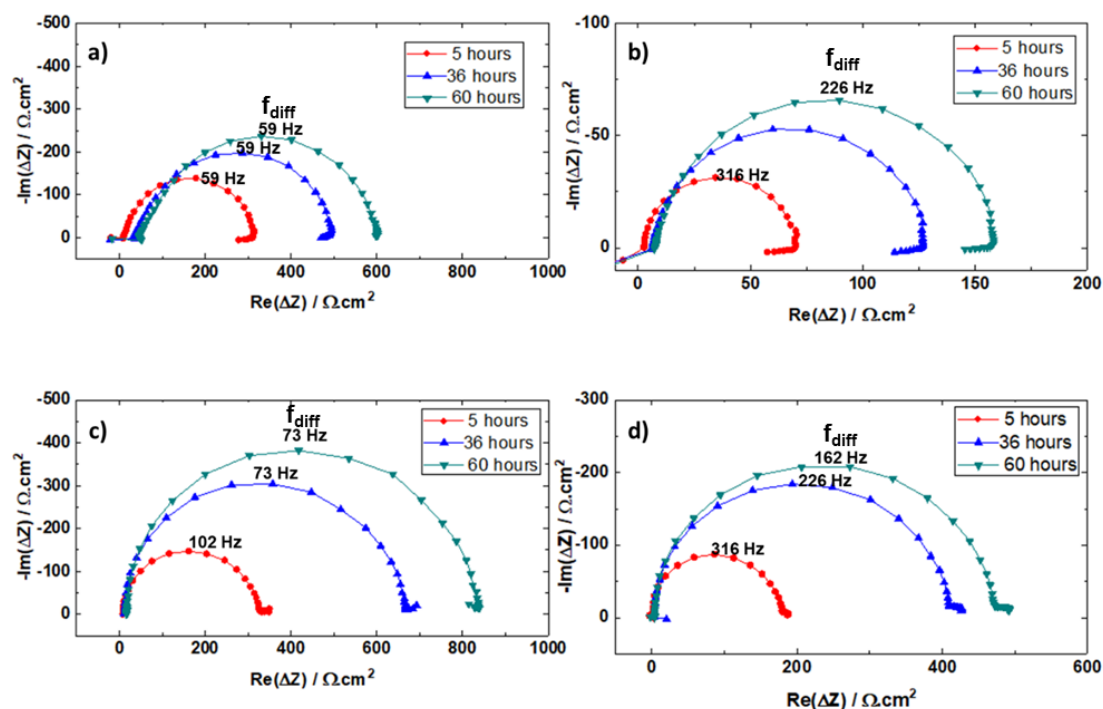


Figure 3.2 Impedance spectra upon aging for Li/Li coin cells containing (a) $\text{C}_1\text{C}_6\text{ImTFSI}$, (b) $\text{C}_1\text{C}_6\text{ImFSI}$, (c) $\text{C}_1\text{C}_6\text{ImTFSI/LiTFSI}$, and (d) $\text{C}_1\text{C}_6\text{ImFSI/LiTFSI}$ measured at OCV at 295 K.

Interestingly, the characteristic frequency f_{diff} of the semi-circle depends on the electrolyte composition, especially on the nature of the anion: with $\text{C}_1\text{C}_6\text{ImTFSI}$, f_{diff} is lower (59 Hz for neat IL or 73 Hz when the LiTFSI salt is added) than the one with $\text{C}_1\text{C}_6\text{ImFSI}$ (226 Hz for neat IL or 162 Hz when LiTFSI salt is added). Therefore, this loop may be associated to the formation of the SEI in contact with neat ILs and electrolytes.

It is possible to fit the time difference impedance spectra using the simple circuit ΔR_{el} in series with $\Delta R_{\text{int}}/\Delta \text{CPE}_{\text{int}}$, (Figure 3.3).

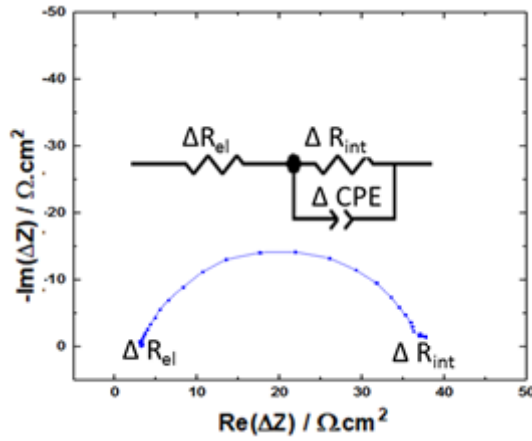


Figure 3.3 Randles circuit used to fit the time difference impedance spectra.

Note, that the parallel circuit R/CPE has a characteristic angular frequency (ω) represented by the equation 3.3-a, where Y and n are the pseudo-capacitance and the exponent of the CPE ($Z_{CPE}=1/Y(j\omega)^n$), respectively:²⁴

$$R * Y * \omega^n = 1 \quad (\text{Eq. 3.3-a})$$

The equivalent capacitance that would give in the R/C circuit the same characteristic angular frequency obeys the same law with $n=1$, equation 3.3-b:

$$R * C * \omega = 1 \quad (\text{Eq. 3.3-b})$$

Therefore, one can calculate the equivalent capacitance of the circuit by combining both equations 3.3-a and 3.3-b (equation 3.4):

$$\Delta C_{int} = \Delta R_{int}^{(1-n)/n} * \Delta Y_{int}^{1/n} \quad (\text{Eq. 3.4})$$

The evolutions of the time difference of the electrolyte interphase resistances, ΔR_{el} and ΔR_{int} , and of the inverse of the equivalent capacitance, $1/\Delta C_{int}$, as a function of the square root of aging time are depicted in the Figures 3.4-a, 3.4-b and 3.4-c, respectively.

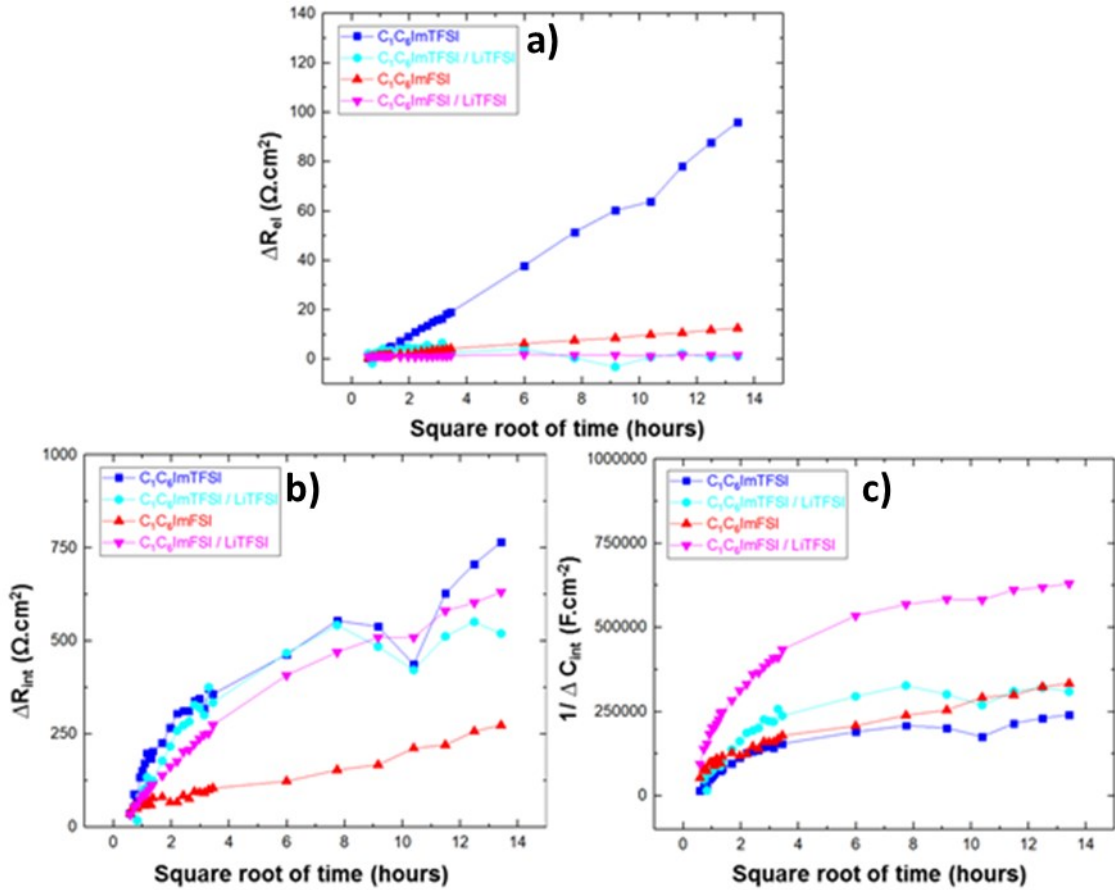


Figure 3.4 Evolution as a function of the square root of aging time, (a) of the electrolyte resistance ΔR_{el} , (b) of the interface resistance ΔR_{int} , and (c) of the inverse of the capacitance $1/\Delta C_{int}$.

Surprisingly, the ΔR_{el} of neat $C_1C_6ImTFSI$ shows a linear evolution as a function of the square root of time with a pronounced slope (Fig. 3.4-b). The ΔR_{el} of neat C_1C_6ImFSI evolves in a similar way with less pronounced slope. In the presence of LiTFSI lithium salt, for both IL, the slope of ΔR_{el} is reduced, and is fairly steady after 24 h of aging time.

From the equation 3.1, it is clear that the significant increase of R_{el} values for neat $C_1C_6ImTFSI$ must be attributed to a modification of its effective conductivity σ_{eff} . This evolution could result either from a poor wettability of the separator or a chemical change of the ILs during the aging process.

To exclude the hypothesis of poor wettability, the effective conductivity (σ_{eff}) was compared with the experimental conductivity (σ_0) (see experimental part in chapter 2).

The ratio $\sigma_{\text{eff}} / \sigma_0$ is related to the effective tortuosity (τ_{eff}) and the porosity (ε) of the separator following the equation 3.5:²⁵

$$\tau_{\text{eff}} = \frac{\sigma_0}{\sigma_{\text{eff}}} \varepsilon \quad (\text{Eq. 3.5})$$

The results of this equation are given in Table 3.1:

Table 3.1 Ionic conductivities (σ_0) at T = 298.15 K obtained from VFT fit, electrolyte resistances measured by EIS, effective conductivities (σ_{eff}) of electrolytes and tortuosity of Viledon separators (τ). ε separator taken as 0.4 (technical data from Freudenberg).

Combination	$\sigma_{22^\circ\text{C}}$ (mS.cm ⁻¹)	R _{el} .S (Ω .cm ²)	σ_{eff} (mS.cm ⁻¹)	τ
C ₁ C ₆ ImTFSI	1.94	28.7	0.91	1.3
C ₁ C ₆ ImTFSI + LiTFSI	0.72	85.3	0.30	1.4
C ₁ C ₆ ImFSI	3.80	12.1	2.15	1.1
C ₁ C ₆ ImFSI + LiTFSI	1.91	26.5	0.98	1.2

A theoretical value of the tortuosity (τ_0) can be calculated knowing the porosity ε of the separator from the equation 3.6:²⁵

$$\tau_{\text{th}} = 1 - 0.5 * \ln \varepsilon = 1 - 0.5 * \ln(0.4) = 1.2 \quad (\text{Eq. 3.6})$$

The similarities of τ_{eff} and τ_0 values exclude the poor wettability of the separators.

Consequently, the R_{el} increase would result from a chemical transformation of the bulk properties of ILs related to their decomposition on lithium metal surface. Thus, with neat ILs, the results suggest that some degradation compounds are partially soluble in ILs which may modify the IL viscosity, for example,²⁶ leading to a reduction of the effective conductivity. Note that for C₁C₆ImFSI, the increase of R_{el} is less pronounced suggesting a higher stability compared to C₁C₆ImTFSI (Fig. 3-3b) or less soluble byproducts.

The addition of LiTFSI salt protects both neat ILs from progressive bulk decomposition. This could be related to the increase of the electrochemical window range

upon addition of lithium salt *e.g.* the cathodic limit of C₁C₆ImTFSI changes from + 0.64 V vs. Li⁺/Li to - 0.28 V vs. Li⁺/Li when LiTFSI (1 mol.L⁻¹) is added.²⁰

Concerning the interface at medium frequency (Figures 3.3-c and 3.3-d), for both neat ILs and electrolytes, in this representation after a linear increase of ΔR_{int} and $1/\Delta C_{int}$ for the first 15 hours, the slope angle diminishes suggesting a lowering of the interface resistance evolution. This linearity is not trivial since it verifies that the growth of the fresh passive layer follows a diffusion law *i.e.* roughly, the interphase resistance is proportional to \sqrt{Dt} , where D is a diffusion coefficient.

One can notice that the initial slope of the curves depends on the nature of the anion. In the case of C₁C₆ImTFSI and related electrolyte these slopes are similar, whereas in C₁C₆ImFSI it is rather lower. For C₁C₆ImFSI doped with LiTFSI an intermediate behavior is observed. This variance in the slopes of the curves suggest a different mechanism of degradation of the TFSI and FSI anions on lithium surface, leading to a different chemical composition of the fresh SEI. This is confirmed by the two sets of values of the characteristic frequencies, f_{diff} , of the fresh SEI (see Figure 3.2) depending on the nature of the anions for both neat ILs.

From the initial slopes of the resistance and inverse capacitance as function of \sqrt{t} , rough estimates of the diffusion coefficient (D) and of the conductivity (σ) of the fresh SEI can be calculated²⁴ using the equations 3.7 and 3.8, assuming a diffusion limited growth of its thickness, l_{int} :

$$\Delta R_{int} = \frac{l_{int}}{\sigma S} = \frac{\sqrt{Dt}}{\sigma S} \quad (\text{Eq. 3.7})$$

$$\frac{1}{\Delta C_{int}} = \frac{l_{int}}{\varepsilon_r \varepsilon_0 S} = \frac{\sqrt{Dt}}{\varepsilon_r \varepsilon_0 S} \quad (\text{Eq. 3.8})$$

Where ε_r , is the relative dielectric permittivity of the passive layer and ε_0 the vacuum dielectric permittivity. Nonetheless, the value of ε_r depends on the chemical composition of the SEI. In Table 3.2 we give some information from the literature about the relative permittivity values of typical species in the SEI.

Table 3.2 Relative permittivity for various surface species that forms the SEI.²⁷⁻²⁹

Species	Relative permittivity
Li ₂ CO ₃	6.9 ²⁷ , 5 ²⁴
Li ₂ O	9.8 ²⁴
LiF	5.2 ²⁷ , 8.3 ²⁹
LiOH	8.5 ²⁷

The relative permittivity of these species varies in a limited range 5-10. In order to applicate the equations 3.7 and 3.8, an average value will be use for the calculations. Besides, the slopes of the curves ΔR_{int} vs. \sqrt{t} and $1/\Delta C_{int}$ vs. \sqrt{t} need to calculated (see previous Figure 3.4). However, a rough estimation of the slopes can only be obtained in the first 16h of aging time. After that time the evolutions of the resistances and capacitances become slower and eventually the thickness of the SEI ($l \approx \sqrt{Dt}$) reaches a limit value. The calculated values for the ionic conductivities, diffusion coefficients and thicknesses of the fresh SEI after 16h of aging time are listed in Table 3.3. Two different average values of the relative permittivity of the SEI have been considered.

Table 3.3 Estimated diffusion coefficients, conductivities and thicknesses of the fresh SEI formed by IL electrolytes at lithium surface at OCV and T=295 K.

	$\epsilon_r = 5$			$\epsilon_r = 10$		
	σ_{SEI} (10 ⁻⁸ S.m ⁻¹)	D_{SEI} (10 ⁻²³ m ² .s ⁻¹)	$l = \sqrt{Dt}$ t=16h (nm)	σ_{SEI} (10 ⁻⁸ S.m ⁻¹)	D_{SEI} (10 ⁻²³ m ² .s ⁻¹)	$l = \sqrt{Dt}$ t=16h (nm)
C ₁ C ₆ ImTFSI	6	9	2	11	37	5
C ₁ C ₆ ImTFSI + LiTFSI	4	11	3	8	44	5
C ₁ C ₆ ImFSI	15	1	1	31	6	2
C ₁ C ₆ ImFSI + LiTFSI	6	6	2	13	25	4

Note that the ionic conductivity of the fresh SEI is larger with FSI anion, and the diffusion coefficients are higher when ILs are doped with LiTFSI.

This approach allows us to propose a bilayer SEI model for the interfacial response corresponding to one contribution at higher frequencies (1.2 ± 0.2 kHz) due to the native layers that do not evolve over time, and a second contribution at medium frequencies (200 ± 100 Hz) which increases continuously during the cell aging, constituting the fresh SEI generated by the electrolyte decomposition on the lithium surface.

Therefore, we can propose an electric equivalent circuit based on two (R_{int}/CPE) in series in order to describe the interfacial loop (Figure 3.5). The first contribution (R_{native}/CPE_{native}) has been fitted on the initial spectrum and all the parameters have been fixed for the following registered spectra assuming that all the evolution are due to the lower frequency contribution (R_{fresh}/CPE_{fresh}).

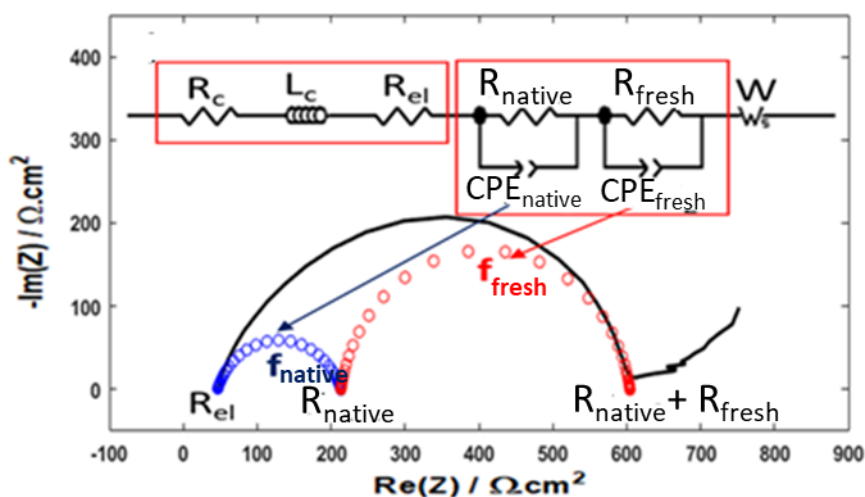


Figure 3.5 Equivalent electrical circuit for a bilayer SEI model

With this approach, we have been able to obtain excellent fitting of the data without any ambiguity on the determined parameters. The evolution of the set of parameters as a function of time is depicted in Figure 3.6.

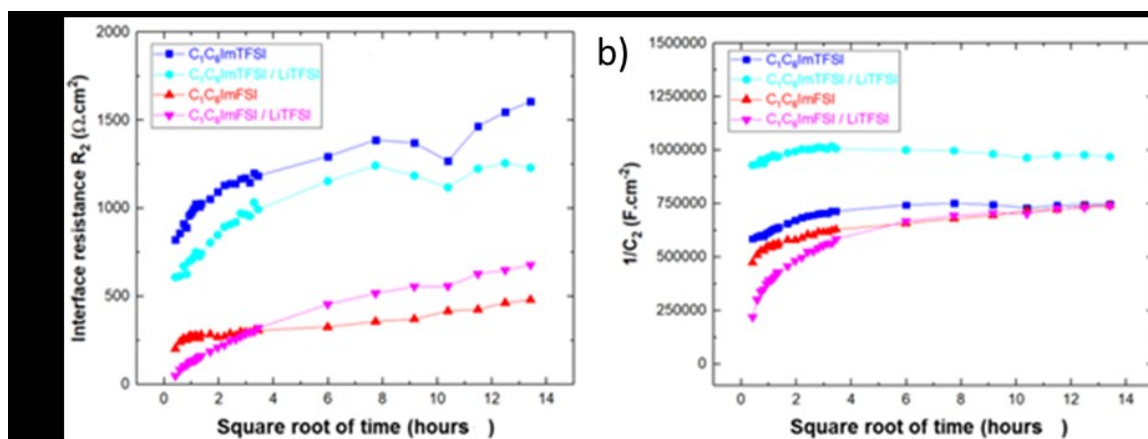


Figure 3.6 Evolution as a function of the root square of aging of: (a) The interface resistance R_{fresh} and (b) the inverse of capacitance $1/C_{\text{fresh}}$.

Note in Figure 3.6 how the resistances of the combinations containing FSI anion are systematically lower in a factor of 2-3 than the ones with TFSI anion, highlighting the strong impact of the nature of anion. To validate the results of the bilayer model, the thicknesses of the native and fresh layers formed at $t = 16$ h have been calculated in Table 3.4, using an average relative permittivity of $\epsilon_r = 10$. The results are in good agreement with those in Table 3.3.

Table 3.4 Estimated thicknesses of the native and fresh SEI formed by IL electrolytes at lithium surface at OCV and $T=295$ K. ($\epsilon_r = 10$)

Combination	l_{native}	$l_{\text{fresh at } t = 16 \text{ h}}$	$l_{\text{fresh at } t = 7 \text{ days}}$
C ₁ C ₆ ImTFSI	9	6	6
C ₁ C ₆ ImTFSI + LiTFSI	9	9	9
C ₁ C ₆ ImFSI	9	6	7
C ₁ C ₆ ImFSI + LiTFSI	10	5	7

These results constitute only a rough estimation of the size of the deposition layer. The main inconvenient of this model is the assumption that the deposit of species on the lithium metal is constituted of a stacking of homogeneous layers with a known value of the relative permittivity of each layer. Evidently, this is not the case and the real situation must be similar to the mosaic model of the SEI.²²

In order to obtain some information about the morphology and homogeneity of the layers formed on lithium metal, the surface of the lithium electrodes has been

characterized by the SEM/AES technique. In Figure 3.7 and Figure 3.8, show the morphologies and chemical composition of lithium electrodes in contact with neat ILs $C_1C_6ImTFSI$ and C_1C_6ImFSI after 7 days of aging.

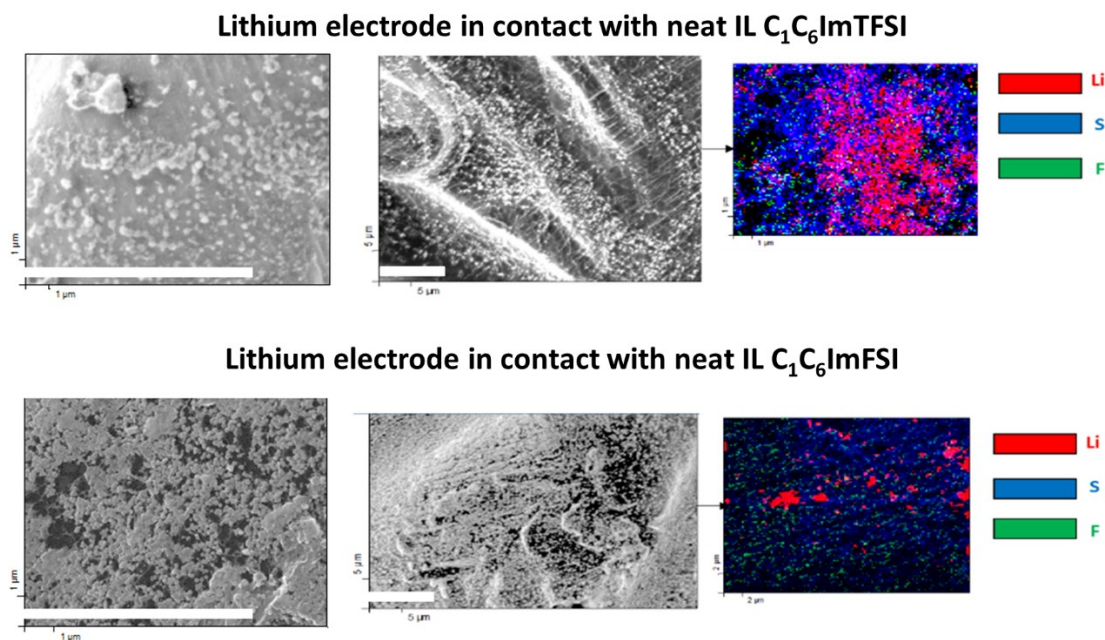


Figure 3.7 SEM micrographs and AES chemical maps of lithium electrodes in contact with neat ILs after 7 days. The white bars represent a length of 10 μm .

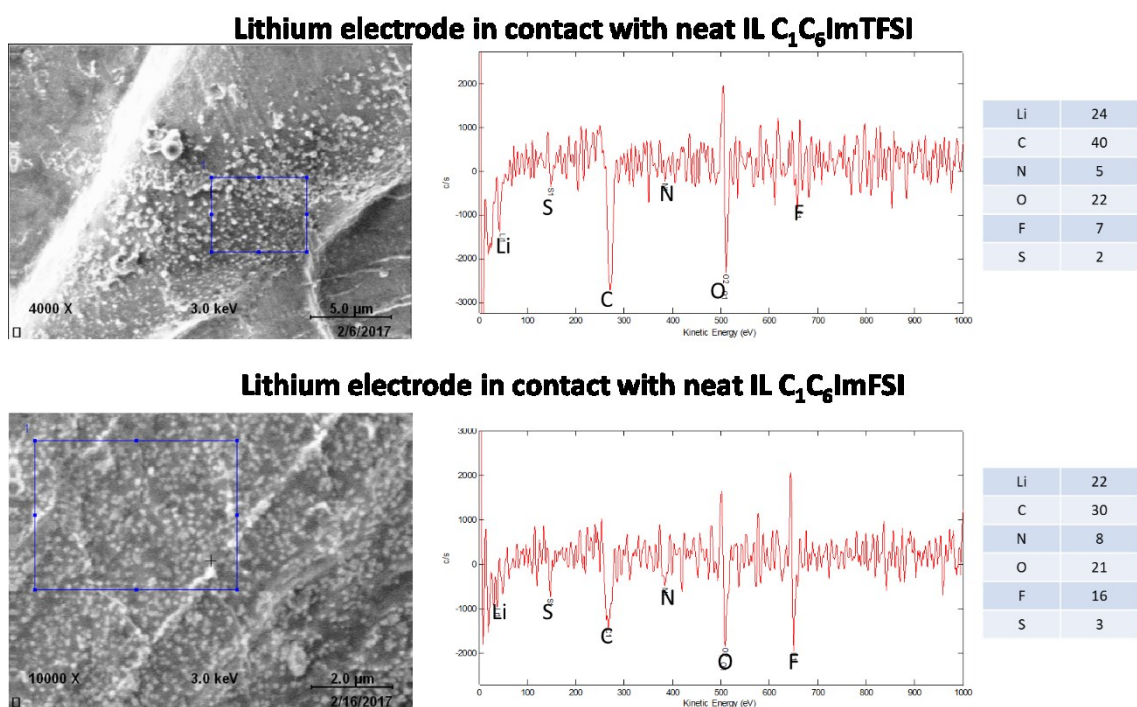


Figure 3.8 SEM micrographs and AES spectra maps of lithium electrodes in contact with neat ILs after 7 days. The atomic concentration of each element (%) is listed in the tables.

The AES chemical analysis was performed with special care since some byproduct are sensitive to beam exposition. Hence, the SEM/AES technique was performed using a 3 keV beam in order to avoid beam damage.

The chemical mapping and the SEM analysis show the formation of deposits for the case of both neat ILs. However, from the chemical maps it is clear that the deposit of C_1C_6ImFSI byproducts covers most of the surface area and is more homogenous than in the case of $C_1C_6ImTFSI$.

The results demonstrate the presence mainly of lithium, carbon and oxygen coming from the native lithium passivation layer. Interestingly, the concentration of fluorine in general is higher than the ones of nitrogen or sulfur, and it is 2 times higher in the case of C_1C_6ImFSI than with $C_1C_6ImTFSI$.

Besides, for the case of the FSI based IL, the concentration of carbon diminishes and the peak of lithium is screened by the noise of the signal than in the case of $C_1C_6ImTFSI$. This suggest that the layer produced by C_1C_6ImFSI is thicker and more homogeneous because of a higher concentration of fluorinated species (typically LiF).

These last results show the difficulty in estimating an average thickness of the layers formed on lithium metal by ILs by means of simple models using EIS technique. For the case of C_1C_6ImFSI a model of a fresh SEI layer composed only by LiF could be justified but not in the case of $C_1C_6ImTFSI$. Nonetheless, the chemical maps demonstrate the presence of isolated lithium in some parts of the analyzed regions where the deposition of IL byproducts is practically inexistent. In this case, the order of magnitude of the thicknesses in Tables 3.3 and 3.4 is justified, knowing that the depth of analysis of the AES technique is ~ 2 nm.

Herein, in order to complete these observations a coupling with other techniques is necessary. Therefore, in the next section these results will be contrasted with the chemical environment information of the deposited byproducts provided by XPS.

3.2.2. Chemical environment evolution of the bulk electrolyte and the interface upon aging at OCV conditions

In the last section the EIS and AES techniques were used to estimate the thicknesses and evaluate the morphologies of the byproduct deposits, respectively. However, in contrast with its high lateral resolution (~ 8 nm, AES PHI 700ULVAC PHI), the chemical resolution of the AES technique does not allow an easy identification of the different chemical environments of a sample. Therefore, in this section the XPS technique will be used to obtain a more accurate vision of the evolution of the chemical environment of both, electrolytes and lithium surface after aging at OCV conditions.

3.2.2.1. Visual inspection of the separators

Before XPS measurements, several photos of the separators were taken during cell disassembly in a glove box (Figure 3.9).

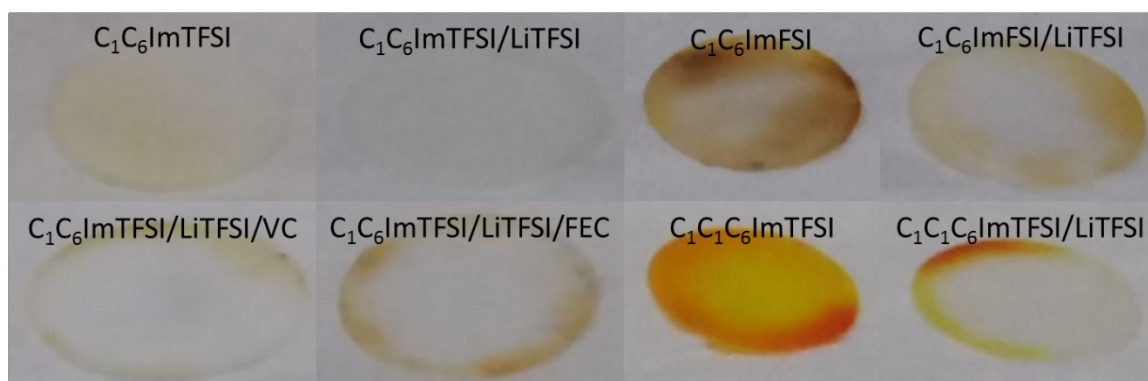


Figure 3.9 ©Viledon separators of the Li/Li coin cells after aging one week in the eight combinations of ionic liquids and electrolytes.

The yellowish coloration of the separators containing C_1C_6ImFSI and $C_1C_6ImTFSI$ is more pronounced. This coloration is partially attenuated when adding $LiTFSI$ salt.

These observations can be correlated to the EIS observation as the $LiTFSI$ improves the stabilization of ionic liquids preventing them from further degradation. Note that the coloration change does not necessary mean a stronger degradation, but it means that the degradation byproducts are different in each case. However, a direct correlation between

coloration change and intrinsic R_{el} and/or R_{int} change cannot be found. In order to clarify the origin of the coloration, we have performed XPS analyses on the separators without any washing process.

In contrast, considering that the average depth of analysis for an XPS measurement is approximately 5 nm, the chemical characterization of the SEI requires that the lithium electrodes to be analyzed must be washed with some organic solvent, in order to remove the excess of electrolyte.

The effect of the washing procedure on the sample is still an open question and the *ex-situ* analysis is not always considered as a reliable tool.^{30–32} On the other hand, Howlett *et al.*¹⁴ have used mechanical methods to try to remove the remainder IL on cycled lithium electrodes. Besides, Bhatt *et al.*⁶ affirm that only a washing process using dimethyl carbonate (DMC) and hexane is effective to remove the traces of IL and avoid the mask of surface features and the charging effects during a SEM analysis.

In order to establish our own protocol, we washed two portions of the same *post-mortem* lithium electrode with DMC for 5 and 30 seconds, respectively. The chemical structure of the lithium surface probed by XPS is reported in Figure 3.10.

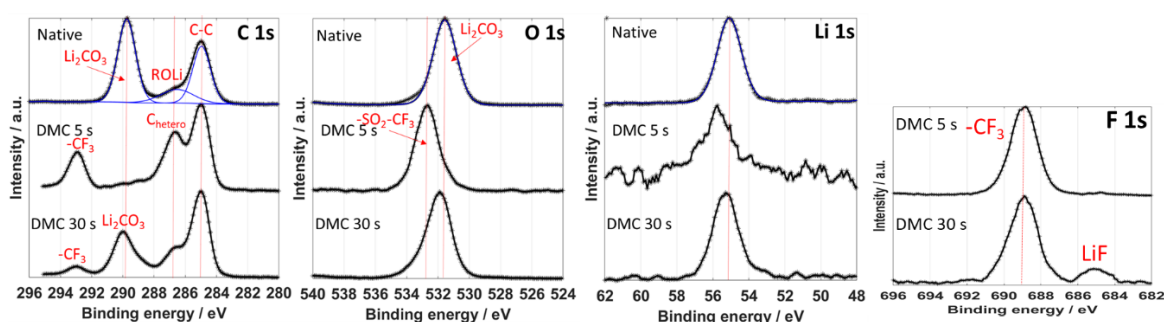


Figure 3.10 XPS spectra of a pristine foil of lithium and XPS spectra of the same lithium electrode aged in a coin cell system with $C_1C_6ImTFSI/LiTFSI$ electrolyte and washed 5 and 30 seconds with DMC

We noticed a different spectral signature depending on the time of washing with DMC. Five seconds of washing are insufficient to remove the traces of $C_1C_6ImTFSI/LiTFSI$ electrolyte. Although, the C1s and F1s spectra recorded after 5 second of washing are similar to the reference spectra of the electrolyte, we can notice the presence of small carbonates related peak (Li_2CO_3) at 290 eV and a shoulder between 288 and 289 eV

assigned to carbonate species. After 30 seconds, the carbonates related peak is more intense and some LiF is observed with a diminution of the concentrations of $-\text{CF}_3$ and C_{hetero} . The diminution of the $-\text{CF}_3$ and C_{hetero} related peaks is associated to the effective process of removing the IL traces by the DMC. However, the presence of carbonates could be attributed to the initial native layers as can be seen in the spectra corresponding to a pristine foil of lithium (this reference has been also reported in Chapter 2). The LiF is, hence, assigned to a passivating layer issued from the electrolyte degradation process.

In this work, all *post-mortem* XPS measurements were performed on lithium electrodes washed with DMC during 30 seconds.

3.2.2.2. Chemical structure of bulk and interface resolved by XPS

The evolution of the chemical structure of the bulk electrolyte was probed by XPS through the analyses of the separators after aging and without washing with DMC. Furthermore, the evolution of the passivation layer at the interface electrolyte/lithium was probed by XPS performed onto the aged surface of lithium and after washing. Both bulk and interface XPS evolution was studied relatively to neat IL and IL based electrolytes.

Figure 3.11 shows the C1s core levels of the ILs and electrolytes for the case of (a) the neat reference, (b) the separator and (c) the surface of the lithium electrode. The XPS spectra of the references have been discussed in chapter 2 and are shown here just for comparison. The XPS peak assignments have been done according to data reported in the literature.^{33,34}

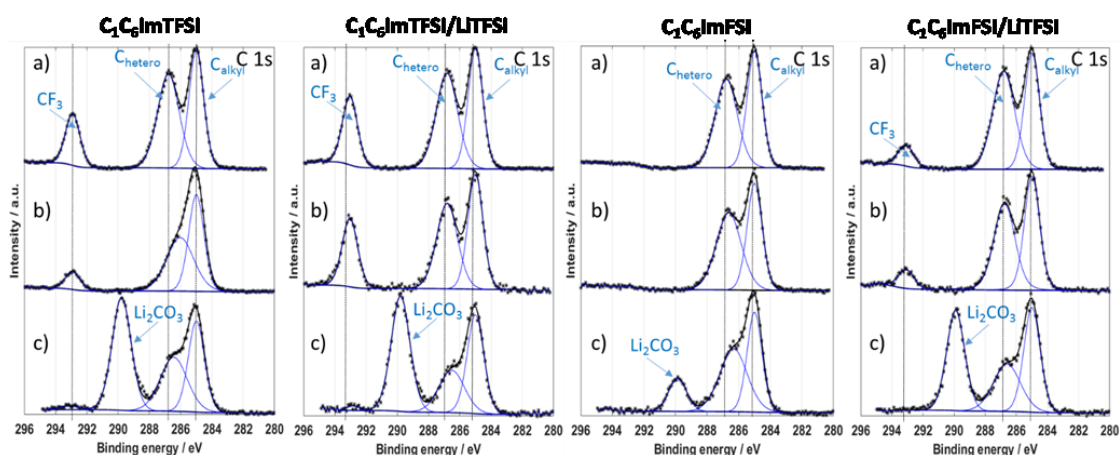


Figure 3.11 XPS spectra of carbon C1s core level registered at the surface of a) neat IL based electrolytes, b) on separator and c) on lithium electrode surfaces.

After aging, the spectra recorded on the Viledon separators do not show significant changes (Figure 3.11-b) for C_1C_6ImFSI , $C_1C_6ImTFSI/LiTFSI$ and $C_1C_6ImFSI/LiTFSI$. However, for $C_1C_6ImTFSI$ the relative intensities of $-CF_3$ and C_{hetero} related peaks in comparison with C_{alkyl} are reduced. Moreover, the position of the peak C_{hetero} is shifted to lower binding energies (286.0 eV), and its full width at half maximum (FWHM) become broader compared to the neat reference. These observations suggest that chemical modifications or degradations of $C_1C_6Im^+$ cation occurred during aging. Similar behavior was observed in the C1s peak recorded in the bulk of C_1C_6ImFSI . In this case the shift toward lower binding energies and the broadness of FWHM is clearly less pronounced.

On lithium electrodes (Figure 3.11-c), the spectra of C1s are different and mainly dominated by a peak at 289.8 eV identified as Li_2CO_3 . The presence of Li_2CO_3 has as origin the initial native layer on the surface of the lithium electrode as it has been discussed in chapter 2. Surprisingly, the intensity of the peak corresponding to $-CF_3$ group is negligible in every case, and disappears in the cases of C_1C_6ImFSI and $C_1C_6ImFSI/LiTFSI$, whereas the peak at 285.0 eV is clearly still visible. By comparison with the C1s spectra of the pristine lithium foil (chapter 2, Figure 2.18), the peak corresponds to the native carbon layer and not to a residuary C_{alkyl} from ILs. This explains the fading of the $-CF_3$ peak and the shifts of the C_{hetero} peak that correspond probably to the formation of precipitated organic complexes from the $C_1C_6Im^+$ degradation.

On the other hand, since the Li_2CO_3 related peak is still visible, the deposited SEI layer coming from decomposition products of IL based electrolytes must be thinner than ~ 5 nm (depth probed by XPS). In the case of the C_1C_6ImFSI IL, the Li_2CO_3 contribution is less pronounced which is a signature of thicker and/or more uniform SEI.

Regarding the N1s core levels on Viledon separators (Figure 3.12-b), the atomic concentration ratio N_{cation}/N_{anion} decreases, in comparison with the neat references, from 1.9 to 0.3 for $C_1C_6ImTFSI$ and from 1.9 to 0.8 for C_1C_6ImFSI . For both ILs doped with $LiTFSI$ the ratio N_{cation}/N_{anion} varies only from 1.4 to 1.1. These observations confirm the stronger degradation of the $C_1C_6Im^+$ cation in presence of TFSI instead of FSI anions, as well as an improved stability of the cation, whatever the anions, when neat ILs are doped with $LiTFSI$.

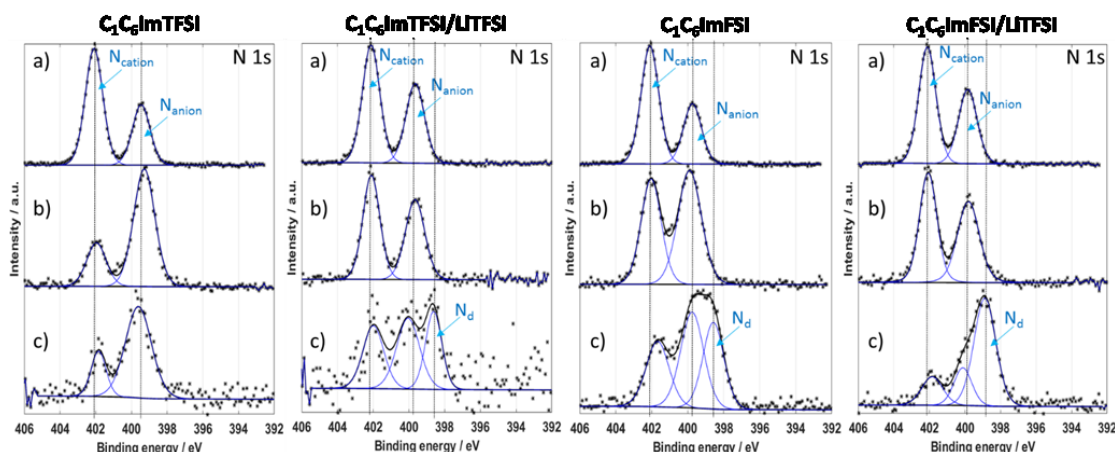


Figure 3.12 XPS spectra of nitrogen N1s core level registered at the surface of a) neat IL based electrolytes, b) on separator and c) on lithium electrode surfaces.

On lithium surface electrodes (Figure 3.12-c), the peaks of N_{cation} and N_{anion} still remain visible with an enlargement of its FWHM and a new peak labelled N_d around 398.6 – 398.9 eV is formed. This peak can be attributed to decomposition products from $C_1C_6Im^+$ cation *e.g.* N- heterocyclic carbenes formation.³⁵

From the C1s and N1s core level analyses, in the case of neat $C_1C_6ImTFSI$, $C_1C_6Im^+$ cation reacts with the lithium affording byproducts partially soluble in the electrolytic solution, which induces a continuous change in the IL composition that strongly affects its conductivity as observed by EIS. The cation byproducts are almost absent in the bulk electrolyte with neat C_1C_6ImFSI . That effect might be due to a better passivation layer induced by the FSI anion degradation on the lithium surface than with TFSI anion.

In the Figure 3.13-a, the spectra of fluorine F1s core level show two peaks corresponding to the $-CF_3$ group for TFSI anion at 688.9 eV and the SO_2-F bonds in FSI anion at 687.8 eV. Although, both peaks are also present in the separators without significant changes (Figure 3.13-b), they are accompanied by a new peak positioned at 685 eV associated to LiF salt traces mainly for FSI based IL and electrolyte.

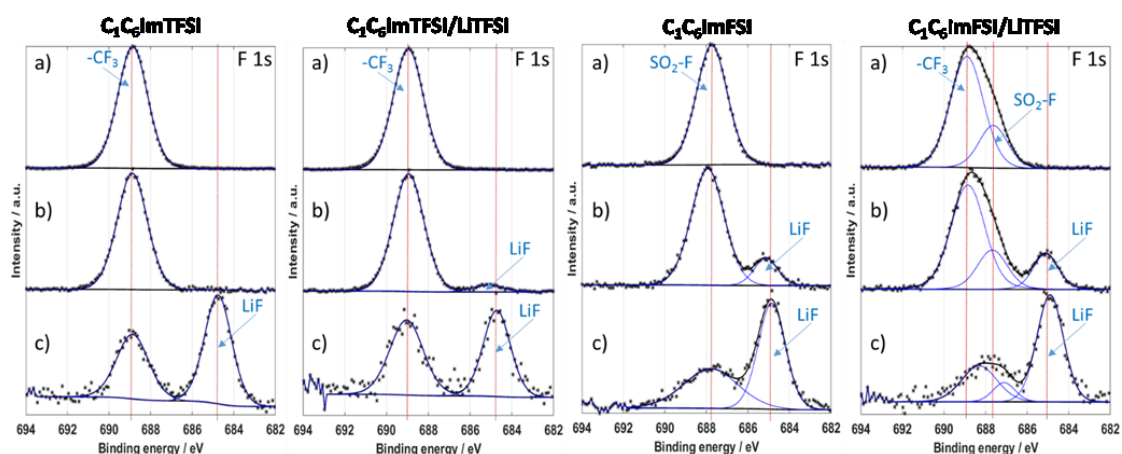


Figure 3.13 XPS spectra of fluorine F1s core level registered at the surface of a) neat IL based electrolytes, b) on separator and c) on lithium electrode surfaces.

On the lithium electrodes (Figure 3.13-c), the LiF related peak is more intense especially in the case of FSI based IL and electrolyte. Besides, the broad peak between 687 – 689 eV associated to the formation of fluorine derivatives from anion such as $C_2F_xLi_y$,³⁶ since there is not more initial $-CF_3$ group, as it was demonstrated in the C1s spectra (*vide supra*).

Considering that LiF is scarcely soluble in IL,³⁷ and that it has been proposed as an agent that stabilizes the SEI layer preventing any side reaction,³⁸ we can suggest that FSI decomposition byproducts leads to the formation of a more passivating interface than in the case of TFSI decomposition. This leads to the formation of a SEI layer mainly constituted of LiF which could prevent further decomposition of the $C_1C_6Im^+$ cation.

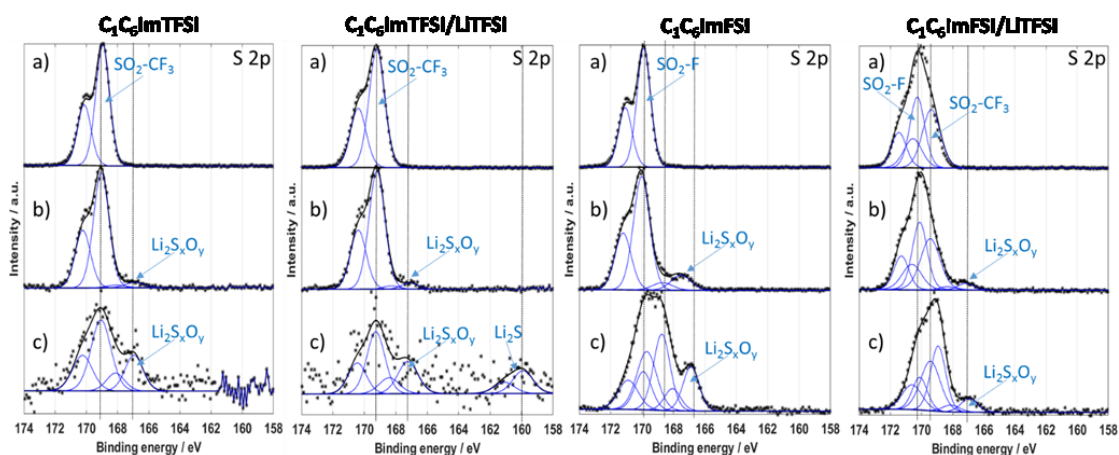


Figure 3.14 XPS spectra of sulfur S 2p core level registered at the surface of a) neat IL based electrolytes, b) on separator and c) on lithium electrode surfaces.

Regarding the S2p spectra (Figure 3.14), it contains the initial doublets (S2p_{3/2-1/2}) assigned to the SO₂-CF₃ bonds at 169.0 eV and SO₂-F bonds at 169.9 eV. For the IL and electrolyte in the separator, one can notice that at lower binding energies, Li₂S_xO_y species are also present at 167.0 eV. The amount of degraded anion into Li₂S_xO_y is more important onto the lithium electrode surfaces, especially in the FSI based IL and electrolyte. We noticed a small contribution of lithium sulfide Li₂S (159.9 eV) at the surface of lithium aged in C₁C₆ImTFSI doped with LiTFSI, which was also observed in previous works.^{14,17} This contribution remains minor in our case.

The reference spectra of oxygen O1s core levels of neat ILs (Figure 3.15-a) exhibit only one peak centered around 532.7 – 533.1 eV related to -N-SO₂- bonds.

On the Viledon separators, these peaks are present but are no more symmetric, and a new peak of reduced intensity is present at 531.3 – 531.5 eV (Figure 3.15-b). This new peak could be related to traces of Li₂S_xO_y products (167 eV, S2p spectra). As H₂O contamination cannot be excluded, these peaks can also be assigned to LiOH located in the same binding energy range.

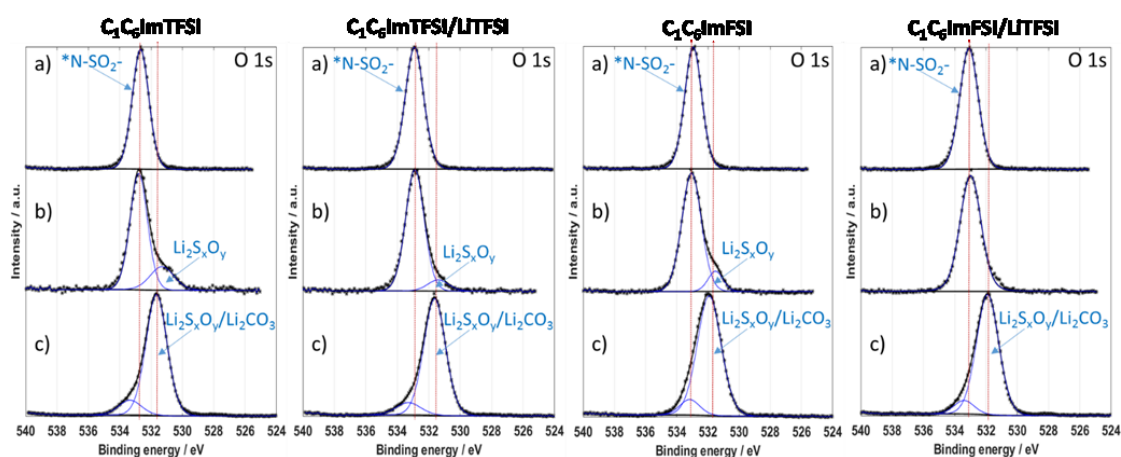


Figure 3.15 XPS spectra of oxygen O 1s core level registered at the surface of a) neat IL based electrolytes, b) on separator and c) on lithium electrode surfaces.

The lithium electrodes (Figure 3.15-c) exhibit the same two sets of peaks, the first one between 533.2 – 533.4 eV representing the -N-SO₂- bonds with a low intensity and the second one between 531.7 – 531.9 eV, more intense, associated to Li₂CO₃ (289.8 eV, C1s spectra), but that can also be related to the formation of Li₂S_xO_y products.

In order to compare the compositions of the layers formed in each case, Figure 3.16 depicts the atomic concentration of the different products that compose the surface layers of the lithium electrodes aged in contact with IL based electrolytes. Note that the surface is mainly dominated by carbonates, but in the case of C_1C_6ImFSI is evident that more degradation byproducts are formed masking the carbonates coming from the native lithium. The formation of degradation byproducts of sulfur is attenuated when $LiTFSI$ is added to C_1C_6ImFSI .

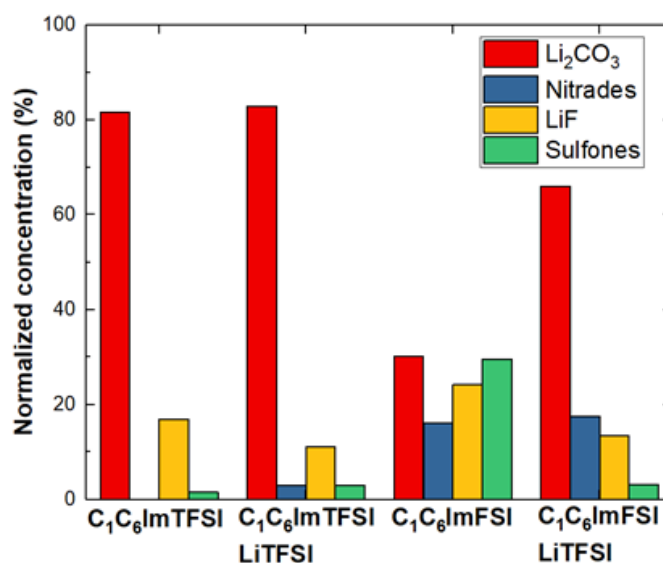


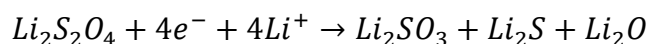
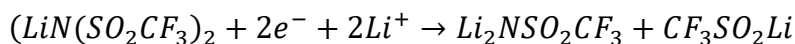
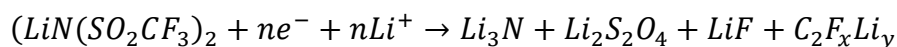
Figure 3.16 XPS estimated atomic concentration of lithium carbonates and degradation byproducts Li_3N , LiF , $Li_2S_xO_y$, Li_2S detected at the lithium surface.

3.2.3. Intermediate conclusions about the degradation mechanisms

In all of the combinations, XPS analyses on the lithium surface show the deposition of thin layers of inorganic and organic byproducts resulting from anion and cation decomposition giving rise to the deposition of mainly LiF , $Li_2S_xO_y$ and Li_3N species. In parallel, the slope of the interfacial resistance evolution as function of time at OCV seems to be characteristic of the anion type with a stronger slope with combinations containing TFSI rather than FSI. Especially in the case of FSI based combinations, the presence of LiF byproducts is observed and it seems to favor the formation of a more homogeneous and less resistive passive layer.

The degradation of the anions TFSI or FSI seems to play the main role in the formation of the species that compose the SEI. The formation of inorganic lithium salts can be

explained by the chemical reactions proposed by Aurbach et al.³⁹ for the reaction of LiTFSI based electrolytes with lithium:



The mechanism of the first reaction leads directly to the formation of LiF, Li₂S₂O₄ and Li₃N as main components of the SEI, which is in agree with the XPS results. Besides, as it is proposed by the third and fourth mechanisms, the formation of Li₂S and Li₂O implies a reaction with four or six electrons and Li⁺ ions and therefore, the probability of presence of these species is low as it has been demonstrated by our analyses by XPS.

Concerning the differences between the degradation byproducts produced by TFSI and FSI based electrolytes, Cao *et al.*⁴⁰ et Miao *et al.*⁴¹ based on studies by XPS identify the presence of higher concentration of LiF and LiSO_x species when the electrolytes contain LiFSI salt, whereas for electrolytes containing only LiTFSI the content of LiF is lower and the degradation mechanisms leads directly to the formation of LiS_x species. Cao *et al.* supports these observations with DFT calculations of the different bond strengths.

These observations are in agree with our XPS results, taking into account that we are use the neat IL C₁C₆ImFSI instead of the lithium salt LiFSI. Indeed, we have demonstrated that the byproducts of this IL on the lithium surface are mainly LiF (~685 eV) and Li₂S_xO_y (~167-168 eV) species.

On the other hand, the high presence of carbonates Li₂CO₃ in all of the cases suggest that the thickness of the fresh SEI must be in the order of some nm, as the typical analysis depth of the XPS technique is ~5 nm. The Li₂CO₃ must be coming mainly from the native layer, as it was shown in chapter 2. The thicknesses measured by EIS support partially these hypotheses. However, the EIS technique predicts similar thicknesses for the fresh and native layers and similar thicknesses for the layers produced by TFSI and FSI based electrolytes.

Based on the XPS observations of the neat IL C₁C₆ImFSI, the thickness produced by this IL must be thicker than the other combinations as the concentration of Li₂CO₃ is lower (screening by the fresh SEI containing a great concentration of LiF). In addition, based on XPS etching experiments, we have deduced a thickness of the native layer of at least 30 nm (see chapter 2).

If the different products of degradation of the anions are well known, the stability and degradation products of the imidazolium cation must be discussed further. Herein, it has been reported that the proton in the C2 position is highly instable, leading to the deprotonation of the imidazolium cycle,^{18,19} producing N-heterocyclic carbenes (NHC), Figure 3.17.

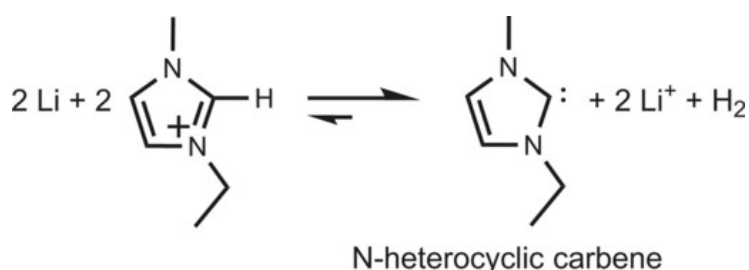


Figure 3.17 NHC carbene formation after deprotonation of the imidazolium cation.¹⁹

Besides, these NHC leads to the formation of dimers which are stable by means of the Wanzlick equilibrium,⁴² Figure 3.18.

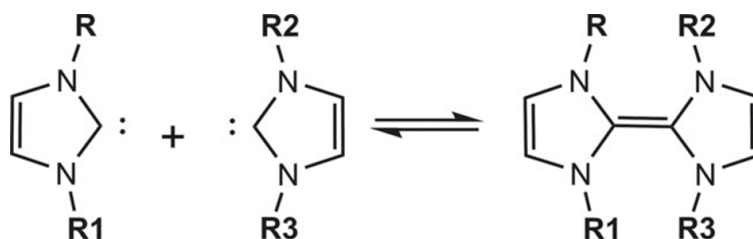


Figure 3.18 Formation of dimers in chemical equilibrium with their carbenes (Wanzlick equilibrium).¹⁹

Nonetheless, the experimental observation of these NHC have not been proved by the XPS technique, probably because the corresponding peaks are overlapped by the peaks of N_{cation} (~402 eV) and C_{hetero} (~286.7 eV). To the best of our knowledge, the XPS references are scarcely in the literature.³⁵ However, our results have been proved that the

imidazolium cation, for the case of the neat IL C₁C₆ImTFSI, suffers a decomposition forming soluble byproducts that do not precipitate to form the fresh SEI, but modify the conductivity of the IL.

Another point to be explained is the inhibition of the decomposition of the imidazolium cation when the anion is replaced by FSI, as suggest the EIS and XPS measurements. Certainly, the decomposition of the FSI leads to the formation of a more homogeneous SEI composed mainly by LiF that could modify the reactivity between of the imidazolium cation and the lithium surface. In addition, Bonhote *et al.*⁴³ signal that the deprotonation of the imidazolium cation is feasible with strong bases that lead to quite stable carbenes. This agrees with our observations of more strong interactions between cation-anion when the anion is FSI, which is weaker base than TFSI.

Finally, a last point to be clarified is the stabilization of the neat ILs after the addition of LiTFSI. With regards to the study of reference (chapter 2) of the electrochemical properties of the IL based electrolytes, we have established a solid support of the hypothesis that the lithium cation and the TFSI anion are associated, forming Li(TFSI)₂ complexes. Therefore, these complexes play a role in the stabilization of the IL, probably by a better affinity to the lithium surface formed mainly by Li₂CO₃.

Coupling the result of EIS, XPS and SEM/AES, we can propose the following schema of the different degradation byproducts presented at the surface of the aged lithium electrode at the OCV condition (Figure 3.19).

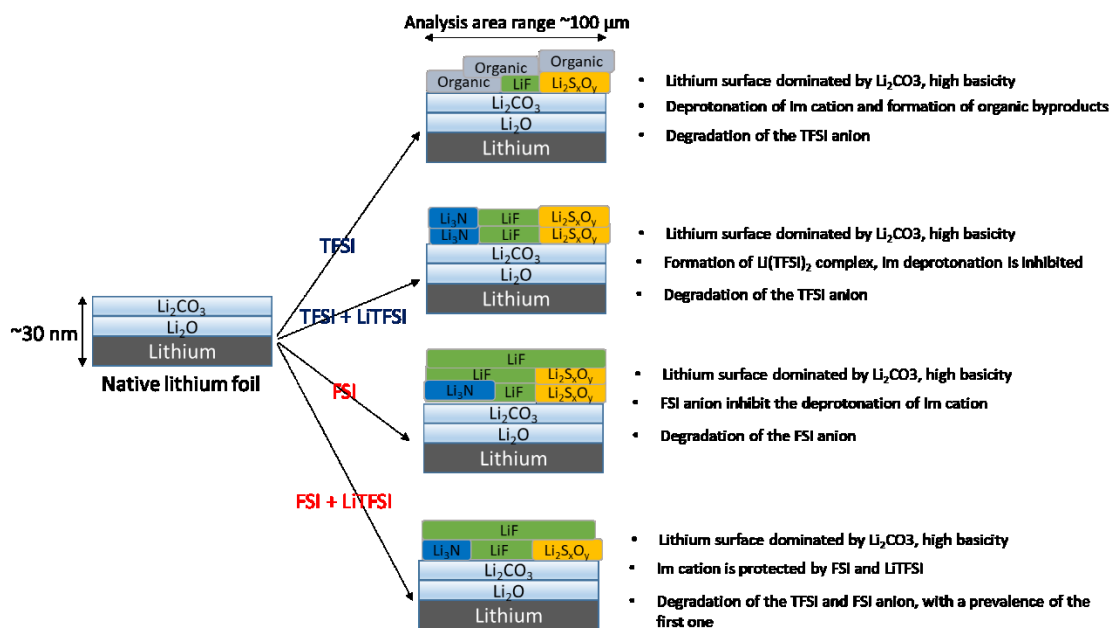


Figure 3.19 Proposed schema of the different degradation byproducts formed at the surface of lithium electrodes aged at the OCV condition based on a XPS analysis area range of 100 μm.

3.3. Effect of cation methylation and ILs based electrolyte solvent doping

It appears that the role and the nature of the anion and the salt concentration in the electrolytic solution affect the reactivity of C₁C₆Im⁺ cation toward lithium electrode surfaces. However, the C₁C₆Im⁺ is not intrinsically stable vs. lithium, and the cycle can be opened through the acidic proton on C2 position as proposed in literature.^{18,19}

Two strategies in an attempt to stabilize the imidazolium ring will be studied in this section. The first one consists in aging on the molecular structure of the C₁C₆Im⁺ cation by grafting a methyl group in the instable C2 position, avoiding the deprotonation of the imidazolium cation. A second strategy to be tested is to modify the macroscopic properties of the ILs such as the viscosity by means of the addition of additive solvents (VC and FEC), whose decomposition products have been signaled as responsible of the formation of a more homogenous SEI layer.^{31,44}

3.3.1. The effect of the methylation

Figure 3.20 show the impedance spectra evolutions for symmetrical Li/Li coin cells containing the ILs $C_1C_6\text{ImTFSI}$ and $C_1C_1C_6\text{ImTFSI}$ with and without LiTFSI.

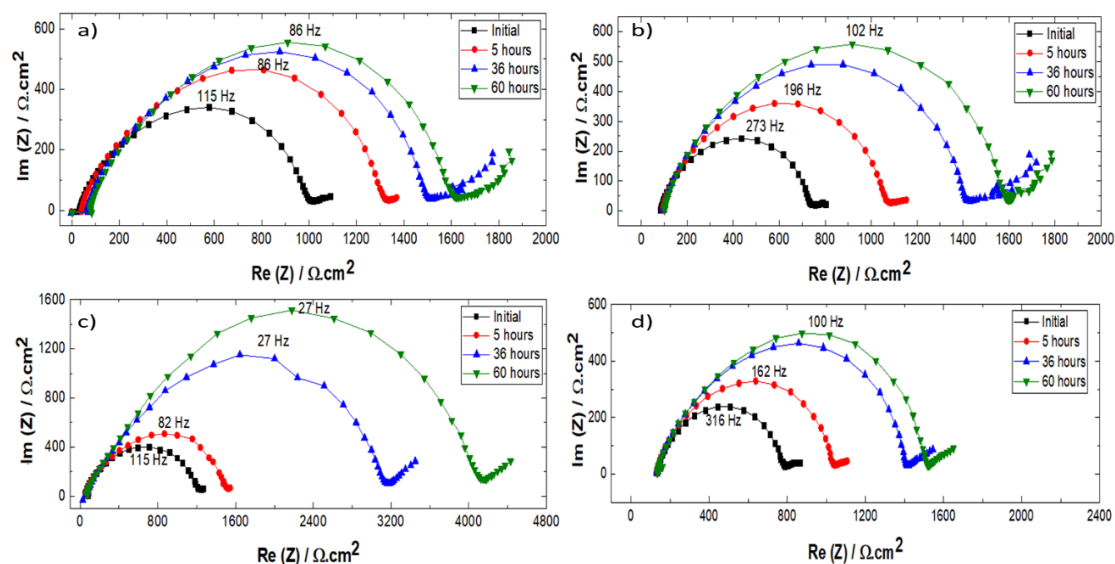


Figure 3.20 Evolution of the impedance response as a function of time measured at OCV at 295 K for Li/Li coin cells containing: a) $C_1C_6\text{ImTFSI}$, b) $C_1C_6\text{ImTFSI/LiTFSI}$, c) $C_1C_1C_6\text{ImTFSI}$ and d) $C_1C_1C_6\text{ImTFSI/LiTFSI}$.

For the neat ILs (Figure 3.20 a,c), the impedance of $C_1C_1C_6\text{ImTFSI}$ is more than two times higher than in the case of $C_1C_6\text{ImTFSI}$ after 7 days of aging at OCV. In contrast, the evolution of the electrolytes (Figure 3.20 b,d) is similar with almost the same variation of the characteristic frequency. Herein, it is clear the impact of the addition of LiTFSI in the methylated IL, diminishing the interface resistance values. The fit of the spectra allows to plot the evolution of the electrolyte and interface resistances, depicted in Figure 3.21.

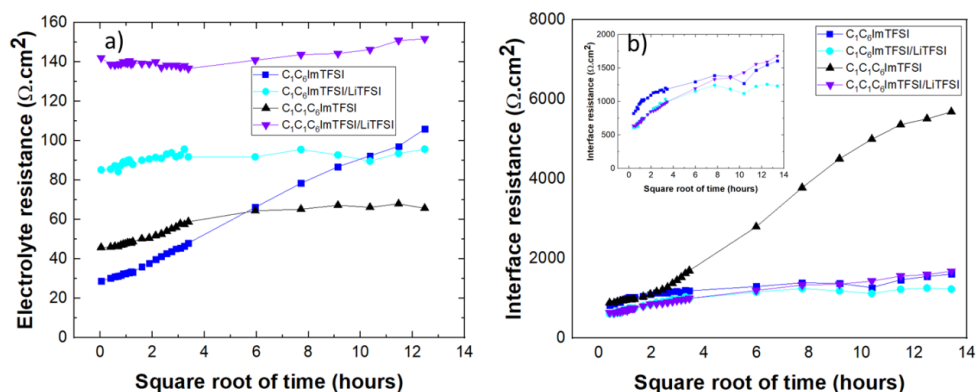


Figure 3.21 Evolution as a function of time of a) electrolyte resistance, and b) fresh SEI resistance for the systems $C_1C_6\text{ImTFSI}$ and $C_1C_1C_6\text{ImTFSI}$.

With regards to the previous study of the electrolyte stability, the R_{el} of the cell containing $C_1C_1C_6ImTFSI$ seems to be stable than $C_1C_6ImTFSI$ in spite of an increase of R_{el} in the first 12h.

Considering the R_{el} (Figure 3.21-a), the addition of LiTFSI salt stabilizes R_{el} , whatever the electrolyte composition, as highlighted in the previous section.

Regarding the evolution of R_{fresh} , shown in Figure 3.21-c, when neat IL $C_1C_1C_6ImTFSI$ is used, R_{fresh} is higher and evolves quickly than with $C_1C_6ImTFSI$ during the first 12h before stabilization. This result evidenced that the methylation of the C2 carbon induces the formation of a different passivation layer, much more resistive, than with the protonated ring.

XPS recorded spectra of the separators and lithium electrodes in contact with $C_1C_1C_6ImTFSI$ and $C_1C_1C_6ImTFSI/LiTFSI$ are depicted in Figure 3.22.

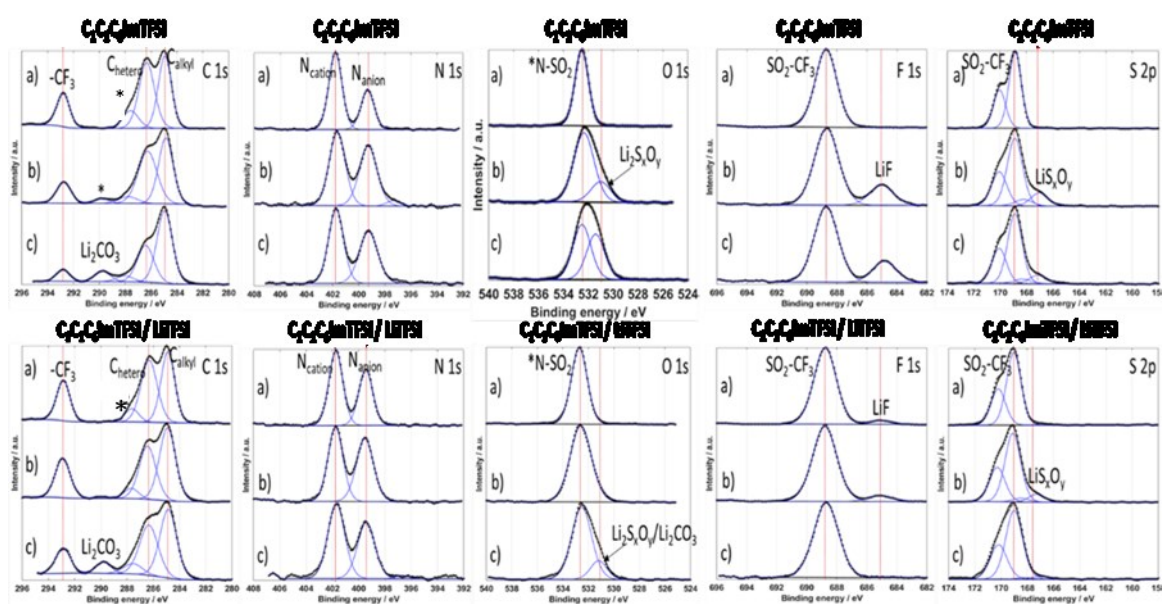


Figure 3.22 XPS core levels registered at the surface of (a) neat IL based electrolytes, (b) on separator and (c) on lithium electrode surface.

Regarding the separators Figure 3.22-b, the analysis of the spectrum corresponding to the neat IL $C_1C_1C_6ImTFSI$ exhibits some important differences with respect to the reference. Concerning the cation, the spectrum of C1s shows that the peak * at 287 eV associated to the methyl radical has slightly diminish its concentration. For the case of the N1s core level, the peak corresponding to N_{cation} has suffered a slight widening,

whereas the N_{anion} peak has increase its intensity. Although the changes in the spectra of the separators and of the IL reference are weaker compared to the neat $C_1C_6\text{ImTFSI}$, a slight instability of the $C_1C_1C_6\text{Im}^+$ cation is noticed. Moreover, a degradation of TFSI leads to the formation of LiF and $\text{Li}_2\text{S}_x\text{O}_y$ in a significant concentration.

In conclusion, regarding the fresh layer formed at the lithium surface, the neat $C_1C_1C_6\text{ImTFSI}$ suffers from a different mechanism of degradation than the neat $C_1C_6\text{ImTFSI}$. For the methylated IL, the cation suffers a degradation that probably forms organic products that are not soluble in the IL (such in the case of $C_1C_6\text{ImTFSI}$) but precipitates on the lithium surface increasing significantly the interface resistance as it has been observed by EIS measurements. In addition, the anion TFSI suffers also a strong degradation with the formation of LiF and $\text{Li}_2\text{S}_x\text{O}_y$.

A different situation is observed for the case of the $C_1C_1C_6\text{ImTFSI/LiTFSI}$ electrolyte. From the analysis of the separator, the new peaks of C1s and N1s are similar to the reference. Only few concentrations of LiF and $\text{Li}_2\text{S}_x\text{O}_y$ can be detected as a consequence of the degradation of the TFSI anion. However, the analysis of the lithium electrode exhibit peaks very similar to the neat IL without the presence of inorganic decomposition byproducts except by the presence of the Li_2CO_3 from the native layer. In any case, the results suggest an improved stability of the anion TFSI in this case or the presence of different decomposition byproducts of organic nature.

3.3.2. The effect of the additives

The evolutions of the impedance spectra for the case of $C_1C_6\text{ImTFSI/LiTFSI}$ with and without additives are shown in Figure 3.23. In the previous section it was demonstrated a good correlation of the characteristic frequencies of $C_1C_6\text{ImTFSI/LiTFSI}$ and $C_1C_1C_6\text{ImTFSI/LiTFSI}$. For the case with additives, the electrolytes doped with VC and FEC exhibit almost the same characteristic frequencies that are slightly higher than the case without additive. Moreover, the impedance values for the case of the electrolytes doped with VC or FEC are clearly inferior.

From this simple observation of the characteristic frequencies, it is possible to predict a different chemical evolution of the systems contained only IL + LiTFSI and the systems doped with additives.

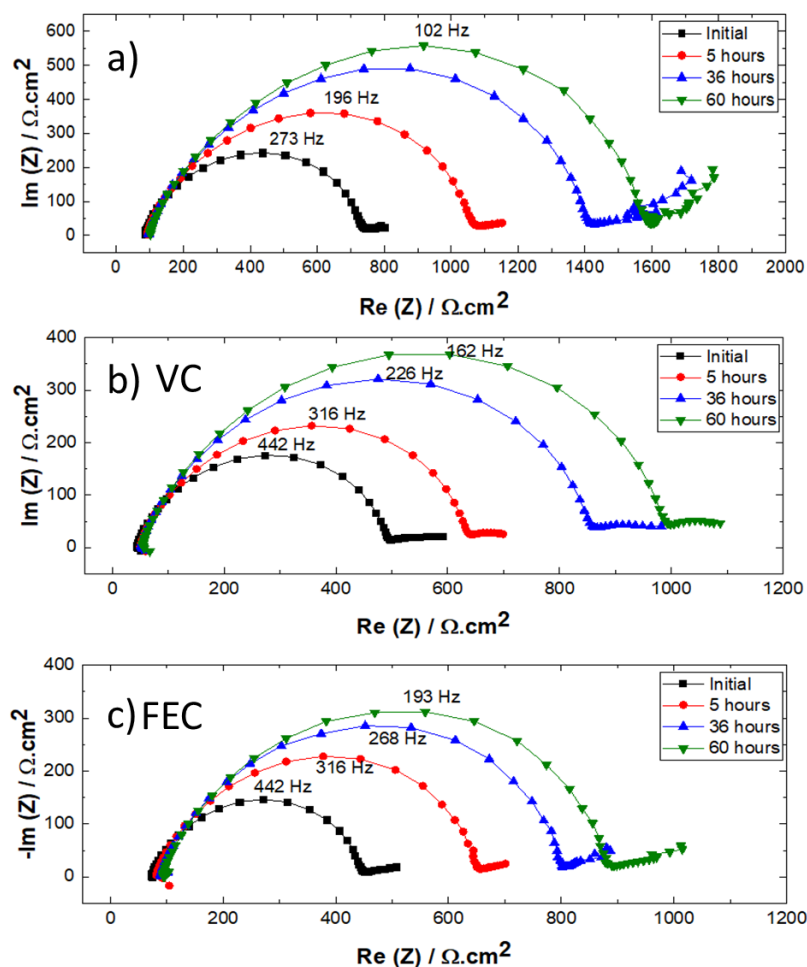


Figure 3.23 Evolution of the impedance response as a function of time measured at OCV at 295 K for Li/Li coin cells containing: a) $C_1C_6ImTFSI/LiTFSI$, b) $C_1C_6ImTFSI/LiTFSI/VC$ and c) $C_1C_1C_6ImTFSI/LiTFSI/FEC$.

In Figure 3.24, the evolutions of R_{el} and R_{fresh} have been plotted. In general, all the combinations of electrolytes are stable or the increase of the R_{el} values is very slow as a function of the time. It is clear, that the values of R_{el} diminishes in the presence of additives, in special VC, which is in agree with the ionic conductivity measurements (chapter 2).

For the interfaces, the additives lower the R_{fresh} values. Nonetheless, the R_{fresh} corresponding to the electrolyte doped with VC is continuously increasing, whereas for the case of FEC the values or R_{fresh} exhibit a very slow evolution after 36 h.

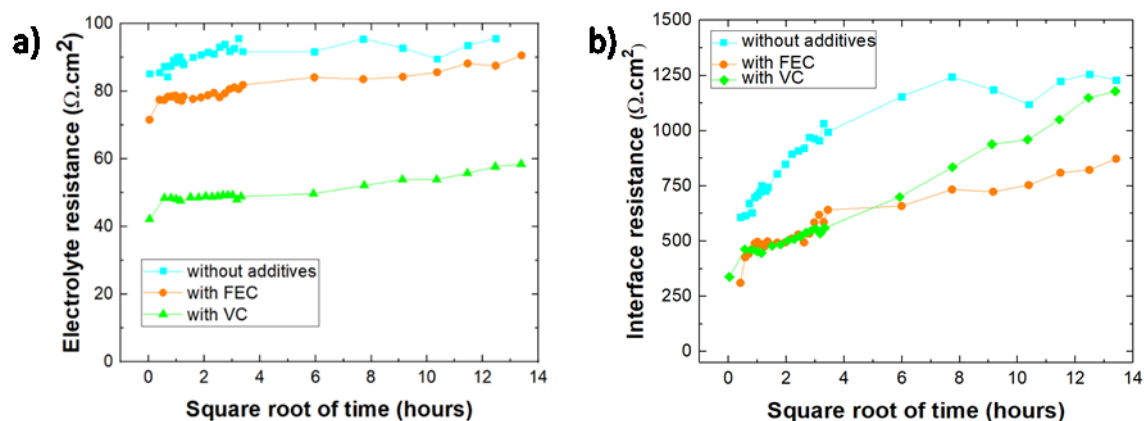


Figure 3.24 Evolution as a function of time of a) electrolyte resistance, and b) fresh SEI resistance for the system $C_1C_6ImTFSI/LiTFSI$ without any additive and doped with VC and FEC.

The corresponding XPS analysis of the separators and lithium electrodes for Li/Li coin cells containing electrolytes doped with VC and FEC, are shown in Figure 3.25. For both of the cases, no significant variations between the peaks of the separators and the peaks of the pristine references are observed, suggesting an excellent stability of the electrolytes doped with these solvents. This could be related with the formation of new types of complexes such as $[Li(TFSI)_{3.5}(VC)_{0.5}]^m$.⁴⁵

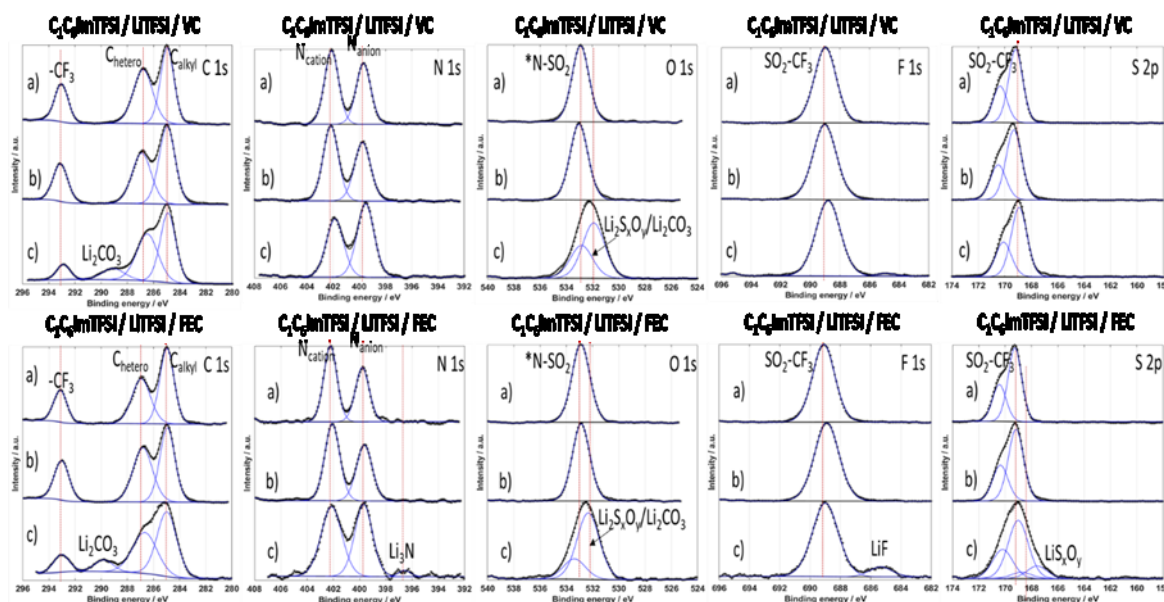


Figure 3.25 XPS core levels registered at the surface of (a) neat IL based electrolytes, (b) on separator and (c) on lithium electrode surface.

For the case of the lithium electrodes, the situation is in principle similar to the case of $C_1C_6ImTFSI/LiTFSI$, with a very scarcely formation of LiF and LiS_xO_y byproducts. This results contrasts with the well-known affirmation that these solvents are decomposed forming LiF .⁴⁴ However, the degradation of VC/FEC occurs typically at 0.8-0.9 V vs. Li^+/Li . In contrast, it is possible to notice other kind of variations in the core level peaks.

For the C1s core level, we notice that the peaks at ~ 290 eV commonly associated to Li_2CO_3 are asymmetrical for both of the cases VC and FEC. Moreover, the peak at 286.7 eV associated to the carbons C_{hetero} is wider and more intense than in the references. Note also the widening of the peaks of O1s and F1s. All these observations suggest the formation of new decomposition byproducts of organic nature (Figure 3.26) that are responsible for the decrease of the interface resistance when adding VC or FEC.

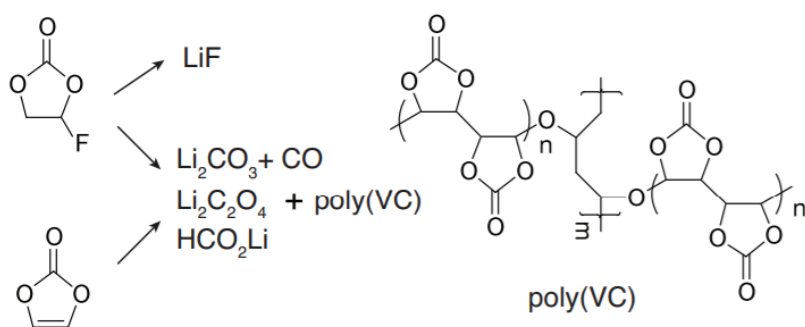


Figure 3.26 Schema of the probable reduction byproducts of the vinylene and fluoroethylene carbonate. A possible structure for a crosslinking site of poly(VC) is indicated.⁴⁶

3.4. Conclusions

The interaction between lithium metal and two different imidazolium-based ionic liquids $C_1C_6ImTFSI$ and C_1C_6ImFSI , neat and laden with 1 mol.L^{-1} of $LiTFSI$ in symmetric Li/Li coin cell systems has been studied at the OCV by EIS and XPS coupled study.

The bulk electrolyte resistance of both neat ILs was found to be not stable in contact of lithium surface even in the OCV condition, mainly in the case of neat $C_1C_6ImTFSI$. The changes in the IL resistivity upon aging followed by EIS, was related to the presence of soluble byproduct of the IL decomposition and especially of the cation imidazolium onto the lithium surface. This has been confirmed by the XPS analyses performed at the

surface of the separators after cell disassembling which evidenced the presence of $C_1C_6Im^+$ degradation products, especially in the case of neat $C_1C_6ImTFSI$.

In both ILs, the addition of LiTFSI induces stabilization of the bulk electrolyte resistance and the disappearance of the cation degradation byproduct. The increase of TFSI/ $C_1C_6Im^+$ ratio seems to play the role of charge screening around the cation constituting the IL. This result was reported by several authors, showing that upon LiTFSI addition, the local reorganizations of the IL lead to the formation of negative $Li(TFSI)_2$ complexes, protecting the cation from complexation and/or decomposition.

In all combinations, XPS analyses on the lithium surface show the deposition of thin layers of inorganic and organic byproducts resulting from the anion and cation decomposition giving rise to the deposition of mainly LiF, $Li_2S_xO_y$ and organic species resulting from cation decomposition N-heterocyclic carbenes. In parallel, the slope of the interfacial resistance evolution as function of time at OCV seems to be characteristic of the anion type with a more pronounced slope when the combination contains TFSI rather than FSI. Especially, in case of FSI the presence of LiF byproducts is observed and it seems to favor the formation of a more homogeneous and less resistive passive layer.

Similar results were obtained with electrolytes modified either by the addition of methyl group in the C2 position of imidazolium cation or in the presence of an organic additive VC or FEC. However, in both cases a higher protection from further decomposition of cation in contact to lithium electrode is evidenced.

In conclusion, our results contribute to highlight the major impact of the nature of the anion and of the presence of lithium salt in the electrolyte to design robust electrolytes able to produce stable and protecting SEI avoiding continuous decomposition of the bulk electrolyte.

REFERENCES

- (1) Xu, W.; Wang, J.; Ding, F.; Chen, X.; Nasybulin, E.; Zhang, Y.; Zhang, J.-G. Lithium Metal Anodes for Rechargeable Batteries. *Energy Environ. Sci.* **2014**, 7 (2), 513–537.
- (2) Takeda, Y.; Yamamoto, O.; Imanishi, N. Lithium Dendrite Formation on a Lithium Metal Anode from Liquid, Polymer and Solid Electrolytes. *Electrochemistry* **2016**, 1994–1995.

- (3) Peled, E. The Electrochemical-Behavior of Alkali and Alkaline-Earth Metals in Non-Aqueous Battery Systems - the Solid Electrolyte Interphase Model. *J. Electrochem. Soc.* **1979**, 126 (12), 2047–2051.
- (4) Cheng, X.-B.; Zhang, R.; Zhao, C.-Z.; Zhang, Q. Toward Safe Lithium Metal Anode in Rechargeable Batteries: A Review. *Chem. Rev.* **2017**, 117 (15), 10403-10473.
- (5) Lin, D.; Liu, Y.; Cui, Y. Reviving the Lithium Metal Anode for High-Energy Batteries. *Nat. Publ. Gr.* **2017**, 12 (3), 194–206.
- (6) Bhatt, a. I.; Kao, P.; Best, a. S.; Hollenkamp, a. F. Understanding the Morphological Changes of Lithium Surfaces during Cycling in Electrolyte Solutions of Lithium Salts in an Ionic Liquid. *J. Electrochem. Soc.* **2013**, 160 (8), A1171–A1180.
- (7) Sacci, R. L.; Dudney, N. J.; More, K. L.; Parent, L. R.; Arslan, I.; Browning, N. D.; Unocic, R. R. Direct Visualization of Initial SEI Morphology and Growth Kinetics during Lithium Deposition by in Situ Electrochemical Transmission Electron Microscopy. *Chem. Commun.* **2014**, 50, 2104.
- (8) Zeng, Z.; Liang, W. I.; Liao, H. G.; Xin, H. L.; Chu, Y. H.; Zheng, H. Visualization of Electrode-Electrolyte Interfaces in LiPF₆/EC/DEC Electrolyte for Lithium Ion Batteries via in Situ TEM. *Nano Lett.* **2014**, 14 (4), 1745–1750.
- (9) Cohen, Y. S.; Cohen, Y.; Aurbach, D. Micromorphological Studies of Lithium Electrodes in Alkyl Carbonate Solutions Using in Situ Atomic Force Microscopy. *J. Phys. Chem. B* **2000**, 104 (51), 12282–12291.
- (10) Aurbach, D.; Weissman, I.; Zaban, A.; Chusid, O. Correlation between Surface Chemistry, Morphology, Cycling Efficiency and Interfacial Properties of Li Electrodes in Solutions Containing Different Li Salts. *Electrochim. Acta* **1994**, 39 (1), 51–71.
- (11) Girard, G. M. A.; Hilder, M.; Dupre, N.; Guyomard, D.; Nucciarone, D.; Whitbread, K.; Zavorine, S.; Moser, M.; Forsyth, M.; MacFarlane, D. R.; et al. Spectroscopic Characterization of the SEI Layer Formed on Lithium Metal Electrodes in Phosphonium Bis(Fluorosulfonyl)Imide Ionic Liquid Electrolytes. *ACS Appl. Mater. Interfaces* **2018**, 10 (7), 6719–6729.
- (12) Grissa, R.; Fernandez, V.; Fairley, N.; Hamon, J.; Stephant, N.; Rolland, J.; Bouchet, R.; Lecuyer, M.; Deschamps, M.; Guyomard, D.; et al. XPS and SEM-EDX Study of Electrolyte Nature Effect on Li Electrode in Lithium Metal Batteries. *ACS Appl. Energy Mater.* **2018**, 1 (10), 5694–5702.
- (13) Aurbach, D.; Zaban, A. Impedance Spectroscopy of Lithium Electrodes. *J. Electroanal. Chem.* **1993**, 348 (1–2), 155–179.
- (14) Howlett, P. C.; Brack, N.; Hollenkamp, a. F.; Forsyth, M.; MacFarlane, D. R. Characterization of the Lithium Surface in N-Methyl-N-Alkylpyrrolidinium Bis(Trifluoromethanesulfonyl)Amide Room-Temperature Ionic Liquid Electrolytes. *J. Electrochem. Soc.* **2006**, 153 (3), A595.
- (15) Budi, A.; Basile, A.; Opletal, G.; Hollenkamp, A. F.; Best, A. S.; Rees, R. J.; Bhatt, A. I.; O'Mullane, A. P.; Russo, S. P.; Imide, P. F.; et al. Study of the Initial Stage of Solid Electrolyte Interphase Formation upon Chemical Reaction of Lithium Metal and N-Methyl-N-Propyl-Pyrrolidinium-Bis(Fluorosulfonyl)Imide. *J. Phys. Chem. C* **2012**, 116 (37), 19789–19797.
- (16) Basile, A.; Bhatt, A. I.; O'Mullane, A. P. Stabilizing Lithium Metal Using Ionic Liquids for Long-Lived Batteries. *Nat. Commun.* **2016**, 7 (11794), 1–11.
- (17) Olschewski, M.; Gustus, R.; Höfft, O.; Lahiri, A.; Endres, F. Monochromatic X-Ray

- Photoelectron Spectroscopy Study of Three Different Ionic Liquids in Interaction with Lithium-Decorated Copper Surfaces. *J. Phys. Chem. C* **2017**, 121 (5), 2675–2682.
- (18) Sowmiah, S.; Srinivasadesikan, V.; Tseng, M. C.; Chu, Y. H. On the Chemical Stabilities of Ionic Liquids. *Molecules* **2009**, 14 (9), 3780-813.
- (19) Schmitz, P.; Jakelski, R.; Pyschik, M.; Jalkanen, K.; Nowak, S.; Winter, M.; Bieker, P. Decomposition of Imidazolium-Based Ionic Liquids in Contact with Lithium Metal. *ChemSusChem* **2017**, 10 (5), 876–883.
- (20) Srour, H.; Rouault, H.; Santini, C. C. Study on Cycling Performance and Electrochemical Stability of 1-Hexyl-3-Methylimidazolium Bis(Trifluoromethanesulfonyl)Imide Assembled with $\text{Li}_4\text{Ti}_5\text{O}_{12}$ and LiFePO_4 at 333 K. *J. Electrochem. Soc.* **2013**, 160 (6), A781–A785.
- (21) Thevenin, J.; Muller, R. Impedance of Lithium Electrodes in a Propylene Carbonate Electrolyte. *J. Electrochem. Soc.* **1987**, 134 (2), 273–280.
- (22) Peled, E. Advanced Model for Solid Electrolyte Interphase Electrodes in Liquid and Polymer Electrolytes. *J. Electrochem. Soc.* **1997**, 144 (8), L208.
- (23) Aurbach, D. Review of Selected Electrode-Solution Interactions Which Determine the Performance of Li and Li Ion Batteries. *J. Power Sources* **2000**, 89 (2), 206–218.
- (24) Bouchet, R.; Lascaud, S.; Rosso, M. An EIS Study of the Anode Li/PEO-LiTFSI of a Li Polymer Battery. *J. Electrochem. Soc.* **2003**, 150 (10), A1385–A1389.
- (25) Barrande, M.; Bouchet, R.; Denoyel, R. Tortuosity of Porous Particles. *Anal. Chem.* **2007**, 79 (23), 9115–9121.
- (26) Yazami, R.; Reynier, Y. F. Mechanism of Self-Discharge in Graphite-Lithium Anode. *Electrochim. Acta* **2002**, 47 (8), 1217–1223.
- (27) Aurbach, D.; Zaban, A. Impedance Spectroscopy of Lithium Electrodes. *J. Electroanal. Chem.* **1994**, 367 (1–2), 15–25.
- (28) Bouchet, R. Batteries: A Stable Lithium Metal Interface. *Nat. Nanotechnol.* **2014**, 9 (August), 1–2.
- (29) Gon, H. B.; Veeraiyah, N. Dielectric Properties of LiF Single Crystals. *J. Mater. Sci.* **1981**, 16 (9), 2571–2574.
- (30) Younesi, R.; Hahlin, M.; Roberts, M.; Edström, K. The SEI Layer Formed on Lithium Metal in the Presence of Oxygen: A Seldom Considered Component in the Development of the Li-O₂ Battery. *J. Power Sources* **2013**, 225, 40–45.
- (31) Ghazi, Z. A.; Sun, Z.; Sun, C.; Qi, F.; An, B.; Li, F.; Cheng, H. M. Key Aspects of Lithium Metal Anodes for Lithium Metal Batteries. *Small* **2019**, 1900687, 1–26.
- (32) Philippe, B.; Hahlin, M.; Edstrom, K.; Gustafsson, T.; Siegbahn, H.; Rensmo, H. Photoelectron Spectroscopy for Lithium Battery Interface Studies. *J. Electrochem. Soc.* **2016**, 163 (2), A178–A191.
- (33) Lovelock, K. R. J.; Villar-Garcia, I. J.; Maier, F.; Steinrück, H. P.; Licence, P. Photoelectron Spectroscopy of Ionic Liquid-Based Interfaces. *Chem. Rev.* **2010**, 110 (9), 5158–5190.
- (34) Cremer, T.; Kolbeck, C.; Lovelock, K. R. J.; Paape, N.; Wölfel, R.; Schulz, P. S.; Wasserscheid, P.; Weber, H.; Thar, J.; Kirchner, B.; et al. Towards a Molecular Understanding of Cation-Anion Interactions-Probing the Electronic Structure of Imidazolium Ionic Liquids by NMR Spectroscopy, X-Ray Photoelectron Spectroscopy

- and Theoretical Calculations. *Chem. - A Eur. J.* **2010**, 16 (30), 9018–9033.
- (35) Aydogan Gokturk, P.; Salzner, U.; Nyulászi, L.; Ulgut, B.; Kocabas, C.; Suzer, S. XPS-Evidence for in-Situ Electrochemically-Generated Carbene Formation. *Electrochim. Acta* **2017**, 234, 37–42.
- (36) Aurbach, D.; Weissman, I.; Schechter, A.; Cohen, H. X-Ray Photoelectron Spectroscopy Studies of Lithium Surfaces Prepared in Several Important Electrolyte Solutions. A Comparison with Previous Studies by Fourier Transform Infrared Spectroscopy. *Langmuir* **1996**, 12 (16), 3991–4007.
- (37) Sun, Y.; Xin, N.; Prausnitz, J. M. Solubilities of Five Lithium Salts in 1-Butyl-3-Methylimidazolium Dicyanamide and in 1-Butyl-3-Methylimidazolium Tetrafluoroborate from 298.15 to 343.15 K. *J. Chem. Eng. Data* **2018**, 63 (12), 4524–4531.
- (38) Choudhury, S.; Archer, L. Lithium Fluoride Additives for Stable Cycling of Lithium Batteries at High Current Densities. *Adv. Electron. Mater.* **2016**, 2 (2), 1500246.
- (39) Aurbach, D.; Zaban, A.; Ein-Eli, Y.; Weissman, I.; Chusid, O.; Markovsky, B.; Levi, M.; Levi, E.; Schechter, A.; Granot, E. Recent Studies on the Correlation between Surface Chemistry, Morphology, Three-Dimensional Structures and Performance of Li and Li-C Intercalation Anodes in Several Important Electrolyte Systems. *J. Power Sources* **1997**, 68 (1), 91–98.
- (40) Cao, R.; Chen, J.; Han, K. S.; Xu, W.; Mei, D.; Bhattacharya, P.; Engelhard, M. H.; Mueller, K. T.; Liu, J.; Zhang, J. G. Effect of the Anion Activity on the Stability of Li Metal Anodes in Lithium-Sulfur Batteries. *Adv. Funct. Mater.* **2016**, 26 (18), 3059–3066.
- (41) Miao, R.; Yang, J.; Feng, X.; Jia, H.; Wang, J.; Nuli, Y. Novel Dual-Salts Electrolyte Solution for Dendrite-Free Lithium-Metal Based Rechargeable Batteries with High Cycle Reversibility. *J. Power Sources* **2014**, 271, 291–297.
- (42) Böhm, V. P. W.; Herrmann, W. A. The “Wanzlick Equilibrium.” *Angew. Chemie - Int. Ed.* **2000**, 39 (22), 4036–4038.
- (43) Bonhôte, P.; Dias, A.-P.; Armand, M.; Papageorgiou, N.; Kalyanasundaram, K.; Grätzel, M. Hydrophobic, Highly Conductive Ambient-Temperature Molten Salts. *Inorg. Chem.* **1996**, 35 (5), 1168–1178.
- (44) Zhang, S. S. Problem, Status, and Possible Solutions for Lithium Metal Anode of Rechargeable Batteries. *ACS Appl. Energy Mater.* **2018**, 1 (3), 910–920.
- (45) Bolimowska, E.; Castiglione, F.; Devemy, J.; Rouault, H.; Mele, A.; Pádua, A. A. H.; Santini, C. C. Investigation of Li⁺ Cation Coordination and Transportation, by Molecular Modeling and NMR Studies, in a LiNTf₂-Doped Ionic Liquid-Vinylene Carbonate Mixture. *J. Phys. Chem. B* **2018**, 22(36), 8560–8569.
- (46) Michan, A. L.; Parimalam, B. S.; Leskes, M.; Kerber, R. N.; Yoon, T.; Grey, C. P.; Lucht, B. L. Fluoroethylene Carbonate and Vinylene Carbonate Reduction: Understanding Lithium-Ion Battery Electrolyte Additives and Solid Electrolyte Interphase Formation. *Chem. Mater.* **2016**, 28 (22), 8149–8159.

CHAPTER 4: Behavior of the ionic liquid based electrolytes in contact with lithium metal under polarization

This chapter begins with a detailed study of the electrochemical window of the IL based electrolytes. The reduction and oxidation limits respect to the Li^+/Li reference are reviewed. The degradation byproducts formed during the reduction cycle at potentials of 1 V and 0.5 V vs. Li^+/Li are analyzed by XPS.

Then, the evolution of the cell potential during the application of different current densities to symmetrical Li/Li coin cells was studied. Two different regimes of lithium dendrite formation were evidenced and discussed using the Chazalviel's model. The EIS measurement, allowed us to extract the transport numbers with comparison to NMR based results.

In addition to the study of the transport properties, the chemical composition of the SEI during polarization for the different electrolyte combinations was revealed by XPS and compared with the performances of the studied cells.

4.1.	Introduction	117
4.2.	Electrochemical window of the IL-based electrolytes	118
4.2.1.	Literature review	118
4.2.2.	IL-based electrolytes behavior under oxidation	120
4.2.3.	Effect of the additives and the cations.....	122
4.2.4.	Behavior of the IL-based electrolytes under reduction	126
4.2.5.	Performances of the IL-based electrolytes below 0 V vs. Li^+/Li	128
4.5.	Study by XPS of the reduction of the system lithium/copper	129
4.6.	The Li/Li system under the application of an electrical current.....	136
4.6.1.	Experimental part	136
4.6.2.	The Chazalviel's model.....	137
4.6.3.	Experimental verification of the inverse-square law $\tau \propto 1/J^2$	141
4.6.4.	Transport properties of the electrolytes.....	146
4.7.	<i>Post-mortem</i> XPS analysis of the cells after chronopotentiometry.....	151
4.8.	SEM/AES analyses of the electrodes after chronopotentiometry	155
4.8.1.	The regime of divergence of the potential.....	155
4.8.2.	The regime of short-circuits	157
4.9.	Conclusions	159

4.1. Introduction

The performance of the lithium metal batteries (LMB) are affected by two main problems, the loss of capacity during repeated cycles of charge/discharge (low Coulombic efficiency) and the formation of dendrites.¹⁻⁴

Regarding these problems, the selection of high-voltage cathode materials for LMB with high power density is limited stability of the electrochemical window (EW) of conventional electrolytes. To avoid the electrolyte oxidation or reduction, at the anode and the cathode electrodes, respectively, it is suitable to widen the electrochemical window of the selected electrolyte.

It has been signaled that the EW of the ILs is in a broad range typically spanning 4.5 V and wider.⁵⁻⁷ This electrochemical property is of great importance because of the growing interest for cathode materials working at potential higher than 4.4 V vs. Li^+/Li and the revived interest in the lithium metal anode.^{1,8,9} Therefore, the blocking point to achieve high voltage lithium based accumulator is the reactivity of lithium metal toward the electrolytic media. Nonetheless, there is a need of a better understanding of ILs based electrolyte surface reactivity in lithium metal batteries (LMB) and therefore lithium dendrite growth mechanism in such media.

Several strategies have been designed for overcome the dendrite growth in LMB.^{10,11} However, most of the studies carried out in ILs based electrolytes/lithium metal system do not correlate properly the transport properties of the electrolytes with the dendrite growth.¹²⁻¹⁴ Besides, the Chazalviel's model¹⁵ establish a correlation between the onset time of dendrite formation, the current density that crosses the system and the transport properties of the electrolyte. This model has been tested in lithium metal polymer cells with relative success in spite of its simplicity.¹⁶⁻¹⁸

Hence this chapter will be dedicated to study two main aspects in LMB using ILs as electrolyte, the electrolyte stability and the dendrite growth process. Therefore, in the first part of this chapter the electrochemical window of the IL-based electrolytes will be evaluated with special attention to the reduction and oxidation processes happening even at low current density ($< 5 \mu\text{A}\cdot\text{cm}^{-2}$). The performance of the IL based electrolyte during

lithium plating/stripping process will be discussed using copper/lithium and stainless steel/lithium half-cells. The chemical composition of the degradation byproducts of the electrolytes during the first cycle of reduction will be determined by XPS.

In the second part, we will focus on the correlation between the electrolyte composition and the dendrite growth at different current densities. The different regimes of dendrite formation will be studied and compared in the framework of EIS in comparison with NMR measurements in term of the transport number and diffusion coefficients of the electrolytes. The shape and the surface chemistry around the dendrite will be discussed based on XPS and SEM/AES study.

It is largely accepted that the formation of a homogeneous SEI limit the formation of dendrites.^{4,19} The role of the additives such as vinylene carbonate (VC) and fluoroethylene carbonate (FEC) is preponderant in the improvement of the SEI properties.^{20–22}

In the last part of this chapter, the correlation between, the SEI properties formed on both side electrodes, positive and negative in Li/Li coin cell after the dendrite growth will be discussed based on XPS and SEM/AES study.

4.2. Electrochemical window of the IL-based electrolytes

4.2.1. Literature review

The main care to correctly measure the EW of the electrolytes concerns the choice of the right electrodes to perform the voltammetry measurements. Tułodziecki *et al.*²³ have demonstrated several differences in the CVs of C₁C₂ImTFSI with 0.12 mol.L⁻¹ LiTFSI when using stainless steel, platinum and glassy carbon as WE due to the specific electrocatalytic effects, depending on the surface chemistry of the electrodes. Furthermore, the choice of the cathodic and anodic limits of reduction and oxidation must be established in an electrochemical standard instead of an arbitrary choice.

The reported data in the literature, regarding all of these criteria, do not provide a uniformity in the reported data. In the Table 4.1, some results from literature in ILs electrolyte EW have been selected, showing the differences on the reference electrodes

and the criterion to establish the EW limits. Some of this data have been referenced to the ferrocene couple potential Fc^+/Fc which most of the authors report at a potential of + 400 mV vs. SHE (standard hydrogen electrode).^{24,25} In this work, all the potential will be referenced to the Li^+/Li couple (-3.04 V vs. SHE).²⁶

Table 4.1 Electrochemical window of selected ILs and electrolytes.

Electrolyte	Cathodic limit (V vs. Li^+/Li)	Anodic limit (V vs. Li^+/Li)	E.W.	Reference electrode	T (K)	Scan rate ($\text{mV}\cdot\text{s}^{-1}$)	Current density limit ($\mu\text{A}\cdot\text{cm}^{-2}$)	Reference literature
$\text{C}_1\text{C}_6\text{ImTFSI}$	0.64	5.73	5.09	Ag/AgCl	303	100	-	27
$\text{C}_1\text{C}_6\text{ImTFSI}$ LiTFSI	-0.28	5.83	6.11	Ag/AgCl	303	100	-	27
$\text{C}_1\text{C}_2\text{ImTFSI}$	0.95	5.55	4.6	Pt (I_3^-/I^-)	298	50	1000	28
$\text{C}_1\text{C}_2\text{ImTFSI}$	0.95	5.45	4.5	Pt (I_3^-/I^-)	298	50	1000	28
$\text{Pyr}_{14}\text{TFSI}$	0.83	5.34	4.51	Li	298	5	100	29
$\text{Pyr}_{13}\text{TFSI}$	0.45	5.75	5.3	Pt (I_3^-/I^-)	298	50	1000	28
$\text{Pip}_{13}\text{TFSI}$	0.05	5.95	5.9	Pt (I_3^-/I^-)	298	50	1000	28
$\text{Pip}_{13}\text{TFSI}$	0.25	5.85	5.6	Pt (I_3^-/I^-)	298	50	1000	28

In addition to these results, Schmitz *et al.*³⁰ have performed linear sweep voltammetry (LSV) using nickel as WE and lithium as CE and RE. For the ILs $\text{C}_1\text{C}_2\text{ImTFSI}$, $\text{C}_1\text{C}_4\text{ImTFSI}$ and $\text{Pyr}_{14}\text{TFSI}$ doped with $0.3 \text{ mol}\cdot\text{L}^{-1}$ LiTFSI , they found an electrochemical stability window wider than 5 V ($\text{C}_1\text{C}_2\text{ImTFSI}$: 5.13 V, $\text{C}_1\text{C}_4\text{ImTFSI}$: 5.20 V, $\text{Pyr}_{14}\text{TFSI}$: 5.22 V). The limits were taken when the current density exceeded $100 \mu\text{A}\cdot\text{cm}^{-2}$.

Although, the information reported by all these authors is correct and the results exhibit some similarities. For instance, these ILs are not stable under 0 V vs. Li^+/Li except when they are doped with LiTFSI , and the oxidation limits are higher than 5 V vs. Li^+/Li . Hence the choice of a same reference electrode and an adequate scan rate would help to improve the uniformity of the measurements.

However, in most of the studies published in literature, the criterion on the current density value taken to define the limits of stability in both reduction or oxidation, are above several tens of $\mu\text{A}\cdot\text{cm}^{-2}$ even until $1 \text{ mA}\cdot\text{cm}^{-2}$. This criterion is artificial and does not reflect the thermodynamic stability, because above $1 \mu\text{A}\cdot\text{cm}^{-2}$, one can say that the electrolyte is not stable and is reduced (or oxidized). Indeed, accumulated in the cycle life

of a battery a degradation current as low as $1 \mu\text{A}\cdot\text{cm}^{-2}$ would lead to a large variation of the electrolyte composition, which would strongly shorten the number of cycle. Therefore, from the literature point of view, there is a large discrepancy of values of EWs which need to be rationalized.

Recently, Kerner et al.³¹ have reported studies of stability of IL-based polymers performing LSV at a scan rate of $1 \text{ mV}\cdot\text{s}^{-1}$ and taking into account the reductions and oxidations produced by currents at the order of some $\mu\text{A}\cdot\text{cm}^{-2}$. Their results clearly demonstrate that the reported limits of stability need to be revised (Figure 4.1).

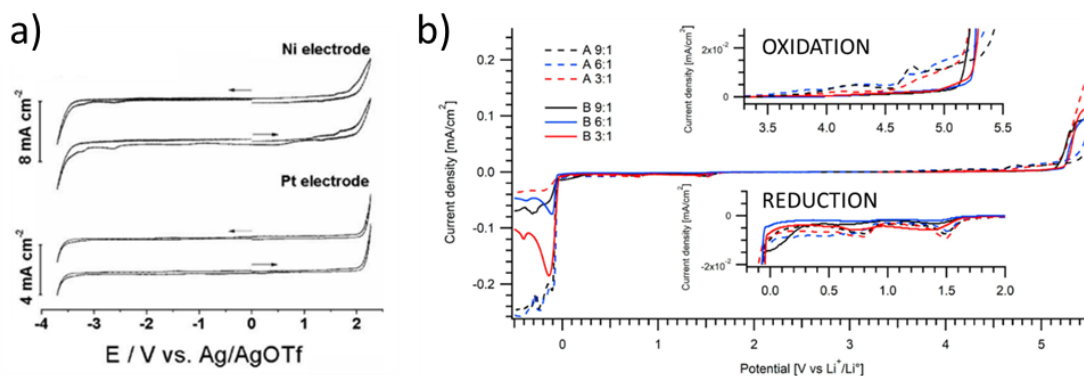


Figure 4.1 a) CV using different references for the IL Pyrr₁₃FSI.¹² Note the high current densities used to establish the stability limits $> 1 \text{ mA}\cdot\text{cm}^{-2}$, which means an EW as high as 6 V. b) LSV measurements performed in IL-based polymers.³¹ Note the oxidation processes starting even at 3.6 V vs. Li^+/Li and the reduction processes at 1.5 V vs. Li^+/Li .

4.2.2. IL-based electrolytes behavior under oxidation

In order to study the behavior of our electrolytes under oxidation, we have chosen to assemble two electrodes coin cells using stainless steel as WE and lithium as CE and RE. The protocol of characterization was described in chapter 2.

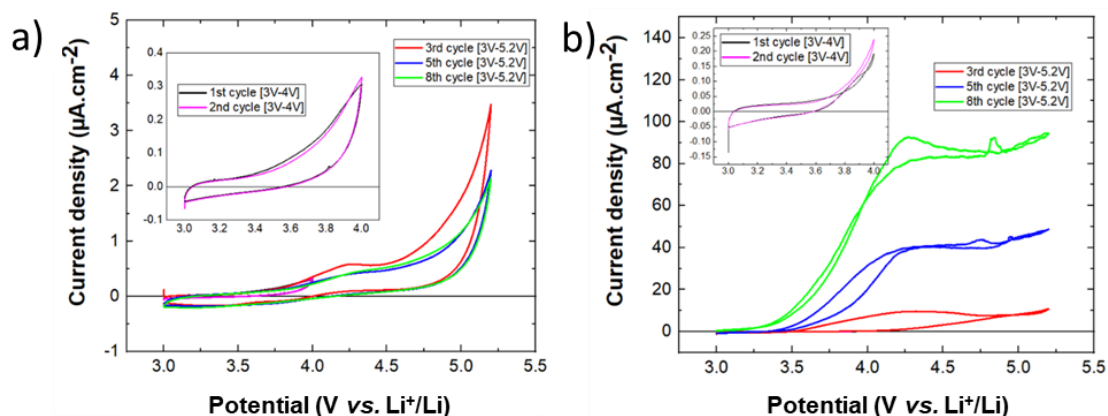


Figure 4.2 The cyclic voltammograms for the C₁C₆ImTFSI/LiTFSI and C₁C₆ImFSI/LiTFSI electrolytes are showed in Figure 4.2, a and b, respectively. For each electrolyte, cells were cycled between 3 V to 4 V vs. Li⁺/Li for the first two cycles, and then between 3 V to 5.2 V vs. Li⁺/Li for the further cycles. The scan rate was low and fixed to 0.1 mV.s⁻¹.

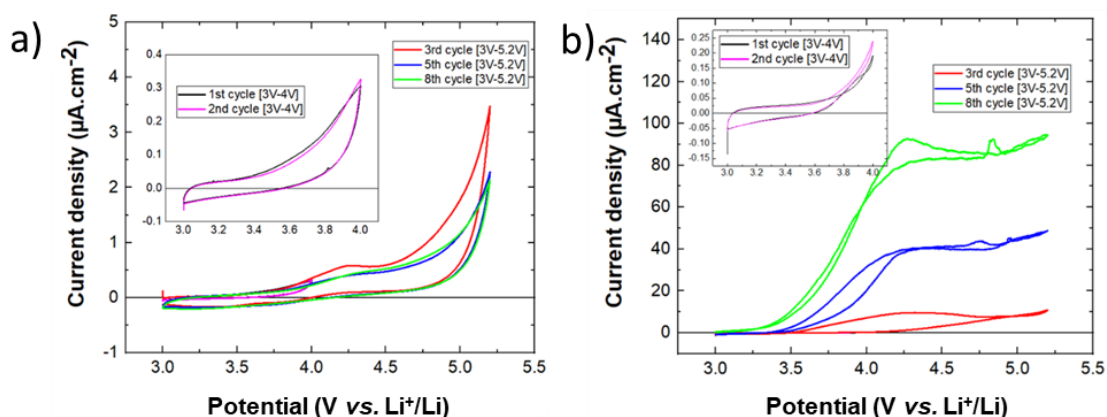


Figure 4.2 Voltammograms from 3 V to 5.2 V vs. Li⁺/Li of a) C₁C₆ImTFSI/LiTFSI and b) C₁C₆ImFSI/LiTFSI. The first two cycles between 3 V to 4 V vs. Li⁺/Li are shown in the inset. W.E: stainless steel, scan rate $\nu = 0.1 \text{ mV}\cdot\text{s}^{-1}$.

The voltammograms show a beginning of oxidation at 3.5 V vs. Li⁺/Li for C₁C₆ImTFSI/LiTFSI and C₁C₆ImFSI/LiTFSI which is lower than the potential values reported in Table 4.1. Besides, the second cycle is almost identical to the first one. Nonetheless, the current densities recorded for the first two cycles are less than 1 $\mu\text{A}\cdot\text{cm}^{-2}$ which most of the authors considered negligible.

For the third and further CVs, extending the sweep up to the cutoff potential of 5.2 V vs. Li⁺/Li, reveals a peak at 4.2 V vs. Li⁺/Li in the case of the IL based on only TFSI anion and an increase of the current density above 4.5 V vs. Li⁺/Li. For this IL, a slight decrease

of the current is observed between the 3rd and the 5th cycle which suggests a slight passivation of the stainless steel surface. In contrast, for the case of C₁C₆ImFSI/LiTFSI the current density increases above 3.5 V *vs.* Li⁺/Li during cycles and reaches a plateau, which demonstrates the continuous IL oxidation of some bulk species that lead to a diffusion limitation current.

These results show that even at potentials lower than 4.0 V *vs.* Li⁺/Li tiny oxidation currents are induced. Beyond this voltage the situation is different, depending on the type of electrolyte, but clearly C₁C₆ImFSI/LiTFSI seems to be not suitable to work with high voltage cathodes.

The effect of the induced oxidation currents can be evaluated by measuring the changes in the electrolyte resistance by PEIS technique performed at OCV after each CV (see Table 4.2). For the case of C₁C₆ImTFSI/LiTFSI, there is a significant evolution of R_{el} after the first cycle, then after continuous cycling the value remains stable. For the FSI based system, the R_{el} is stable when cycling until 4 V *vs.* Li⁺/Li, and increase beyond 5.2 V *vs.* Li⁺/Li. The R_{el} starts to increase confirming the bulk degradation of the C₁C₆ImFSI/LiTFSI. For the ILs studied in this work, we demonstrated that non negligible oxidation processes occurs even before the potentials reported as an anodic limit (typically reported higher than 5.4 V *vs.* Li⁺/Li, Table 4.1).

Table 4.2 Evolution of the electrolyte resistance during CV measurements.

System	R _{el} (Ω.cm ²) Initial	R _{el} (Ω.cm ²) End of 2 nd cycle [3 V, 4 V]	R _{el} (Ω.cm ²) End of 6 th cycle [3 V, 5.2 V]
C ₁ C ₆ ImTFSI/LiTFSI	98	153	150
C ₁ C ₆ ImFSI/LiTFSI	21.6	21.4	32.6

4.2.3. Effect of the additives and the cations

We are interested in knowing the effect of VC and FEC additives as they have been signaled as beneficial for the SEI. Besides, another point of interest in this work is to evaluate the effect of the methylation of the C₁C₆Im⁺ cation. Therefore, a comparison of CVs performed for different systems is shown in Figure 4.3.

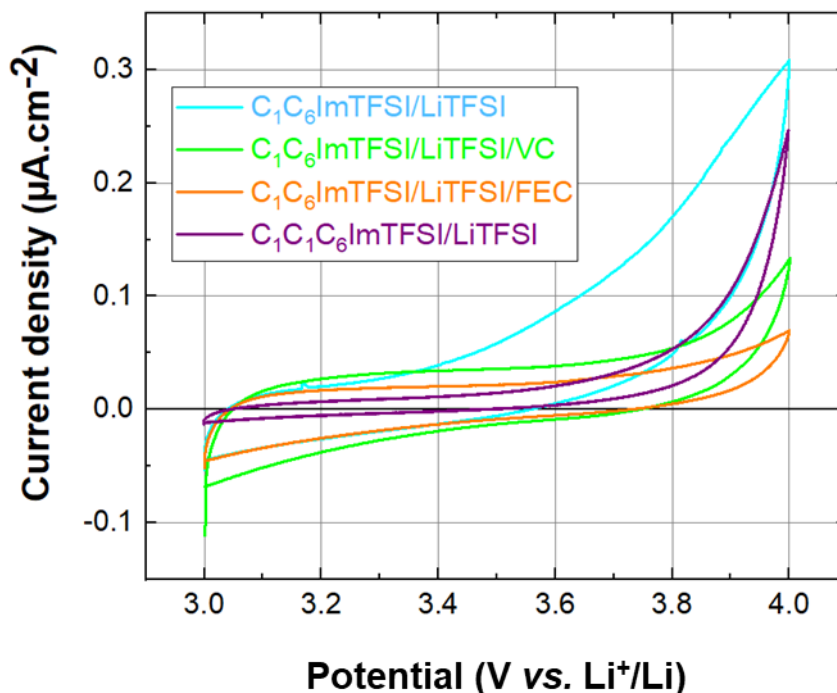


Figure 4.3 Voltammograms of the first cycle performed between 3 V to 4 V vs. Li^+/Li for the electrolytes $\text{C}_1\text{C}_6\text{ImTFSI/LiTFSI}$ and $\text{C}_1\text{C}_1\text{C}_6\text{ImTFSI/LiTFSI}$ with and without additives. W.E: stainless steel, scan rate $\nu = 0.1 \text{ mV}\cdot\text{s}^{-1}$.

Interestingly, even if the order of magnitude of the current densities are similar at 4V vs. Li^+/Li , the oxidation current for $\text{C}_1\text{C}_1\text{C}_6\text{ImTFSI/LiTFSI}$ is slightly lower compared to $\text{C}_1\text{C}_6\text{ImTFSI/LiTFSI}$. For the same current density $0.1 \mu\text{A}\cdot\text{cm}^{-2}$, $\text{C}_1\text{C}_1\text{C}_6\text{ImTFSI/LiTFSI}$ oxidizes 300 mV above than the other electrolyte. Herein, the methylation at the C2 position improves the imidazolium cation stability.

Finally, the addition of VC and FEC strongly reduces the oxidation current and improve the anodic stability. The FEC and VC are generally used to stabilize the negative electrode thanks to the formation of stable and uniform SEIs.^{21,32,33} However, as carbonates, these additives are also known to be stable at least until 4 V vs. Li^+/Li . Therefore, we can deduce that the addition of FEC or VC modifies the structure/composition of the IL, especially at the interface with the stainless steel electrode.

In Figure 4.4 (a) (3rd scan) and (b) (8th scan), the CVs are performed at the potentials [3 V, 5.2 V] vs. Li^+/Li . When additives are used the peak around 4.1 V vs. Li^+/Li disappears, but for all of the electrolytes the current increases above 4.5 V vs. Li^+/Li . In

Figure 4.4 (b), we observe that the current density values have decreased compared with the first scan demonstrating a passivation of the stainless steel electrode. It appears that the $C_1C_1C_6ImTFSI/LiTFSI$ and $C_1C_6ImTFSI/LiTFSI/FEC$ are the most stable at high voltages.

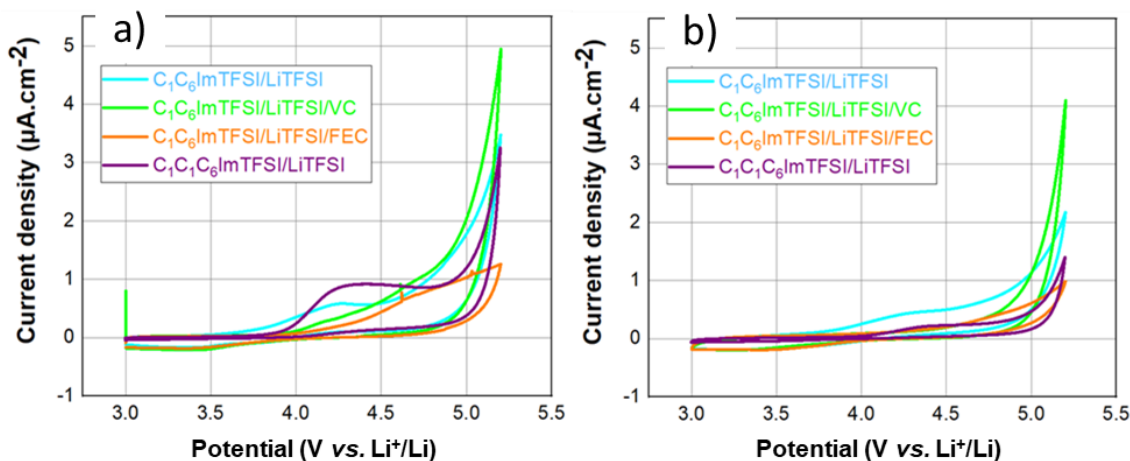


Figure 4.4 Voltammograms of the a) 3rd and b) 8th cycle performed between 3 V to 5.2 V vs. Li^+/Li for the electrolytes $C_1C_6ImTFSI/LiTFSI$ and $C_1C_1C_6ImTFSI/LiTFSI$ with and without additives. W.E: stainless steel, scan rate $v = 0.1 \text{ mV.s}^{-1}$.

Note in Figure 4.4, that only for the electrolytes without additive there is a peak at 4.2 V vs. Li^+/Li (same as seen in Figure 4.2-a). These results suggest that the cation is the first species to be oxidized at this potential, whereas the anion TFSI is oxidized above 4.5 V vs. Li^+/Li . The anodic instability of the cation has been reported by Ong *et al.*³⁴ based on a combination of molecular dynamics (MD) simulations and density functional theory (DFT) calculations. Besides, Xu *et al.*³⁵ have reported an anodic limit for the anion TFSI of 5.3 V vs. Li^+/Li .

The evolutions of the electrolyte resistance are given in Table 4.3. Although $C_1C_1C_6ImTFSI/LiTFSI$ shows an improved passivation at high voltages, the electrolyte resistance is slightly increasing after several cycles. For the case of the electrolyte with VC, R_{el} increases slowly. Finally, the best result is obtained when adding FEC in good accordance with the CV results.

Table 4.3 Evolution of the electrolyte resistance during CV measurements.

System	R_{el} ($\Omega.cm^2$) Initial	R_{el} ($\Omega.cm^2$) End of 2 nd cycle [3 V, 4 V]	R_{el} ($\Omega.cm^2$) End of 8 th cycle [3 V, 5.2 V]
C ₁ C ₆ ImTFSI/LiTFSI	98	153	150
C ₁ C ₆ ImTFSI/LiTFSI/VC	39.4	45.8	48.6
C ₁ C ₆ ImTFSI/LiTFSI/FEC	67.8	69.4	70.2
C ₁ C ₁ C ₆ ImTFSI/LiTFSI	129.2	141.2	146.6

To conclude, we extract the corrosion potential E_{corr} (start of the oxidation) from the polarization curves $\log |i|$ vs. E (Figure 4.5), calculated from the CV data. The corrosion potential is taken at the potential when $\log |i|$ tends to minus infinity. In Table 4.4, we give the values obtained at the first cycle between [3 V, 4 V] vs. Li⁺/Li and the 3rd and 8rd cycles during the scans at [3 V, 5.2 V] vs. Li⁺/Li.

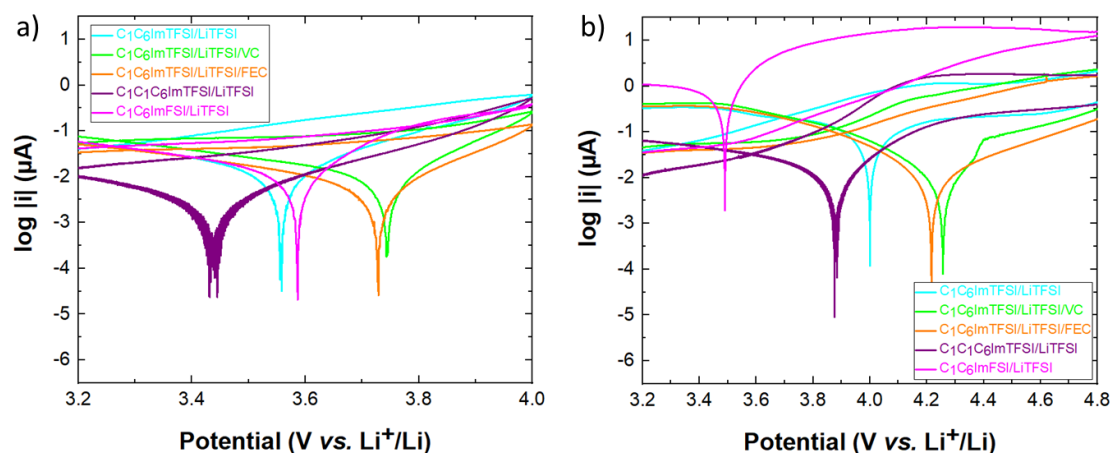


Figure 4.5 $\log |i|$ vs. E plots of de CV recorded at a) the first cycle of oxidation between [3 V, 4 V] vs. Li⁺/Li and b) the third cycle of oxidation between [3 V, 5.2 V] vs. Li⁺/Li

Table 4.4 Oxidation limits for the ILs based electrolytes.

System	E_{corr} 1 st cycle (V vs. Li ⁺ /Li)	E_{corr} 3 rd cycle (V vs. Li ⁺ /Li)	E_{corr} 8 th cycle (V vs. Li ⁺ /Li)
C ₁ C ₆ ImTFSI/LiTFSI	3.5	4.0	4.1
C ₁ C ₆ ImTFSI/LiTFSI/VC	3.7	4.2	4.3
C ₁ C ₆ ImTFSI/LiTFSI/FEC	3.7	4.2	4.2
C ₁ C ₁ C ₆ ImTFSI/LiTFSI	3.4	3.8	4.1
C ₁ C ₁ C ₆ ImFSLi/LiTFSI	3.5	3.4	3.0

4.2.4. Behavior of the IL-based electrolytes under reduction

To study the behavior under reduction, coin cells were assembled using copper as WE and lithium as CE and reference electrode. The coin cells have been cycled firstly between the OCV to 50 mV vs. Li^+/Li to evidence the electrolyte reduction and lately they were cycled between 2 V to 50 mV vs. Li^+/Li . Figure 4.6 shows the voltammograms recorded for $\text{C}_1\text{C}_6\text{ImTFSI}$ and $\text{C}_1\text{C}_6\text{ImFSI}$ doped with LiTFSI.

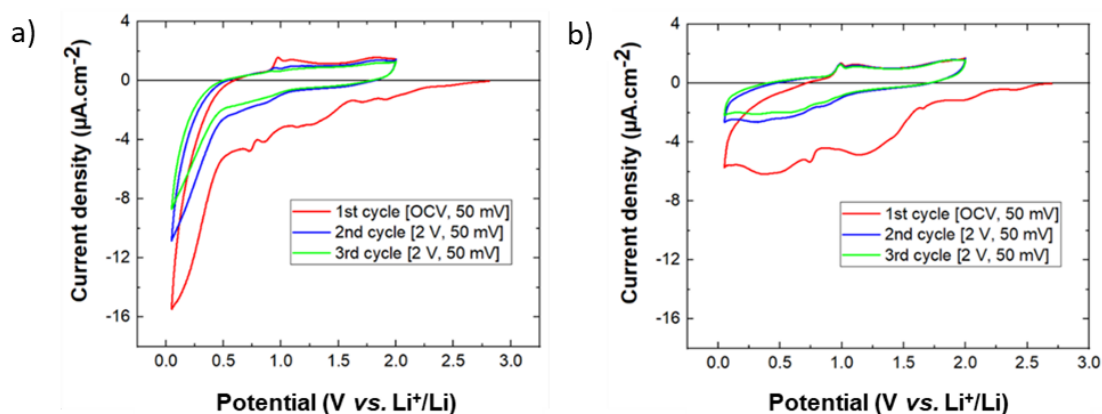


Figure 4.6 Voltammograms for the electrolytes a) $\text{C}_1\text{C}_6\text{ImTFSI}/\text{LiTFSI}$ and b) $\text{C}_1\text{C}_6\text{ImFSI}/\text{LiTFSI}$. W.E: copper, scan rate $v = 0.1 \text{ mV.s}^{-1}$.

The results demonstrate a beginning of reduction at potential below 1.5 V vs. Li^+/Li . In addition, the first cycle exhibits the presence of many peaks (1.2, 0.85 and 0.73 V vs. Li^+/Li) which can be related to the presence of impurities such as water or coming from the eventual degradation of cation or anion. These aspects will be investigated in the next section by XPS.

The origin of these peaks is commonly attributed in the literature to the presence of impurities, mainly water. However, Howlett *et al.*³⁶ have studied the electrochemical reduction of the IL $\text{Pyrr}_{13}\text{TFSI}$. They reported until three peaks denoted C1 around 1.45 V vs. Li^+/Li , C2 around 0.75 V vs. Li^+/Li and C3 around 0.45 V vs. Li^+/Li . The positions and intensities of these peaks depend on the type of substrate (Cu, Ni, Pt, glassy carbon) and the impurities. Nonetheless, authors attributed them to the processes of reduction of the TFSI anion supported by *ab-initio* calculations. Their results suggest that TFSI reduction begin at around 2.15 V vs. Li^+/Li .

Regarding our results in Figure 4.6, from the second cycle, especially the first broad peak below 1.5 V vs. Li⁺/Li has disappeared, as an effect of the passivation of the copper surface, and the reduction starts below 1 V vs. Li⁺/Li. In the case of C₁C₆ImTFSI/LiTFSI a strong reduction appears below 0.5 V vs. Li⁺/Li. Therefore, it appears that the C₁C₆ImFSI/LiTFSI shows an improved reduction stability in comparison with C₁C₆ImTFSI/LiTFSI.

Although the reduction current densities diminish along cycling, they are enough high near the lithium voltage (below 0.5 V vs. Li⁺/Li) to render very delicate the use of these ILs for lithium metal batteries.

In Figure 4.7 we extend this analysis to the other combinations of electrolytes. From the Figure 4.7-a, it is clear that the reduction current densities at around 1.5 V vs. Li⁺/Li decrease with the additives VC or FEC, especially when compared with the C₁C₁C₆ImTFSI/LiTFSI. Thus, VC and FEC seem, as expected, to inhibit the reduction of the IL structure around these potentials.

In the Figure 4.7-b, it is observed that after the first cycle, all of the combinations of electrolytes have a very similar behavior with a broad but limited reduction below 1 V vs. Li⁺/Li except for C₁C₆ImTFSI/LiTFSI that shows a quick increase of the current below 0.5 V vs. Li⁺/Li as previously described. Finally, the modification of the imidazolium cation and/or the use of additive prove to be effective to mitigate the electrolyte reduction at low potential.

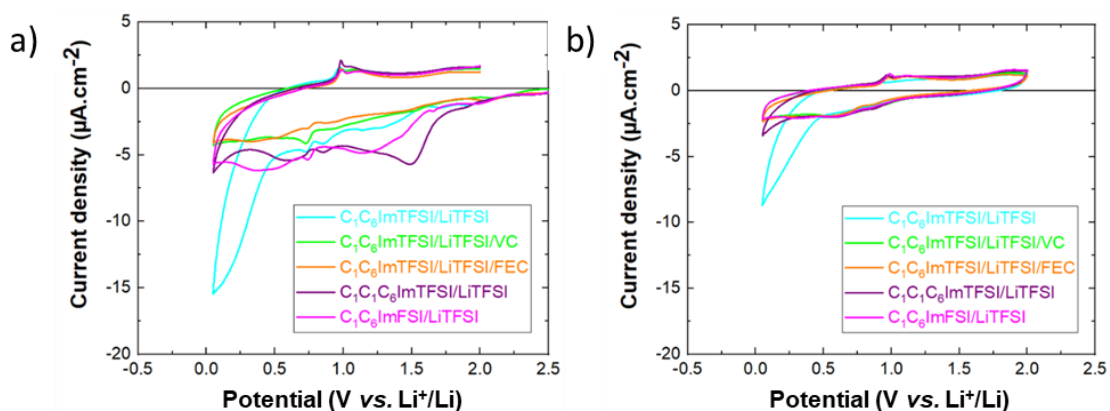


Figure 4.7 Voltammograms of the reduction cycles for all of the combinations of electrolytes during the a) first cycle at [OCV, 50 mV] and b) third cycle at [2 V, 50 mV]. W.E: copper, $\nu = 0.1 \text{ mV.s}^{-1}$.

4.2.5. Performances of the IL-based electrolytes below 0 V vs. Li⁺/Li

Although in the last section it was demonstrated that the ILs electrolytes used in this study start to reduce before the lithium potential, which is true for most of the common organic electrolytes,^{35,37} the behavior of these electrolytes below 0 V vs. Li⁺/Li need to be correctly evaluated. For this reason, CVs were performed at the voltages [2 V, -0.1 V]. Figure 4.8 show the first cycle obtained. The graphs were divided into two groups depending on the reversibility of the lithium plating/stripping. The first group, presented in Figure 4.8-a, is composed by the electrolytes C₁C₆ImTFSI/LiTFSI and C₁C₁C₆ImTFSI/LiTFSI for which we found an irreversible lithium plating, *i.e.*, the current is always negative above 0 V vs. Li⁺/Li and the stripping of the lithium electrodeposited does not take place.

The situation is different for the second group presented in Figure 4.8-b, where the lithium stripping loop is observed with at least a partial reversibility. Obviously, for a lithium metal battery, the plating/stripping reversibility is mandatory. In the case of C₁C₆ImFSI/LiTFSI a very low lithium plating current density is obtained with a reversibility below 15% (*cf.* Table 4.5). The addition of VC or FEC allows the lithium plating with current densities of the order of 100-150 μA.cm⁻² at -0.1 V vs. Li⁺/Li associated with a plating/stripping efficiency above 70%. This is a clear demonstration of the strong impact of both additives on the reversibility of the lithium/plating stripping processes, the mechanism of which staying to be elucidated.

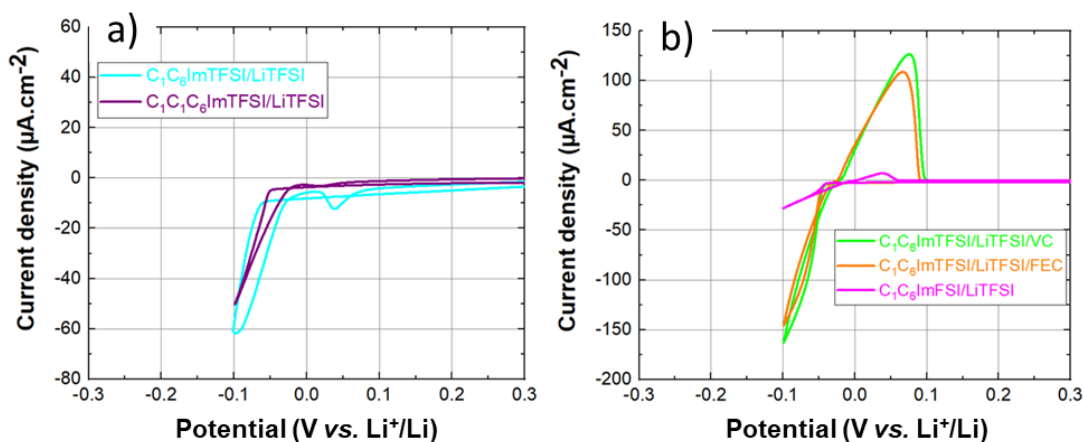


Figure 4.8 Voltammograms of the first cycle at [2 V, -0.1 V] for all of the combinations of IL based electrolytes. W.E: copper, $\nu = 0.1 \text{ mV.s}^{-1}$.

The values of the capacity obtained for the lithium plating and stripping as well as the efficiency of the whole process are given in Table 4.5. Based on these results, the addition of an additive such as VC or FEC in this IL based electrolytes is crucial, however the efficiencies are lower than 80 %.

Table 4.5 Values of the capacities obtained or the first three cycles for the lithium plating (Qp) and the lithium stripping (Qs). The efficiencies Qs/Qp are also given.

Electrolyte	C ₁ C ₆ ImTFSI/LiTFSI/VC			C ₁ C ₆ ImTFSI/LiTFSI/FEC			C ₁ C ₆ ImFSI/LiTFSI		
Q reduction μA.h	60.1	57.2	55.6	50.6	50.2	51.0	12.8	7.1	4.6
Q oxidation μA.h	46.7	42.1	42.0	40.9	35.1	38.9	1.2	1.0	0.7
Efficiency %	77.7	73.6	75.5	80.8	69.9	76.3	9.4	14.1	15.2

4.5. Study by XPS of the reduction of the system lithium/copper

As we have demonstrated in Figure 4.7, the reduction of the IL based electrolytes start at potentials around 1.5 – 2 V vs. Li⁺/Li. In order to understand the origin of this electrochemical result, XPS analyses have been performed in Cu/Li coin cells stopped at different potentials during the CVs.

Experiments has been carried out in coin cells containing C₁C₆ImTFSI/LTFSI electrolyte doped and not with FEC solvent. In Figure 4.9, the potentials of each analyzed coin cell are depicted:

- Coin cells stopped at 0.5 V vs. Li⁺/Li during the first reduction scan [OCV, 0.5 V], corresponding to point 1.
- Coin cells stopped at 1.0 V vs. Li⁺/Li during the first reduction scan [OCV, 1.0 V], corresponding to point 2.
- Coin cells stopped at 0 V vs. Li⁺/Li during the second reduction scan [2 V, - 0.1 V] immediately after lithium plating, corresponding to point 3.

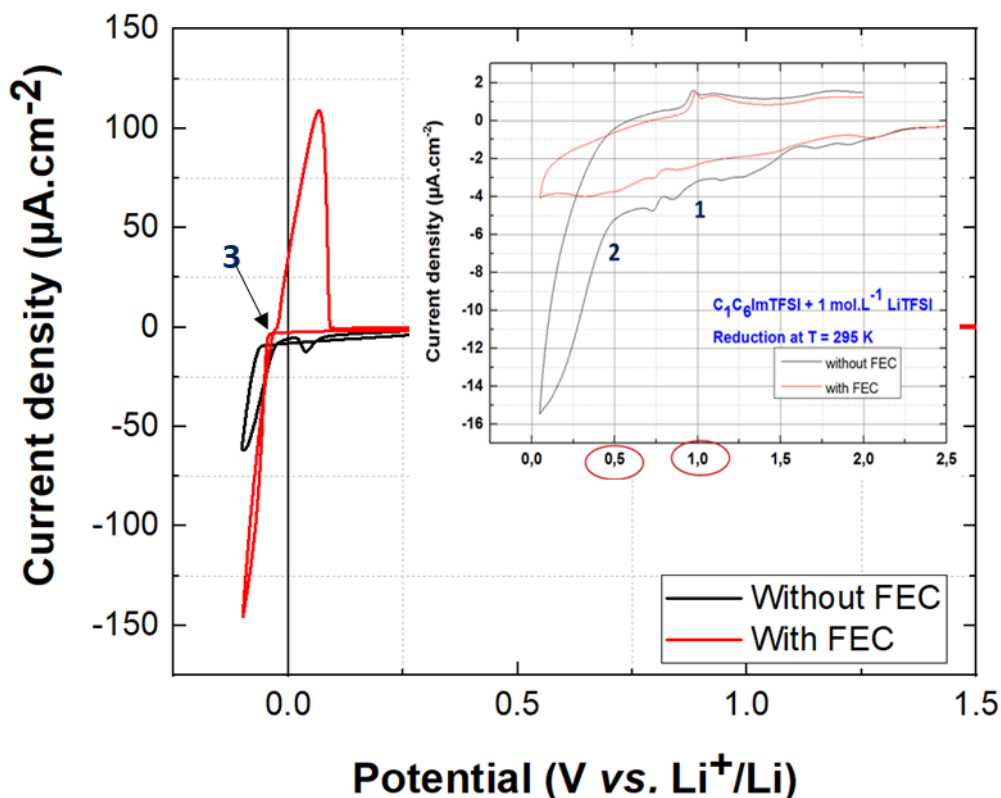


Figure 4.9 Potentials of the Cu/Li coin cells before post-mortem analysis: 1) 0.5 V during the first scan of reduction, 2) 1.0 V during the first scan of reduction and, 3) 0 V after plating at the second cycle.

During the post-mortem protocol, the Cu working electrodes were extracted in a glove box (MBraun, H_2O , $\text{O}_2 < 5$ ppm) and washed for 30 s with DMC solvent to remove the traces of IL electrolyte. Then, the Cu electrodes were transferred to the XPS instrument.

The core peaks of Cu2p are shown in Figure 4.10. The XPS signal recorded at the surface for most of the cases is flat. Taking into account the depth resolution of the XPS, the result indicates that at least 5 nm, or more, thick SEI is formed at the surface of copper.

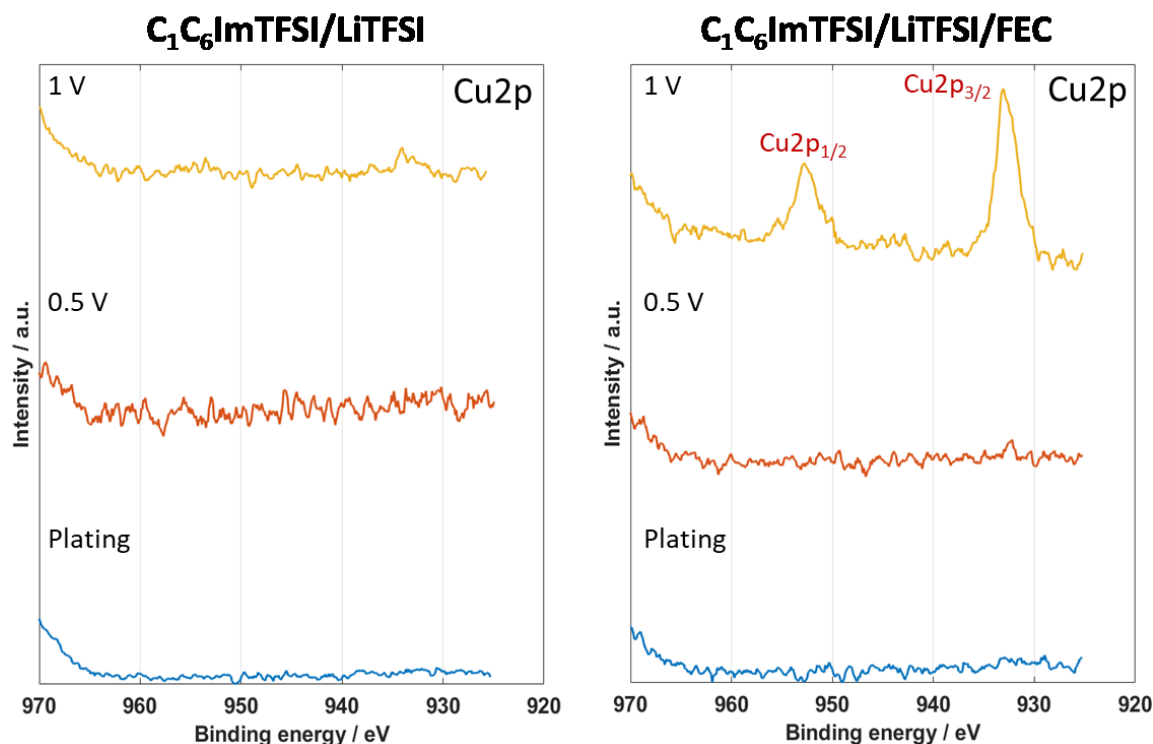


Figure 4.10 XPS spectra of Cu2p core levels of the Cu/Li coin cells stopped at 1V, 0.5 V and after plating.

We notice that the Cu2p core level peak (933.1 eV and 952.8 eV for $Cu2p_{3/2}$ and $Cu2p_{1/2}$, respectively) recorded at 1 V vs. Li^+/Li , is only visible for the case of the electrolyte doped with FEC. This confirms the protective effect of the FEC on the electrolyte avoiding a strong degradation, since in this case the thickness of the formed SEI layer is less than 5 nm.

To reveal the nature of the formed layers on the Cu electrodes, the XPS spectra of F1s and S2p core levels are shown in Figure 4. 11. The first spectra (referenced as Ref) correspond to the XPS spectra recorded on droplets of neat IL electrolytes and are shown just as reference. For the spectra recorded on the Cu electrodes, in all of the cases LiF (~685 eV) and Li_2S (~161 eV) are the main products with some contribution of $Li_2S_xO_y$ species. The initial $-CF_3$ peaks of F1s (689 eV) have been decomposed, probably to form $C_2F_xLi_y$ species.³⁸ In any case, the decomposition of the TFSI anion is evident even at 1.0 V vs. Li^+/Li .

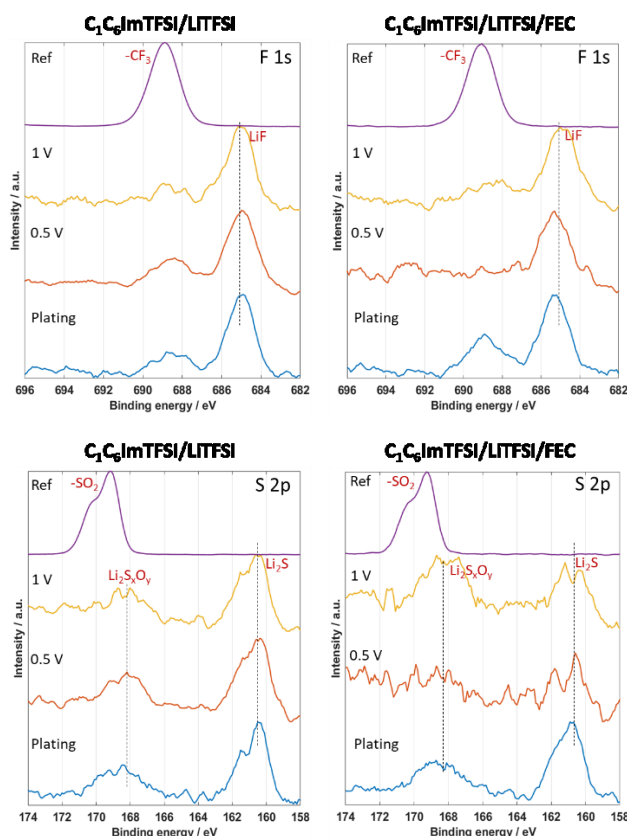


Figure 4. 11 XPS spectra of F1s and S2p core levels of the Cu/Li coin cells stopped at 1V, 0.5 V and after plating.

The XPS spectra of the N1s and O1s core levels are shown in Figure 4.12. Note also the decomposition of the N_{anion} (~ 399 eV) peak in all of the cases, whereas there is no evidence of Im^+ cation decomposition byproducts. This could be related to the fact that the cationic decomposition species (probably carbenes and other organic compounds) are removed by the washing of the Cu electrodes with DMC solvent.

The O1s core levels evidenced the presence of a peak at 531.4 eV that can be associated to the formation of $\text{Li}_2\text{S}_x\text{O}_y$ species. Besides, another peak at ~ 528.6 eV can be attributed to the formation of Li_2O . Herein, we postulate that the presence of Li_2O does not come from a decomposition of the TFSI anion, but it is due to the fast oxidation of highly reactive metallic lithium after cell disassembling. Note in addition, that the intensity of Li_2O peak remains constant for the case of the electrolyte without FEC, whereas for the doped electrolyte the intensity increases between 1 V and 0.5 V vs. Li^+/Li and then decreases after Li plating (Figure 4.12).

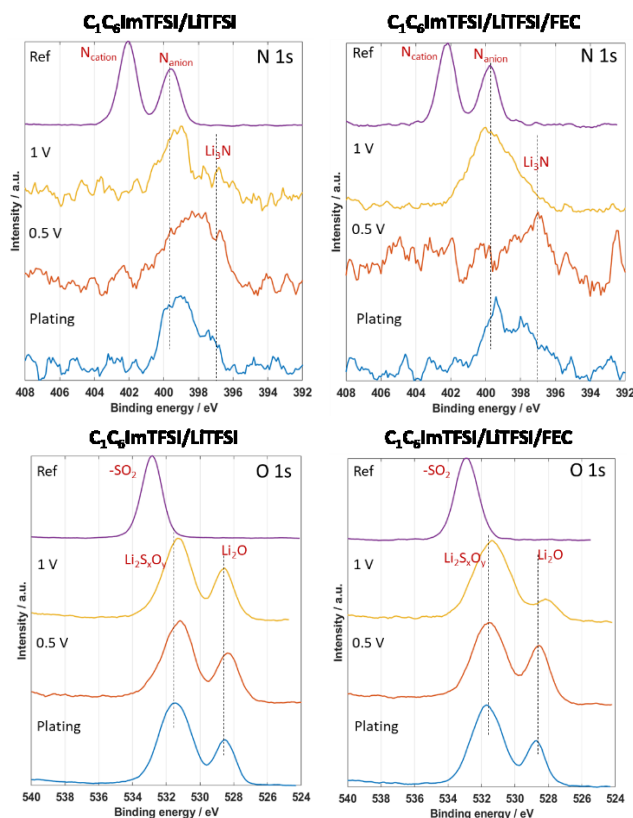


Figure 4.12 XPS spectra of N1s and O1s core levels of the Cu/Li coin cells stopped at 1V, 0.5 V and after plating.

The C1s peaks, showed in Figure 4.13, corroborate the decomposition of anion since the $-\text{CF}_3$ and hetero structure related peaks disappear. The broadness of the peak labeled as related to C-C groups, and the shoulder at 286 eV detected at 1 V and 0.5 V could be assigned of alkyl groups and complex cationic combination such as carbenes, respectively. These last species cannot be clearly evidenced from the signature of the C1s peak, since their position overlaps with hetero carbon related peak.

We noticed, that the C1s peak recorded after plating, shows two news component at 286.7 and 290 eV, signature of lithium alkyl carbonate. This can find an origin in the reactivity of fresh deposited lithium to glove box atmosphere.

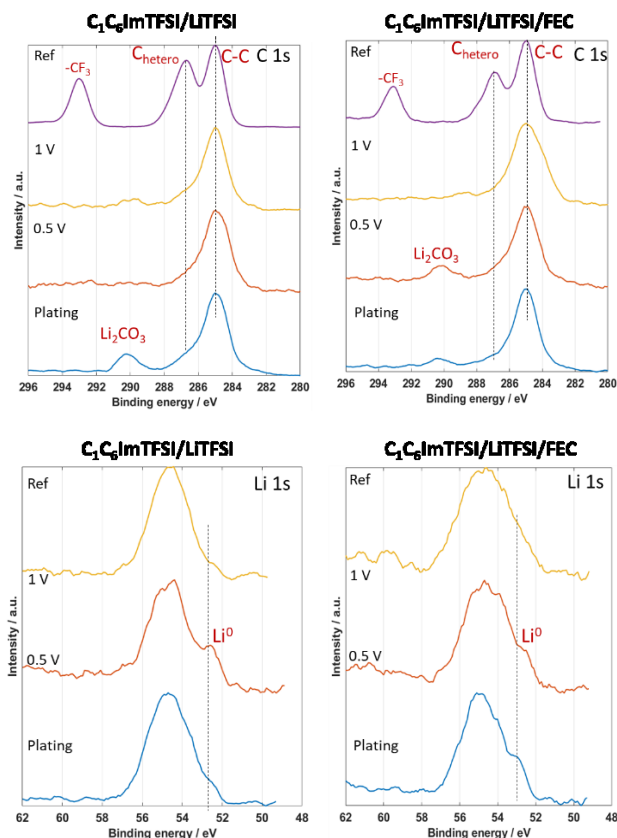


Figure 4.13. XPS spectra of C1s and Li1s core levels of the Cu/Li coin cells stopped at 1V, 0.5 V and after plating.

As a complement to the XPS measurements, Figure 4.14 shows the AES and SEM coupled analysis of the copper surface at 1.0 V vs. Li^+/Li of $\text{C}_1\text{C}_6\text{ImTFSI}/\text{LiTFSI}$ with and without FEC. The SEM micrographs exhibit the presence of a layer deposited on the copper surface composed of carbon (270 eV), oxygen (512 eV) and fluorine (654 eV). The presence of sulfur (152 eV) is only detected for the case of the electrolyte without FEC, which is consistent with the XPS result. In conclusion, at this potential the anion TFSI is degraded whatever the electrolyte is, leading to the formation of LiF and $\text{Li}_2\text{S}_x\text{O}_y$ species.

The analysis of the copper surface at 0 V vs. Li^+/Li after lithium plating is shown in Figure 4.15. Note that for both cases the morphology of the copper surface presents a deposit in the form of a multilayer structure (similar than in the case at 1 V vs. Li^+/Li), with the presence of several grain-like and needle-like particles for the case of the electrolyte without and with FEC.

In contrast to the chemical composition of the copper surface at 1 V vs. Li^+/Li , after plating the AES results only show the presence of carbon, and mostly oxygen, but no traces of sulfur or fluorine are detected. Note that the peak at ~ 40 eV can be associated to the Li plated that is highly reactive and becomes Li_2O .

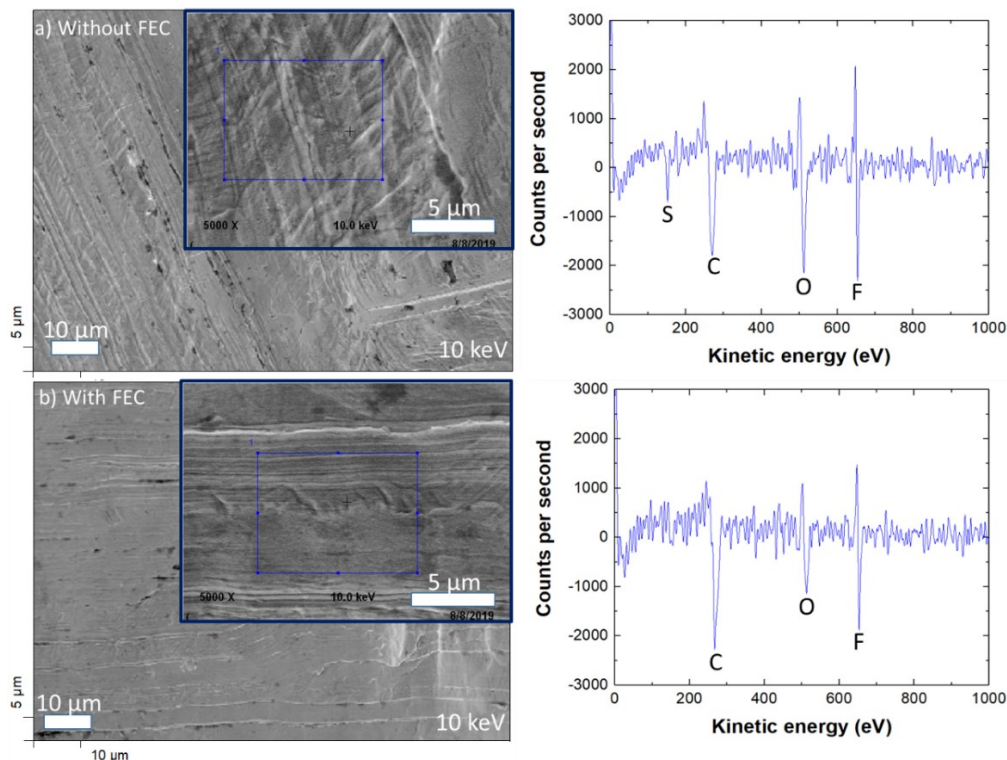


Figure 4.14 SEM micrographs of copper electrodes at 1.0 V vs. Li^+/Li and AES spectra recorded in the zones with blue box in the insets.

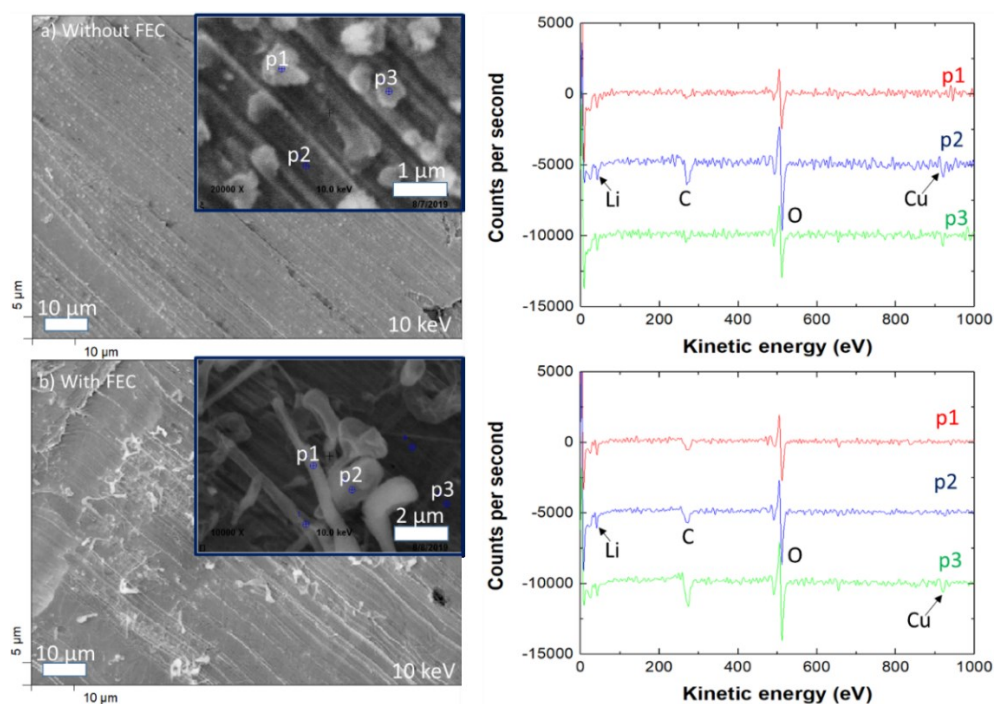


Figure 4.15 SEM micrographs of copper electrodes at 0 V vs. Li^+/Li and AES spectra recorded in the points p1, p2 and p3.

4.6. The Li/Li system under the application of an electrical current

In chapter 3, the evolution of the interfaces Li/IL based electrolyte was studied at the OCV conditions. Herein, we extend the analysis to the condition where a constant current is applied to the system. Therefore, in this section, the performance of symmetrical lithium/lithium coin cells will be evaluated after performing the chronopotentiometry technique at different current densities.

Different regimes of dendrite growth and the evolutions of the interfaces Li/IL based electrolyte will be characterized by EIS, XPS and SEM/AES.

4.6.1. Experimental part

Symmetrical Li/Li coin cells containing C₁C₆ImTFSI/LiTFSI or C₁C₆ImFSI/LiTFSI were assembled as described in chapter 2. In contrast with most of the works reported in the literature, where repeated cycles of charge/discharge are applied, herein only the charge with an electrical current density between 30 and 150 $\mu\text{A}\cdot\text{cm}^{-2}$ was performed, based on the works of Brissot, Chazalviel and Rosso.¹⁶⁻¹⁸

Figure 4.16 shows the voltage of the cells as a function of time for different applied current densities at $T = 298\text{ K}$. The voltage variations ($\pm 5\text{ mV}$) of the signals are due to an incorrect data recording setting. In Figure 4.16-b the signal for $J=75\ \mu\text{A}\cdot\text{cm}^{-2}$ has been filtered for $t > 6\text{ h}$.

Regarding the voltage curves, two different behaviors have been obtained depending on the type of electrolyte.

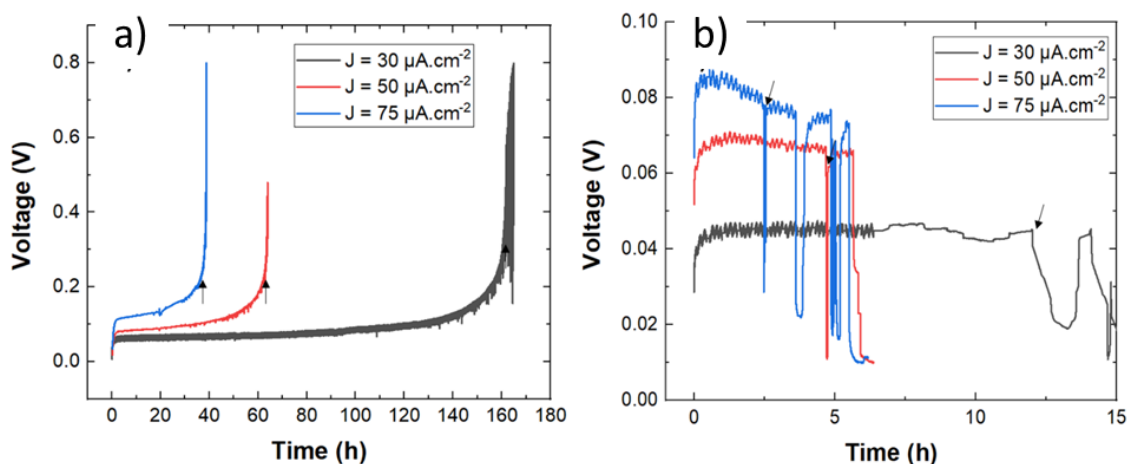


Figure 4.16 Variation of the voltage in the symmetrical Li/Li coin cells as a function of time for different current densities at $T = 298$ K for a) C₁C₆ImTFSI/LiTFSI and b) C₁C₆ImFSI/LiTFSI. The characteristic times of voltage divergence (τ_d) or time of short-circuit (τ_{sc}) are shown by arrows.

For the case of C₁C₆ImTFSI/LiTFSI, after reaching a plateau, the voltage is continuously increasing at a slow rate, then after some time depending on the current density it diverges. This divergence is characterized by a Sand's behavior and the time where the voltage diverge is called τ_d .¹⁷

For the case of C₁C₆ImFSI/LiTFSI, after a stationary state, the voltage profile manifest a successive sudden voltage drop. The first drop of voltage is due to a short circuit (soft herein) and the time where it occurs is called τ_{sc} .³⁹

In order to establish a correlation between the voltage profile and the applied current density, we will discuss the previous results in the framework of a simple electrochemical model based on the works of of Brissot, Chazalviel *et al.*^{15,17}

4.6.2. The Chazalviel's model

The model describes the evolution of the concentration profiles between two flats and parallels lithium electrodes separated by a distance L , and submitted to a constant current (Figure 4.17).

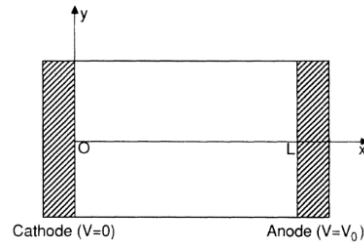


Figure 4.17 Scheme of the electrochemical cell in the Chazalviel's model.

In this model, the transport parameters of the electrolyte (ionic diffusion coefficients) do not depend on the concentration and the temperature gradients. The calculation has been made for a binary electrolyte, *i.e.* one anion and a Li^+ cation that reacts reversibly at the lithium interfaces.

The concentration profile evolving as a function of time $C(t, x)$ is calculated from the Fick's law as following:

$$\frac{\partial C_c}{\partial t} = D_c \frac{\partial^2 C_c}{\partial x^2} + \mu_c \frac{\partial}{\partial x} \left(C_c \frac{\partial V}{\partial x} \right) \quad \text{Eq. 4.1}$$

$$\frac{\partial C_a}{\partial t} = D_a \frac{\partial^2 C_a}{\partial x^2} - \mu_a \frac{\partial}{\partial x} \left(C_a \frac{\partial V}{\partial x} \right) \quad \text{Eq. 4.2}$$

- The parameters c and a in subscripts refer to the cation and the anion, respectively.
- C_i, D_i, μ_i are the concentration, diffusion coefficient and mobility of the cation or anion, respectively.
- V is the electrostatic potential

Considering the electroneutrality condition, $z_c C_c = z_a C_a = C$, where z_c, z_a are the number of charges of the cation and the anion, respectively, the Eq. 4.1 and 4.2 become:

$$\frac{\partial C}{\partial t} = D \frac{\partial^2 C}{\partial x^2} \quad \text{Eq. 4.3}$$

Where D is the ambipolar diffusion coefficient, given by:

$$D = \frac{D_a \mu_c + D_c \mu_a}{\mu_c + \mu_a} \quad \text{Eq. 4.4}$$

On the other hand, since the anions are not involved in the electrochemical reactions, the boundary conditions at the electrodes $x=0$ are $J_a = 0$ and $J_c = J$ leading to :

$$-D_c \frac{\partial C_c}{\partial x} - \mu_c C_c \frac{\partial V}{\partial x} = \frac{J}{z_c e} \quad \text{Eq. 4.5}$$

$$-D_a \frac{\partial C_a}{\partial x} + \mu_a C_a \frac{\partial V}{\partial x} = 0 \quad \text{Eq. 4.6}$$

Where $e = 1.6 \times 10^{-19} \text{C}$ is the elementary charge. Therefore, we can write:

$$\frac{\partial C(x=0)}{\partial x} = \frac{-J\mu_a}{eD(\mu_a + \mu_c)} \quad \text{Eq. 4.8}$$

From Eq. 4.8, it is possible to identify two different conditions:

a) If $\partial C/\partial x < 2C_0/L$, the ionic concentration evolves to a steady state where the concentration gradient is constant and the concentration at $x=0$ is not null. The voltage reaches also a steady state. Teyssot⁴⁰ describes the behavior of the voltage at this regime, considering an Ohmic contribution and a Nernstian contribution:

$$V(t) = V_{Ohm} + V_{Nernst} = I * R_{int} + \frac{RT}{zF} \ln \left(\frac{C(t, x=0)}{C_0} \right) \quad \text{Eq. 4.9}$$

where I and R_{int} are the current and the internal resistance of the cell, respectively.

The profile of the cell voltage is shown in Figure 4.18 (A) and the profile of the concentration in Figure 4.18 (B). Note that at the time t_{STEADY} , the cell voltage stabilizes.

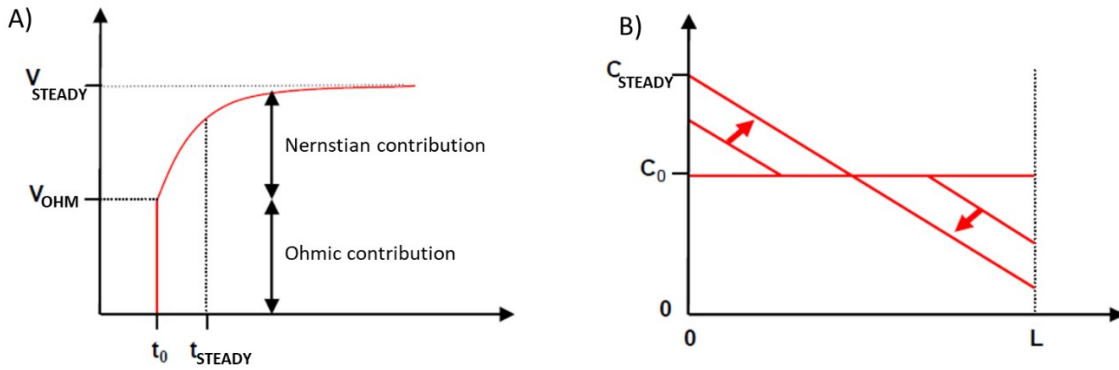


Figure 4.18 A) Voltage profile and B) Concentration profile for the condition $\partial C/\partial x < 2C_0/L$ (Reproduced from A. Teyssot thesis⁴⁰).

b) If $\partial C/\partial x > 2C_0/L$, the ionic concentration goes to zero at the negative electrode at a time called “Sand’s time” (assuming a semi-infinite condition, *i.e.* $(Dt)^{1/2} < L$):

$$\tau_S = \pi D \left(\frac{eC_0}{2Jt_a} \right)^2 \quad \text{Eq. 4.10}$$

$$t_a = \frac{\mu_a}{\mu_a + \mu_c} \quad \text{Eq. 4.11}$$

where t_a is the anionic transport number.

The profile of the cell voltage is shown in Figure 4.19 (A) and the profile of concentration in Figure 4.19 (B). Note that in this condition, the Li^+ concentration at the cathode vanishes at τ_S which produces the divergence of the voltage.

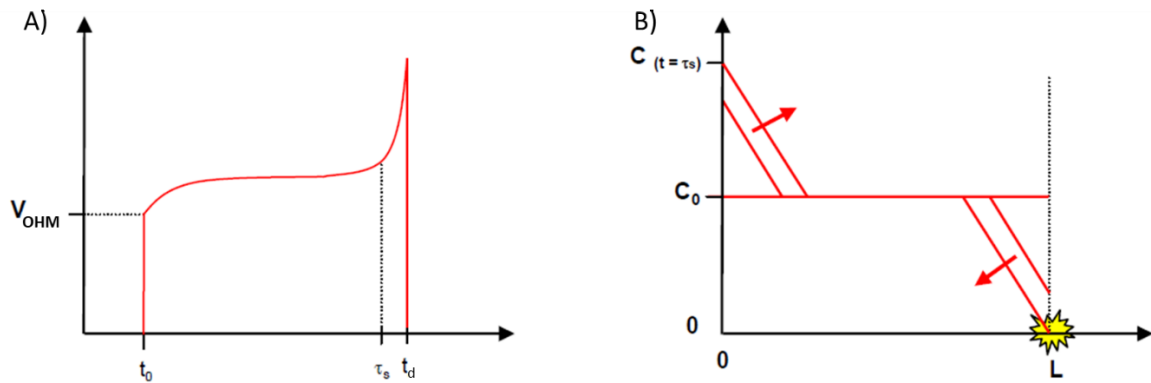


Figure 4.19 A) Voltage profile and B) Concentration profile for the condition $\partial C/\partial x > 2C_0/L$ (Reproduced from A. Teysso⁴⁰).

It is possible to calculate the diffusion current density J^* where occurs the transition between the two regimes:

$$J^* = \frac{2eC_0D}{t_aL} \quad \text{Eq. 4.12}$$

In conclusion:

- | | | |
|-----------------|----------------------------------|-----------|
| a) Steady state | $\partial C/\partial x < 2C_0/L$ | $J < J^*$ |
| b) Divergence | $\partial C/\partial x > 2C_0/L$ | $J > J^*$ |

In addition, for the case (b), Chazalviel has shown that, at the Sand's time, if the anionic concentration falls down to zero, the Li^+ concentration is not null and leads to an excess of positive charges at the negative electrode. This behavior will result in a local space charge, forming a large electric field, which is the driving force for the nucleation (and finally growth) of Li dendrites. He showed that the speed at which the dendrite grows

is proportional to the anionic mobility, and this process is fast compared to the nucleation process. Therefore, in his model the short-circuit occurs in a time similar to the Sand's time.

4.6.3. Experimental verification of the inverse-square law $\tau \propto 1/J^2$

4.6.3.1. Experiments performed at $T = 298\text{ K}$

In the results of the Figure 4.16 we can distinguish two different behaviors that can be compared with the two conditions described in the Chazalviel's model. For the case of the $C_1C_6ImTFSI/LiTFSI$ the voltage diverges, which is similar to the condition (b) where $J > J^*$ without any trace of short circuit.

On the contrary, for the $C_1C_6ImFSA/LiTFSI$ electrolyte, (soft) short-circuits are systematically observed. This second behavior has been observed by Rosso, Brissot *et al.* in Li/SPE symmetric cells (SPE: solid polymer electrolyte).³⁹ They have shown that the falls of the voltage are produced by dendrites that short circuit the cell. As this dendrite supports all the current that cross the cell, it can eventually be fused by Joule effect and the voltage increases again. This behavior has been called the 'fuse effect' and corresponds to "soft" shorts.

In Figure 4.20, the times of voltage divergence for $C_1C_6ImTFSI/LiTFSI$ or short-circuit for $C_1C_6ImFSA/LiTFSI$ are plotted as a function of the applied current density in log-log scales. The straight lines represent the best fit of the data following a law proportional to the inverse of the square of the current density ($\tau \propto 1/J^2$) in a try to verify the Sand's behavior (Eq. 4.10). Interestingly, in both cases a very good concordance is obtained.

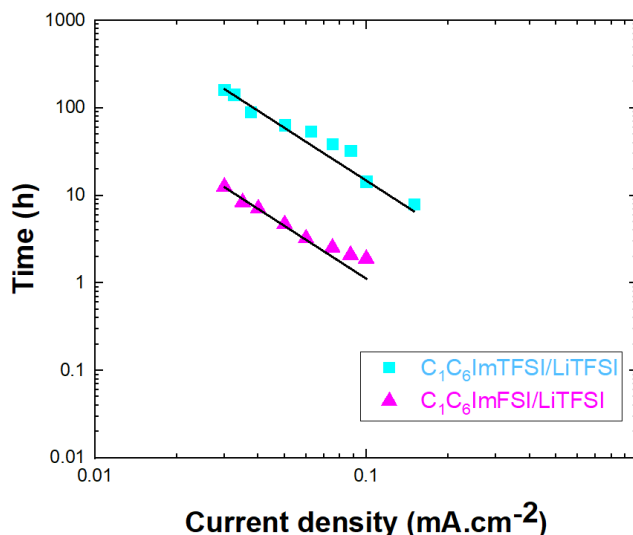


Figure 4.20 Time of voltage divergence (τ_d) or time of short-circuit (τ_{sc}) as a function of the current density J in the symmetric Li/Li coin cells at $T = 298$ K. The straight lines show the Sand's time behavior, *i.e.* $\tau \propto 1/J^2$.

Nonetheless, the complex structure of the IL is far from binary electrolytes used in the Chazalviel's model. Indeed, an ideal binary electrolyte is composed of "diluted" salt solvated in a polar matrix, giving a simple solvated cation and anion. As we have seen in chapter 2, the addition of the LiTFSI salt change the organization of the ions by forming complexes, probably from the type $\text{Li}(\text{TFSI})_2^-$. As a consequence, a Sand's behavior can be observed but with different physical parameters.

4.6.3.2. Experiments performed at $T = 333$ K

In order to verify the Sand's equation at different temperatures, experiments of chronopotentiometry in Li/Li coin cells containing $\text{C}_1\text{C}_6\text{ImTFSI/LiTFSI}$ were performed at a temperature of $T = 333$ K. The log-log plot of the time of divergence of the potential as a function of the applied current density is shown in Figure 4.21 for the experiments performed at 298 K and 333 K.

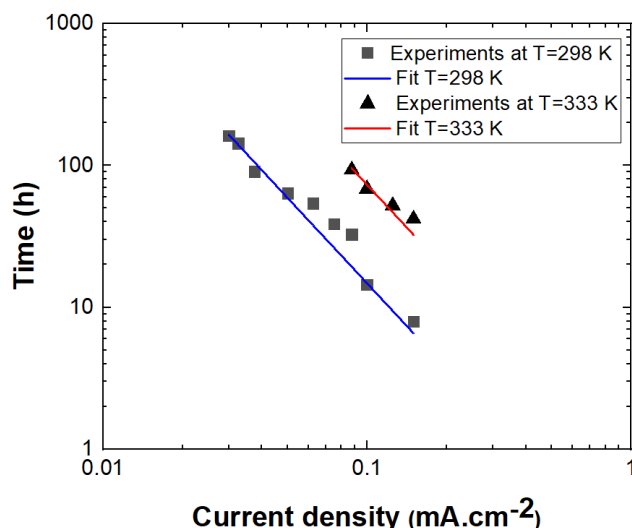


Figure 4.21 Time of voltage divergence (τ_d) as a function of the current density for the $C_1C_6ImTFSI/LiTFSI$ system at two different temperatures 298 K and 333 K.

In spite of the consideration that the system is more complex than a simpler binary electrolyte, for these current densities the inverse-square law seems to be appropriated. As a consequence, according to the equation of the Sand's time (Eq. 4.10), the slopes of the curves in Figure 4.21 are proportional to D/t_a^2 . In a latter section, the diffusion coefficient and the anionic transport number of the electrolyte will be studied. Before this, we will extend our conclusions to the other electrolyte systems.

4.6.3.3. The effect of the additives VC and FEC

Chronopotentiometry experiments in symmetrical Li/Li coin cells have been also conducted for systems containing $C_1C_6ImTFSI/LiTFSI$ doped with VC and FEC additives. Figure 4.22-a shows the voltage profile during the application of a current density of $50 \mu A.cm^{-2}$. In contrast with the electrolyte without additive, the electrolytes doped with VC or FEC behave like the $C_1C_6ImTFSI/LiTFSI$ electrolyte and exhibit a short-circuit at some time τ_{sc} .

In Figure 4.22-b, the times of short-circuit have been plotted and compared with the electrolyte without additive. If the Sand's law has been verified when the voltage diverges, the systems where a short-circuit is produced seems to deviate from the inverse-square law. Especially for the case of the electrolyte with VC, the straight line in Figure 4.22-b does not coincide with the experimental points at high current densities. Herein,

an exponent $n < 2$ is more adapted to the fit of the experimental data. For instance, a value of $n = 1.4$ in $\text{LiPF}_6/\text{EC}/\text{DMC}$ electrolyte has been reported.⁴¹ This is due to a different mechanism of dendrite nucleation and growth which depends on the current density. Clearly, these systems containing additives need a more advanced treatment than a simple binary electrolyte.

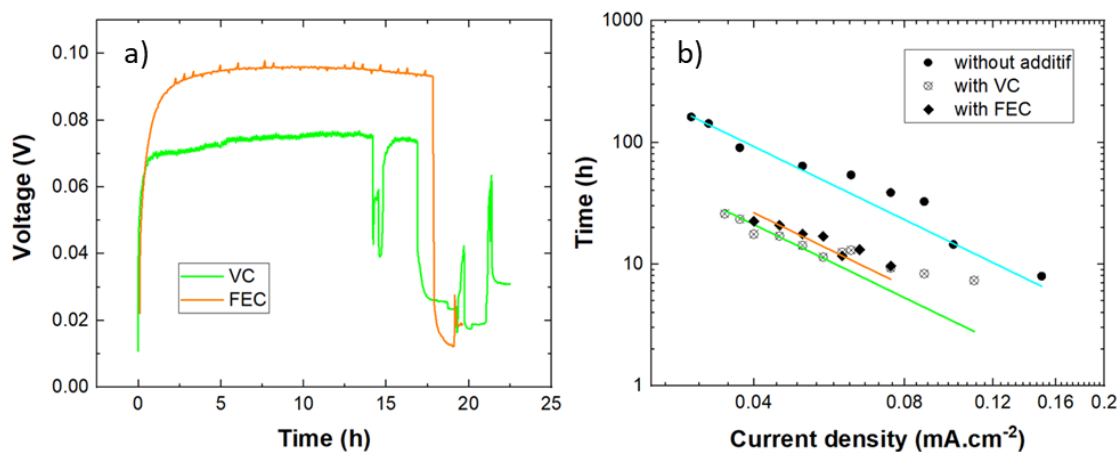


Figure 4.22 a) Voltage as a function of the time for symmetrical Li/Li coin cells containing $\text{C}_1\text{C}_6\text{ImTFSI}/\text{LiTFSI}$ with VC or FEC during the application of a current density of $50 \mu\text{A}\cdot\text{cm}^{-2}$, and b) plots of the time of divergence (τ_d) and time of short-circuit (τ_{sc}). The straight lines show the Sand's time $\propto 1/J^2$.

4.6.3.4. Effect of the methylation of the $\text{C}_1\text{C}_6\text{Im}$ cation

In the case of the $\text{C}_1\text{C}_1\text{C}_6\text{ImTFSI}/\text{LiTFSI}$ the Li/Li cell voltage behavior under polarization, is reported in Figure 4.23. At higher current densities (60 and $75 \mu\text{A}\cdot\text{cm}^{-2}$), the voltage diverges exactly in the same way that for the case of $\text{C}_1\text{C}_6\text{ImTFSI}/\text{LiTFSI}$. In contrast, for lower current densities, it is possible to observe some drops of the voltage, which correspond to the short-circuit regime. In conclusion, it has been found that a transition between the two regimes happens around 50 and $60 \mu\text{A}\cdot\text{cm}^{-2}$.

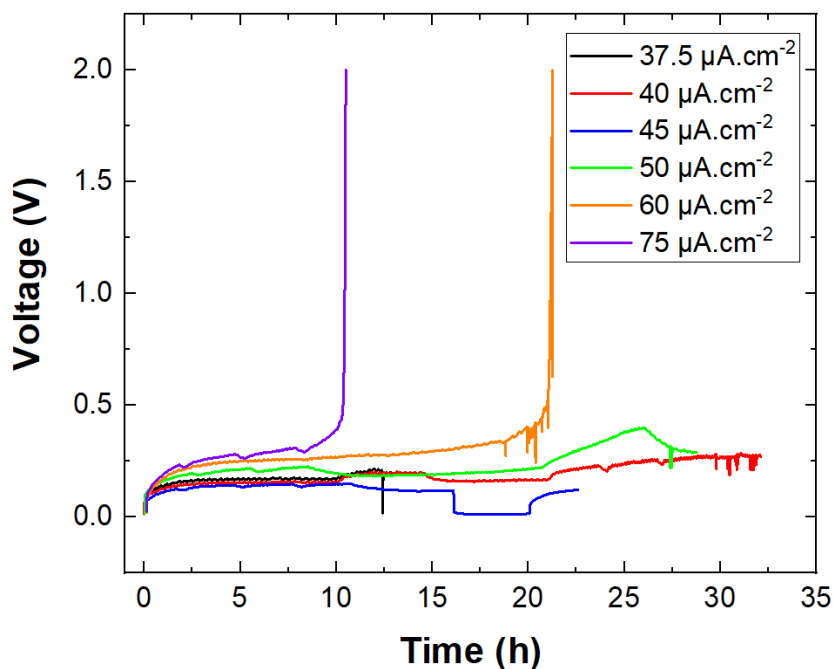


Figure 4.23 Voltage as a function of the time for symmetrical Li/Li coin cells containing $C_1C_1C_6ImFSI/LiTFSI$.

In conclusion, these results demonstrate the existence of two different regimes: a) divergence of potential at higher current densities, and b) drop of potential (short-circuit) at lower current densities. This is in agreement with the results of the Chazalviel's model assuming in the latter a distribution of the current density, with locally a current density above J^* . These regimes exist also for the other combinations of electrolytes, but the results will not be included in this work. Besides, the current density for the transition between the two regimes can be calculated from the Eq. 4.12, but this requires the knowledge of the diffusion coefficient and the transport numbers of the electrolyte.

To resume our results, in Table 4.6 we show the time of divergence of potential for the electrolytes $C_1C_6ImTFSI/LiTFSI$ and $C_1C_1C_6ImTFSI/LiTFSI$ and the time of short-circuit for the electrolytes $C_1C_6ImFSI/LiTFSI$, $C_1C_6ImTFSI/LiTFSI/VC$ and $C_1C_6ImTFSI/LiTFSI/FEC$. Note that the time of short-circuit is lower than the time of divergence of potential.

Table 4.6 Time of divergence of potential and time of short-circuit at T = 298 K for the different combinations of IL based electrolytes used in this work.

Current density ($\mu\text{A}\cdot\text{cm}^{-2}$)	C ₁ C ₆ ImTFSI LiTFSI	C ₁ C ₁ C ₆ ImTFSI LiTFSI	C ₁ C ₆ ImFSI LiTFSI	C ₁ C ₆ ImTFSI LiTFSI/VC	C ₁ C ₆ ImTFSI LiTFSI/FEC
30	162		12.7	-	-
35	-		8.4	25.9	-
40	-		7.1	-	22.5
50	63.9		4.7	14.2	17.7
60	-	22	3.3	12.5	11.7
75	38.7	10.5	2.6	9.3	9.6
100	14.5		1.9	-	-

Until here, we have postponed the discussion about the transport properties of the electrolyte and the type of dendrites formed in each case. In the next sections, the transport properties will be studied from the EIS results of the polarized cells in combination with NMR results from the literature. The morphology of the dendrites and the SEI formed during polarization will be described later from the XPS and SEM/AES *post-mortem* analyses.

4.6.4. Transport properties of the electrolytes

Other than the ionic conductivity σ , for the case of a lithium salt dissolved in neat ionic liquid, it is important to quantify their capacity to transport Li⁺ ions in order to improve the transport properties of the electrolytes. A good electrolyte must satisfy the condition: transference number $\sigma_{\text{Li}}/\sigma_{\text{total}} \approx 1$, where σ_{total} includes the conductivities by other ions in the electrolyte.⁴²

However, in the practice, the reported transference number T_{Li^+} for IL-based electrolyte can be as low as 0.13 because of their high viscosity which limits their transport properties.⁴³ Herein, in this section we will calculate the transference number of the C₁C₆ImTFSI/LiTFSI (1 mol.L⁻¹) electrolyte based on two different methods: 1) pulsed field gradient (PFG-NMR) and 2) impedance spectroscopy.

4.6.4.1. Transport and transference number

The contribution of each ionic species k to the current transport by migration can be quantified by a dimensionless number, which values are between 0 and 1, called the transport number:

$$t_k = \frac{|z_k|u_k C_k}{\sum_k |z_k|u_k C_k} \quad \text{Eq. 4.13}$$

where z_k , u_k and C_k are the charge, the electric mobility and the concentration of the ionic specie k , respectively.

For a simple binary electrolyte, we can consider that it is only composed by one anion and one cation and in conclusion, $t_+ + t_- = 1$, where $t_+ = t_c$ is the cationic transport number and $t_- = t_a$ is the anionic transport number.

In addition, the transport number for a binary system can be calculated from the cationic and anionic diffusion coefficients:

$$t_+ = \frac{D_+}{D_+ + D_-} \quad \text{and} \quad t_- = \frac{D_-}{D_+ + D_-} \quad \text{Eq. 4.14}$$

However, for an IL based electrolyte, the charge can be transported by all the mobile species present in the system, such as simple ions as well as their charged combinations,⁴⁴ e.g., Li^+ , A^+ , X^- , LiX_2^- , etc. Consequently, the description of transport properties in ILs would be more comprehensive with the use of transference numbers, defined as the number of moles of the ion i transported per mole of electrons, *i.e.*, per Faraday. For example when considering only LiX_2^- ionic clusters, the Li^+ transference number can be written:

$$T_{\text{Li}^+} = t_{\text{Li}^+} - t_{\text{LiX}_2^-} \quad \text{Eq. 4.15}$$

T_+ therefore quantifies the net transference of all the Li^+ -containing species which migrate in the electrolyte. Of course, in an ideal system, where there is no ion association $T_+ = t_+$. In addition, from the equation above, it is theoretically possible to have $T_+ < 0$ if the mobility of the $[\text{LiX}_2]^-$ complex is higher than the free Li^+ mobility.

This equation introduces some complications to the binary model and as a consequence, the relation between the transport numbers and the diffusion coefficients is more complex and would need: 1) a quantitative description of the ionic populations and 2) a more sophisticated modelling. Nonetheless, we will give some information about these transport properties based on experimental measurements.

4.6.4.2. PFG-NMR measurements of the transport properties

We will use the data reported by Bolimowska *et al.*⁴⁵ of the diffusion coefficients of the IL C₁C₆ImTFSI doped with LiTFSI (1 mol.L⁻¹) to calculate the lithium and the anionic transference numbers. The results are given in the Table 4.7. The data at 298 K and 333 K does not correspond to the experimental values but were calculated by fitting the PFG-NMR data of the diffusion coefficients by an Arrhenius equation.

Interestingly, the lithium and the anion species share similar (PFG-NMR) diffusion coefficients at RT with a deviation at higher temperatures. This strongly supports the hypothesis of the formation of complexes between the TFSI anion and the Li⁺ ion.

Note, in contrast, that for an ideal system with no ion associations $T_{Li^+}^{NMR} = t_{Li^+}^{NMR}$, and we can use the following equation:

$$T_{Li^+}^{NMR} = t_{Li^+}^{NMR} = \frac{C_0 D_{Li^+}^{NMR}}{C_0 D_{Li^+}^{NMR} + C_1 D_{Im^+}^{NMR} + (C_1 + C_0) D_{TFSI^-}^{NMR}} \quad \text{Eq. 4.16}$$

Where C₀ and C₁ are the concentration of LiTFSI salt and IL, respectively. The results are shown in Table 4.7. Nonetheless, the diffusion coefficients of a nuclear *i* measured by PFG-NMR is an average of the all species containing *i* (*i.e.*, for lithium-Li⁺, neutral LiTFSI, anionic Li(TFSI)₂, etc.), that are not taken into account in this calculation. In fact, a more appropriate result can be calculated from Eq. 4.13 and Eq. 4.15. However, it implies the knowledge of: 1) the different chemical equilibria between the ions in order to calculate their different concentrations, and 2) the diffusion coefficient of each specie. This study is out of the scope of this work.

Table 4.7 Diffusion coefficients ($10^{-11} \text{ m}^2\cdot\text{s}^{-1}$) and lithium transference number for $\text{C}_1\text{C}_6\text{ImTFSI/LiTFSI}$, measured by NMR.⁴⁵

T (K)	$\text{C}_1\text{C}_6\text{ImTFSI/LiTFSI}$ (1 mol.L ⁻¹)			
	$[\text{C}_1\text{C}_6\text{Im}]^+$	$[\text{TFSI}]^-$	$[\text{Li}]^+$	$T_{\text{Li}^+}^{\text{NMR}}$
298	0.77	0.39	0.38	0.10
305	1.10	0.59	0.53	0.09
310	1.47	0.78	0.67	0.09
315	1.84	1.23	0.95	0.09
320	2.44	1.67	1.16	0.09
325	3.08	2.26	1.42	0.08
330	3.80	2.60	1.68	0.08
333	4.29	3.17	1.98	0.08
335	4.50	3.21	2.11	0.08

Thereafter, we will compare this results with the impedance spectroscopy method.

4.6.4.3. EIS measurements of the transport properties

During the chronopotentiometry experiments of Li/Li coin cells, we performed operando a galvanostatic EIS (see methods chapter 2). The spectra look very similar to the ones described in chapter 3, *i.e.* the electrolyte resistance at high frequency, the interface behavior at medium frequency and the diffusion process at low frequency. We extracted the values of R_{el} and R_{int} . To compare the results for the two types of cell voltage behavior (divergence vs short-circuit), the evolutions of the polarisation du to the resistances ($R_i \cdot I$) for the systems $\text{C}_1\text{C}_6\text{ImTFSI/LiTFSI}$ with and without VC are depicted in Figure 4.24.

For the electrolyte without additive (Figure 4.24-a), the electrolyte resistance is stable and starts to increase just before the divergence of the voltage. The interface resistance increases progressively since the beginning. For the case where VC is added (Figure 4.24-b), the electrolyte resistance is stable all of the time, however the interface resistance follows the evolution of the cell voltage and eventually the resistance falls down abruptly when a short-circuit happen.

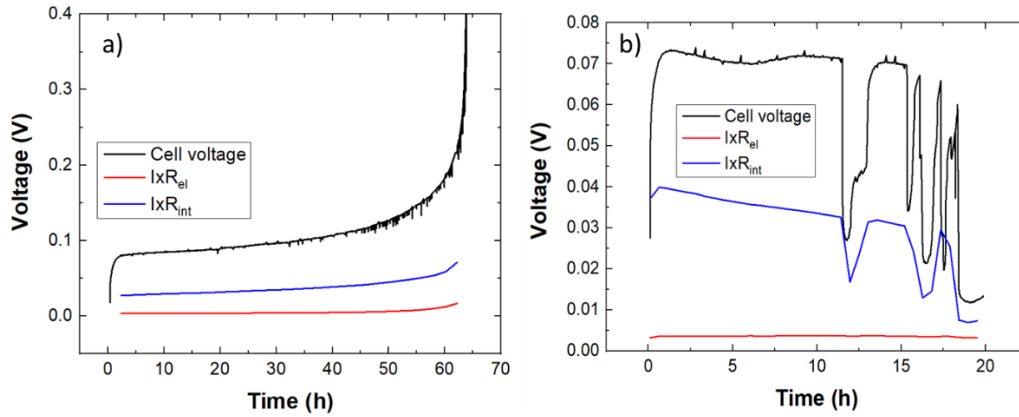


Figure 4.24 Evolution of the cell voltage, electrolyte and interface resistances for symmetrical Li/Li coin cells containing (a) C₁C₆ImTFSI/LiTFSI and (b) C₁C₆ImTFSI/LiTFSI/VC during the application of a current density of 50 μA.cm⁻².

Regarding the lithium transport number, based on EIS measurements during chronopotentiometry experiments, Bruce and Vincent⁴⁶ have proposed a method to measure it, assuming an ideal system with no ion association. Hiller *et al.*⁴⁷ have derived a simple expression for calculation of the lithium transport number with our experiments:

$$t_{Li^+}^{EIS} = \frac{I \times R_{el}}{V - I \times R_{int}} \quad \text{Eq. 4.17}$$

This equation allows to calculate the lithium transport number directly from the Figure 4.24. The results of the different systems are summarized in Table 4.8.

Table 4.8 Calculated Li⁺ transport numbers by EIS for Li/Li cells.

System	Temperature (K)	Current density (μA.cm ⁻²)	$t_{Li^+}^{EIS}$	$T_{Li^+}^{NMR}$
C ₁ C ₆ ImTFSI/LiTFSI	298	50	0.06	0.10
C ₁ C ₆ ImTFSI/LiTFSI	333	175	0.08	0.08

From the Table 4.8, we notice that the values calculated thanks to the PFG-NMR at RT are 1.5-2 times higher than the one obtained by EIS, and very similar at 333 K. The values measured by EIS by Wohde *et al.*⁴⁸ are in very good agreement with ours. However, their values calculated thanks to the NMR are rather high because they do not take into account the ionic concentration of the ions and make directly the ratio of the diffusion coefficients in Eq. 4.16. Finally, Hittorf method and recent development of electrophoretic NMR measurements⁴⁹ allow to access directly to the true transference number and will bring a new light on the transport properties of IL.

4.7. Post-mortem XPS analysis of the cells after chronopotentiometry

The evolution of the lithium electrodes surface upon the application of an electrical polarization ($50\mu\text{A}\cdot\text{cm}^{-2}$) was probed by XPS. The Figure 4.25 shows the C1s and N1s core level spectra of the IL based electrolytes used in this work.

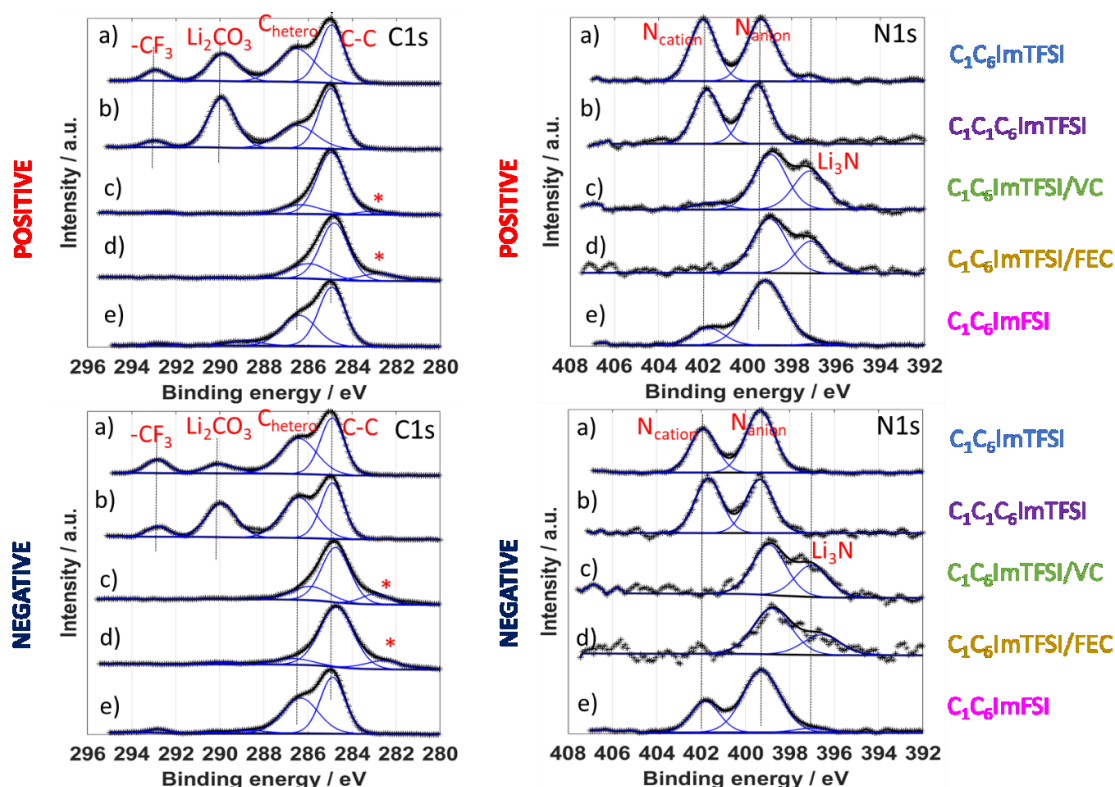


Figure 4.25 XPS spectra of C1s and N1s recorded at the surface of lithium negative (upper spectra) and positive (downer spectra) electrodes after chronopotentiometry experiments in Li/Li coin cells containing (a) $\text{C}_1\text{C}_6\text{ImTFSI}/\text{LiTFSI}$, (b) $\text{C}_1\text{C}_1\text{C}_6\text{ImTFSI}/\text{LiTFSI}$, (c) $\text{C}_1\text{C}_6\text{ImTFSI}/\text{LiTFSI}/\text{VC}$, (d) $\text{C}_1\text{C}_6\text{ImTFSI}/\text{LiTFSI}/\text{FEC}$ and (e) $\text{C}_1\text{C}_6\text{ImFSI}/\text{LiTFSI}$.

For the case of $\text{C}_1\text{C}_6\text{ImTFSI}/\text{LiTFSI}$ and $\text{C}_1\text{C}_1\text{C}_6\text{ImTFSI}/\text{LiTFSI}$, the peaks corresponding to C_{hetero} (286.7 eV) and $-\text{CF}_3$ (293 eV), recorded at the positive and negative electrodes did not change significantly. The presence of Li_2CO_3 related peak (290 eV), associated to the native passivation layer on the surface of lithium electrodes, as it was discussed in chapters 2 and 3, is the signature of the presence of thin SEI layer (below 5nm). It seems that Li_2CO_3 layer is transparent to lithium plating and stripping.

Besides, the peaks corresponding to N_{cation} and N_{anion} related peak do not vary upon lithium deposition.

For the cases $C_1C_6\text{Im}/\text{TFSI}$ doped with VC and FEC additives, the spectra exhibit the decrease of intensities of the peaks $-\text{CF}_3$, C_{hetero} , as well as the Li_2CO_3 peak. In parallel the N_{cation} 1s peak disappears followed by a widened of the N_{anion} (~ 399 eV) peak that leads to the formation of Li_3N (~ 397 eV). Note that this decomposition of the TFSI anion is accompanied by the disappearance of the peak associated to Li_2CO_3 , signature of the presence of thicker SEI layer compared to the non-doped electrolyte. Similarly, in the case of FSI based electrolyte, the SEI layer seems to be thicker than 5 nm, without the formation of Li_3N species.

In Figure 4.26 the F1s and S2p core levels spectra are presented. In the case of the electrolytes $C_1C_6\text{ImTFSI}/\text{LiTFSI}$ and $C_1C_1C_6\text{ImTFSI}/\text{LiTFSI}$, beside the peak at ~ 689 eV, which is attributed to the $-\text{CF}_3$ group, we noticed the formation of LiF (685 eV) at the surface of both electrodes.

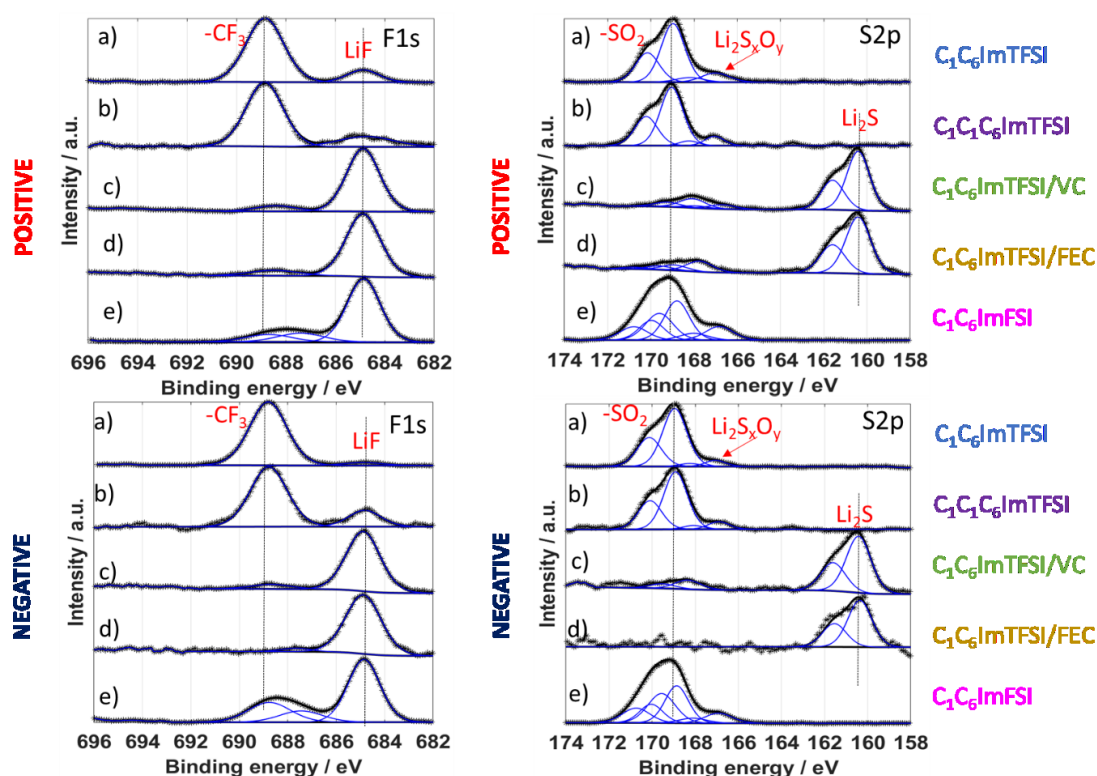


Figure 4.26 XPS spectra of F1s and S2p recorded at the surface of lithium negative (upper spectra) and positive (downer spectra) electrodes after chronopotentiometry experiments in Li/Li coin cells containing (a) $C_1C_6\text{ImTFSI}/\text{LiTFSI}$, (b) $C_1C_1C_6\text{ImTFSI}/\text{LiTFSI}$, (c) $C_1C_6\text{ImTFSI}/\text{LiTFSI}/\text{VC}$, (d) $C_1C_6\text{ImTFSI}/\text{LiTFSI}/\text{FEC}$ and (e) $C_1C_6\text{ImFSI}/\text{LiTFSI}$.

Regarding the S2p spectra, for the first two combinations of electrolytes, we noticed a slight decomposition of $-\text{SO}_2$ (peak at 169 eV) related group to form $\text{Li}_2\text{S}_x\text{O}_y$ species (peak at ~ 167 eV). A similar trend is observed for the $\text{C}_1\text{C}_6\text{ImFSI/LiTFSI}$ electrolyte, although the initial peak of $-\text{SO}_2$ becomes wider.

The situation is completely different for the case of cell polarized using additives doped electrolytes, the initial $-\text{SO}_2$ peak has disappeared, however there is no evidence of a decomposition that leads to the formation of $\text{Li}_2\text{S}_x\text{O}_y$. Instead of this, we identify an intense Li_2S related S2p peak at ~ 161 eV.

In conclusion, for $\text{C}_1\text{C}_6\text{ImTFSI/LiTFSI}$ and $\text{C}_1\text{C}_6\text{ImTFSI/LiTFSI}$, very few decomposition products are observed and the SEI seems to be thinner than 5 nm. For the case of $\text{C}_1\text{C}_6\text{ImFSI/LiTFSI}$, the SEI is thicker because of the formation of LiF and SO_x species.

In contrast, for the cases of additives doped electrolytes the application of an electric current, induces the formation of a SEI layer thicker than 5 nm composed mainly by Li_3N , LiF and Li_2S .

In Figure 4.27, the O1s and Li1s core levels spectra are depicted. As it has been regarded in the F1s and S2p core levels, herein the spectra without additives still preserves the peak related to the $-\text{SO}_2$ bonds at ~ 533 eV, which is accompanied by a peak at ~ 532 eV which can be attributed either to carbonates, $\text{Li}_2\text{S}_x\text{O}_y$ or even LiOH formed by residual traces of water in the electrolytes.

The situation is different in the cases of the cells polarized using additives doped electrolyte. We noticed a broad peak at ~ 531 eV which can be assigned to the presence of $\text{Li}_2\text{S}_x\text{O}_y$, carbonates, LiOH and other degradation byproducts of the additives such as ROLiO_2 . The presence of an intense peak of Li_2O (~ 528 eV) can be examined in the frame of the high reactivity of the fresh plated or striped lithium during polarization. The presence of Li_2O was not evidenced in the case of the aged cell at the OCV conditions.

Finally, the peaks of the Li1s core levels exhibit the presence of a broad peak centered at ~ 55 eV which can be attributed to the different lithium salts formed upon the

polarization (LiF , $\text{Li}_2\text{S}_x\text{O}_y$, Li_3N , Li_2S). These peaks will not be fitted since their exact position is difficult to distinguish. However, for the case of the negative electrodes of the cell polarized using electrolyte containing VC or FEC additive, the presence of a shoulder at ~ 53 eV is a signature of the presence of deposited metallic lithium Li^0 . This affirmation is corroborated by the presence of the characteristic satellite peak (*) of the metallic lithium at energies higher than 58 eV. This result corroborates, the presence of Li_2O due to the high reactivity of the Li^0 formed at the surface.

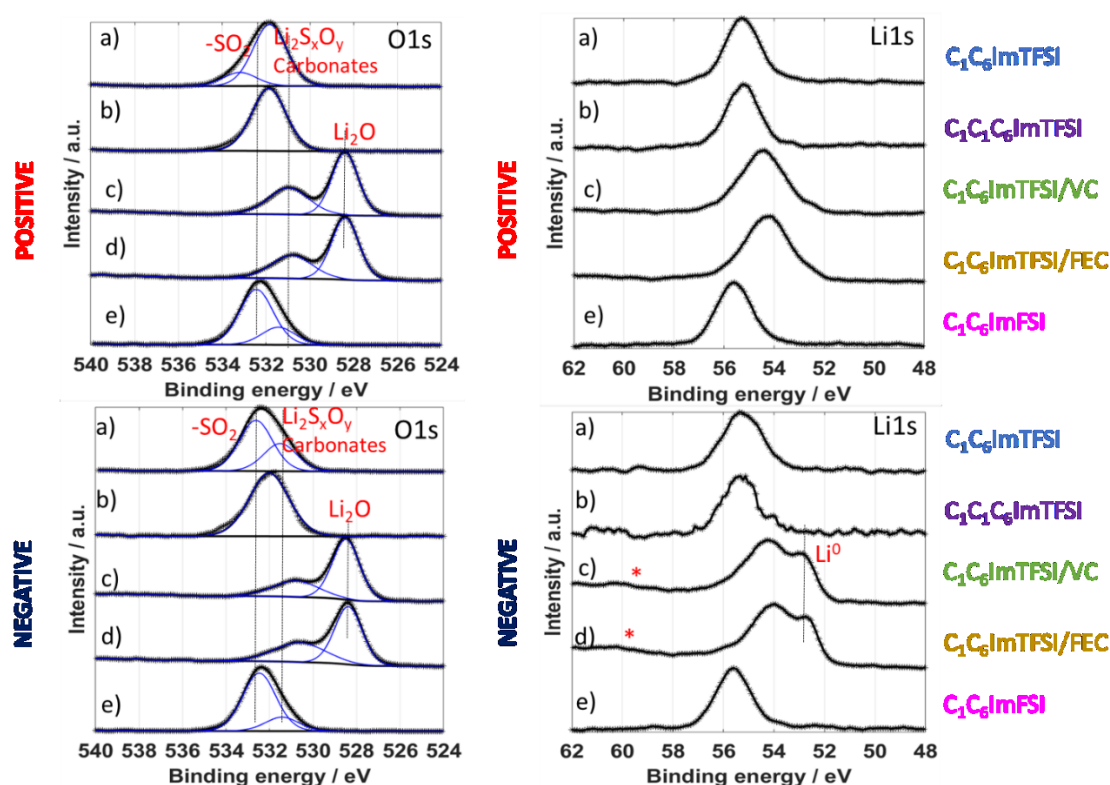


Figure 4.27 XPS spectra of O1s and Li1s recorded at the surface of lithium negative (upper spectra) and positive (downer spectra) electrodes after chronopotentiometry experiments in Li/Li coin cells containing (a) $\text{C}_1\text{C}_6\text{ImTFSI}/\text{LiTFSI}$, (b) $\text{C}_1\text{C}_1\text{C}_6\text{ImTFSI}/\text{LiTFSI}$, (c) $\text{C}_1\text{C}_6\text{ImTFSI}/\text{LiTFSI}/\text{VC}$, (d) $\text{C}_1\text{C}_6\text{ImTFSI}/\text{LiTFSI}/\text{FEC}$ and (e) $\text{C}_1\text{C}_6\text{ImTFSI}/\text{LiTFSI}$.

4.8. SEM/AES analyses of the electrodes after chronopotentiometry

In this section the morphology of the lithium surface electrodes at the different voltage regimes (divergence and short-circuit) as far as the type of dendrites and the chemical composition of the SEI will be discussed based on the SEM/AES analyses.

The photography of the Viledon separators taken after Li/Li cell potential divergence and short-circuit, when $C_1C_6ImTFSI/LiTFSI$ and $C_1C_6ImFSI/LiTFSI$ are used, respectively, are reported in Figure 4.28-a and b. After divergence, the separator is completely covered by a dense deposit of lithium that cannot be removed just by washing the separator. In the case of short-circuit, the little particles of lithium (dendrites) have crossed the separator. Some of these dendrites are not firmly adhered to the separator and can be removed by washing process.

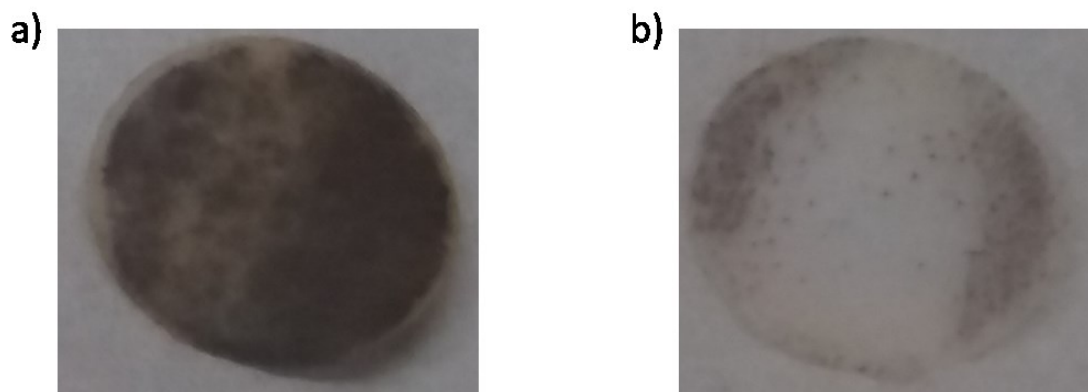


Figure 4.28 Viledon separators of Li/Li coin cells after the application of a current density of $50 \mu A.cm^{-2}$ with the electrolytes: a) $C_1C_6ImTFSI/LiTFSI$ and b) $C_1C_6ImFSI/LiTFSI$.

4.8.1. The regime of divergence of the potential

Figure 4.29-a shows the SEM images of the positive electrode recorded at the chronopotentiometry of $50 \mu A.cm^{-2}$ for a coin cell containing the $C_1C_6ImTFSI/LiTFSI$ electrolyte. Two different types of morphologies are observed, a layer that covers most of the electrode surface, and rectangular like domains that seem to be induced by the fissures across the surface layer.

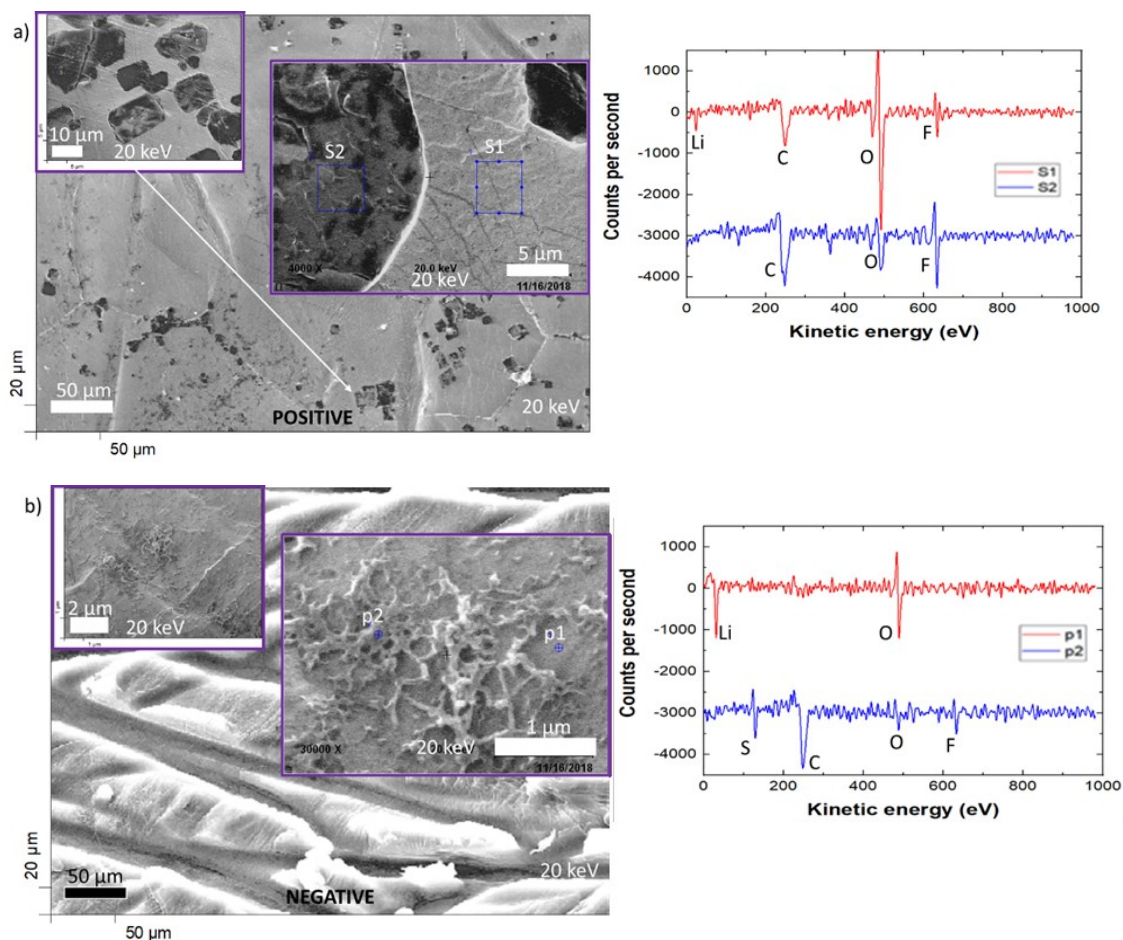


Figure 4.29 SEM images and AES spectra of the positive electrode (a) and the negative electrode (b) after a chronopotentiometry at $50 \mu\text{A}\cdot\text{cm}^{-2}$ using $\text{C}_1\text{C}_6\text{ImTFSI/LiTFSI}$.

Both structures were analyzed by AES, indicate the presence of carbon, oxygen, fluorine and lithium as demonstrated by XPS.

The AES spectra recorded at the surface of the rectangular domains shows the presence of mainly fluorine and carbon. The oxygen is present in a minor concentration. The presence of fluorine can be attributed to the formation of LiF salt. The origin of the observed domains is unknown, however, there are detected also when the cell is polarized at $65 \mu\text{A}\cdot\text{cm}^{-2}$ (Figure 4.30-b), as well as in experiments with pouch cells. The brightness contrast, suggest that both domains have different electronic conductivities, however their origins needs additional investigations.

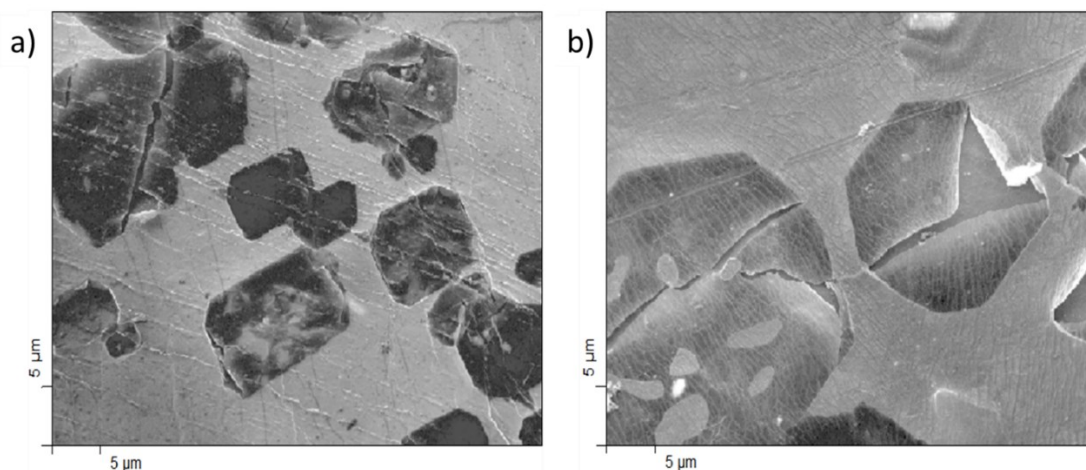


Figure 4.30 SEM images of the rectangular domains presents at the surface of the positive electrode after chronopotentiometry recorded at (A) $50 \mu\text{A}\cdot\text{cm}^{-2}$ and (B) $65 \mu\text{A}\cdot\text{cm}^{-2}$ using $\text{C}_1\text{C}_6\text{ImTFSI/LiTFSI}$.

For the negative electrode, the layer at the surface corresponds with the case at OCV with the presence of fluorine and sulfur degradation byproducts (Figure 4.29-b). Note in inset the presence of a different deposited structure (p2), which morphology seem to be associated to some kind of dendrites. However, AES analysis shows the presence of fluorine and sulfur byproducts but not the presence of lithium. Therefore, they can difficult be associated to the deposited like-mossy lithium which presence is confirmed in the analysis of the Viledon separator (Figure 4.28-a).

4.8.2. The regime of short-circuits

The Figure 4.31-a shows the SEM images of the positive electrode for the system $\text{C}_1\text{C}_6\text{ImFSI/LiTFSI}$. The lithium surface is covered by an homogenous film and dispersed particles. The AES spectra, recorded at different position of the positive electrode, show the presence of fluorine and sulfur, corroborating the XPS measurments (LiF and $\text{Li}_2\text{S}_x\text{O}_y$). Note that the native lithium layer is still visible (point p2) since the AES analysis shows only the presence of lithium and oxygen.

For the SEM image and AES spectra recorded at the surface of the negative electrode (Figure 4.31-b), we notice the presence of lithium dendrite as well as the presence of SEI layer constituted of fluorine and sulfur.

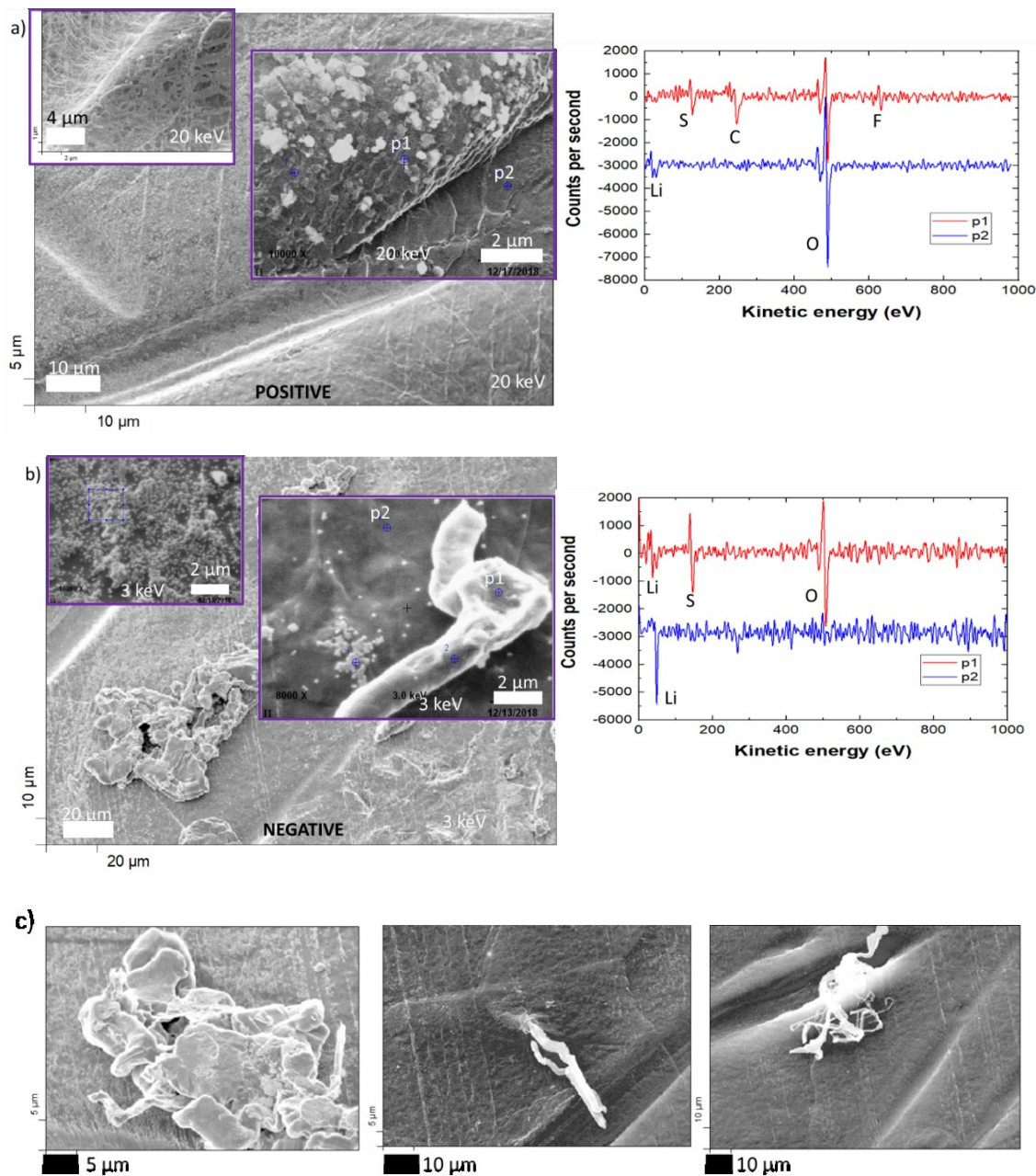


Figure 4.31 SEM images and AES spectra recorded at the surface of (a) the positive and (b) negative electrode after chronopotentiometry using $C_1C_6ImFSI/LiTFSI$. (c) Different structures identified as dendrites for the negative electrode.

4.9. Conclusions

The first part of this chapter has allowed us to revise the oxidation and reduction limits of our IL based electrolytes against lithium metal. We have demonstrated that even at potentials as low as 3.5 V vs. Li⁺/Li, non-negligible oxidation current densities start to appear, which can lead to the decrease of the performance of the system. In special, the C₁C₆ImFSI/LiTFSI electrolyte is not stable at higher potentials since the current density increases upon the cycles. For the other combinations, the role of methylation and additives, mainly FEC, leads to the enhancement of the anodic stability through a surface passivation process.

Regarding the reduction limit, all IL based electrolytes start to reduce at a potential of 2.0 V vs. Li⁺/Li. The reduction by-products have been characterized by XPS for the case of the electrolytes C₁C₆ImTFSI/LiTFSI with and without FEC.

In the case of C₁C₆ImTFSI/LiTFSI, we observe a quick increase of the reduction current density at potentials lower than 0.5 V vs. Li⁺/Li that can be associated to the reduction and/or complexation of the C₁C₆Im⁺ cation to form carbenes species.

The other electrolyte combinations show a relatively good passivation at low potentials until 0.05 V vs. Li⁺/Li with reduction current densities lower than 5 μA.cm⁻². Nonetheless, the CV performed until -0.1 V vs. Li⁺/Li have demonstrated that only with the addition of VC or FEC additives allowed an efficiency higher than 70 % of the plating/stripping process.

In addition, we have studied the polarization of Li/Li coin cell system under current density application. We have evidenced the existence of two regimes of polarisation (divergence of potential and short-circuit), that are in agree with the model predicted by Chazalviel's. For the regime of divergence, the experimental results seem to be in agreement with the inverse-square law ($\tau \propto 1/J^2$).

The EIS experiments have demonstrate differences in the values of the transport number of the electrolyte with respect to the values given by NMR. This confirm that when LiTFSI is added to the neat IL other complexes such as Li(TFSI)₂ are formed. The

values given by EIS highlight the fact that this transport number is very low (~0.06) for IL based electrolytes and need to be improved.

The XPS analysis combined with SEM/AES analyses have demonstrate that two types of SEI are formed:

- For the electrolytes C₁C₆ImTFSI/LiTFSI and C₁C₁C₆ImTFSI/LiTFSI, the SEI is thinner than 5 nm, the reversibility of the plating/stripping process is not possible leading to the deposit of mossy-like lithium or dispersed structures.
- For the electrolytes containing VC or FEC and for C₁C₆ImFSI/LiTFSI, a SEI thicker than 5 nm rich in LiF is formed, favoring the reversibility of the plating/stripping process. However, this layer is susceptible to be crossed by needle-like dendrites. The properties of this kind of SEI can be enhanced with additives as it is demonstrating by the increase of the onset time of short-circuit with respect to the case with C₁C₆ImFSI/LiTFSI.

REFERENCES

- (1) Lin, D.; Liu, Y.; Cui, Y. Reviving the Lithium Metal Anode for High-Energy Batteries. *Nat. Publ. Gr.* **2017**, 12 (3), 194–206.
- (2) Guan, X.; Wang, A.; Liu, S.; Li, G.; Liang, F.; Yang, Y. W.; Liu, X.; Luo, J. Controlling Nucleation in Lithium Metal Anodes. *Small* **2018**, 14 (37), 1–21.
- (3) Cheng, X.-B.; Zhang, R.; Zhao, C.-Z.; Zhang, Q. Toward Safe Lithium Metal Anode in Rechargeable Batteries: A Review. *Chem. Rev.* **2017**, 117 (15), 10403–10473.
- (4) Bouchet, R. Batteries: A Stable Lithium Metal Interface. *Nat. Nanotechnol.* **2014**, 9 (August), 1–2.
- (5) Galiński, M.; Lewandowski, A.; Stepniak, I. Ionic Liquids as Electrolytes. *Electrochim. Acta* **2006**, 51 (26), 5567–5580.
- (6) Appetecchi, G. B.; Montanino, M.; Passerini, S. Ionic Liquid-Based Electrolytes for High Energy, Safer Lithium Batteries. *ACS Symp. Ser.* **2012**, 1117 (January), 67–128.
- (7) Zhang, S.; Sun, N.; He, X.; Lu, X.; Zhang, X. Physical Properties of Ionic Liquids: Database and Evaluation. *J. Phys. Chem. Ref. Data* **2006**, 35 (4), 1475–1517.
- (8) Ghazi, Z. A.; Sun, Z.; Sun, C.; Qi, F.; An, B.; Li, F.; Cheng, H. M. Key Aspects of Lithium Metal Anodes for Lithium Metal Batteries. *Small* **2019**, 1900687, 1–26.
- (9) Tarascon, J. M.; Armand, M. Issues and Challenges Facing Rechargeable Lithium Batteries. *Nature* **2001**, 414 (November), 359–367.

- (10) Zhang, K.; Lee, G. H.; Park, M.; Li, W.; Kang, Y. M. Recent Developments of the Lithium Metal Anode for Rechargeable Non-Aqueous Batteries. *Adv. Energy Mater.* **2016**, 1–14.
- (11) Li, L.; Li, S.; Lu, Y. Suppression of Dendritic Lithium Growth in Lithium Metal-Based Batteries. *Chem. Commun.* **2018**, 54 (50), 6648–6661.
- (12) Bhatt, A. I.; Best, A. S.; Huang, J.; Hollenkamp, A. F. Application of the N-Propyl-N-Methyl-Pyrrolidinium Bis(Fluorosulfonyl)Imide RTIL Containing Lithium Bis(Fluorosulfonyl)Imide in Ionic Liquid Based Lithium Batteries. *J. Electrochem. Soc.* **2010**, 157 (1), A66.
- (13) Best, a. S.; Bhatt, a. I.; Hollenkamp, a. F. Ionic Liquids with the Bis(Fluorosulfonyl)Imide Anion: Electrochemical Properties and Applications in Battery Technology. *J. Electrochem. Soc.* **2010**, 157 (8), A903.
- (14) Basile, A.; Bhatt, A. I.; O’Mullane, A. P. Stabilizing Lithium Metal Using Ionic Liquids for Long-Lived Batteries. *Nat. Commun.* **2016**, 7 (11794), 1–11.
- (15) Chazalviel, J. N. Electrochemical Aspects of the Generation of Ramified Metallic Electrodeposits. *Phys. Rev. A* **1990**, 42 (12), 7355–7367.
- (16) Brissot, C.; Rosso, M.; Chazalviel, J. N.; Baudry, P.; Lascaud, S. In Situ Study of Dendritic Growth in Lithium/PEO-Salt/Lithium Cells. *Electrochim. Acta* **1998**, 43 (10-11), 1569-1574.
- (17) Brissot, C.; Rosso, M.; Chazalviel, J. N.; Lascaud, S. Dendritic Growth Mechanisms in Lithium/Polymer Cells. *J. Power Sources* **1999**, 81-82, 925-929.
- (18) Rosso, M.; Gobron, T.; Brissot, C.; Chazalviel, J. N.; Lascaud, S. Onset of Dendritic Growth in Lithium/Polymer Cells. *J. Power Sources* **2001**, 97–98, 804–806.
- (19) Aurbach, D.; Zinigrad, E.; Cohen, Y.; Teller, H. A Short Review of Failure Mechanisms of Lithium Metal and Lithiated Graphite Anodes in Liquid Electrolyte Solutions. *Solid State Ionics* **2002**, 148 (3–4), 405–416.
- (20) Xu, W.; Wang, J.; Ding, F.; Chen, X.; Nasybulin, E.; Zhang, Y.; Zhang, J.-G. Lithium Metal Anodes for Rechargeable Batteries. *Energy Environ. Sci.* **2014**, 7 (2), 513–537.
- (21) Michan, A. L.; Parimalam, B. S.; Leskes, M.; Kerber, R. N.; Yoon, T.; Grey, C. P.; Lucht, B. L. Fluoroethylene Carbonate and Vinylene Carbonate Reduction: Understanding Lithium-Ion Battery Electrolyte Additives and Solid Electrolyte Interphase Formation. *Chem. Mater.* **2016**, 28 (22), 8149–8159.
- (22) Zhang, X. Q.; Cheng, X. B.; Chen, X.; Yan, C.; Zhang, Q. Fluoroethylene Carbonate Additives to Render Uniform Li Deposits in Lithium Metal Batteries. *Adv. Funct. Mater.* **2017**, 27 (10), 1–8.
- (23) Tułodziecki, M.; Tarascon, J.-M.; Taberna, P.-L.; Guéry, C. Catalytic Reduction of TFSI-Containing Ionic Liquid in the Presence of Lithium Cations. *Electrochem. commun.* **2017**, 77 (17), 128–132.
- (24) Gagne, R. R.; Koval, C. A.; Lisensky, G. C. Ferrocene as an Internal Standard for Electrochemical Measurements. *Inorg. Chem.* **1980**, 19 (9), 2854-2855.
- (25) Pavlishchuk, V. V.; Addison, A. W. Conversion Constants for Redox Potentials Measured versus Different Reference Electrodes in Acetonitrile Solutions at 25°C. *Inorganica Chim. Acta* **2000**, 298 (1), 97-102.
- (26) Huston, R.; Butler, J. N. The Standard Potential of the Lithium Electrode in Aqueous Solutions. *J. Phys. Chem.* **1968**, 72 (12), 4263–4264.

- (27) Srour, H.; Rouault, H.; Santini, C. C. Study on Cycling Performance and Electrochemical Stability of 1-Hexyl-3-Methylimidazolium Bis(Trifluoromethanesulfonyl)Imide Assembled with $\text{Li}_4\text{Ti}_5\text{O}_{12}$ and LiFePO_4 at 333 K. *J. Electrochem. Soc.* **2013**, 160 (6), A781–A785.
- (28) Matsumoto, H.; Sakaebe, H.; Tatsumi, K.; Kikuta, M.; Ishiko, E.; Kono, M. Fast Cycling of Li/LiCoO₂ Cell with Low-Viscosity Ionic Liquids Based on Bis(Fluorosulfonyl)Imide [FSI]-. *J. Power Sources* **2006**, 160 (2 SPEC. ISS.), 1308–1313.
- (29) Baek, B.; Lee, S.; Jung, C. Pyrrolidinium Cation-Based Ionic Liquids with Different Functional Groups: Butyl, Butyronitrile, Pentenyl, and Methyl Butyrate. *Int. J. Electrochem. Sci.* **2011**, 6 (12), 6220–6234.
- (30) Schmitz, P.; Jakelski, R.; Pyschik, M.; Jalkanen, K.; Nowak, S.; Winter, M.; Bieker, P. Decomposition of Imidazolium-Based Ionic Liquids in Contact with Lithium Metal. *ChemSusChem* **2017**, 10 (5), 876–883.
- (31) Kerner, M.; Johansson, P. Pyrrolidinium FSI and TFSI-Based Polymerized Ionic Liquids as Electrolytes for High-Temperature Lithium-Ion Batteries. *Batteries* **2018**, 4 (1), 10.
- (32) Ko, J.; Yoon, Y. S. Recent Progress in LiF Materials for Safe Lithium Metal Anode of Rechargeable Batteries: Is LiF the Key to Commercializing Li Metal Batteries? *Ceram. Int.* **2019**, 45 (1), 30–49.
- (33) Yang, Y.; Xiong, J.; Lai, S.; Zhou, R.; Zhao, M.; Geng, H.; Zhang, Y.; Fang, Y.; Li, C.; Zhao, J. Vinyl Ethylene Carbonate as an Effective SEI-Forming Additive in Carbonate-Based Electrolyte for Lithium-Metal Anodes. *ACS Appl. Mater. Interfaces* **2019**, 11, 6118–6125.
- (34) Ong, S. P.; Andreussi, O.; Wu, Y.; Marzari, N.; Ceder, G. Electrochemical Windows of Room-Temperature Ionic Liquids from Molecular Dynamics and Density Functional Theory Calculations. *Chem. Mater.* **2011**, 23 (11), 2979–2986.
- (35) Xu, K. Electrolytes and Interphases in Li-Ion Batteries and Beyond. *Chem. Rev.* **2014**, 114 (23), 11503–11618.
- (36) Howlett, P. C.; Izgorodina, E. I.; Forsyth, M.; MacFarlane, D. R. Electrochemistry at Negative Potentials in Bis(Trifluoromethanesulfonyl)Amide Ionic Liquids. *Zeitschrift für Phys. Chemie* **2006**, 220 (10), 1483–1498.
- (37) Xu, K. Nonaqueous Liquid Electrolytes for Lithium-Based Rechargeable Batteries. *Chem. Rev.* **2004**, 104 (10), 4303–4417.
- (38) Aurbach, D.; Weissman, I.; Zaban, A.; Chusid, O. Correlation between Surface Chemistry, Morphology, Cycling Efficiency and Interfacial Properties of Li Electrodes in Solutions Containing Different Li Salts. *Electrochim. Acta* **1994**, 39 (1), 51–71.
- (39) Rosso, M.; Brissot, C.; Teyssot, A.; Doll, M.; Sannier, L.; Tarascon, J. M.; Bouchet, R.; Lascaud, S. Dendrite Short-Circuit and Fuse Effect on Li/Polymer/Li Cells. *Electrochim. Acta* **2006**, 51 (25), 5334–5340.
- (40) Teyssot, A.; Armand, M. Étude de l'Interface Lithium Métal / Électrolyte Polymère Fondu et Gélifié., Thèse Doctorale, LPMC, **2005**.
- (41) Bai, P.; Li, J.; Brushett, F. R.; Bazant, M. Z. Transition of Lithium Growth Mechanisms in Liquid Electrolytes. *Energy Environ. Sci.* **2016**, 13–17.
- (42) Goodenough, J. B.; Kim, Y. Challenges for Rechargeable Li Batteries. *Chem. Mater.* **2010**, 22 (3), 587–603.

- (43) Watanabe, M.; Thomas, M. L.; Zhang, S.; Ueno, K.; Yasuda, T.; Dokko, K. Application of Ionic Liquids to Energy Storage and Conversion Materials and Devices. *Chem. Rev.* **2017**, 117 (10), 7190-7239
- (44) Lewandowski, A.; Świdorska-Mocek, A. Ionic Liquids as Electrolytes for Li-Ion Batteries-An Overview of Electrochemical Studies. *J. Power Sources* **2009**, 194 (2), 601–609.
- (45) Bolimowska, E.; Castiglione, F.; Devemy, J.; Rouault, H.; Mele, A.; Pádua, A. A. H.; Santini, C. C. Investigation of Li⁺ Cation Coordination and Transportation, by Molecular Modeling and NMR Studies, in a LiNTf₂-Doped Ionic Liquid-Vinylene Carbonate Mixture. *J. Phys. Chem. B* **2018**, 122 (36), 8560-8569.
- (46) Bruce, P. G.; Vincent, C. A. Steady State Current Flow in Solid Binary Electrolyte Cells. *J. Electroanal. Chem.* **1987**, 225 (1–2), 1–17.
- (47) Hiller, M. M.; Joost, M.; Gores, H. J.; Passerini, S.; Wiemhöfer, H. D. The Influence of Interface Polarization on the Determination of Lithium Transference Numbers of Salt in Polyethylene Oxide Electrolytes. *Electrochim. Acta* **2013**, 114, 21–29.
- (48) Wohde, F.; Balabajew, M.; Roling, B. Li⁺ Transference Numbers in Liquid Electrolytes Obtained by Very-Low-Frequency Impedance Spectroscopy at Variable Electrode Distances. *J. Electrochem. Soc.* **2016**, 163 (5), A714–A721.
- (49) Gouverneur, M.; Schmidt, F.; Schönhoff, M. Negative Effective Li Transference Numbers in Li Salt/Ionic Liquid Mixtures: Does Li Drift in the “Wrong” Direction? *Phys. Chem. Chem. Phys.* **2018**, 20 (11), 7470–7478.

CHAPTER 5: Operando XPS a novel approach for the study of lithium/electrolyte interphase

The current development of the lithium metal batteries is intimately related to the comprehension of the chemical structure and the reactivity of the electrolytes at the surface of the lithium electrode. Thus, it is essential to understand the interfacial processes that induce the degradation of the electrolytes and lead to the decrease of the Coulombic efficiency and promote the growth of lithium dendrites. A deep fundamental research on the mechanisms involved during the electrochemical cells operating is required to bring optimal solutions with higher safety and efficiency requirement. Within this framework, the most understanding of redox process and solid electrolyte interphase (SEI) formation, occurring in the electrochemical cells, are based on ex-situ characterization protocols involving glove boxes, transfer vessels, and specific washing process, which may spoil the coveted information. One of the direct tools to probe both SEI growth and redox process during electrochemical cycling is the X-ray photoemission spectroscopy (XPS). However, most of XPS investigation are performed through a post-mortem process, involving well established protocols. Nevertheless, surface contamination or evolution after cell de-assembling are source of artefact. Hence, the aim of this work is to design a new electrochemical cell adapted for the study of the interface electrode/electrolyte by XPS in operando mode. Besides developing a compatible electrochemical cell for operando XPS (O-XPS) studies, this new approach will be devoted to study the degradation process occurring at the interface between electrolyte and lithium metal.

5.1.	Introduction	165
5.2.	Operando characterization for battery technology	165
5.2.1.	Optical techniques	166
5.2.2.	Electron beam based techniques.....	168
5.2.3.	X-ray techniques	171
5.2.4.	Scanning Probe Microscopy.....	171
5.2.5.	Neutron based techniques.....	172
5.2.6.	X-ray photoelectrons spectroscopy	172
5.2.7.	Conclusion.....	174
5.3.	OXPS Experimental set-up	174
5.3.1.	XPS spectrometer and sample holder up-grade.....	174
5.3.2.	Cell design.....	176
5.3.3.	OXPS sampling and protocol	177
5.3.4.	OXPS sample optimization and connectivity to the potentiostat	178
5.3.5.	X-ray beam and acquisition parameter optimization.....	179
5.4.	OXPS study of the interface lithium/imidazolium based IL electrolyte, result and discussion	180
5.4.1.	OXPS study of lithium/IL based electrolyte/lithium under chronoamperometry 180	
5.4.2.	OXPS study of lithium/IL based electrolyte/lithium at the OCV.....	182
5.4.3.	OXPS study of the interface Lithium/IL electrolyte under polarization	183
5.5.	Conclusions	187

5.1. Introduction

The characterization of the chemical environment of the SEI frequently requires the use of *post-mortem* protocols to extract and prepare the electrodes to analyze their surface. Although the results of this protocol are largely accepted by the scientific community through several years of research, there exist some controversial about the possibility of alteration of the chemical state of the electrodes during the disassembling of the cells, the washing of the electrodes and their transport until the characterization equipment.

Controlling the lithium dendrite growth from lithium represents a key factor to unblock the use of lithium metal as negative electrode for lithium battery technology. Metallic lithium anode which gives the high theoretical specific capacity is limited by the occurrence of dendritic growth during the charge of the battery. In battery technology, the interface plays a crucial role, particularly the surface of lithium in contact with the electrolyte is usually covered by a passivation layer which affects the capacity stability and safety hazards of lithium batteries. The complete understanding of this phenomenon might pave the way for the best operating conditions for lithium batteries. Most of the characterization tools used to perform post-mortem analyses in battery field have been explored to design and perform operando studies. However, neither has been conclusive to be well established protocol with high figure of merit, especially surface sensitive techniques such as XPS.

5.2. Operando characterization for battery technology

We noticed that the post-mortem characterization protocol is largely accepted by the scientific community through several years of research. However, the possibility of alteration of the chemical state of the electrodes during the disassembling of the cells, the washing of the electrodes and their transport until the characterization equipment, is source of controversy.

In the frame of lithium battery technology, several techniques have been developed to follow in *operando* condition the lithium surface reactivity toward liquid and solid electrolytes and in the meantime the dendrite growth process. Besides, the knowledge of the redox processes obtained by these techniques, some limitation, associated to material

sensitivity and characterization tools constraint, are still a breakdown to widen our pictures regarding the origin of LIB fading origin. This leads to the development of *operando* characterization techniques.

Since lithium battery cell are not transparent, it is necessary to design the electrochemical system to be adapted to the constraint imposed by each characterization tool. Moreover, several of them are operating under high vacuum conditions, which is a challenge to perform operando analyses with volatile electrolyte based batteries. Hence, the development of operando protocols must take in consideration, the constraint associated to the battery system and characterization equipment. Here, we are listing the most state of art techniques that have been adapted to perform operando analyses.

5.2.1. Optical techniques

5.2.1.1. Operando Optical microscopy

The optical microscope was used mainly to visualize the dendrite growth during lithium plating and stripping. The electrochemical cell used for this purpose is a simplified transparent representation of lithium battery. Most designed cells, reported in the literature, are quasi bi-dimensional parallelepiped cells, made of two glass plates as reported in Figure 5.1.¹

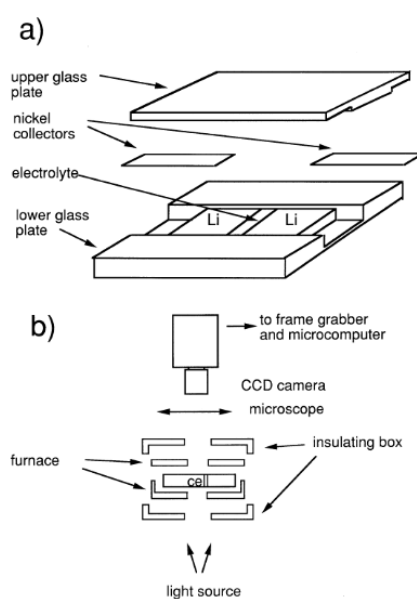


Figure 5.1 (a) schematic representation of designed electrochemical cell for optical visualization of lithium dendrite growth, (b) experimental setup connected to the microscope including CCD (charge-coupled device) camera and furnace.¹

This designed cell was used in lithium/polymer/lithium cell mainly to study the lithium dendrite growth in the framework of Chazalviel's model.² The evolution of the cell potential with time was evaluated by impedance measurements performed while the cells under *in-situ* optical microscopy observation were polarized. In conjunction with a simple equivalent circuit model, these experiments enable to quantitatively describe the evolution of dendrites with time and a thermo-fusible effect predicted by Bouchet *et al.*³

Hence, this experimental set-up allowed the simultaneous measurement of the cell potential, and the evolution of the dendrite growth with regards to the ionic concentration gradient in the electrolyte near the Li surface at a characteristic Sand time.

In a lithium/polymer electrolyte/lithium cell, the inter-electrode *in-situ* ionic concentration evolution has been reported by studying the light absorption profile across the cell during the aging.⁴ However, the experiment does not allow to follow this evolution during long times due to the electrochemical production of impurities at the surface of the electrodes affording ionic concentration instabilities in the cell.

Since the surface morphology of lithium anode affects the performance of the cell and the nature of the dendrite growth regime, this optical cell does not allow reproducible measurements and moreover hardly adapted to other lithium ion battery system. Moreover, the resolution of optical microscopy is fundamentally restricted by the diffraction limit of visible light, which is not sufficient to monitor microstructural changes. However, electrochemically induced macroscopic structural changes of electrodes and dendritic lithium formation which can be investigated through (digital) optical microscopy.

Note that with graphite electrode, the coloration of lithiated graphite is a measure of its state of charge,⁵ the (de)lithiation process of graphite can be studied with an optical microscope by tracking the color evolution.

5.2.1.2. Operando Raman and Fourier transform infrared spectroscopy

The use of *in-situ* Raman in electrochemical field has been reviewed by Stancovski *et al.*⁶ As, the laser light in Raman spectroscopy must reach electrode, as with the optical

microscope, all designed cells are configured with a hole to expose the surface electrode to the light beam.^{7,8} Therefore, the amount of liquid electrolyte in the pathway of the laser light can be kept to a minimum limiting the undesired light scattering by the electrolyte which decreases the cell performance. Infrared spectroscopy (FTIR) technique based on the absorption of infrared light, is often applied to probe the nature of the interfacial reactions between a working electrode and the electrolyte in the reactive mode, but also to identify gas products that can be formed. A relatively large numbers of different battery setups for *in situ* FTIR research have been designated.^{9,10} Several window materials *e.g.* KBr, CaF₂ and diamond., transparent to infra-red light allowing the beam to reach the working electrode, have been applied. Most of the experimental setups do not have a conventional half-cell, sandwich-like structure but have a more open structure with the counter electrode positioned aside the working electrode. This configuration ensures good accessibility to the electrode of interest which is necessary as the infrared beam is incident at an angle fixed to obtain a maximum reflection intensity. Such a design furthermore allows the incorporation of a reference electrode.

5.2.2. Electron beam based techniques

5.2.2.1. *In situ* scanning electron microscopy (SEM) observations of Li plating and stripping

Due to the drastic vacuum conditions needed to perform SEM images, gel or polar electrolyte are not adequate for *in-situ* observations. In the case of polymer electrolyte, which requires operating at higher temperatures (greater than 80°C), the equipment must be able to heat the cell. Most of the developed cells are based layered anode/electrolyte/cathode system using a polymer electrolyte consists of poly(ethylene oxide) (PEO) and a LiN(CF₃SO₂)₂ lithium salt referred to as (LiTFSI).^{11,12} These approaches allowed to observe the dendrite growth occurring right after a short-circuit upon polarization, however the correlations between electrolytic properties and dendrite growth were not successful.

Since the main question is to comes-out with the origin of lithium dendrite growth in real battery system, in relation with electrolyte and surface electrode properties, Ota *et al.*¹³ have studied by the mean of quasi *in-situ* SEM the effect of the electrolyte

composition on the shape and the morphology of the growth dendrites. The surface and cross-sectional morphologies of deposited lithium on a nickel substrate in LiN(SO₂C₂F₅)₂ (LiBETI) electrolytes with ethylene carbonate (EC) + tetrahydropyran (THP), dimethoxyethane, dimethylcarbonate (DMC), propylenecarbonate (PC), γ -butyrolactone (GBL) (1:1) binary solvents were investigated by *in-situ* SEM observation. The authors found out that lithium cycling efficiency increases following the order THP > DME > DMC > PC > GBL. Moreover, THP containing electrolyte exhibits a fine particle morphology. The authors claimed that the reductive stability of the solvents plays a role in the lithium dendrite formation. The evolutions of the lithium cycling efficiency and the lithium surface morphology when the organic electrolyte EC containing LiBETI is mixed with organic additives are depicted in Table 5.1. Dendrites are not observed in the mixture EC :THP (1:1).¹³

Table 5.1 relation between lithium cycling efficiency and surface morphology in various EC mixed solvent containing LiBETI.¹³

Solute	Solvent	Lithium deposition current density (mA/cm ²)	Lithium deposition charge quantity (C/cm ²)	Li cycling efficiency(%)		Morphology	Thickness after 50 cycles (μm)
				Average 1-20 cycles	Average 1-50 cycles		
LiBETI	EC + THP (1:1)	0.2	0.5	92	91	Fine particle	11
		0.2	1.0	93	92	Particle	26
		0.2	2.0	94	92	Large particle	49
		0.6	0.5	88	88	Particle	14
		1.0	0.5	84	81	Particle and dendritic	38
	EC + DME (1:1)	0.6	0.5	88	87	Particle and dendritic	28
	EC + DMC (1:1)	0.6	0.5	84	82	Particle and dendritic	38
	EC + PC (1:1)	0.6	0.5	69	72	Dendritic	47
	EC + GBL (1:1)	0.6	0.5	60	62	Dendritic	52

A similar study on lithium dendrite formation with a EC and THF mixed solvent several lithium salts LiPF₆, LiTFSI, and LiBTI was reported, Table 5.2.¹³ Obviously, the nature of the anion has a key role, higher are its steric hindrance and its charge delocalization lower are the dendrite formation and higher the cycling stability.

Table 5.2 effect of electrolyte temperature by change of solute in EC and THF mixed solvent.¹³

Solute	Temperature (°C)	Li cycling efficiency(%)		Cycle stability	Morphology	Thickness after 50 cycles (μm)
		Average 1-20 cycles	Average 1-50 cycles			
LiPF ₆	0	78	74	Bad	Dendritic	29
	25	80	80	Good	Particle and dendritic	24
	50	81	79	Good	Flat	41
LiTFSI	0	81	72	Bad	Dendritic	26
	25	87	83	Bad	Dendritic	29
	50	89	89	Very good	Large particle	31
LiBETI	0	83	81	Good	Fine particle	24
	25	87	88	Very good	Particle	15
	50	89	89	Very good	Large particle	24

5.2.2.2. Transmission Electron Microscopy

Recent breakthrough in the field of *in situ* techniques for battery research has been the development of *in-situ* transmission electron microscopy (TEM). After the initial work of Huang *et al.*¹⁴ in 2010 on the (de)lithiation of a single SnO₂ nanowire, many reports on nanostructured electrodes studied by *in-situ* TEM have been published.¹⁵ Only ultra-thin samples *i.e.*, nano-batteries, can be investigated, which makes the technique challenging and creates some source of artefacts such as local heat or current distribution across the cell induced by energetic electron beam. This technique informs on the morphology changes during battery operation, and additionally with its additional integrated techniques, such as electron diffraction and electron energy loss spectroscopy (EELS), can provide data on the chemical composition and structure changes at the electrode surface. In this approach two types of devices have been designed all-solid-state batteries and a cells¹⁵ with a SnO₂ partially nanowire flooded in an ionic liquid, Figure 5.2.^{14,15}

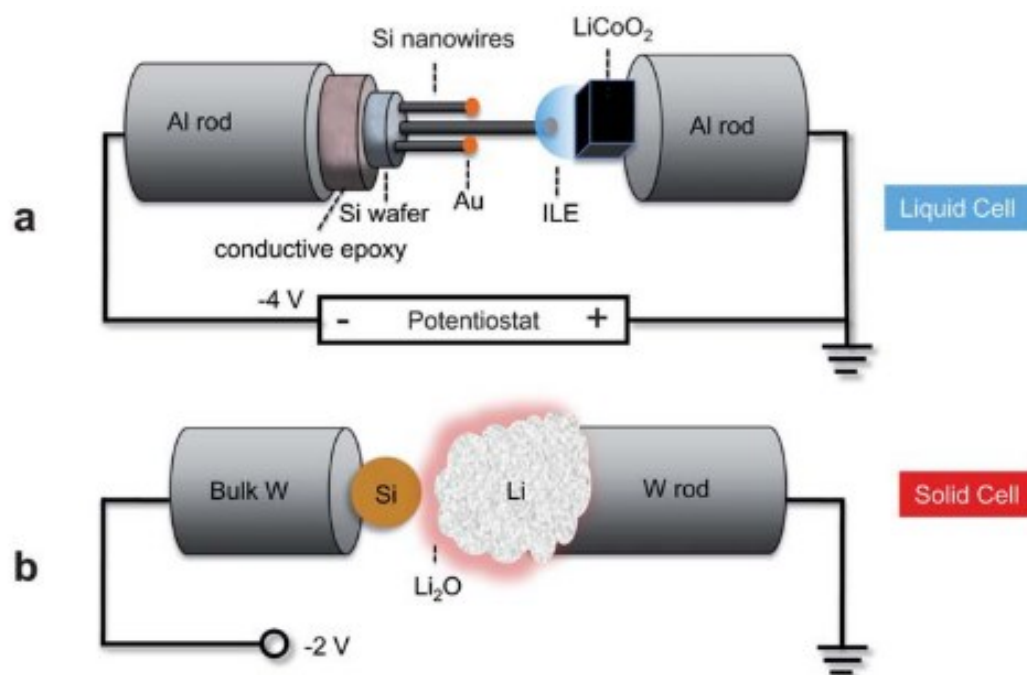


Figure 5.2 Schematic representation of the open nano-cell setup enabling *in-situ* TEM. (a) Ionic liquid based electrolyte configuration,¹⁴ (b) solid state electrolyte based cell.¹⁵

5.2.3. X-ray techniques

5.2.3.1. X-ray diffraction

The operando XRD, represent the most well established technique among the adapted characterization tools for operando measurement. XRD can be used to investigate how intercalants modify the crystal structure, morphology, and mechanical properties of host 2D materials. X-ray transparent window needs to be incorporated in the design in order to allow the X-rays penetration to the targeted electrode(s).^{16,17} Battery designs for *in situ* XRD measurements are available, for which a proper pressure applied to the cell is essential to obtain reliable results. The high energy photons sources available at the synchrotron radiation facilities allowed conduct operando XRD measurements on real cell in the transmission mode in order to obtain simultaneously 2D-diffraction patterns on both cathode and anode electrodes.¹⁸

5.2.3.2. X-ray tomography microscopy

X-ray tomographic microscopy is an advanced form of transmission X-ray microscopy (TXM) for which the *in situ* cell can be rotated over 180° to obtain a series of 2D images that can be reconstructed using a tomographic algorithm to establish a 3D microstructure representation. The changes in attenuation coefficient is related to changes in composition and mass density, enabling visualization and quantification of the phase transitions of electrode or even dendrite growth with regards the cycling conditions.^{19,20}

5.2.4. Scanning Probe Microscopy

Atomic Force microscopy (AFM), electrochemical strain microscopy (ESM), and scanning ion conductance microscopy (SICM) can bring valuable information on the surface change by scanning the evolution of the interface between the electrode and liquid electrolyte. Thus volume change and/or SEI formation upon cycling can be visualized. With AFM tip acting as current collector, it is now possible to study the surface potential and topography changes as a function of the applied voltage.

5.2.5. Neutron based techniques

Due to the large penetration depth of the neutrons, measurements can be performed on unmodified commercial cells and diffraction patterns of the anode and cathode can be obtained simultaneously.²¹ However, the technique is very sensitive to the hydrogen present in the separators and liquid electrolytes of commercial cells, which unfortunately gives rise to large background signals from incoherently scattered neutrons.^{22,23}

5.2.6. X-ray photoelectrons spectroscopy

Regarding the XPS studies on batteries materials, the most understanding of redox process and solid electrolyte interfaces (SEI) formation, occurring in the electrochemical cells, are based on *ex-situ* characterization protocols involving glove boxes, transfer vessels, and specific washing process, which may spoil the coveted information. However, it is a direct and non-destructive tools to probe both SEI growth and redox process during electrochemical cycling.

Only few works have been reported on the O-XPS investigations of electrochemical systems since the spectroscopic tool is not compatible with volatile electrolyte.^{24–26} The Ultra High Vacuum (UHV), necessary to perform XPS, consist a strong limitation of this new approach as well as the depth analyses in laboratory XPS which is around 5 nm and X-ray beam size dimension which do not exceed the 10 μ m in the modern XP spectrometers.

In this framework, all solid battery present certain compatibilities to perform operando measurement. However, the most designed cells attempt to perform O-XPS on a hole made on the working electrode by ionic etching. These methods induce several artefacts related to the preferential sputtering induced by ion beam (surface roughness, chemical modification and surface contamination).

One of the alternative to all solid battery, is the use of ionic liquid based electrolyte since it has low vapor pressure ($\sim 10^{-10}$ Pa) allowing compatibility with UHV techniques such as XPS.

Weingarth *et al.*²⁶ performed an *in situ* XPS analysis of the anodic reaction of 1-ethyl-3-methylimidazolium tetrafluoroborate/Pt ($[\text{C}_1\text{C}_2\text{Im}][\text{BF}_4]/\text{Pt}$) performed in three electrode cell using activated carbon as working electrode and Pt as reference and counter electrode.²⁶

This *in situ* XPS cell consists on a reaction vessel made from Polyether ether ketone (PEEK) (1). The working electrode (WE) (3) is placed in a position appropriate for XPS analysis and fixed with a piece of titanium. Reference (RE) and counter electrode (CE) (5) are prepared of activated carbon (AC, YP17) wetted with the IL, and placed on the opposite side walls of the vessel where they are contacted with titanium wires. Kapton insulated wires (7) are used to independently connect WE, CE and RE to the respective contact. The WE is connected to the ground of the XPS system via the specimen holder. Since WE, RE and CE have to be insulated against each other, PEEK screws as well as a PEEK interlayer are used. Within the analyzer chamber, the sample holder is put into the fitting of the manipulator arm (9) and the connections of RE and CE are established with sliding contacts, Figure 5.3.²⁶

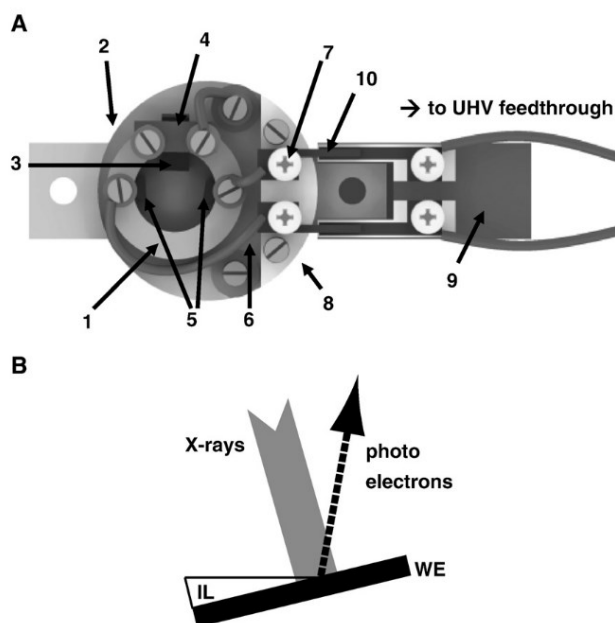


Figure 5.3 The operando cell proposed by Weingarth *et al.*²⁶ (A) and the analyzed area probed by XPS (B).

By using this setup, the authors have observed a change in the core level spectra under a cyclic voltammetry sequence, however, the origin of the shift is not clearly identified.

It seems that the binding energy shift is associated to a potential drop at the interface electrolyte/electrode rather than chemical change. The authors did not mention on the wettability of the IL, hence, it is hardly to admit that the sketch in the Figure 5.3 (B) is representative to the surface of the probed area.

Xiaohan Wu *et al.* studied in all solid battery A mixture of LiCoO_2 (LCO) and $(\text{Li}_2\text{S})_3\text{-P}_2\text{S}_5$ (LPS) cycled vs. InLi_x . Their setup did not allow to make direct correlation between lithium insertion and the redox process, however, it allows to follow the surface potential change as a function of the applied potential.²⁵

5.2.7. Conclusion

The surface sensitivity of XPS requires lot of care to establish accurate operando protocol with regards of representative electrochemical measurement.

In this thesis work, based on step-by-step coupling XPS within post-mortem and operando analyses allowed as to validate both approaches in order to study the surface reactivity of the lithium electrode towards IL based electrolytes at the OCV and cycling conditions.

5.3. OXPS Experimental set-up

5.3.1. XPS spectrometer and sample holder up-grade

The OXPS was performed on the VersaProbe-II from ULVAC-PHI, equipped with an upgraded stage allowing an external connection to perform electrical, thermal or electrochemical solicitation. The XPS is equipped with micro-focused X-ray beam (10 to $200 \mu\text{m}^2$). The spectrometer allowed the realization of secondary electron induced X-ray image. This imaging mode will be used to precisely define the analyzed area during OXPS.

ULVAC-PHI has developed an adapted sample holder with four contact facilities and hot plate, using the Peltier effect, to heat in situ the sample within temperature range of -140 to 800°C (Figure 5.4).

The spectrometer can be connected and adapted to different potentiostats. In this work, we have used two different potentiostats, VMP-300 from BioLogic Science Instrument and Solartron 1260 Impedance Analyzer (Figure 5.4-b).

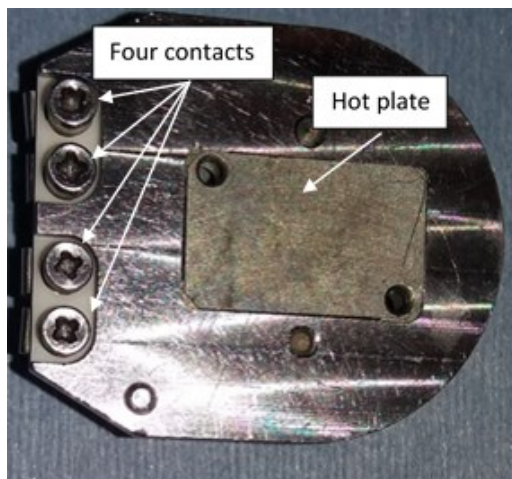


Figure 5.4 ULVAC-PHI sample holder equipped with four contacts and hot plate (-140 to 800°C) using Peltier effect.

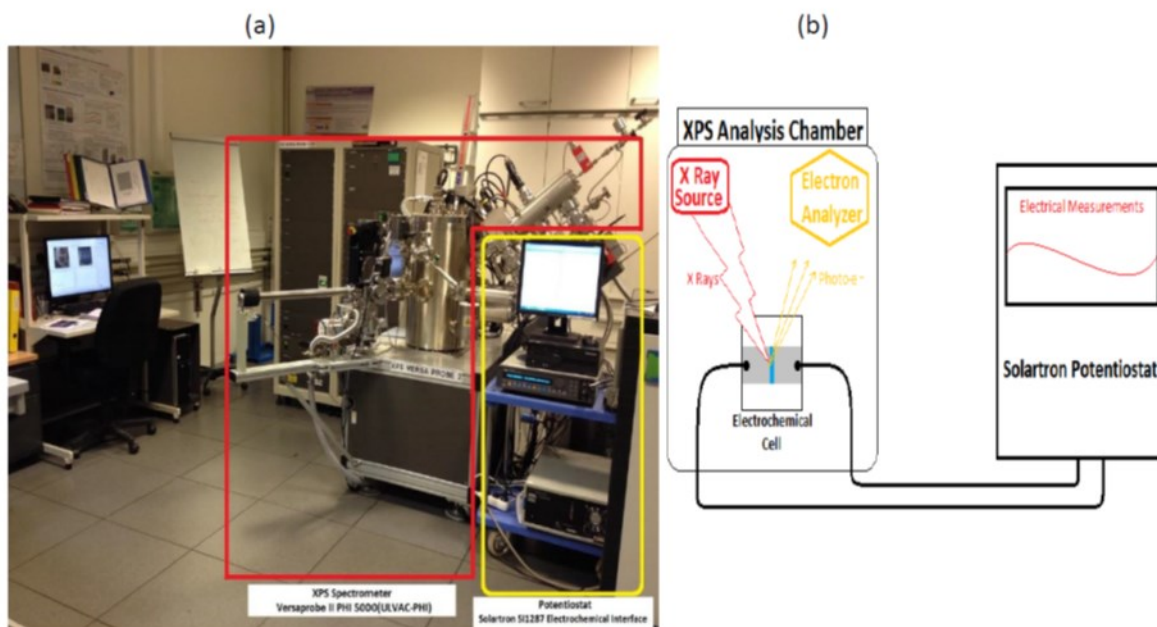


Figure 5.5 XPS VersaProbe-II connected to a Solartron 1260 Impedance Analyzer.

5.3.2. Cell design

Different cells were designed to perform the OXPS based on two main architectures, reaction vessel-like and planar cell-like as reported in Figure 5.6-a and b, respectively.

The reaction vessel-like made from PEEK is inspired from Weingarth *et al.* work and allowed three electrode device.²⁶ Both cells allowed XPS. The planar-like cell, is made from transparent glass allowing both OXPS and optical visualization of the interface between lithium and electrolyte and eventually the presence of dendrites.

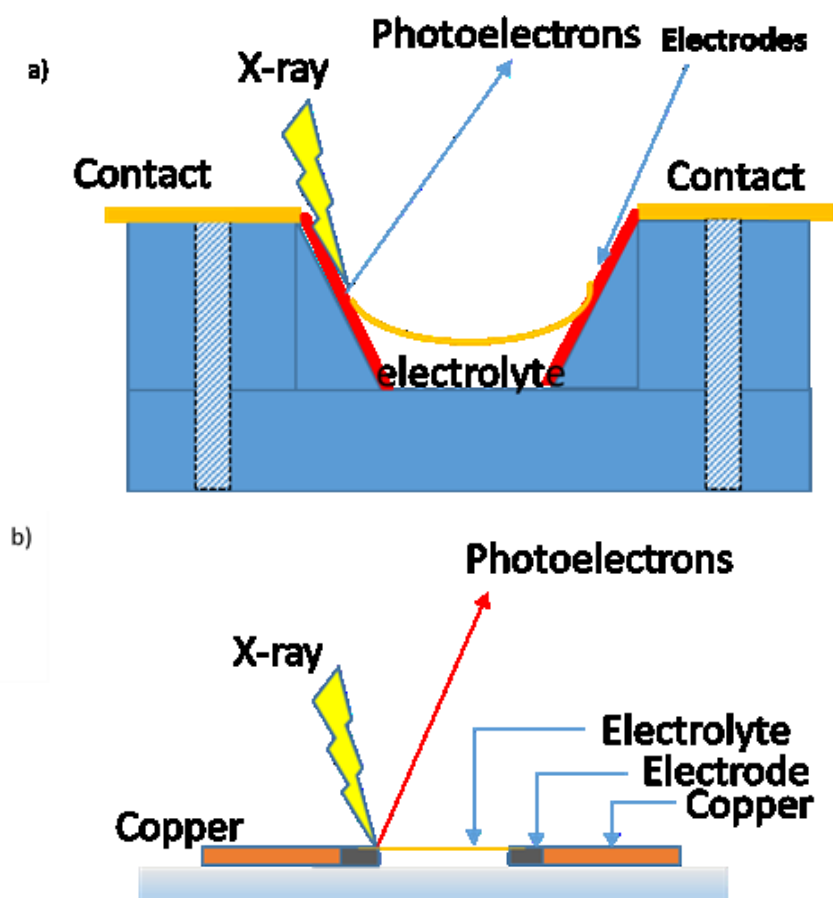


Figure 5.6 Sketch of reaction vessel-like and planar-like designed cell for OXPS.

In this manuscript all results are discussed based on the planar like cell. The cell is encapsulated using the pouch cell like technology, allowing a better current flow and an electrolyte control between parallel electrodes.

5.3.3. OXPS sampling and protocol

5.3.3.1. Sample preparation

In a glove box filled with argon, two parallel foils of lithium, of 0.5 cm large, 1 cm long and 135 μm thick, connected to copper current collectors are placed in parallel and distanced by 0.02-0.03 cm in the planar cell. After encapsulating, the cell is filled with 50 μL of electrolyte and connected to the four contact sample holder. The cell is transferred to the spectrometer using a dedicated transfer vessel. Figure 5.7 shows an encapsulated planar-like cell, filled with IL based electrolyte, connected to four contact ULVAC-PHI sample holders.

Once the cell is hosted in the introduction chamber of the spectrometer, the cell is kept under vacuum ~ 1 hour until 10^{-7} mbar to remove any residual trapped bubbles inside the cell.

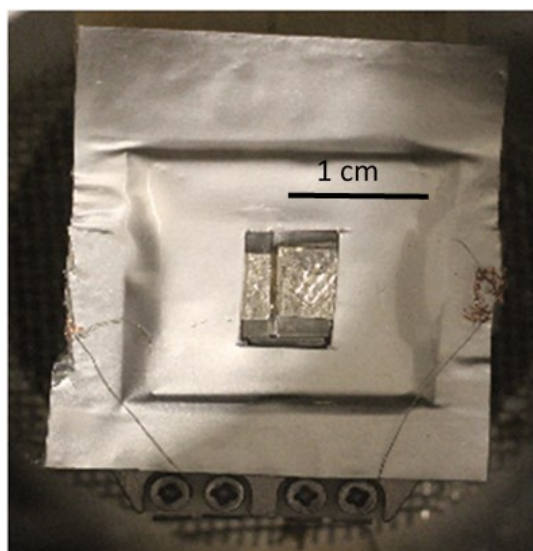


Figure 5.7 Symmetrical lithium/lithium OXPS planar cell encapsulated and filled with electrolyte and connected to the four contact sample holders.

5.3.4. OXPS sample optimization and connectivity to the potentiostat

Before cell transferring to the analyze chamber, the sample holder is connected to the potentiostat through armored cable to minimize the eventual electrical noises between the sample holder and the electrochemical devise.

The sample holder inside the XPS stage, is grounded to the potentiostat to avoid the electrical noise induced by the XP spectrometer.

Systematically, the open circuit voltage is recorded before sample transfer in order to measure the OCV before and after sample transfer. This simple check procedure allows a direct identification of the electrical noise level between the sample holder and potentiostat, since the symmetrical cell, Li/IL electrolyte/Li, must have an OCV around zero volt.

After introducing the cell, the X-ray beam is turned on to perform sample optimization along z-axis (Z-align), while the OCV is recorded (Figure 5.8).

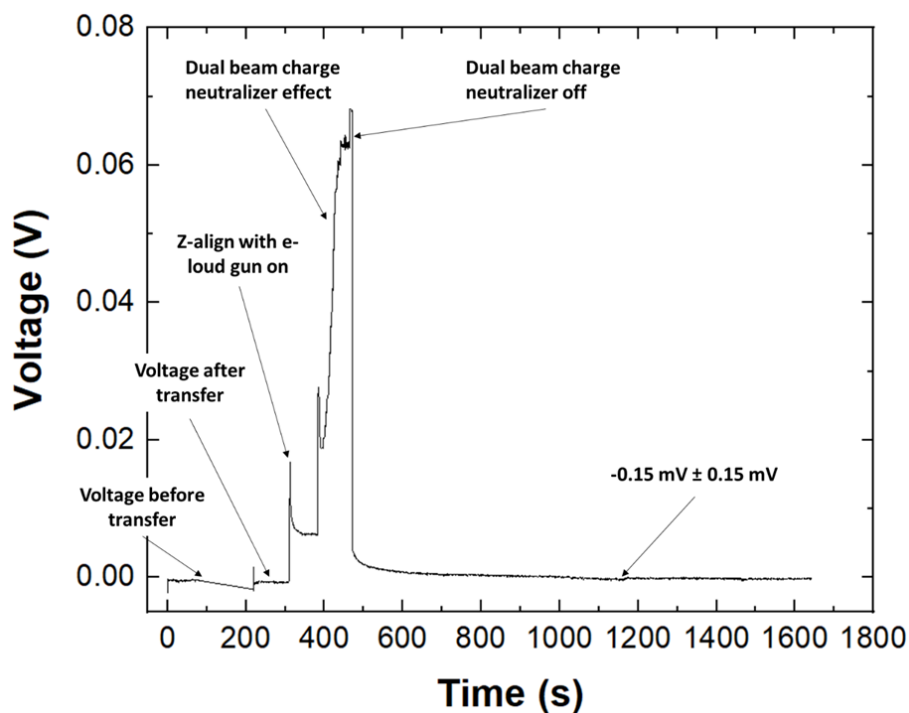


Figure 5.8 Open circuit voltage evolution before and after cell connection to the XPS stage. The effect of electron and argon gun used for charge neutralization is highlighted through the OCV deviation from the equilibrium voltage.

While the cell is introduced to the analysis chamber and connected to the potentiostat, the OCV is measured to be $0.15 \text{ mV} \pm 0.1 \text{ mV}$. The Z-align performed without charge neutralization does not perturb the measured OCV, however, the flood gun and the dual beam charge neutralization induce a voltage increase. After switching off the charge neutralization the OCV drop to the cell voltage in few hundreds of seconds ($0.1 \pm 0.1 \text{ mV}$).

Hence, all OXPS measurements are performed without charge neutralization to avoid any artefact that may disturb the electrochemical process inside the operando cell.

5.3.5. X-ray beam and acquisition parameter optimization

The interface between the lithium (positive and negative electrode) and the electrolyte is selected based on the secondary X-ray induced image (SXI) allowing the exact localization of the targeted analysis area (Figure 5.9).

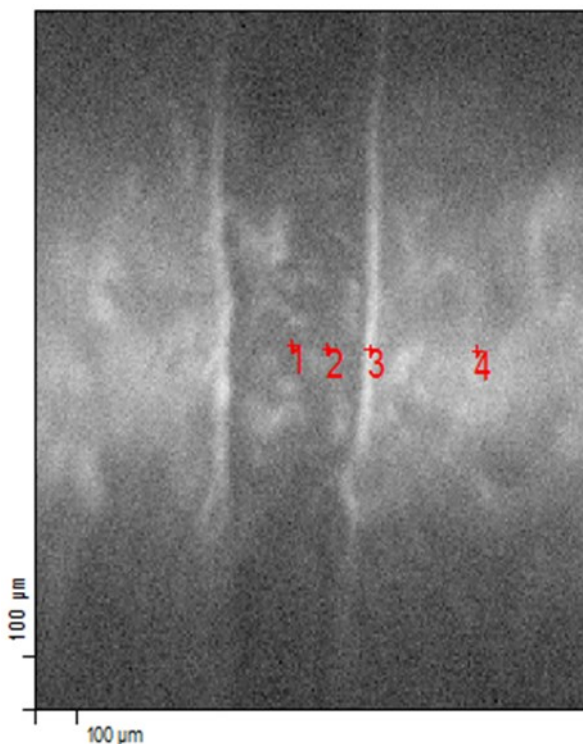


Figure 5.9 SXI performed with a X-ray beam of $100\mu\text{m}^2$ allowing a visualization of lithium anode and electrolyte. The electrolyte analyzed area are labeled (1, and 2), the lithium/electrolyte interface (3) and lithium surface (4).

The beam size can be tuned from $10\ \mu\text{m}^2$ to $200\ \mu\text{m}^2$. The X-ray spectra were recorded without charge neutralization, *vide supra*. The survey and the high resolution spectra were recorded with a pass energy of 117 and 29 eV, respectively. The F1s, C1s, O1s, N1s, S2p and Li1s were recorded within the energy range of 20 eV within a scan rate of 0.1 eV and scan step of 20 ms. Two scans for each core level peak was enough to have a good noise to spectrum ratio. The spectra were not calibrated in order to follow the surface potential while controlling the voltage of the cell through the potentiostat.

5.4. OXPS study of the interface lithium/imidazolium based IL electrolyte, result and discussion

5.4.1. OXPS study of lithium/IL based electrolyte/lithium under chronoamperometry

The chronoamperometry is an electrochemical technique in which the potential of the working electrode is stepped and the resulting current from faradaic processes occurring at the electrode (caused by the potential step) is monitored as a function of time. For this purpose, we have used $\text{C}_1\text{C}_6\text{ImTFSI/LiTFSI}$ as electrolyte to correlate the potential change of the working electrode to the surface potential change between the lithium, selected as the negative electrode, and the electrolyte.

Figure 5.10 shows the resulting current from faradaic processes occurring at the lithium anode (caused by the potential step) and monitored as a function of time.

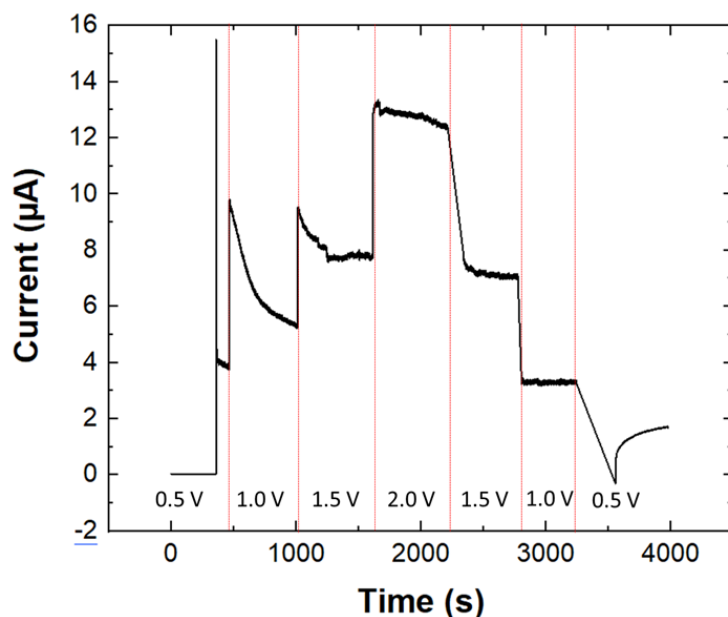


Figure 5.10 Chronoamperometry evolution between 0.5 and 2.0 V with voltage step of 0.5 V. The XPS was performed during potential step.

We noticed that the relaxation profile after each voltage changes as a function of the applied voltage. This result indicates that our electrochemical cell can be used to diffusion process through the Cottrell equation:

$$i = \frac{nFC_0A\sqrt{D}}{\sqrt{t}\pi}$$

Where i is the current in A, n is the number of electrons, F is Faraday constant, A is the area of the planar electrode in cm^2 , C_0 is the initial concentration of the electrolyte in $\text{mol}\cdot\text{cm}^{-3}$. D is the diffusion coefficient for species in $\text{cm}^2\cdot\text{s}^{-1}$, t is the time in second. Under controlled-diffusion circumstances, the current-time plot reflects the concentration gradient of the solution near the electrode surface. The current is directly proportional to the concentration at the electrode surface.

The C1s, N1s and S2p XPS core peaks measured at different voltages, is reported in Figure 5.11. We noticed that all core peaks down shift by ~ 1.5 eV without peak shape change (Table 5. 3). The core level binding energy shift exhibits a linear and reversible correlation with the applied voltage of -1 eV/V. In the frame of rigid band model, this could find origin in the change of the Fermi level of the surface electrolyte with respect to the analyzer.

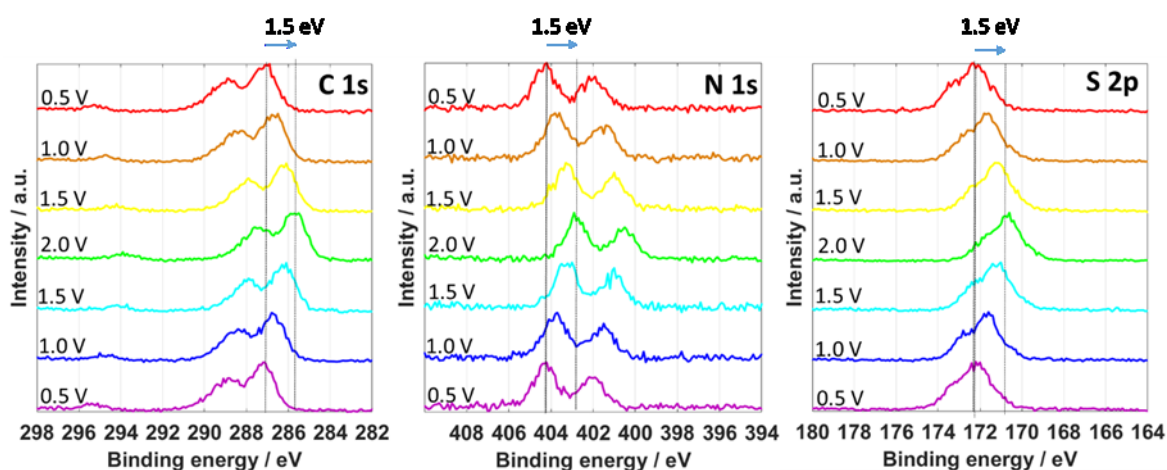


Figure 5.11 C1s, N1s, S2p core level shift as function of the applied potential between cell electrodes.

Table 5. 3 Binding energy shift as a function of the applied voltage.

Applied Voltage	C 1s	N 1s	S 2p
0.5	287.0	404.2	172.3
1.0	286.6	403.8	171.7
1.5	286.2	403.2	171.2
2.0	285.6	402.9	170.7
1.5	286.2	403.0	171.1
1.0	286.7	403.7	171.6
0.5	287.2	404.3	172.1

5.4.2. OXPS study of lithium/IL based electrolyte/lithium at the OCV

For comparison with the study performed in the chapter 3, we have studied the EIS evolution the cell at the OCV in the OXPS condition. We have chosen for this purpose, the C₁C₆ImTFS/LiTFSI based electrolyte system. We noticed that in the case of coin cell configuration, the EIS was measured right after cell assembling, whereas in the case of the operando cell the EIS measurement was performed after one two hours after assembling in the glove box (delay time due to cell transfer between the glove box and pumping the XPS introduction chamber). In order to compare the EIS results of the planar operando and the coin cell, we have established a geometrical ratio of the lithium active surface in contact with the electrolyte of both cells. We found out that the active surface of the operando cell is ten time smaller than the coin cell case.

The Figure 5.12-a, shows the Nyquist plot evolution recorded in the case of Li/C₁C₆ImTFSI- LiTFSI/Li cell in OXPS conditions. The inset figure represents the characteristic EIS signature of the same system in the coin cell configuration. Using the same approach reported in the chapter 3, we reported the evolution of the R_{el} and R_{int} in comparison with the coin cell values, Figure 5.12-b.

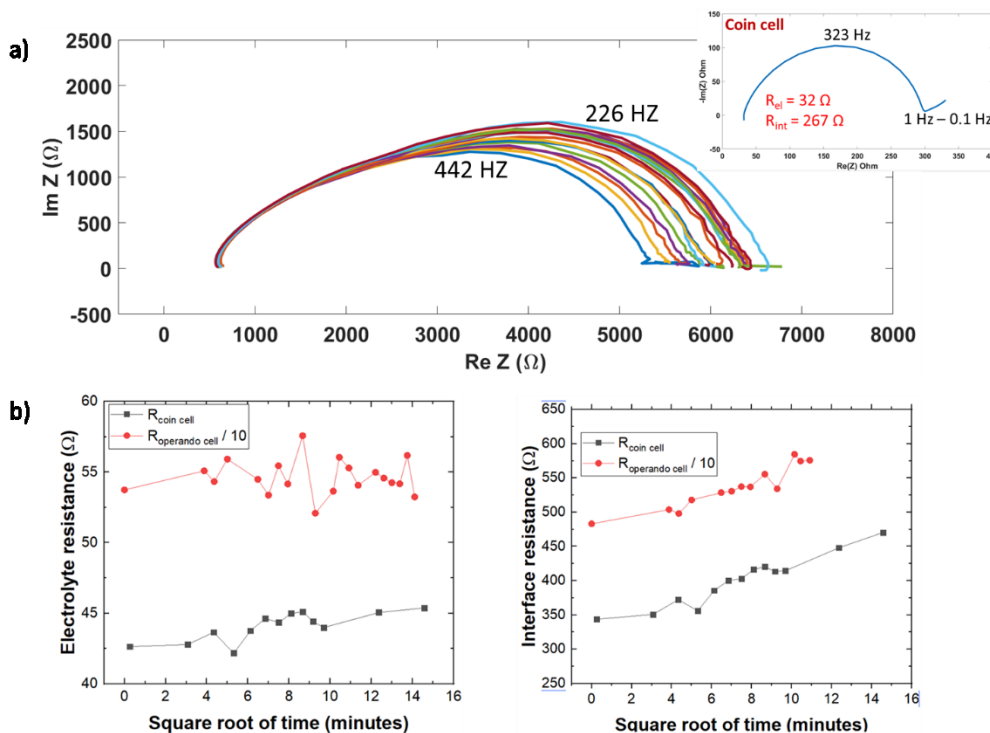


Figure 5.12 a) Nyquist plot recorded at the OCV in the OXPS condition in the Li/C₁C₆ImTFSI-LiTFSI/Li. The inset figure is the Nyquist plot recorded in the case of the coin cell. b) R_{el} and R_{int} evolution at the OCV as a function of the time.

We notice that a linearity test between 20 to 100 mV have shown that the Nyquist plot has the same shape with regards of the characteristics frequencies. Hence, the EIS spectra were recorded between 1 MHz and 1 mHz with an amplitude signal of 50 mV. The R_{el} and R_{int} measured at the OCV evolve similarly to that recorded in the case of the coin cell. This result evidences that our OXPS protocol has a potential to pave the way toward new coupling studies between XPS and EIS in operando mode.

5.4.3. OXPS study of the interface Lithium/IL electrolyte under polarization

5.4.3.1. C₁C₆ImFSI/LiTFSI based electrochemical cell

We have applied a current of 100 μA (eq. to 200 μA.cm⁻² in coin cell configuration) to the symmetrical cell. The Figure 5.13 shows the voltage profile over time. It is clearly

seen that the cell voltage exhibits two behaviors: Ohmic behavior up to 0.15 V, followed by a Nernstian profile. The voltage profile is similar to that recorded in the coin cell configuration (chapter 4). The first short circuit occurs after ~40 min (28 min in the coin cell configuration), followed by a successive fuse effect. The optical image recorded before and after cell polarization, shows clearly the presence of lithium dendrite growing from the negative to the positive electrode.

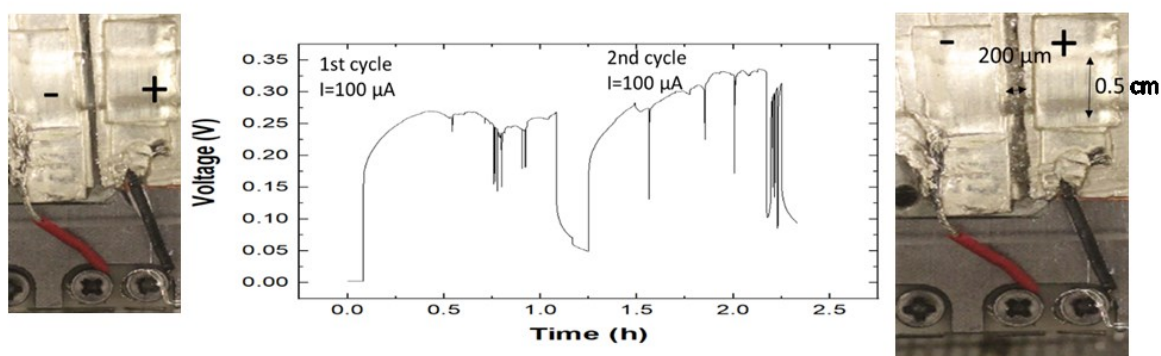


Figure 5.13 Operando voltage profile recorded in the XPS chamber, showing short circuit and fuse effect behavior. Lithium dendrite growing from the negative to the positive electrode is observed after cell polarization.

The EIS measured before and after cell polarization is reported in the Figure 5.14. We noticed a decrease of the R_{int} as the lithium dendrite growth. The Nyquist plot evidences the growth of SEI layer upon polarization. In order to understand the chemical structure of the SEI layer we have performed OXPS measurement upon polarization. We noticed that the X-ray beam did not disturb the voltage profile.

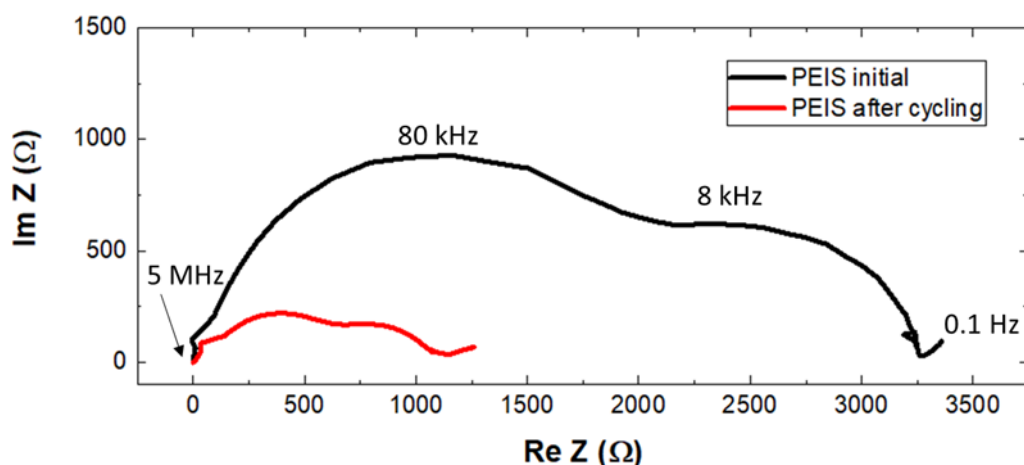


Figure 5.14 PEIS evolution before and after cell polarization.

The OXPS recorded at the interface Li/C₁C₆ImFSI-LiTFSI during the first and second polarizations, at current density of 200 μA.cm⁻², is reported in Figure 5.15.

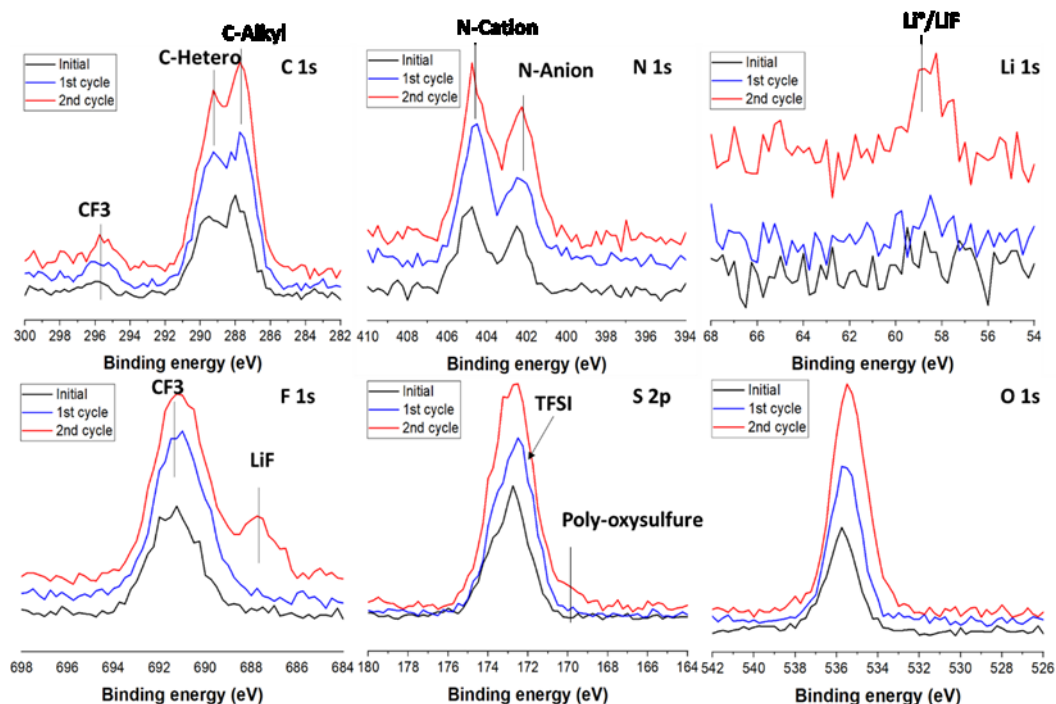


Figure 5.15 OXPS recorded at the interface Li/C₁C₆ImFSI-LiTFSI during the first and second polarization, at current density of 200 μA.cm⁻².

Our result evidenced the formation of SEI layer mainly composed of LiF. The high intensity of Li1s, is signature of accumulation of lithium at the interface in accordance with the formation of lithium dendrite and/or LiF.

The cell was di-assembled in the glove box and transferred to the Auger spectrometer to perform the SEM image of the lithium negative electrode lateral section (Figure 5.16). The SEM image was performed without washing with DMC solvent. Hence, we still observe the presence of IL electrolyte that screen the lithium dendrite. The optical microscope of the space between the lithium negative and positive is reported as well.

We can observe that the dendrite has needle like shape, as reported in chapter 4. This result is at preliminary stage and need some optimization to avoid lithium dendrite detachment during cell manipulation in the glove box.

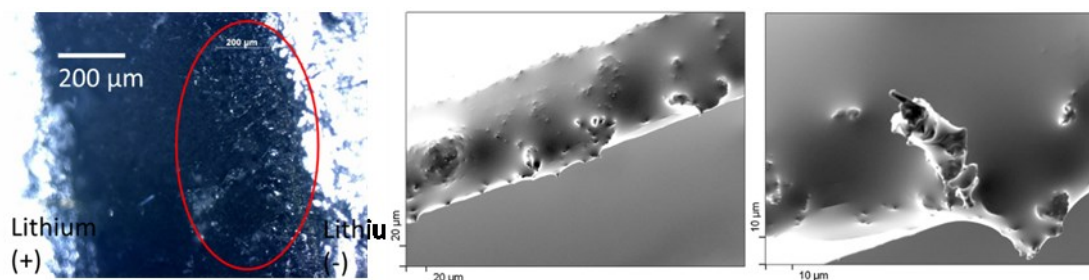


Figure 5.16 Optical microscope and SEM image of the lithium negative electrode after operando cell polarization.

5.4.3.2. $C_1C_6ImTFSI/LiTFSI$ based electrochemical cell

We have performed similar study on $Li/C_1C_6ImTFSI-LiTFSI/Li$. The Figure 5.17 reports the polarization profile recorded at the applied current of $25\mu A$, corresponding to $150\mu A.cm^{-2}$ in coin cell configuration. The GEIS is recorded, every 20 min, to evaluate the interface resistance evolution upon voltage change. We notice the interface resistance increases, whereas the interface and diffusional processes measured at low frequencies vary, signature of SEI formation.

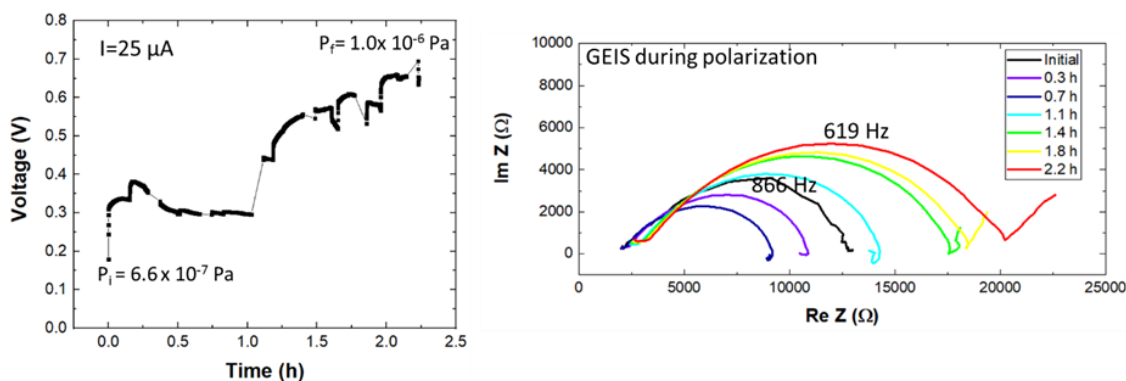


Figure 5.17 Voltage profile change under fixed applied current density ($150\mu A.cm^{-2}$). The GEIS is recorded every 20 min.

The voltage profile shows a divergence behavior similar to that evidenced in the chapter 4. In parallel the pressure inside the XPS analysis chamber, keep increasing, signature of gas evolution during SEI formation. The experiment was stopped after 2 hours, since the pressure conditions start to be critical for the spectrometer sources and analyzer.

The OXPS was recorded between to GEIS measurement at the interface Li (negative)/IL electrolyte. The core level peaks evolution is reported in the Figure 5.18.

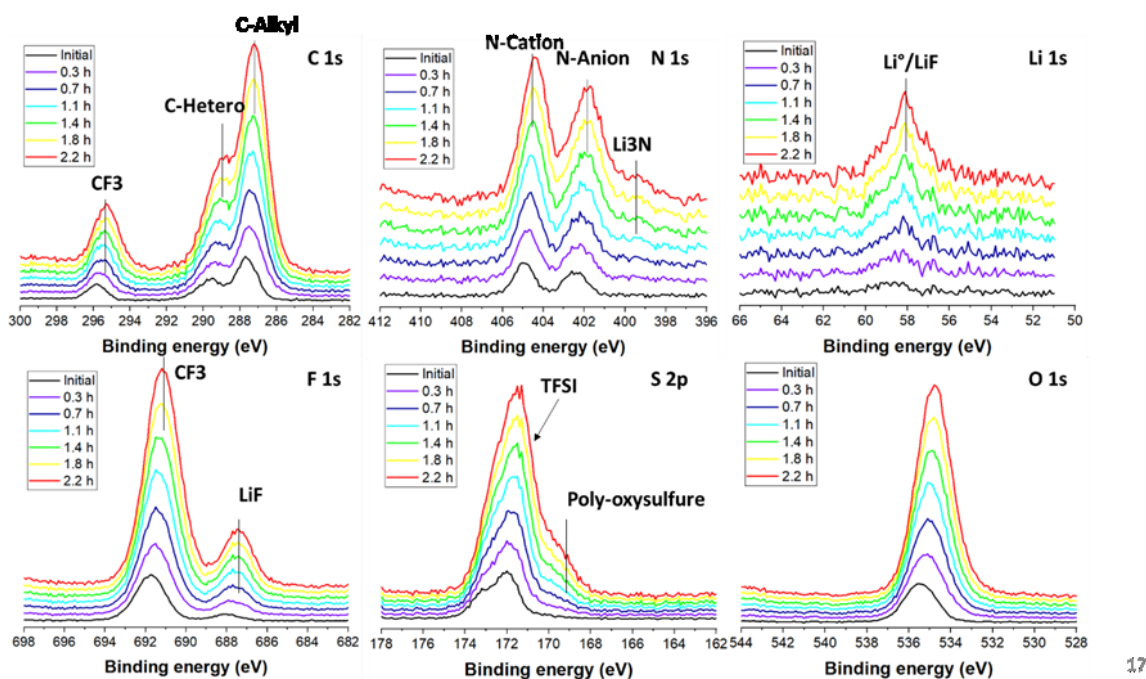


Figure 5.18 OXPS recorded at the interface $\text{Li}/\text{C}_1\text{C}_6\text{ImTFSI-LiTFSI}$ during the polarization, at current density of $150\mu\text{A}\cdot\text{cm}^{-2}$.

The OXPS evolution clearly proved the formation of LiF layer and the anion degradation by-products (poly-oxy sulfur, Li_3N). We noticed an increase of the intensity of the C1s alkyl related peak, suggesting the decomposition of cationic hetero structure to form a putative NHC carbene (see chapter 3). The O1s and F1s binding energy down shift and the vanish of the S2p spin-orbit doublet related to TFSI, confirm a chemical structure change induced by the decrease of lithium ions concentration at the interface with lithium negative electrode.

5.5. Conclusions

In this chapter, we have described our approach for developing the operando XPS, OXPS, that allowed direct correlation between electrochemical properties and the chemical structure evolution at the lithium/IL electrolyte interface. To our knowledge, such study has never been developed with such accuracy, paving the way for better understanding of the chemical structure of the SEI without inducing external artefacts.

Toward an accurate OPXS, we have developed and designed several cells, to perform as much as possible a realistic electrochemical behavior. The contact wires between the stage and the potentiostat were optimized to reduce noise level.

Two systems, Li/C₁C₆ImTFSI-LiTFSI/Li and Li/C₁C₆ImFSI-LiTFSI/Li, have been studied by OXPS and compared to post-mortem results (chapters 3 and 4). Beside the gain of time and the matter saving the OXPS results corroborate the conclusions reported in the chapter 3 and 4.

For instance:

- Lithium reactivity toward IL electrolyte at the OCV
- Dendrite growth following two regimes, short-circuit in the case of Li/C₁C₆ImFSI-LiTFSI/Li and divergence regime for Li/C₁C₆ImTFSI-LiTFSI/Li.

The OXPS developed in this thesis can be extended to all solid batteries and supercapacitor devices.

REFERENCES

- (1) Brissot, C.; Rosso, M.; Chazalviel, J. N.; Baudry, P.; Lascaud, S. In Situ Study of Dendritic Growth in Lithium/PEO-Salt/Lithium Cells. *Electrochim. Acta* **1998**, 43 (10-11), 1569-1574.
- (2) Brissot, C.; Rosso, M.; Chazalviel, J. N.; Lascaud, S. Dendritic Growth Mechanisms in Lithium/Polymer Cells. *J. Power Sources* **1999**, 81-82, 925-929.
- (3) Bouchet, R.; Lascaud, S.; Rosso, M. An EIS Study of the Anode Li/PEO-LiTFSI of a Li Polymer Battery. *J. Electrochem. Soc.* **2003**, 150 (10), A1385–A1389.
- (4) Teysot, A.; Belhomme, C.; Bouchet, R.; Rosso, M.; Lascaud, S.; Armand, M. Inter-Electrode in Situ Concentration Cartography in Lithium/Polymer Electrolyte/Lithium Cells. *J. Electroanal. Chem.* **2005**, 584 (1), 70–74.
- (5) Maire, P.; Evans, A.; Kaiser, H.; Scheifele, W.; Novák, P. Colorimetric Determination of Lithium Content in Electrodes of Lithium-Ion Batteries. *J. Electrochem. Soc.* **2008**, 155 (11), 862–865.
- (6) Stancovski, V.; Badilescu, S. In Situ Raman Spectroscopic-Electrochemical Studies of Lithium-Ion Battery Materials: A Historical Overview. *J. Appl. Electrochem.* **2014**, 44 (1), 23–43.
- (7) Gross, T.; Giebeler, L.; Hess, C. Novel in Situ Cell for Raman Diagnostics of Lithium-Ion Batteries. *Rev. Sci. Instrum.* **2013**, 84 (7).
- (8) Lanz, P.; Novák, P. Combined in Situ Raman and IR Microscopy at the Interface of a

- Single Graphite Particle with Ethylene Carbonate/Dimethyl Carbonate. *J. Electrochem. Soc.* **2014**, 161 (10), 1555–1563.
- (9) Sharabi, R.; Markevich, E.; Borgel, V.; Salitra, G.; Aurbach, D.; Semrau, G.; Schmidt, M. A. In Situ FTIR Spectroscopy Study of Li/LiNi_{0.8}Co_{0.15}Al_{0.05}O₂ Cells with Ionic Liquid-Based Electrolytes in Overcharge Condition. *Electrochem. Solid State Lett.* **2010**, 13 (4), A32–A35.
 - (10) Akita, Y.; Segawa, M.; Munakata, H.; Kanamura, K. In-Situ Fourier Transform Infrared Spectroscopic Analysis on Dynamic Behavior of Electrolyte Solution on LiFePO₄ Cathode. *J. Power Sources* **2013**, 239, 175–180.
 - (11) Dollé, M.; Sannier, L.; Beaudoin, B.; Trentin, M.; Tarascon, J.-M. Live Scanning Electron Microscope Observations of Dendritic Growth in Lithium/Polymer Cells. *Electrochem. Solid-State Lett.* **2002**, 5 (12), A286.
 - (12) Orsini, F.; Du Pasquier, A.; Beaudouin, B.; Tarascon, J. M.; Trentin, M.; Langenhuizen, N.; De Beer, E.; Notten, P. In Situ SEM Study of the Interfaces in Plastic Lithium Cells. *J. Power Sources* **1999**, 81–82, 918–921.
 - (13) Ota, H.; Sakata, Y.; Wang, X.; Sasahara, J.; Yasukawa, E. Characterization of Lithium Electrode in Lithium Imides/Ethylene Carbonate and Cyclic Ether Electrolytes. *J. Electrochem. Soc.* **2004**, 151 (3), A437.
 - (14) Huang, J. Y.; Zhong, L.; Wang, C. M.; Sullivan, J. P.; Xu, W.; Zhang, L. Q.; Mao, S. X.; Hudak, N. S.; Liu, X. H.; Subramanian, A.; et al. In Situ Observation of the Electrochemical Lithiation of a Single SnO₂ Nanowire Electrode. *Science (80-.)*. **2010**, 330 (6010), 1515–1520.
 - (15) Liu, X. H.; Huang, J. Y. In Situ TEM Electrochemistry of Anode Materials in Lithium Ion Batteries. *Energy Environ. Sci.* **2011**, 4 (10), 3844–3860.
 - (16) Villevieille, C.; Sasaki, T.; Novák, P. Novel Electrochemical Cell Designed for Operando Techniques and Impedance Studies. *RSC Adv.* **2014**, 4 (13), 6782–6789.
 - (17) Wilson, B. E.; Smyrl, W. H.; Stein, A. Design of a Low-Cost Electrochemical Cell for in Situ XRD Analysis of Electrode Materials. *J. Electrochem. Soc.* **2014**, 161 (5), 700–703.
 - (18) Brant, W. R.; Schmid, S.; Du, G.; Gu, Q.; Sharma, N. A Simple Electrochemical Cell for In-Situ Fundamental Structural Analysis Using Synchrotron X-Ray Powder Diffraction. *J. Power Sources* **2013**, 244, 109–114.
 - (19) Ebner, M.; Marone, F.; Stampanoni, M.; Wood, V. Visualization and Quantification of Electrochemical and Mechanical Degradation in Li Ion Batteries. *Science (80-.)*. **2013**, 342 (6159), 716–720.
 - (20) Schausser, N. S.; Harry, K. J.; Parkinson, D. Y.; Watanabe, H.; Balsara, N. P. Lithium Dendrite Growth in Glassy and Rubbery Nanostructured Block Copolymer Electrolytes. *J. Electrochem. Soc.* **2015**, 162 (3), A398–A405.
 - (21) Sharma, N.; Peterson, V. K.; Elcombe, M. M.; Avdeev, M.; Studer, A. J.; Blagojevic, N.; Yusoff, R.; Kamarulzaman, N. Structural Changes in a Commercial Lithium-Ion Battery during Electrochemical Cycling: An in Situ Neutron Diffraction Study. *J. Power Sources* **2010**, 195 (24), 8258–8266.
 - (22) Sharma, N.; Peterson, V. K. Current-Dependent Electrode Lattice Fluctuations and Anode Phase Evolution in a Lithium-Ion Battery Investigated by in Situ Neutron Diffraction. *Electrochim. Acta* **2013**, 101, 79–85.
 - (23) Siegel, J. B.; Stefanopoulou, A. G.; Hagans, P.; Ding, Y.; Gorsich, D. Expansion of

- Lithium Ion Pouch Cell Batteries: Observations from Neutron Imaging. *J. Electrochem. Soc.* **2013**, 160 (8), 1031–1038.
- (24) Favaro, M.; Jeong, B.; Ross, P. N.; Yano, J.; Hussain, Z.; Liu, Z.; Crumlin, E. J. Unravelling the Electrochemical Double Layer by Direct Probing of the Solid/Liquid Interface. *Nat. Commun.* **2016**, 7 (May), 1–8.
- (25) Wu, X.; Villevieille, C.; Novák, P.; El Kazzi, M. Monitoring the Chemical and Electronic Properties of Electrolyte-Electrode Interfaces in All-Solid-State Batteries Using Operando X-Ray Photoelectron Spectroscopy. *Phys. Chem. Chem. Phys.* **2018**, 20 (16), 11123–11129.
- (26) Weingarh, D.; Foelske-Schmitz, a.; Wokaun, a.; Kötz, R. In Situ Electrochemical XPS Study of the Pt/[EMIM][BF₄] System. *Electrochem. commun.* **2011**, 13 (6), 619–622.

General conclusions

The current lithium ion battery technology is facing against new challenges because of the growing demand of more energetic storage systems for electronic devices and electric vehicles. It is necessary the development of safer electrolytes with improved electrochemical stability, being able to work with cathode material at potentials higher than 5 V vs. Li^+/Li . These challenges have brought out the need of use of anode material such as the lithium metal, which can be integrated into new battery technologies such as lithium/sulfur and lithium/oxygen.

Regarding the electrolytes, ionic liquids (ILs) have been studied in this work because of their retarded flammability, wide electrochemical window and weak vapor pressure, being suitable for the study at ultra-high vacuum conditions, as require most of the surface analysis techniques. However, the reactivity of these electrolytes against lithium metal have not been extensively studied from a fundamental point of view, giving priority of the study of the performances of these systems negligent the comprehension of the different chemical and electrochemical phenomena happening at the interfaces electrolyte/lithium.

In order to understand all of these processes, a fundamental study of the IL based electrolytes and the initial state of the pristine lithium electrode have been detailed in chapter 2. Herein, the use of the VFT model to fit the conductivities of the electrolytes have demonstrated the dependency of thermodynamic parameters (B , activation volume and T_0 , glass transition temperature) on the changes in the transport properties of the ILs (conductivity and viscosity) upon the addition of LiTFSI salt and carbonate additives and the methylation of the $\text{C}_1\text{C}_6\text{Im}^+$ cation at the C2 position.

With $\text{C}_1\text{C}_6\text{ImTFSI}$, the data of conductivity, viscosity and diffusion coefficient (measured by NMR) have been compared, showing a good correlation between all of the parameters. This comparison has been extended to the case of the same IL doped with LiTFSI. The results have demonstrated a good correlation with the physical transport equations when the formation of complexes like $[\text{Li}(\text{TFSI})_2]^-$ is considered.

The characterization of the ILs by XPS have highlighted based on core-level binding energies shifts, the change in the molecular organization and in the cation-anion interactions depending on i) the type of cation and anion and ii) the use of LiTFSI and additives.

Regarding the initial state of the lithium metal electrode, XPS measurements evidence the presence of a passivation layer covering the surface and constituted of Li_2O buried beneath a Li_2CO_3 layer. After etching the lithium surface with a monoatomic Ar^+ or cluster beam, the measurements have been carried out to determine the thickness of Li_2O and Li_2CO_3 layers. However, the induction of new kind of morphologies and the formation of Li_2O have been demonstrated in these experiences, modifying the initial state of the lithium surface.

The results of the chapter 2 serve us as reference to undertake the study of the reactivity of the IL based electrolytes at open circuit conditions and under the application of an electrical current.

During OCV conditions, the electrical resistance of the electrolyte and interphases were characterized by EIS. By means of this technique, we highlight the different stabilities of the neat ILs which can be ordered from the most stable to the least stable as following: $\text{C}_1\text{C}_6\text{ImFSI} > \text{C}_1\text{C}_1\text{C}_6\text{ImTFSI} > \text{C}_1\text{C}_6\text{ImTFSI}$. Moreover, EIS show an improved stability when LiTFSI is added. This order of stability has been validated by the XPS analyses of the separators, showing an accelerated decomposition of the $\text{C}_1\text{C}_6\text{Im}^+$ cation in neat IL. In the presence of LiTFSI, the improvement stability can be related to the formation of $[\text{Li}(\text{TFSI})_2]^-$ complexes. As a consequence, the imidazolium cation remains protected from the attack of Li^+ ions. The effect of C2 methylation and additives have been discussed, giving rise to better stabilities of the electrolyte and a protection from further decomposition of cation in contact to lithium electrode

Regarding the interphases formed at OCV, EIS shows that the electrolyte combinations containing the FSI anion are the less resistive compared to TFSI based combinations. However, for any IL doped with LiTFSI the evolution of the resistances seems to be managed by the decomposition of the TFSI anion or of the organic additive (VC and FEC) when they are present. Note that with FEC, an effective stabilization of the $\text{C}_1\text{C}_6\text{ImTFSI}/\text{LiTFSI}$ interphase has been evidenced.

The XPS analyses of the lithium surface after aging in contact with IL based electrolytes at OCV shows the formation of fresh SEI layers composed mainly by Li_2CO_3 , LiF and $\text{Li}_2\text{S}_x\text{O}_y$. The presence of Li_2CO_3 , present at the surface of native lithium was used to estimate the thickness evolution of the SEI layer, which seems to be thinner than 5 nm. This result is in good accordance with the thickness of the SEI estimated by EIS. With anion FSI, the formation of LiF and sulfones byproducts are favored leading to the formation of a homogeneous SEI evidenced by the SEM/AES technique.

The behavior of the IL based electrolyte at different potentials has been studied by cycling voltammetry. Results shows that the used combinations of imidazolium ILs exhibit an onset potential of oxidation around 4.5 V vs. Li/Li^+ with better stability for the combinations containing only the TFSI anion and the FEC additive. For the case of the reduction, decompositions of the electrolytes started even before 1.0 V vs. Li/Li^+ . This is in contradiction with the literature, where several publications affirm a great stability window of IL based electrolytes even for the case of LMB. We have highlight the fact that even at these potentials the current densities are in the order of some $\mu\text{A}\cdot\text{cm}^{-2}$ which leads to a decrease of the performances and the consumption of the electrolyte during prolonged cycling.

The study when an electrical current is applied to the Li/Li systems shows the formation of two different regimes of polarization depending of the type of electrolyte at current densities between 60 and 100 $\mu\text{A}\cdot\text{cm}^{-2}$. For the first regime (electrolytes $\text{C}_1\text{C}_6\text{ImTFSI}/\text{LiTFSI}$ and $\text{C}_1\text{C}_1\text{C}_6\text{ImTFSI}/\text{LiTFSI}$) the voltage of the cell diverges at some time which coincide with the formation of mossy-like lithium deposition. While with ($\text{C}_1\text{C}_6\text{ImTFSI}/\text{LiTFSI}/\text{VC}$, $\text{C}_1\text{C}_6\text{ImTFSI}/\text{LiTFSI}/\text{FEC}$ and $\text{C}_1\text{C}_6\text{ImFSI}/\text{LiTFSI}$) the voltage falls down and eventually banishes, corresponding to the formation of needle-like dendrites that produces short-circuit of the system.

The onset time of the divergence regime seems to follow the inverse-square law ($\tau \propto 1/J^2$), in agreement with the Sand's law and the Chazalviel's model. For the case of the short-circuit regime, the onset times exhibit some variations with the Sand's law. This study has allowed to evaluate the transport number of the Li^+ ions which are weak as 0.06 at room temperature independently of the imidazolium IL based electrolytes.

The XPS analyses have demonstrate that the type of interphase formed during polarization depends on the type of electrolyte. For $C_1C_6ImTFSI/LiTFSI$ and $C_1C_1C_6ImTFSI/LiTFSI$, the interphase is mainly composed by Li_2CO_3 coming from the native layer, suggesting that the fresh SEI is thin with a low concentration of LiF which does not allow a good reversibility of the plating/stripping processes favored the formation of mossy-like deposits. For the other combinations ($C_1C_6ImTFSI/LiTFSI/VC$, $C_1C_6ImTFSI/LiTFSI/FEC$ and $C_1C_6ImFSI/LiTFSI$), the peak of Li_2CO_3 is less intense corresponding to the formation of a thicker layer composed mainly by LiF and $Li_2S_xO_y$ species. However, this layer can easily be crossed by needle-like dendrites.

When VC and FEC are present in the electrolyte, the cycled interphase exhibits the formation of Li_2O and Li_2S in great concentrations. Herein, we hypothesized that the formation of these species comes from the high reactivity of the Li^+ ions during the process of plating. This agree with the good reversibility of the plating/stripping process proved by cyclic voltammetry and the observation of the peak of lithium metal (~ 53 eV) in the XPS spectra.

In conclusion, we can propose that in order to design more performant systems two considerations have to be taken into account. The first one correspond to the macromolecular transport properties of the electrolyte: high ionic conductivity and high Li^+ transport number. The second one correspond to the engineering of the SEI layer. This work demonstrates that the use of additives is crucial for the efficiency of the plating/stripping process. In addition, the degradation mechanism of the anion that leads to the formation of a more homogeneous interphase must be considered. Nonetheless, the anion FSI seems to be highly reactive and not suitable for work with cathode materials with potentials higher than 4.5 V vs. Li^+/Li . A good choice of combination IL + lithium salt + additive must be considered.

Finally, the last chapter, consecrated to the development of the OXPS that allowed direct correlation between electrochemical properties and the chemical structure evolution of the interface lithium/IL electrolyte under electrochemical sollicitation. To our knowledge, such study has never been developed with such accuracy, paving the way for better understanding of the chemical structure of the SEI without inducing external artefact. The OXPS results was discussed based on the XPS post-mortem and operando EIS results developed in the chapter 3 and 4.

APPENDIX 1: Electrochemical impedance spectroscopy

Electrochemical impedance spectroscopy (EIS) in a general sense is a vector quantity describing the relationship between a potential wave and a current wave, when an electrochemical system is perturbed by an alternating current or potential. Impedance extends the concept of resistance to alternating current. In EIS, the response of current (or potential) is measured when a sinusoidal perturbation of potential (or current) is applied at different frequencies. Perturbation has to be limited to small amplitude in order to ensure linear (or pseudo-linear) relationship between the current and potential wave. In a linear (or pseudo-linear) system, the current response to a sinusoidal potential will be a sinusoid at the same frequency but shifted in phase (Figure A1.1).

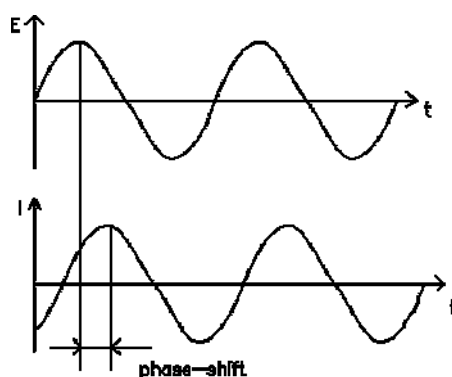


Figure A1.1 Sinusoidal current response in a linear system.

The excitation signal, expressed as a function of time, has the form:

$$E_t = E_0 \sin(\omega t) \quad \text{Eq. A1.1}$$

Where E_t is the potential at time t , E_0 is the amplitude of the signal, and ω is the radial frequency. The relationship between radial frequency ω (expressed in radians/second) and frequency f (expressed in Hertz) is:

$$\omega = 2\pi f \quad \text{Eq. A1.2}$$

In a linear system, the response signal, I_t , is shifted in phase (ϕ) and has a different amplitude than I_0 .

$$I_t = I_0 \sin(\omega t + \phi) \quad \text{Eq. A1.3}$$

An expression analogous to Ohm's Law allows us to calculate the impedance of the system as:

$$Z = \frac{E_t}{I_t} = \frac{E_0 \sin(\omega t)}{I_0 \sin(\omega t + \phi)} = Z_0 \frac{\sin(\omega t)}{\sin(\omega t + \phi)} \quad \text{Eq. A1.4}$$

The impedance is therefore expressed in terms of a magnitude, Z_0 , and a phase shift, ϕ .

If we plot the applied sinusoidal signal E_t on the X-axis of a graph and the sinusoidal response signal I_t on the Y-axis, the result is an oval (Figure A1.2). This oval is known as a "Lissajous Figure".

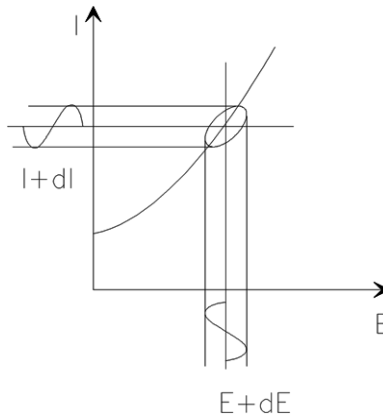


Figure A1.2 Lissajous Figure.

With Euler's relationship, where $j = \sqrt{-1}$:

$$\exp(j\phi) = \cos \phi + j \sin \phi \quad \text{Eq. A1.5}$$

It is possible to express the impedance as a complex function. The potential is described as,

$$E_t = E_0 \exp(j\omega t) \quad \text{Eq. A1.6}$$

And the current response as,

$$I_t = I_0 \exp(j\omega t - \phi) \quad \text{Eq. A1.7}$$

The impedance is then represented as a complex number,

$$Z(\omega) = \frac{E_t}{I_t} = Z_0 \exp(j\phi) = Z_0(\cos \phi + j \sin \phi) \quad \text{Eq. A1.8}$$

The components of $Z(\omega)$ thus consist of an imaginary part referred to as Z_i and a real part referred to as Z_r . When plotting Z_i versus Z_r , one obtains a semicircle called a “Nyquist” plot, as described below. Note that in the absence of capacitance and inductance, the Nyquist plot for a simple resistor would be a simple vertical straight line with the intercept on the Z_r axis representing the value of the resistor in ohms. For complex systems representing electrodes in cells and batteries, the Nyquist plots can be interpreted in terms of various electrode-electrolyte parameters such as solution resistance, kinetics (charge transfer), and capacitance; inductive effects are generally not observed in these electrochemical systems. To relate the complex impedance of the electrode/electrolyte interface to electrochemical parameters, it is necessary to model an equivalent circuit to represent the dynamic characteristics of the interface. The model consists of a number of impedance elements in networks based on series, parallel, or series/parallel combinations. For example, the total impedance for n elements in series is given by:

$$Z_{total} = Z_1 + Z_2 + Z_3 + \dots + Z_n \quad \text{Eq. A1.9}$$

For n elements in parallel, the impedance will be given by:

$$\frac{1}{Z_{total}} = \frac{1}{Z_1} + \frac{1}{Z_2} + \frac{1}{Z_3} + \dots + \frac{1}{Z_n} \quad \text{Eq. A1.10}$$

The important elements to be considered in modeling EIS data to electrodes are summarized in Table A1.1. A realistic model will then allow one to determine the electrochemical parameters for an electrode/electrolyte interface, which is discussed below.

Table A1.1 Equivalent circuit elements

Circuit element	Impedance
Resistance, R	R
Capacitance, C	$1/Cj\omega$
Constant phase element, Q (CPE)	$1/Q(j\omega)^\alpha$
Warburg impedance, W (infinite)	$1/Y(j\omega)^{1/2}$
Warburg impedance, W (finite)	$\tan [\delta D^{-1/2}(j\omega)^{-1/2}]/\gamma (j\omega)^{1/2}$
Inductance, L	$j\omega L$

In all of the equivalent circuits and Nyquist figures shown below the double layer capacity is represented by C , which is the symbol used for a pure (ideal) capacitor. However, due to surface inhomogeneity and faradaic current (*i.e.*, a “leaky” capacitor), for most electrochemical systems the double layer rarely behaves as an ideal capacitor. In this case, the capacity C is replaced by a constant phase element (CPE) in which the impedance is given by:

$$Z_{CPE} = \frac{1}{Q(j\omega)^\alpha} \quad \text{Eq. A1.11}$$

where α is an adjustable parameter. When $\alpha=1$, the CPE acts as an ideal capacitor, *i.e.*, $Q=C$, and when $\alpha=0$, the CPE is equivalent to a pure resistor. As indicated in Table A1.1, there are two ways to represent the Warburg impedance based on an infinite or finite diffusion layer thickness. For the latter, the relation for the impedance contains the thickness of the diffusion layer (δ) and the diffusion coefficient (D) for the diffusing species.

In modeling the electrode/electrolyte interface for a single electrode, the adjustable (fitting) parameters include R , C , Q , Y , L , and α . It is therefore important to select a realistic model for the analyses of EIS data. The equivalent circuit for the basic model of the electrode/electrolyte originally proposed by Randles (*Disc. Faraday Soc.* 1, 11 1947) is shown in Figure A1.3-a, and the basic Nyquist plot for this equivalent circuit is shown in Figure A1.3-b, where R_s is the electrolyte solution resistance, C_{dl} is the double layer capacitance, and R_{ct} is the charge transfer resistance from which the exchange current density can be calculated.

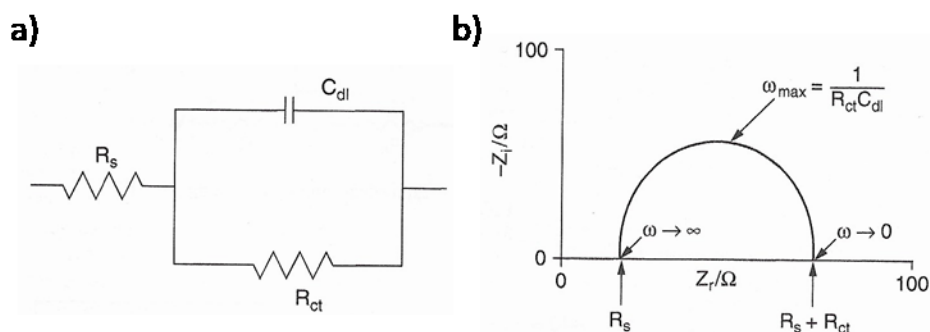


Figure A1.3 a) Randles' basic equivalent circuit for an electrode/electrolyte interface, b) schematic Nyquist plot for the Randles' circuit.

If the system exhibits diffusion control, this can be accounted for by the circuit shown in Figure A1.4-a in which the Warburg impedance is added in series with R_{ct} . The corresponding Nyquist plot is shown in Figure A1.4-b where the Warburg impedance appears at low frequencies as a straight line with a slope of 45° .

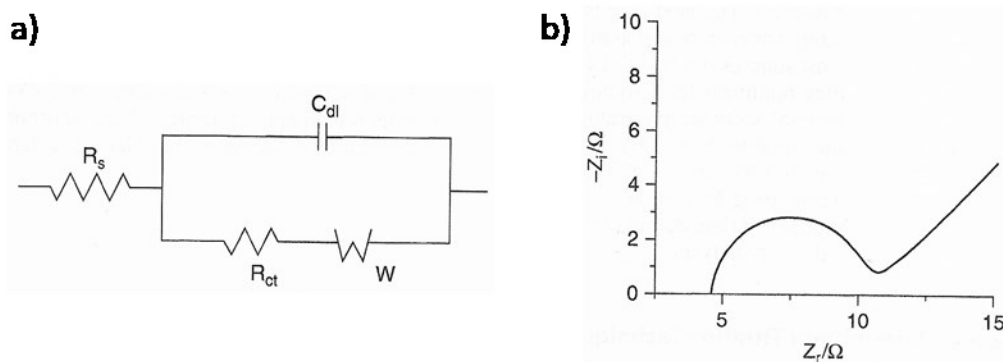


Figure A1.4 a) Randles' equivalent circuit for an electrode/electrolyte interface including the Warburg impedance, b) schematic Nyquist plot for the Randles' circuit.

APPENDIX 2: X-ray photoelectron spectroscopy

X-Ray Photoelectron Spectroscopy also known as electron spectroscopy for chemical analysis (ESCA) is based on the photoelectric effect. The general working principle of XPS is shown in Figure A2.1.

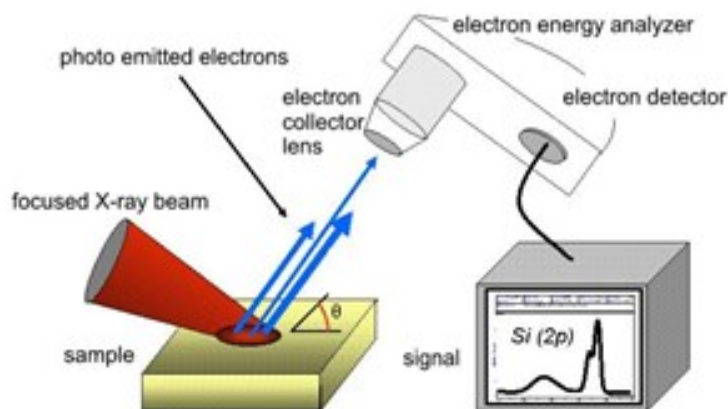


Figure A2.1 Schema of the XPS technique.

The basic mechanism behind an XPS instrument is illustrated in Figure A2.1. During an XPS measurement high energy X-ray photons ($\text{Al } K_{\alpha} = 1486.6 \text{ eV}$, $\text{Mg } K_{\alpha} = 1253.6 \text{ eV}$) are incident on the sample. Core electrons are emitted as photoelectrons from matter as a consequence of their absorption of energy from electromagnetic radiation. Energy of the emitted electron is described as per Einstein's explanation of the photoelectric effect. From the kinetic energy of the outgoing photoelectron, its binding energy can be calculated using equation:

$$BE = h\nu - KE - \phi \quad \text{Eq. A2.1}$$

BE = binding energy

$h\nu$ = energy of the incident X-rays

KE = kinetic energy of the ejected photoelectron

Φ = work function of the instrument

The binding energy may be regarded as the energy difference between the initial and final states after the photoelectron has left the atom. Because there is a variety of possible final states of the ions from each type of atom, there is a corresponding variety of kinetic energies of the emitted

electrons. Moreover, there is a different probability or cross-section for each final state. Relative binding energies and ionization cross-sections for an atom are shown schematically in Figure A2.2.

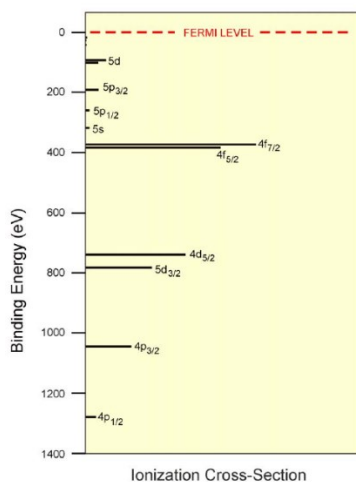


Figure A2.2 Relative binding energies and ionization-cross section for U.

The Fermi level corresponds zero binding energy (by definition), and the depth beneath the Fermi level in the figure indicates the relative energy of the ion remaining after electron emission, or the binding energy of the electron. The line lengths indicate the relative probabilities of the various ionization processes. The p, d and f levels become split upon ionization, leading to vacancies in the p_{1/2}, p_{3/2}, d_{3/2}, d_{5/2}, f_{5/2} and f_{7/2}. The spin-orbit splitting ratio is 1:2 for p levels, 2:3 for d levels and 3:4 for f levels.

Because each element has a unique set of binding energies, XPS can be used to identify and determine the concentration of the elements in the surface. Variations in the elemental binding energies (the chemical shifts) arise from differences in the chemical potential and polarizability of compounds. These chemical shifts can be used to identify the chemical state of the materials being analyzed.

In addition to photoelectrons emitted in the photoelectric process, Auger electrons may be emitted because of relaxation of the excited ions remaining after photoemission. This Auger electron emission occurs roughly 10^{-14} seconds after the photoelectric event. The competing emission of a fluorescent x-ray photon is a minor process in this energy range. In the Auger process Figure A2.3, an outer electron falls into the inner orbital vacancy, and a second electron is

simultaneously emitted, carrying off the excess energy. The Auger electron possesses kinetic energy equal to the difference between the energy of the initial ion and the doubly charged final ion, and is independent of the mode of the initial ionization. Thus, photoionization normally leads to two emitted electrons: a photoelectron and an Auger electron. The sum of the kinetic energies of the electrons emitted cannot exceed the energy of the ionizing photons.

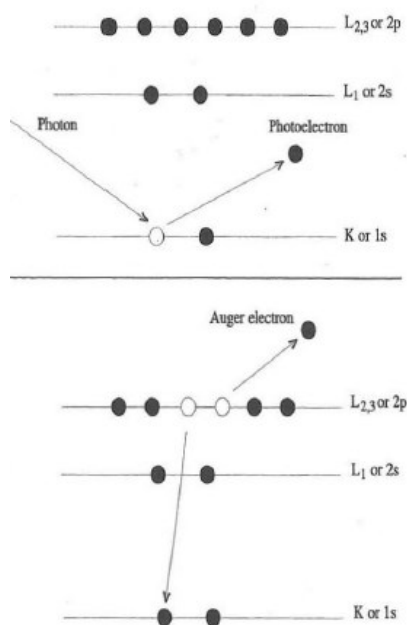


Figure A2.3 The XPS emission process (top) for a model atom. An incoming photon causes the ejection of the photoelectron. The relaxation process (bottom) for a model atom resulting in the emission of a $KL_{2,3}L_{2,3}$ electron. The simultaneous two-electron coulombic rearrangement results in a final state with two electron vacancies.

Probabilities of electron interaction with matter far exceed those of the photons, so while the path length of the photons is of the order of micrometers, that of the electrons is of the order of tens of angstroms. Thus, while ionization occurs to a depth of a few micrometers, only those electrons that originate within tens of angstroms below the solid surface can leave the surface without energy loss. These electrons which leave the surface without energy loss produce the peaks in the spectra and are the most useful. The electrons that undergo inelastic loss processes before emerging form the background.

The electrons leaving the sample are detected by an electron spectrometer according to their kinetic energy. The analyzer is usually operated as an energy window, referred to as the pass energy, accepting only those electrons having an energy within the range of this window. To maintain a constant energy resolution, the pass energy is fixed. Incoming electrons are adjusted to the pass energy before entering the energy analyzer. Scanning for different energies is accomplished by applying a variable electrostatic field before the analyzer. This retardation voltage may be varied from zero up to and beyond the photon energy. Electrons are detected as discrete events, and the number of electrons for a given detection time and energy is stored and displayed.

APPENDIX 3: Binding energies, relative atomic concentrations and FWHM of the XPS core levels of IL based electrolytes

	Chemical bond	C ₁ C ₆ ImTFSI	C ₁ C ₆ ImTFSI LiTFSI	C ₁ C ₆ ImTFSI LiTFSI/VC	C ₁ C ₆ ImTFSI LiTFSI/FEC
C 1s	C _{alkyl}	285.0 (19.9) (1.2)	285.0 (18.6) (1.2)	285.0 (19.4) (1.2)	285.0 (22.0) (1.3)
	C _{hétéro}	286.7 (23.6) (1.7)	286.8 (21.5) (1.7)	286.8 (19.5) (1.7)	286.9 (17.1) (1.7)
	-CF ₃	292.8 (8.6) (1.1)	293.0 (11.1) (1.2)	293.0 (9.6) (1.2)	293.1 (8.7) (1.2)
N 1s	N _{cation}	402.0 (12.5) (1.2)	402.1 (11.8) (1.2)	402.1 (12.0) (1.3)	402.2 (12.1) (1.2)
	N _{anion}	399.4 (6.5) (1.2)	399.6 (8.4) (1.3)	399.7 (10.3) (1.3)	399.8 (9.0) (1.2)
O 1s	*SO ₂ -CF ₃	532.6 (8.8) (1.3)	532.9 (8.9) (1.4)	532.9 (9.4) (1.5)	532.9 (10.7) (1.6)
F 1s	-CF ₃	688.8 (7.9) (1.7)	688.9 (7.4) (1.7)	689.0 (7.3) (1.7)	689.1 (7.8) (1.7)
S 2p	*SO ₂ -CF ₃ 3/2	168.9 (7.8) (1.1)	169.2 (7.9) (1.2)	169.2 (8.0) (1.3)	169.3 (8.2) (1.2)
	*SO ₂ -CF ₃ 1/2	170.1 (3.9) (1.1)	170.4 (3.9) (1.2)	170.4 (4.0) (1.3)	170.4 (4.1) (1.2)

	Chemical bond	C ₁ C ₆ ImFSI	C ₁ C ₆ ImFSI LiTFSI	C ₁ C ₁ C ₆ ImTFSI	C ₁ C ₁ C ₆ ImTFSI LiTFSI
C 1s	C _{alkyl}	285.0 (22.2) (1.2)	285.0 (19.4) (1.2)	284.9 (19.6) (1.2)	284.9 (18.1) (1.2)
	C _{hétéro}	286.7 (24.9) (1.7)	286.8 (23.8) (1.7)	286.3 (21.1) (1.4)	286.3 (18.9) (1.5)
	Ch ₂	-	-	287.6 (5.6) (1.4)	287.6 (3.3) (1.2)
	-CF ₃	-	293.0 (3.6) (1.2)	292.8 (9.0) (1.2)	292.9 (10.0) (1.2)
N 1s	N _{cation}	402.1 (13.8) (1.2)	402.1 (11.9) (1.2)	401.8 (8.1) (1.2)	401.7 (11.6) (1.2)
	N _{anion}	399.7 (7.0) (1.2)	399.8 (8.1) (1.3)	399.3 (4.2) (1.2)	399.5 (8.8) (1.2)
O 1s	*SO ₂	532.9 (10.0) (1.3)	533.0 (9.3) (1.4)	532.5 (13.0) (1.3)	532.7 (9.0) (1.5)
F 1s	S-F	687.7 (9.0) (1.8)	687.7 (2.5) (2.0)	-	-
	-CF ₃	-	688.8 (7.6) (2.0)	688.7 (7.8) (1.7)	688.8 (7.3) (1.7)
	LiF	-	-	-	685.1 (0.3) (1.6)
S 2p	*SO ₂ -F 3/2	169.8 (8.5) (1.1)	170.0 (7.5) (1.4)	-	-
	*SO ₂ -F 1/2	171.0 (4.2) (1.1)	171.1 (3.7) (1.4)	-	-
	*SO ₂ -CF ₃ 3/2	-	169.2 (1.4) (1.3)	168.9 (7.6) (1.1)	169.0 (8.2) (1.3)
	*SO ₂ -CF ₃ 1/2	-	170.1 (0.7) (1.4)	170.0 (3.8) (1.1)	170.2 (4.1) (1.3)

ABSTRACT

The major challenges in the field of the electrochemical energy storage, need of a fundamental research effort on the nature of the chosen materials and their interfaces with electrolytes. This work is crucial for a gain in performance, durability and safety of such systems.

In this context, it is vital a further understanding of the interfacial processes affording to the degradation of the lithium metal-electrolyte interface causing a decrease in the Coulombic efficiency and promoting dendritic growth.

To make progress in these fields, in this thesis we have chosen to study the reactivity, face to lithium metal, of two ionic liquids composed of the anions [TFSI]⁻ and [FSI]⁻ associated with the cation 1-hexyl-3-methylimidazolium in the presence of the LiTFSI salt (1mol.L⁻¹). The *ex-situ* reference study of the different electrolyte combinations aged in Li/Li button cells, by coupling EIS/XPS techniques, have allowed us to understand the different formation mechanisms of the SEI at the interface electrolyte/lithium, according to the nature of the anions, the modification of the cation and the addition of VC and FEC additives. On the other hand, during the electrical polarization, we have highlighted two different dendrite growth regimes depending on the current density applied. The different chemical and morphological states of the lithium surface during these regimes have been compared by studies coupling XPS and SEM/Auger.

Finally, in order to be as close as possible to the real conditions of the phenomena studied, this *ex-situ* study have allowed us to make rigorous progress in the design and implementation of the *operando* XPS characterization protocol, paving the way for a better understanding of the chemical structure of the SEI in real time.

RÉSUMÉ

Face aux grands défis industriels dans les domaines du stockage électrochimique de l'énergie, un effort de recherche fondamentale sur la nature des matériaux choisis et de leurs interfaces avec les électrolytes est aujourd'hui crucial pour gagner en performance, en durabilité et en sécurité.

Dans ce contexte, il est primordial de comprendre les processus interfaciaux mis en jeu qui induisent la dégradation de l'interface SEI lithium métal-électrolyte et entraînent une baisse du rendement Coulombique et favorisent la croissance dendritique.

Pour progresser dans ces domaines, dans ce travail nous avons choisi d'étudier la réactivité, face au lithium métal, de deux liquides ioniques constitués des anions [TFSI]⁻ et [FSI]⁻ associés au cation 1-hexyl-3-méthylimidazolium en présence du sel LiTFSI (1mol.L⁻¹). L'étude de référence *ex-situ* par couplage EIS/XPS des différentes combinaisons d'électrolyte vieilles en piles bouton Li/Li, nous a permis d'appréhender les différents mécanismes de formation de la SEI aux interfaces électrolyte/lithium métal selon la nature des anions, la modification du cation et l'ajout des additives VC et FEC. D'autre part, lors de la polarisation électrique de ces piles, nous avons mis en évidence deux régimes différents de croissance des dendrites dépendantes de la densité de courant appliquée. Les différents états chimiques et morphologiques de la surface du lithium lors de ces régimes sont comparés par des études couplant XPS et SEM/Auger.

Finalement, afin d'être au plus près des conditions réelles des phénomènes étudiés, cet étude *ex-situ* nous a permis d'avancer de manière rigoureuse dans la conception et la réalisation du protocole de caractérisation *operando* XPS, ouvrant la voie à une meilleure compréhension de la structure chimique de la SEI en temps réel.